

1-1-2011

# Control of satellites using environmental forces : aerodynamic drag / solar radiation pressure

Surjit Varma  
*Ryerson University*

Follow this and additional works at: <http://digitalcommons.ryerson.ca/dissertations>



Part of the [Aerospace Engineering Commons](#)

---

## Recommended Citation

Varma, Surjit, "Control of satellites using environmental forces : aerodynamic drag / solar radiation pressure" (2011). *Theses and dissertations*. Paper 676.

This Dissertation is brought to you for free and open access by Digital Commons @ Ryerson. It has been accepted for inclusion in Theses and dissertations by an authorized administrator of Digital Commons @ Ryerson. For more information, please contact [bcameron@ryerson.ca](mailto:bcameron@ryerson.ca).

**CONTROL OF SATELLITES USING ENVIRONMENTAL  
FORCES: AERODYNAMIC DRAG / SOLAR RADIATION  
PRESSURE**

by

Surjit Varma

B.Tech., Electronics Engineering, Cochin University of Science And Technology, 2000

M.Sc., Control Systems, The University of Sheffield, 2005

A dissertation presented to Ryerson University  
in partial fulfillment of the requirements for the degree of

DOCTOR OF PHILOSOPHY

in the Program of

Aerospace Engineering

Toronto, Ontario, Canada, 2011

© Surjit Varma 2011

All rights reserved



## AUTHOR'S DECLARATION

I hereby declare that I am the sole author of this thesis.

I authorize Ryerson University to lend this thesis to other institutions or individuals for the purpose of scholarly research.

---

I further authorize Ryerson University to reproduce this thesis by photocopying or by other means, in total or in part, at the request of other institutions or individuals for the purpose of scholarly research.

---



## ABSTRACT

### CONTROL OF SATELLITES USING ENVIRONMENTAL FORCES: AERODYNAMIC DRAG / SOLAR RADIATION PRESSURE

Surjit Varma, Doctor of Philosophy, Aerospace Engineering  
Ryerson University, Toronto, 2011

The dynamics of a satellite involves orbit and attitude motion. Both orbit and attitude motion are required to be controlled for achieving any mission objectives. This thesis examines both of these motion with a focus on formation flying and attitude stabilization using aerodynamic drag or solar radiation pressure. The concept of satellite formation flying involves the distribution of the functionality of a single satellite among several smaller, cooperative satellites. Autonomous multiple satellite formation flying space missions offer many promising possibilities for space exploration. A large quantity of fuel is typically required onboard any conventional satellite to carry out its attitude and orbital positioning, and satellite formation flying has a higher fuel requirement. As on-board fuel is a scarce commodity, it is important to have control methods requiring little or no fuel. Keeping this in mind, this thesis presents the results of using aerodynamic drag or solar radiation pressure for satellite formation flying. This methodology has potential to have significant commercial advantage as it pertains to almost negligible fuel requirement. A leader/follower formation architecture is considered for the formation flying system. The control algorithms are derived based on adaptive sliding mode control technique. Aerodynamic drag is used to accomplish multiple satellite formation flying in low Earth orbit whereas solar radiation pressure is used in geostationary orbit. Due to the nature of the aerodynamic drag, in-plane control can only be accomplished by the suitable maneuvering of the drag plates mounted on the satellites. Solar radiation pressure is able to accomplish in-plane and out-of-plane control by maneuvering of the solar flaps. Efficacy of the control methodology in performing various scenarios of formation flying including formation reconfiguration is validated by numerical simulation in both the cases. The numerical results demonstrate the effectiveness of the proposed control techniques for satellite formation flying using

aerodynamic drag or solar radiation pressure. Formation flying accuracies of less than 5 m are achieved in both the cases.

Next, this thesis investigates the use of aerodynamic drag or solar radiation pressure for satellite attitude control. In the case of the aerodynamic drag stabilized satellite, the drag plates are considered to be attached to the satellite while the solar flaps are fixed to the satellite in the case of the solar radiation pressure stabilized satellite. In both the cases, the control algorithm is developed based on adaptive sliding mode control technique. The effectiveness of this methodology is numerically evaluated under various scenarios including the presence of failure/fault in the solar flaps or drag plates attached to the satellite. The satellite attitude is stabilized within reasonable limits in all the cases thereby demonstrating robust performance in the presence of external disturbances.

## ACKNOWLEDGEMENTS

First and foremost I would like to convey my heartfelt gratitude to my thesis supervisor Dr. Krishna Dev Kumar, for his guidance, support and patience throughout my doctoral studies. Without his useful insights, encouragement and help, I am sure this dissertation would not have been possible. I would also like to thank my Ph.D committee members, Dr. Arun K. Misra, Dr. Soosan Beheshti, Dr. Kamran Behdinin, Dr. Jeffrey Yokota, and Dr. Hekmat Alighanbari for reviewing my work and providing valuable suggestions in improving the quality and clarity of the thesis.

I have to thank all my colleagues, past and present at the Space Systems Dynamics and Control Lab, especially Dr.Youdong Pan, Dr.Anmin Zou, Dr.Xi Liu, Junquan Li, Tarun Patel, Mike Alger, Daren Lee, Noel Abreu, Bryan Stuurman and Frank Wong, for all the professional and personal help during the past three and half years. Two other individuals I would like to make a special acknowledgment of are Godard and Kam Shahid. I am deeply indebted to both of them for all the help and support extended to me during their doctoral studies and beyond. A big thank you to Dr. Godard and Dr. Kamran Shahid, it was a real pleasure to be working with you guys. Many thanks to Sajjan Abdul, Tom Dzamba, Geoff McVittie, and Dimitri Ignakov for the coffee breaks, discussions, lunches and gaming sessions. I shall definably carry with me indelible memories of the great time spent with all you guys. Special thanks to Kim Gallo, Kirsti Piironen, Sally Noce, Luisa Chan, and Jean-Francois Lemelin for providing the various TA duties.

Nothing would have been possible without the unconditional love and affection of my parents and my sister. I am truly indebted to them for their endless support, trust and love throughout my life and standing by me at all times. Above all I would like to thank God Almighty for all the blessings.



*To ... Achan, Amma, Chechi, and Valiyamma*



# Contents

Author’s Declaration .....	iii
Abstract.....	v
Acknowledgements.....	vii
Dedication.....	ix
List of Figures.....	xv
List of Tables.....	xxi
Nomenclature.....	xxiii
Abbreviations.....	xxvii
List of Publications.....	xxix
<b>1 Introduction</b> .....	<b>1</b>
1.1 Research Motivation .....	2
1.1.1 Rationale Behind the Use of Aerodynamic Drag .....	3
1.1.2 Rationale Behind the Use of Solar Radiation Pressure .....	4
1.1.3 Non-Affine Control Inputs .....	6
1.1.4 Nonlinear Control .....	7
1.1.5 Application to Satellite Formation Flying or Attitude Control .....	8
1.2 Literature Review .....	9
1.2.1 Aerodynamic Drag .....	10
1.2.2 Solar Radiation Pressure .....	12
1.3 Problem Statement .....	16
1.4 Research Objectives .....	18
1.5 Research Contributions .....	20
1.6 Thesis Outline .....	22
<b>2 Satellite Formation Dynamics and Control Methodology</b> .....	<b>23</b>
2.1 SFF System Model .....	23
2.1.1 Equations of Motion .....	24
2.1.2 Hill-Clohessy-Wiltshire Equations .....	26
2.2 Desired Formation Geometry .....	27

---

2.3	External Perturbations . . . . .	30
2.3.1	Aerodynamic Drag Model . . . . .	31
2.3.2	Solar Radiation Pressure Model . . . . .	37
2.4	Control Methodology . . . . .	40
<b>3</b>	<b>Satellite Formation Control Using Aerodynamic Drag</b>	<b>45</b>
3.1	SFF Model and Systems Equations of Motion . . . . .	46
3.1.1	Coordinate Frames and Equations of Motion . . . . .	46
3.1.2	Aerodynamic Drag Model . . . . .	47
3.2	Design of Control Law . . . . .	48
3.2.1	Design of Sliding Manifold . . . . .	49
3.2.2	Control Formulation . . . . .	51
3.2.3	Dynamic System Stability Analysis . . . . .	54
3.2.4	Observer Design . . . . .	56
3.3	Performance Evaluation . . . . .	58
3.3.1	Projected circular formation and Circular formation . . . . .	60
3.3.2	Along-track formation . . . . .	64
3.3.3	Multiple Satellite Formation . . . . .	66
3.3.4	Qualitative Analysis . . . . .	73
3.3.5	Hardware-In-Loop (HIL) testing . . . . .	75
3.4	Summary . . . . .	77
<b>4</b>	<b>Satellite Formation Control Using Solar Radiation Pressure</b>	<b>81</b>
4.1	SFF System Model and Equations of Motion . . . . .	82
4.1.1	Solar Radiation Pressure Model . . . . .	82
4.2	Design of Control Law . . . . .	84
4.2.1	Adaptive Control Formulation and Stability Analysis . . . . .	86
4.3	Performance Evaluation . . . . .	88
4.3.1	Projected circular formation and Circular formation . . . . .	89
4.3.2	Along-track Formation . . . . .	94
4.3.3	Multiple Satellite Formation . . . . .	94

---

4.4	Summary . . . . .	97
<b>5</b>	<b>Satellite Attitude Control Using Aerodynamic Drag</b>	<b>99</b>
5.1	Proposed System Model . . . . .	100
5.1.1	Coordinate Frames . . . . .	101
5.1.2	Satellite Angular Velocity . . . . .	102
5.1.3	Free Molecular Aerodynamic Drag Model . . . . .	104
5.1.4	Equations of Motion . . . . .	106
5.2	Design of Control Law . . . . .	109
5.2.1	Design of Sliding Manifold . . . . .	110
5.2.2	Adaptive Control Formulation and Stability Analysis . . . . .	111
5.3	Performance Evaluation . . . . .	115
5.3.1	Nominal Performance . . . . .	115
5.3.2	Variations in Mass Moment of Inertia . . . . .	116
5.3.3	Eccentricity and External Disturbances . . . . .	119
5.4	Summary . . . . .	123
<b>6</b>	<b>Satellite Attitude Control Using Solar Radiation Pressure</b>	<b>125</b>
6.1	Proposed System Model and Equations of Motion . . . . .	126
6.1.1	Solar Radiation Pressure Model . . . . .	126
6.1.2	Equations of Motion . . . . .	129
6.2	Design of Control Law . . . . .	130
6.2.1	Design of Sliding Manifold . . . . .	131
6.2.2	Adaptive Control Formulation and Stability Analysis . . . . .	132
6.3	Performance Evaluation . . . . .	135
6.3.1	Nominal Performance . . . . .	136
6.3.2	Variations in Mass Moment of Inertia . . . . .	136
6.3.3	Effect of System Parameters . . . . .	138
6.3.4	Eccentricity and External Disturbances . . . . .	140
6.4	Summary . . . . .	142

---

<b>7</b>	<b>Fault Tolerant Satellite Attitude Control Using Solar Radiation Pressure / Aerodynamic Drag</b>	<b>145</b>
7.1	Proposed System Model and Equations of Motion for Pitch Attitude Control	146
7.2	Design of Control Law . . . . .	149
7.3	Adaptive Control Law Design . . . . .	149
7.3.1	Pitch trajectory tracking . . . . .	153
7.4	Performance Evaluation-Pitch Attitude Control . . . . .	155
7.4.1	Nominal performance . . . . .	155
7.4.2	Solar flap failure . . . . .	156
7.4.3	Actuator stuck fault . . . . .	157
7.4.4	Actuator loss of effectiveness . . . . .	158
7.4.5	Time varying actuator fault . . . . .	160
7.5	Three Axis Satellite Attitude Control . . . . .	161
7.5.1	Satellite Attitude Control Using Solar Radiation Pressure . . . . .	161
7.5.2	Satellite Attitude Control Using Aerodynamic Drag . . . . .	163
7.6	Summary . . . . .	166
<b>8</b>	<b>Conclusions</b>	<b>169</b>
8.1	Contributions Outline . . . . .	169
8.1.1	Satellite Formation Control using Aerodynamic Drag . . . . .	170
8.1.2	Satellite Formation Control using Solar Radiation Pressure . . . . .	171
8.1.3	Satellite Attitude Control using Aerodynamic Drag . . . . .	172
8.1.4	Satellite Attitude Control using Solar Radiation Pressure . . . . .	172
8.1.5	Fault Tolerant Satellite Attitude Control Using Solar Radiation Pressure / Aerodynamic Drag . . . . .	173
8.2	Limitations of the proposed technique . . . . .	174
8.3	Future Work . . . . .	174
	<b>Bibliography</b>	<b>177</b>

# List of Figures

1.1	Aerodynamic drag on flat plate (drag plate). . . . .	3
1.2	Force on a non-perfectly reflecting solar flap. . . . .	4
1.3	Taxonomy of AOCS schemes. . . . .	10
1.4	Block diagram representation of an Adaptive Control System . . . . .	19
2.1	Geometry of orbit motion of leader and follower satellite. [Kumar 2006] . . . . .	24
2.2	Along track formation (Courtesy of NASA). . . . .	28
2.3	Projected circular formation. . . . .	29
2.4	Relative $J_2$ disturbance ( $r_p = 6878$ km and $r_d = 0.5$ km, $e=0$ , $\Omega_l = 0^\circ$ , $i_l = 45^\circ$ , and $\omega_l = 0^\circ$ ). . . . .	32
2.5	Relative error due to $J_2$ disturbance. . . . .	32
2.6	Variation of density with altitude. . . . .	35
2.7	Orbit decay under the influence of aerodynamic drag. . . . .	36
2.8	Orbit decay rate under the influence of aerodynamic drag. . . . .	37
2.9	Relative positions of a follower satellite under the influence of differential aerodynamic drag with formation size $r_d = 0.5$ km . . . . .	38
2.10	Force on a non-perfectly reflecting solar flap. . . . .	39
2.11	Relative positions of a follower satellite under the influence of $J_2$ and differential SRP with formation size $r_d = 10$ km. . . . .	41
2.12	Phase portrait of the double integrator under VSC. . . . .	42
3.1	Pictorial representation of the formation system. . . . .	47
3.2	Relative position errors in project circular formation for one day ( $r_d = 0.5$ km). . . . .	61
3.3	Relative position errors control input and adaptive parameter for projected circular formation ( $r_d = 0.5$ km, initial offset errors of 50 m). . . . .	62
3.4	Observed states for projected circular formation ( $r_d = 0.5$ km, initial offset errors of 50 m). . . . .	63

---

3.5	Relative position errors, control input and adaptive parameter for formation reconfiguration from PCF ( $r_d = 0.5$ km) to CF ( $r_d = 1.0$ km). . . . .	63
3.6	Formation reconfiguration from projected circular formation ( $r_d = 0.5$ km) to circular formation ( $r_d = 1.0$ km). . . . .	64
3.7	Relative position errors control angle and adaptive parameter for along track formation ( $r_d = 0.5$ km, initial offset errors of 50 m). . . . .	65
3.8	Relative position errors control angle and adaptive parameter for along track reconfiguration from $r_d = 0.5$ km to $r_d = 5.0$ km. . . . .	66
3.9	Relative position errors during multiple satellite formation flying in projected circular formation ( $r_d = 0.5$ km) . . . . .	67
3.10	Aerodynamic drag plate orientation during multiple satellite formation flying.	68
3.11	Relative position errors during multiple satellite formation flying in projected circular formation for one day. . . . .	69
3.12	System response during multiple satellite reconfiguration in PCF (Sat-1: $r_d = 0.25$ km to $r_d = 0.5$ km; Sat-2: $r_d = 0.5$ km to $r_d = 0.75$ km). . . . .	70
3.13	Variation of mean relative error in x and y- axis for the four follower satellites over a 1000 numerical simulation runs. . . . .	71
3.14	Relative position errors along track formation with $e = 0.001$ . . . . .	72
3.15	Relative position errors along track formation with $e = 0.01$ . . . . .	72
3.16	Leader satellite under the influence of aerodynamic drag . . . . .	74
3.17	Leader satellite under the influence of aerodynamic drag (3-D plot) . . . . .	74
3.18	Relative position errors in projected circular formation with $i = 45^\circ$ , $e = 0.001$ . . . . .	75
3.19	Variation of aerodynamic force with respect to projected area and altitude.	76
3.20	Block diagram of HIL testing. . . . .	76
3.21	Relative position errors and commanded angle during along track formation flying. . . . .	77
3.22	Relative position errors and commanded angle during projected circular formation flying. . . . .	78

---

3.23	Relative position errors and commanded angle during projected circular formation reconfiguration. . . . .	78
4.1	Orientation of the solar flap . . . . .	83
4.2	Relative position errors of the follower satellite in projected circular formation ( $r_d = 10\text{km}$ ). . . . .	90
4.3	Area change and control angle orientation of the solar flaps on the follower satellite in a projected circular formation ( $r_d = 10\text{km}$ ). . . . .	91
4.4	Relative position errors of the follower satellite in projected circular formation ( $r_d = 10\text{km}$ ) with initial offset error of 100 m. . . . .	91
4.5	Area change and control angle orientation of the solar flaps on follower satellite in projected circular formation ( $r_d = 10\text{km}$ ) with initial offset error of 100 m. . . . .	92
4.6	Reconfiguration of follower satellites from a projected circular formation (PCF) of $r_d = 5$ km to a circular formation (CF) of $r_d = 10$ km. . . . .	93
4.7	Area change and control angle orientation of the solar flaps on the follower satellite during formation reconfiguration. . . . .	93
4.8	Relative position errors of the follower satellite in the radial and along-track direction during along track formation flying with $r_d = 10$ km. . . . .	94
4.9	Relative position errors of the follower satellite during multiple satellite formation flying in PCF of size, $r_d = 10$ km. . . . .	95
4.10	Multiple satellite formation reconfiguration. . . . .	96
5.1	Geometry of orbit motion of rigid satellite. . . . .	100
5.2	Performance of the adaptive sliding mode controller during attitude stabilization, $k_1 = 0.3$ , $k_2 = 0.2$ . . . . .	117
5.3	Response of angular velocity and estimated adaptive parameter, $k_1 = 0.3$ , $k_2 = 0.2$ . . . . .	118
5.4	Performance of the adaptive sliding mode controller during attitude stabilization, $k_1 = 0.177$ , $k_2 = 0.177$ . . . . .	119

---

5.5	Response of angular velocity and estimated adaptive parameter, $k_1 = 0.177$ , $k_2 = 0.177$ . . . . .	120
5.6	Performance of the adaptive sliding mode controller during attitude stabilization, $k_1 = 0.3$ , $k_2 = 0.2$ with product of inertia terms. . . . .	120
5.7	Response of angular velocity and estimated adaptive parameter, $k_1 = 0.1$ , $k_2 = -0.2$ . . . . .	121
5.8	Performance of the adaptive sliding mode controller during attitude stabilization, $e=0.01$ . . . . .	122
5.9	Performance of the adaptive sliding mode controller during attitude stabilization, $e=0.1$ . . . . .	122
5.10	Performance of the adaptive sliding mode controller during attitude stabilization in the presence of external disturbances . . . . .	123
6.1	Configuration of the proposed solar controller. . . . .	127
6.2	Geometry of orbit motion of rigid satellite. . . . .	128
6.3	Performance of the adaptive sliding mode controller during attitude stabilization, $k_1 = 0.3$ , $k_2 = 0.2$ . . . . .	137
6.4	Response of angular velocity and estimated adaptive parameter, $k_1 = 0.3$ , $k_2 = 0.2$ . . . . .	137
6.5	Performance of the adaptive sliding mode controller during attitude stabilization, $k_1 = 0.177$ , $k_2 = 0.177$ . . . . .	138
6.6	Response of angular velocity and estimated adaptive parameter, $k_1 = 0.177$ , $k_2 = 0.177$ . . . . .	139
6.7	Performance of the adaptive sliding mode controller during attitude stabilization, $k_1 = 0.3$ , $k_2 = 0.2$ with product of inertia terms. . . . .	139
6.8	Response of angular velocity and estimated adaptive parameter, $k_1 = -0.1$ , $k_2 = 0.2$ . . . . .	140
6.9	Effect of solar aspect angle $\psi$ on solar flap deflection and attitude tracking: (a) $\psi = 45^\circ$ , (b) $\psi = 90^\circ$ , (c) $\psi = 135^\circ$ . . . . .	141
6.10	Performance of the adaptive sliding mode controller during attitude stabilization, $e=0.1$ . . . . .	142

---

6.11	Performance of the adaptive sliding mode controller during attitude stabilization in the presence of external disturbances . . . . .	143
7.1	Configuration of the proposed solar controller. . . . .	146
7.2	Performance of the adaptive sliding mode controller under attitude tracking.	157
7.3	Performance of the adaptive sliding controller under solar flap failure at 0.3 orbit. . . . .	158
7.4	Performance of the sliding controller under solar flap failure at 0.3 orbit. . . . .	159
7.5	Performance of the adaptive sliding controller under actuator stuck fault from 0.3 orbit. . . . .	159
7.6	Performance of the sliding controller under actuator stuck fault from 0.3 orbit.	160
7.7	Performance of the adaptive sliding controller under actuator degradation (90%)fault. . . . .	160
7.8	Performance of the adaptive sliding controller under periodic actuator fault from 0.3 orbits. . . . .	161
7.9	Performance of the adaptive controller under solar flap failure at 0.3 orbit.	162
7.10	Performance of the adaptive controller under actuator stuck fault from 0.3 orbit. . . . .	163
7.11	Performance of the adaptive controller under actuator degradation (90%)fault.	164
7.12	Performance of the adaptive controller under failure at 0.3 orbit. . . . .	165
7.13	Performance of the adaptive controller under actuator stuck fault from 0.3 orbit. . . . .	166
7.14	Performance of the adaptive controller under actuator degradation (90%)fault.	167



# List of Tables

1.1	List of missions making use of aerodynamic drag . . . . .	13
1.2	List of missions making use of solar radiation pressure . . . . .	17
2.1	Optical Coefficients. . . . .	40
3.1	Orbital and system parameters . . . . .	59
3.2	Controller and observer parameters . . . . .	59
3.3	Additional parameters for multiple satellite formation flying . . . . .	69
4.1	Orbital and system parameters . . . . .	89
4.2	Controller parameters . . . . .	90
5.1	System parameters. . . . .	116
5.2	Variations in satellite moments of inertia . . . . .	117
6.1	System parameters. . . . .	135
7.1	Simulation parameters . . . . .	156



## NOMENCLATURE

### List of lowercase symbols

$a_c$	semi-major axis of the reference orbit
$e$	eccentricity of the reference orbit
$e_x$	relative radial position tracking error
$e_y$	relative along-track position tracking error
$e_z$	relative cross-track position tracking error
$e_f$	front surface emission coefficient of solar flap
$e_b$	back surface emission coefficient of solar flap
$f_{dj}$	relative perturbations due to external forces, $j = x, y, z$
$i_l$	orbit inclination of leader satellite
$m_f$	mass of the follower satellite
$n$	outward pointing unit normal vector
$p$	nominal solar radiation pressure constant at 1AU from the Sun
$r_f$	radial position of the follower satellite from the Earth centre
$r_l$	radial position of the leader satellite from the Earth centre
$r_d$	nominal radius of the desired formation
$s$	air speed (Chapter 5)
$t_r$	reaching time
$f_j$	follower satellite control input components, $j = x, y, z$
$x$	radial separation between leader and follower satellite
$y$	along-track separation between leader and follower satellite
$z$	cross-track separation between leader and follower satellite

### List of uppercase symbols

$A$	Area of the drag plates/solar flaps
$B_f$	non-Lambertian coefficient for front surface of solar flaps
$B_b$	non-Lambertian coefficient for back surface of solar flaps

---

$C_D$	Drag coefficient
$C_L^B$	direction cosine matrix
$L$	upper bound of external perturbations
$H$	scale height
$I_r$	satellite mass distribution parameter
$J_2$	second zonal harmonic coefficient of the Earth's gravity field
$K_j$	control gains, $j = 1, 2, 3, 4$
$P_j$	control gains, $j = 1, 2, 3, 4$
$M$	molecular mass
$R_e$	radius of the Earth
$S$	sliding surface
$T$	kinetic energy function
$T_s$	absolute temperature of the satellite surface
$T_a$	atmospheric temperature
$T_{IB}$	rotation matrix to transform from the ECI frame to orbital frame
$V_{rel}$	satellite relative velocity w.r.t local atmosphere

### List of Greek symbols

$\alpha$	satellite pitch angle
$\alpha_s$	solar flap out-of-plane orientation
$\beta$	drag plate/solar flap orientation (Chapter 5 and Chapter 6)
$\gamma$	adaptive gain (Chapter 3)
$\gamma$	satellite yaw angle (Chapter 5 and Chapter 6)
$\delta$	sliding surface boundary layer
$\varepsilon$	angle between the equatorial and ecliptic planes
$\zeta$	adaptive control parameter
$\eta$	positive design scalar to determine sliding surface reaching time
$\theta$	true anomaly
$\mu_e$	geocentric gravitational constant of the Earth
$\rho$	atmospheric density

---

$\rho_d$	diffuse reflection coefficient of the solar flap
$\rho_r$	reflectivity of the front surface of the solar flap
$\rho_s$	specular reflection coefficient of the solar flap
$\sigma$	linear sliding manifold
$\sigma_n$	normal accommodation coefficient in the free molecular aerodynamic force model
$\sigma_t$	tangential accommodation coefficient in the free molecular aerodynamic force model
$\tau$	shearing stress
$\tau_g$	gravity gradient torque
$\phi$	satellite roll angle (Chapter 5 and Chapter 6)
$\phi$	in-plane formation phase angle (Chapter 3 and Chapter 4)
$\phi_s$	solar flap in-plane orientation
$\psi$	solar aspect angle
$\Omega_l$	right ascension of the ascending node of leader satellite orbit
$\omega_0$	magnitude of orbital angular velocity of LVLH frame
$\omega_{BI}^B$	angular velocity vector relative to inertial frame expressed in body frame
$\omega_l$	argument of perigee of leader satellite orbit
$\xi$	observer gain (Chapter 3)
$\xi$	sliding manifold gain (Chapter 5)
$\varsigma$	adaptive gain (Chapter 5)
$\zeta$	adaptive gain (Chapter 4)

### List of reference frames

$\mathfrak{B} - xyz$	satellite body-fixed coordinate frame
$E - XYZ$	Earth centered inertial reference frame
$\mathfrak{L} - x_o y_o z_o$	local vertical local horizontal orbital reference frame

### Notational conventions

$ \cdot $	absolute value
$\ \cdot\ $	Euclidean norm for vectors, induced norm for matrices

$(\cdot)_0$	$(\cdot)$ at $t = 0$
$(\dot{\cdot})$	derivative of $(\cdot)$ with respect to time, $t$
$(\cdot)'$	derivative of $(\cdot)$ with respect to $\theta$
$(\hat{\cdot})$	parameter estimate
$(\tilde{\cdot})$	parameter estimation error

## ABBREVIATIONS

AF	Along-track Formation
AOCS	Attitude and Orbit Control System
CF	Circular Formation
HCW	Hill-Clohessy-Wiltshire
ECI	Earth Centered Inertial
HIL	Hardware-In-Loop
LEO	Low Earth Orbit
LVLH	Local Vertical Local Horizontal
NRLMSISE	Naval Research Laboratory Mass Spectrometer and Incoherent Scatter Radar Exosphere
PCF	Projected Circular Formation
SDRE	State Dependant Riccati Equation
SFF	Spacecraft Formation Flying
SRP	Solar Radiation Pressure
SMC	Sliding Mode Control
VSC	Variable Structure Control



---

## LIST OF PUBLICATIONS

### Articles published or accepted in refereed journals:

1. Varma, S., Kumar, K.D., "Fault tolerant satellite attitude control using solar radiation pressure based on nonlinear adaptive sliding mode," *Acta Astronautica*, Vol. 66, No. 3-4, pp. 486-500, 2010.

### Articles submitted to refereed journals:

1. Varma, S., Kumar, K.D., "Satellite Formation Flying using Differential Aerodynamic Drag," (Log. No.: A30508, Submitted: September, 2010) *AIAA Journal of Spacecraft and Rockets*, pp. 1-41, 2010.
2. Varma, S., Kumar, K.D., "Three-Axis Satellite Attitude Control Using Aerodynamic Drag based on Adaptive Sliding Mode," (Submitted: March 30, 2011) *IEEE Transactions on Aerospace and Electronic Systems*, pp. 1-27, 2011
3. Varma, S., Kumar, K.D., "Satellite Attitude Control Using Four Solar Flaps in Under-actuated Configuration," (Submitted: April 11, 2011) *IEEE Transactions on Control Systems Technology*, pp. 1-32, 2011

### Articles published in refereed conference proceedings:

1. Varma, S., Kumar, K.D., "Satellite Formation Flying using Differential Aerodynamic Drag," *Proceedings of the 20th AAS/AIAA Space Flight Mechanics Meeting - AAS 10-111*, San Diego, CA, Feb. 14-17, 2010.
2. Varma, S., Kumar, K.D., "Three Axis Satellite Attitude Control using Solar Radiation Pressure," *Proceedings of the 20th AAS/AIAA Space Flight Mechanics Meeting - AAS 10-111*, San Diego, CA, Feb. 14-17, 2010.
3. Varma, S., Kumar, K.D., "Satellite Formation Flying using Solar Radiation Pressure and/or Aerodynamic Drag," *Proceedings of the 12th International Space Conference of Pacific-basin Societies (ISCOPS)*, Montreal, Quebec, Canada, July 27 - 30, 2010.

4. Varma, S., Kumar, K.D., "Multiple Satellite Formation Flying Using Differential Solar Radiation Pressure," *Proceedings of the AIAA/AAS Astrodynamics Specialist Conference*, Toronto, Ontario, Canada, August 2-5, 2010.

## CHAPTER 1

# Introduction

---

**A**UTONOMOUS formation flying is currently one of the most important areas of research in satellite dynamics and control. Use of a cluster of smaller, closely flying satellites can distribute the functionality of a single, complex satellite. Space agencies, in particular NASA, ESA and U.S. Air Force have taken a keen interest in developing and deploying reliable autonomous multiple satellite systems. This approach has several advantages including the ability to enhance and/or enable missions through increased resolution of scientific observations, improved flexibility and redundancy. Moreover capability for real-time reconfiguration, adaptable to highly dynamic demands, and lower life cycle cost also drive this methodology. Key challenges involved in these missions include autonomous control of the satellites which are influenced by the different disturbing forces, and to achieve it with minimum fuel consumption. These forces include environmental forces caused by gravity gradient, solar radiation pressure, magnetic, aerodynamic drag, and Earth's oblateness effect [Larson 1999, Kumar 2006], as well as third body perturbations. It is the *Attitude and Orbit Control System* (AOCS), that orients and stabilizes the satellite to the desired position in the presence of these external forces. AOCS consists of sensors to measure states of the satellites, actuators to apply the torques needed to re-orient the satellite to the desired position, and also control laws, i.e., a set of computations that determine how the actuators should operate, based on the sensor measurements. However, some of these disturbing forces, if properly utilized may be used to stabilize the satellite orientation and maintain the formation. Several methods of satellite attitude and orbit control have been developed over the last four decades. These methods may be broadly classified as active and passive/semi-passive methods. Active stabilization methods require expenditure of propellant or energy, leading to an increase in weight and space requirements in the satellite, whereas passive/semi-passive methods depend on natural/environmental forces and

they make use of spin stabilization, dual spin, gravity gradient, solar radiation pressure (SRP), aerodynamic drag, and Earth's magnetic field to achieve the desired performance. These methods are thus less costly and their advancement may provide a viable solution to the development of low cost AOCS for satellites. However, their development poses several challenges including lack of methodologies to utilize these forces effectively, lower achievable accuracies compared to a conventional system, and unavailability of these forces throughout the mission. This thesis investigates the efficacy of "propellant-less" method based on aerodynamic drag or solar radiation pressure for multiple satellite formation flying or attitude control, and develops innovative control algorithms with the goal of achieving a low cost AOCS which is able to exhibit superior performance.

## 1.1 Research Motivation

A large quantity of fuel is typically required onboard any conventional satellite to perform its attitude and orbital control. Satellite formation flying has a much higher fuel requirement in order to maintain the tight formation ( $\sim 10m$ ). As on-board fuel is a scarce commodity, it is important to have satellite control techniques which would require little or no fuel. Hence it would be important to propose a novel method for replacement of on-board fuel. The proposed method must be efficient and guarantee robust system performance. It is here that the method based on environmental forces such as solar radiation pressure or aerodynamic drag find potential usage. Here we propose a technique to harness solar radiation pressure or aerodynamic drag for satellite control. The proposed technique has the potential to have significant cost savings as it pertains to almost negligible fuel requirement in comparison to formation control using thrusters. In other words, this technology will increase the life span of a satellite, and also decrease the overall mass of the satellite thus resulting in significant cost savings for space missions and also enable formation architectures and orbits previously thought to be too fuel-demanding. Furthermore, this approach avoids the problem of thruster plume impingement when satellites are very close in the formation.

Another aspect is the control algorithm involved in the satellite AOCS. The development

of practically viable autonomous satellite control algorithms has not kept pace with new capabilities enabled by novel hardware designs and increased computational power and typically tends to employ linear control algorithms for its attitude and orbital control. Here a more robust control algorithm based on nonlinear Sliding Mode Control (SMC) is proposed.

### 1.1.1 Rationale Behind the Use of Aerodynamic Drag

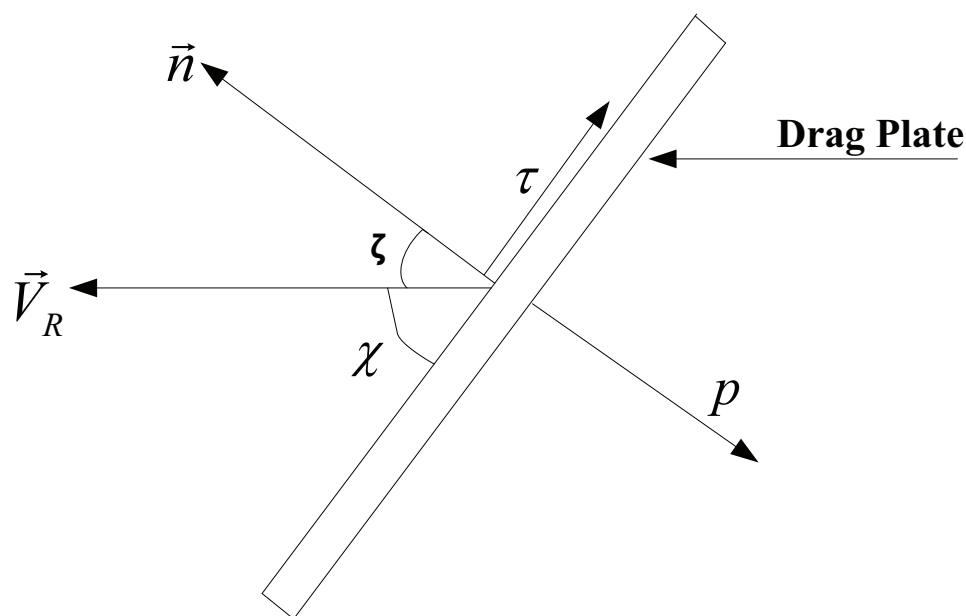


Figure 1.1: Aerodynamic drag on flat plate (drag plate).

Aerodynamic drag has a substantial influence on the motion of near-Earth satellites. Even though the atmosphere in the low Earth orbits (LEO) is extremely thin, it can have a considerable impact on a satellite's orbit by retarding its orbital motion and leading to eventual decay. The atmosphere at LEO consists of diffuse molecules that have very little, if any, interaction with one another. This region, known as the free molecular flow regime, consists of molecules that no longer behave like a fluid, rather they behave as individual particles [Regan 1984]. At orbital speeds, the individual molecular impacts on the satellite can greatly affect the motion of the satellite especially over an extended period of time. When the molecules impact and bounce off the satellite surface, linear momentum

is transferred through the inelastic collisions. This is proportional to the velocity difference between the molecules and the satellite [Wiesel 2003]. Since force is the rate of change of linear momentum, these individual impacts impart an acceleration to the satellite in the direction opposite to its motion. The drag experienced by the satellite is proportional to its drag coefficient, the exposed frontal area, the square of the satellite relative velocity and the density of the local atmosphere. Fig. 1.1 shows a simplified representation of the force due to aerodynamic drag experienced by a flat plate surface of the satellite as it moves in the direction of  $V_r$ .  $\zeta$  is the angle between the relative velocity,  $\vec{V}_R$ , and the outward unit normal vector  $\vec{n}$  of the flat plate. Existing literature on the favorable applications of aerodynamic drag for AOCS is rather small. This may be due to the complex nature of the free molecular forces, rotation of the atmosphere, and strong dependence of density on height, season, sun-position, and local atmospheric variations. The lack of a complete understanding of the atmospheric model also adds to the limited effort in their utilization.

### 1.1.2 Rationale Behind the Use of Solar Radiation Pressure

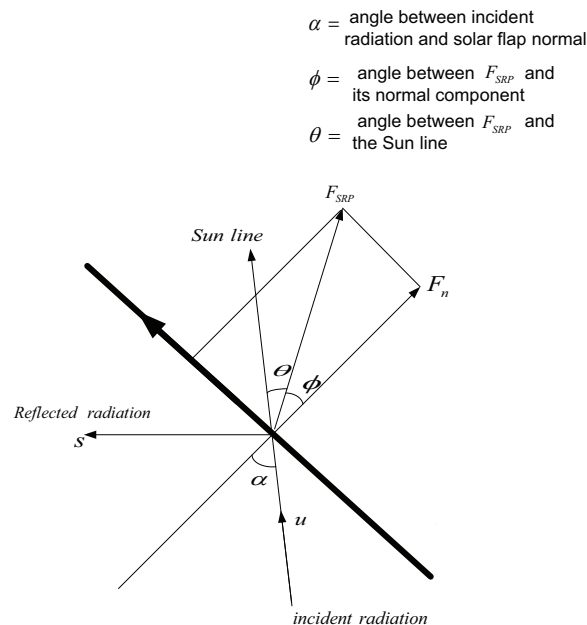


Figure 1.2: Force on a non-perfectly reflecting solar flap.

When a flat plate is illuminated by sunlight, it experiences solar radiation pressure

(SRP). Using quantum mechanics, this pressure can be envisaged as being due to momentum transported by photons, the quantum packets of energy of which light is composed [McInnes 1999]. Fig. 1.2 shows the underlying principle of force due to SRP ( $F_{SRP}$ ), acting on a flat surface. Here  $F_n$  and  $F_t$  represent the normal and transverse components of the force respectively. The pressure exerted by an individual photon is very small, of the order of about  $1 \times 10^{-6} N/m^2$  at Earth radii, but when a large surface is used to intercept the sunlight, significant pressure can be achieved. This can then be harnessed to provide a new form of propulsion for space missions - SRP. SRP is the dominant environmental force in the higher Earth orbits, and hence SRP would be ideal for satellites in geostationary/geosynchronous orbits. The potential SRP applications include orbit raising, de-orbiting, and attitude control. Although the physics of solar radiation pressure is well developed, only recent advancement in technology has made it possible to develop and test extremely light but strong materials necessary for improving the performance of such SRP based systems. The solar flap/sail designs range in size from a few meters to hundreds of meters depending on the mission. In 2005, two industry teams comprised of ATK Space Systems and L'Garde both successfully deployed 20m x 20m solar sails in a high vacuum chamber with appropriate thermal environment. Launch vibration and ascent vent tests were also performed on these systems [Johnson *et al.* 2007]. In 2008, NASA reported the results of a study on the application of solar sail for small satellite propulsion, and NanoSail-D, a cubesat class satellite was built to demonstrate solar sail propulsion. Unfortunately, the satellite was lost in a launch failure aboard Falcon 1 rocket [Johnson *et al.* 2010]. Japan Aerospace Exploration Agency (JAXA) recently launched the IKAROS (Interplanetary Kite-craft Accelerated by Radiation Of the Sun) [Yamaguchi *et al.* 2010] satellite which successfully deployed a square sail of 20 m. The sail membrane is made of 7.5  $\mu m$  thick sheet of polyamide resin deposited with a thin-film of aluminium. Liquid crystal devices which are thin-film instrument that can change the surface reflection characteristics by turning on and off the power of the device are embedded in the sail for attitude control. This is the first instance of a successful mission utilizing solar photons for propulsion. From these recent advancements, we can infer that SRP propulsion is an advancing technology that has the potential to provide cost effective, "propellantless" propulsion that enables

longer mission lifetimes, and critical mass saving.

However, use of aerodynamic drag or solar radiation pressure for autonomous control of a satellite under a wide variety of operating conditions is a challenging task. But with the combination of improved manufacturing techniques and design of a robust control algorithm, use of aerodynamic drag and solar radiation pressure for satellite formation flying or attitude control is highly promising.

### 1.1.3 Non-Affine Control Inputs

Further development of aerodynamic drag and SRP technology will require a robust control system that is able to properly direct the resultant thrust vectors. The control inputs due to SRP or aerodynamic drag are typically the orientation angles. The relationship between these angles and the resultant force is nonlinear. Review of the existing literature on the use of aerodynamic drag or SRP as a means of propulsion shows that majority of the control strategies used to date have been based on linear techniques. This is due to the manner in which the control formulation for aerodynamic drag or SRP enters the system dynamics. Consider the following system that is nonlinear in the state vector  $x$  and linear in the control input  $u$

$$\dot{x} = f(x, t) + B(x, t)u(x, t) \quad (1.1)$$

where  $x \in \mathbb{R}^n$  is the state vector,  $f(x, t) \in \mathbb{R}^n$  represents the nonlinearity of the system,  $B(x, t) \in \mathbb{R}^{n \times m}$  is the input matrix, and  $u \in \mathbb{R}^m$  is the control vector. This dynamic system is classified as affine with respect to the control input  $u$ , since  $u$  appears linearly in the system. A satellite controlled by a conventional propulsion system falls under this category.

Now, consider the following system that is nonlinear in the state vector  $x$  and nonlinear in the control input  $u$

$$\dot{x} = f(x, t) + B(x, t)g[u(x, t)] \quad (1.2)$$

where  $x \in \mathbb{R}^n$  is the state vector,  $f(x, t) \in \mathbb{R}^n$  represents the nonlinearity of the system,  $B(x, t) \in \mathbb{R}^{n \times m}$  is the input matrix, and  $u \in \mathbb{R}^m$  is the control vector, and  $g[u(x, t)]$  is the nonlinear control input function. Such systems are classified as nonaffine with respect to the control input  $u$ , since the resultant input to the system is a nonlinear function of  $u$ .

Another classification of the dynamical systems given by Eqs. (1.1) and (1.2) is based on the actuator configuration. If the number of control inputs,  $m$ , regulating the system in Eqs. (1.1) and (1.2) is equal to the number of degrees of freedom to be controlled ( $p$ ), i.e.,  $m = p$ , then the system is said to be fully actuated. But if  $m < p$ , then for the system in Eqs. (1.1) and (1.2) there are  $p - m$  degrees of freedom that are unactuated. These system are said to be in an underactuated configuration.

The proposed method of using SRP and aerodynamic drag for satellite attitude and orbit control falls into the category of nonaffine, underactuated system. To address these type of systems, nonlinear control techniques are considered in this thesis.

#### 1.1.4 Nonlinear Control

The design of AOCS for a satellite is a complex task because most satellites exhibit inherently coupled nonlinear dynamics. For a nonlinear system undergoing large dynamic changes, a linear controller is likely to have poor performance, when compensating for nonlinearities in the system. Therefore, nonlinear control techniques based on global representation of satellite dynamics are needed to ensure that the control objectives are met over a large range of operating conditions. Satellites commonly operate in the presence of various disturbances (inherent nonlinearities), including environmental and non-environmental torques. The problem of disturbance rejection is important for satellites because their dynamics is substantially affected by most of these preceding nonlinear disturbances. Therefore, nonlinear control techniques must be developed to improve the performance of space systems in the presence of inherent nonlinearities. High-performance tracking is another motivation to justify the use of nonlinear control methods. Simple linear control cannot handle the dynamic demands of efficiently desired trajectories. Specifically, achieving global stabilization using nonlinear control techniques [Slotine & Li 1991] indicates that it is possible to ensure that the satellite tends to a desired equilibrium or trajectory irrespective of the initial conditions. Assuming that the parameters of the satellite are reasonably well known, linear control techniques only provide local stability because many control problems involve uncertainties in the satellite parameters, which may be constant with respect to time, or may slowly vary with respect to the changing environment in which the satellite

is operating. A linear controller based on imprecise values of satellite parameters may degrade the performance of the system significantly by causing the satellite dynamics to deviate largely from its nominal regime. In general, it is very important to systematically explore the use of nonlinear control methods for high precision requirements. A robust adaptive control algorithm should be designed, that is rather independent of system parameters or unknown disturbances, where the uncertainties on constant or slowly-varying parameters are reduced by parameter adaptation and other sources of uncertainties and disturbances are handled by inherent robustness of the controller.

### 1.1.5 Application to Satellite Formation Flying or Attitude Control

Satellite formation flying (SFF) has been identified as an enabling technology for many future space missions [Neeck *et al.* 2005]. Satellite formation flying is the concept that multiple satellites can work together in a group to accomplish the objective of one larger satellite, and is expected to have several advantages over single satellite like simpler design of small satellite, faster build times, cheaper replacement creating higher redundancy and the ability to enhance and/or enable missions through increased resolution of scientific observations, and the ability to view research targets from multiple angles or at multiple times [Bauer *et al.* 2001]. Coordinated autonomous control of satellite formations imposes several stringent requirements on the design of AOCS subsystem because the formation objectives can be achieved efficiently only when all individual satellites are tightly controlled to respond rapidly and accurately to formation coordination commands. The development of a robust controller for SFF poses the following challenges, namely:

*a. Acquisition of a satellite formation:* For large formations, typically all satellites are integrated as one single unit during launch and transfer to orbit. When the carrier spacecraft has reached the target location in orbit, the individual satellites sequentially leave the carrier to reach the specified formation pattern. Therefore, to produce a cohesive formation, the control system must ensure proper relative motion of multiple satellites to maintain the desired formation geometry.

*b. Reconfiguration of the formation geometry:* The ability of a formation to reconfigure

its relative geometry is of primary importance for many missions in order to meet changes in operational needs, or allow for multi-mission capability.

*c. Formation keeping of the satellite:* This is one of the most important control requirements as each satellite in the formation is required to precisely track desired formation trajectories where the external disturbances cause a drift of both the relative positions of the satellite and the formation center.

Traditional feedback controllers consider the aerodynamic drag or SRP as perturbations. Utilizing these environmental forces for control of satellites is a challenging problem as these environmental forces are unpredictable due to several factors. These factors include variations in the solar irradiance, inaccurate coefficients of the optical properties of the satellite surface materials, and variations in aerodynamic coefficients, atmospheric conditions, and satellite mass. This research focuses on the application of aerodynamic drag or SRP for satellite formation control. A system comprising of satellites attached with flaps to utilize these environmental forces is investigated and a robust control technique is developed for suitably rotating these control flaps to achieve the desired satellite performance (position or pointing) in the presence of various external disturbances and uncertainties in the system parameters.

## 1.2 Literature Review

Satellite attitude and orbit control systems can be classified as active control systems and passive or semi-passive control systems. Fig. 1.3 shows the taxonomy of the AOCS classification. The use of SRP or aerodynamic drag as control variable falls under the passive control scheme. When they are used in conjunction with maneuverable plates/flaps, it can be classified under active control. In this section a detailed review of the various missions or feasibility studies carried out with solar radiation pressure and/or aerodynamic drag as the means of orbit control, attitude control or formation flying is presented.

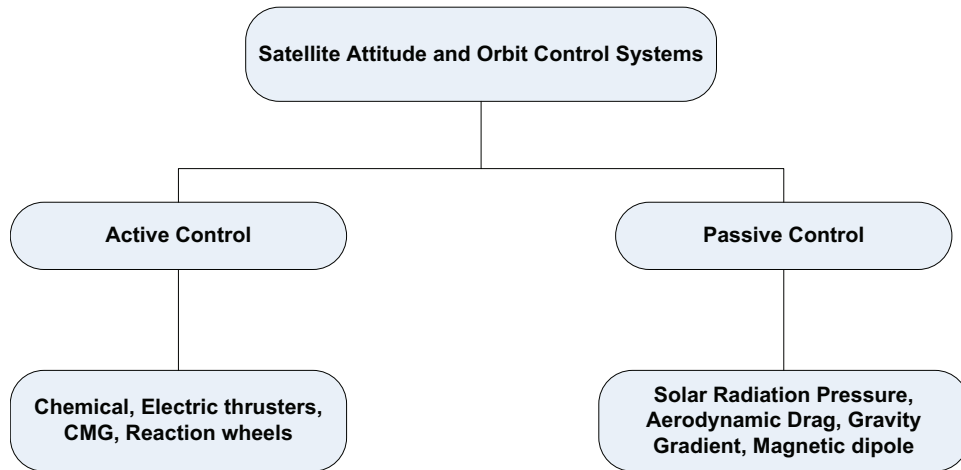


Figure 1.3: Taxonomy of AOCS schemes.

### 1.2.1 Aerodynamic Drag

We start by reviewing the existing literature on the use of aerodynamic drag for satellite attitude and orbit control. First, application of aerodynamic drag for satellite formation flying is reviewed. Existing literature on satellite attitude control using aerodynamic drag is reviewed next followed by the list of missions that employed or proposed to employ aerodynamic drag for satellite control.

#### 1.2.1.1 Formation Flying using Aerodynamic Drag

Formation keeping using aerodynamic forces has been studied by different researchers. Leonard et al. [Leonard *et al.* 2004] considered differential aerodynamic drag while Matthews and Leszkiewicz [Matthews & Leszkiewicz 1988], and Steffy et al. [Steffy *et al.* 1988] varied ballistic coefficients of the satellite for maintaining the formation. Leonard et al. proposed the use of differential drag for orbital control, by simplifying the formation keeping problem to the simultaneous solution of a double integrator and a harmonic oscillator without accounting for  $J_2$  effect. Aorpimai et al. [Aorpimai *et al.* 1999] assumed satellite equipped with aerodynamic wings and varied the angle of attack to establish the formation. The New Millennium Program Earth Observation-1 (NMP EO-1) is an example of successful application of aerodynamic forces for formation flying [Folta & Hawkins 1996]. Another research carried out by Utah State University studied the use of differential aero-

dynamic drag as means of orbital control for formation flying in the Ionospheric Observation Nanosatellite Formation (ION-F) experiment [Swenson *et al.* 2002]. Here the ballistic coefficient was altered for orbital control and controlled permanent magnet torquing method was used for attitude control with GPS information to keep the formation. In [Carter & Humi 2002] a modified Clohessy-Wiltshire equation [Clohessy & Wiltshire 1960] which includes quadratic drag is studied. This modified Clohessy-Wiltshire equation can find application in station keeping and formation flying. In [Kumar *et al.* 2007b] use of differential drag as a means for nanosatellite formation control is studied and a simple PI control law is derived to adjust the cross sectional area of the satellites to maintain an along track formation. Orbital maneuvering using aerodynamic forces was first proposed by London [London 1962] in 1962. Since then, many researchers have worked on this subject; an excellent survey of the past work was presented by Miele [Miele 1996]. Rao [Rao *et al.* 2002] considered optimal aero-assisted orbit transfers from low Earth orbit to geostationary orbit with a large plane change. Lohar *et al.* [Lohar *et al.* 1998] examined orbit transfer between coplanar elliptical orbits using aero-cruise. The use of aerodynamic force for orbit control of a single satellite has been studied by Palmerini [Palmerini *et al.* 2005] and Humi [Humi & Carter 2002]. Formation keeping and rendezvous of multiple satellites have also been investigated [Carter & Humi 2002, Humi & Carter 2001]. In more recent studies, Bevilacqua *et al.* [Bevilacqua & Romano 2008, Bevilacqua *et al.* 2009] examine multiple satellite rendezvous using differential aerodynamic drag by considering the linearized differential equations by Schweighart and Sedwick [Schweighart & Sedwick 2002].

### 1.2.1.2 Attitude Control using Aerodynamic Drag

Aerodynamic drag have been considered for attitude control of satellites over the past three decades. Modi and Shrivastava [Modi & Shrivastava 1973] assumed a system of flaps, and flap rotation to damp the attitude motion of a satellite and it was regulated based on linear feedback control with saturation constraints as well as bang-bang control with linear switching criteria. Using similar flaps, Ravindran and Hughes [Ravindran & Hughes 1972] considered performance optimization of an aerodynamic controller by minimizing a performance index weighted equally with respect to the attitude errors and control surface move-

ments. Successful application of aerodynamic forces for pitch control of COSMOS-149 was reported by Sarychev [Sarychev 1968]. An optimal aerodynamic stabilization of near-Earth satellites was investigated by Pande and Venkatachalam [Pande & Venkatachalam 1979]. Recently Chen Y. H et al. [Chen *et al.* 2000] has proposed the combined use of aerodynamic and gravity gradient torque for three axis stabilization of a microsatellite using gravity gradient boom and vertical tail stabilizer. Propellant-less methods have their own limitations and to overcome these limitations, methods using combinations of various environmental forces have been envisaged, such as aerodynamic and gravity (aero-gravity assist), aerodynamic and magnetic forces. Kumar et al. [Kumar *et al.* 1995] examined passive aerodynamic stabilization and passive magnetic hysteresis damping of attitude rates while Chen et al. [Chen *et al.* 2000] considered aerodynamic torque for yaw stabilization and the gravity gradient torque to stabilize pitch and roll attitudes. Magnetic torquers with a gravity-gradient boom have been applied by Wisniewski [Wisniewski 1997]. Psiaki [Psiaki 2004] considered passive aerodynamic drag torques for stabilization of pitch and yaw motions, and roll motion was controlled by active magnetic torquing of a shuttle-cock type satellite.

### 1.2.1.3 Missions using Aerodynamic Drag

COSMOS-149 [NSSDC 1967], COSMOS-320 [NSSDC 1970], JC2Sat [Kumar *et al.* 2007a, Mierlo 2009] and New Millennium Program Earth Observation-1 (NMP EO-1) [Folta *et al.* 2002], are some of the examples where control based on aerodynamic drag has been applied for satellite attitude control and/or formation flying. In the JC2Sat mission, along track formation control is proposed and the relative states will be controlled by varying the pitch attitude of the satellites in the formation. Details of some of the missions that make use of aerodynamic drag as a means of passive/semi-passive control is provided in Table 1.1.

## 1.2.2 Solar Radiation Pressure

In this section, we review at the existing literature on the use of solar radiation pressure for satellite formation flying, attitude control and also list some of the missions that used

Table 1.1: List of missions making use of aerodynamic drag

Satellite	COSMOS-149 [NSSDC 1967]	COSMOS-320 [NSSDC 1970]	JC2Sat [Mierlo 2009]
Mass	375 kg	300 kg	18 kg
Shape	Domed cylinder	Domed cylinder	Cuboid
Dimension	L = 6.5m; Dia = 1.2m	L = 6.5m; Dia = 1.2m	35cm x 35cm x 15cm
Orbit Inclination	48.4 deg	48.4 deg	Sun-synchronous polar orbit, $i = 97.44$ deg
Apogee	285.0 km	342.0 km	700 km
Perigee	243.0 km	240.0 km	700 km
Eccentricity	0.003159	0.007642	0
Use of aerodynamic drag/plate	Pitch control	Pitch control	Autonomous formation flight using differential drag.
Duration	17 days in orbit	25 days in orbit	1 year

or proposed to use solar radiation pressure for satellite control.

### 1.2.2.1 Formation Flying using Solar Radiation Pressure

Application of SRP for formation maintenance has been investigated by several researchers. Wang [Wang 2001] and Williams and Wang [Williams & Wang 2002] considered a satellite with a solar wing and it was shown that a solar wing of the correct area can prevent the secular out-of-plane growth in a low-Earth orbit formation that is caused by differential nodal drift. Kumar et al. [Kumar *et al.* 2004a] and Fourcade [Fourcade 2005] found that SRP is successful in maintaining the desired formation. However, these studies assumed a simple SRP model and the satellite attitude motion was not considered. Another recent research studied SRP based tetrahedron satellite formation. This research studied the use of SRP to deploy and stabilize a three-dimensional satellite formation for a Heliocentric as well as High Earth Orbit [Smirnov *et al.* 2007], with the diameter of the formation and the stabilization time dependent on the properties of the solar sail. Application of SRP for station-keeping of a geostationary satellite was studied by Black et al. [Black *et al.* 1968] and Circi [Circi 2005]. Black et al. [Black *et al.* 1968] considered east-west station-keeping problem where the use of a very small solar sail and a simple thrust strategy were pro-

posed, while Circi [Circi 2005] examined both east-west and north-south station-keeping problems. The study concluded that use of solar sail was more beneficial when the total satellite mass was reduced, and it was found that for a 300 kg satellite, the required side for a square solar sail is 44 m. Several kinds of missions with solar sail as a propulsion system for orbit transfer have also been proposed: Salvail and Stuiver [Salvail & Stuiver 1995] investigated the problem of transfer to the moon from a geosynchronous orbit, Leipold et al. [Leipold *et al.* 1996] studied the mission for a Mercury polar orbiter, and McInnes et al. [McInnes *et al.* 2003] have presented an investigation of the use of solar sail propulsion for both Mercury orbiter and Mercury sample return missions. Jayaraman [Jayaraman 1980] and Otten and McInnes [Otten & McInnes 2001] present optimum trajectories for Mars missions. Powers and Coverstone [Powers & Coverstone 2001] analyzed spacecraft transfer to Earth and Mars synchronous orbits; McInnes [McInnes 1993] studied the spacecraft transfer to the lunar L2 Lagrange point and to "levitation" orbits, where the solar radiation pressure acceleration balances solar gravity, while rendezvous missions with asteroids is studied by Morrow et al. Solar sail formation flying for deep-space remote sensing is investigated in [Biggs & McInnes 2009]. Kumar et al. [Kumar *et al.* 2004b] carried out the preliminary study wherein the satellite equipped with two sets of wings - aerodynamic and SRP wings - were successfully able to control in-plane relative position errors using aerodynamic wings while the out-of-plane relative position errors were controlled by SRP wings. Solar Blade Heliogyro Nanosatellite [Blomquist 1999], ODISSEE [Leipold *et al.* 1999], MARINER 2, GOES 10, INSAT are some of the examples where solar sails/wings have either been deployed or use of the same have been studied.

### 1.2.2.2 Solar Radiation Pressure for Attitude Control

Several authors have examined the feasibility of SRP for attitude control of satellites. Various configurations such as trailing cone system, weathervane type tail surfaces, reflector-collector system, corner mirror arrays, solar paddles, grated solar sails, and mirror-like surfaces have been suggested for properly utilizing SRP torques [Modi 1995]. The attitude control of the satellite has been accomplished by translatory motions of single or several control surfaces relative to the satellite body [Kumar 1988] or by rotating the control surfaces

about satellite body-fixed axes [Kumar *et al.* 2006]. Some missions have also been flown to verify these concepts. The Mariner IV mission employed solar vanes for achieving passive sun pointing attitude [Scull 1969]. The European Space Agency conducted experiments in which the attitude of the geostationary communication satellite OTS-2 was controlled by rotating solar panels [Renner 1979]. The SRP control torque thus can be utilized to stabilize librational dynamics of a satellite with a desired degree of accuracy. Circi [Circi 2007] recently proposed a satellite attitude controller that combines passive gravity-gradient torque with solar pressure torque for three-axis stabilization of a micro-satellite. A dumbbell satellite configuration was chosen to increase the gravity-gradient torque and three-axis stabilization was performed with the help of small solar sails. Another recent publication was on the use of SRP for satellite pitch attitude control based on a non-linear sliding mode control [Patel *et al.* 2008, Patel *et al.* 2009]. Lievre in [Lievre 1986] proposed an attitude control system for geostationary satellites making use of solar sails and demonstrated its advantage as compared to a thruster based or magnetic torquer based control. In [Sidi 1997], Sidi makes reference to Roll-Yaw attitude control with solar torques. The geometry consists of solar flaps attached to the sides of the solar panels in order to achieve a solar torque about a line in the orbit plane and perpendicular to the sun direction. A control mechanism for satellite attitude control is also derived. A comparative study of two solar sail attitude control implementations is carried out in [Bladt & Lawrence 2005]. One implementation employs four articulated reflective vanes located at the periphery of the sail assembly to generate control torque about all three axes. The second attitude control configuration uses mass on a gimbaled boom to alter the center of mass location relative to the center of pressure producing roll and pitch torque. It also uses a pair of articulated control vanes for yaw control. The combination of SRP and aerodynamic forces was mainly focused on attitude control problem [Modi & Pande 1974b, Modi & Pande 1974a, Kumar *et al.* 2004b]. Modi and Pande [Modi & Pande 1974a] have stated an altitude of 800 km as the switch-over point from control based on aerodynamic forces to control using SRP.

### 1.2.2.3 Missions using Solar Radiation Pressure

Solar Blade Heliogyro Nanosatellite, ODISSEE, MARINER-2, GOES-10, NanoSail-D, IKAROS, INSAT are examples of space missions using SRP. Table 1.2 provides details of some of these missions.

## 1.3 Problem Statement

The previous section listed the existing research scenario on the application of SRP and aerodynamic drag for satellite formation flying and attitude control. It is clearly evident that research has largely been confined to the use of either SRP or aerodynamic drag for satellite attitude control or formation flying with simpler linear control schemes. Also the problem of multiple satellite formation flying using either SRP or aerodynamic drag is yet to be studied. Hence this thesis focuses on the development of a robust nonlinear control technique of application of SRP or aerodynamic drag for satellite formation and attitude control. Utilizing these environmental forces for desired control of satellites is a challenging problem as these disturbing forces are unpredictable in nature. Hence the control scheme to be used should be robust and also adaptive in nature. The problems to be addressed can be classified as:

[**PROB1**] *Nonlinear System Equations*: The inherent nonlinearity in the dynamics of satellite systems is one of the challenges to be overcome for successfully developing a robust system. It is not always the case that a linear model can be built up that sufficiently and accurately describes the dynamic behavior of the system for a wide range of operating conditions.

[**PROB2**] *Non-Affine Control Input*: An additional complexity involved in the nonlinear equation of motion used to describe these systems is the means by which the control input enters the equation of motion. A system where the control inputs do not appear linearly in the plant falls in the category of non-affine control. For SRP and aerodynamic drag based propulsion, the control inputs are the angles that define the orientation of the wings/flaps of the satellite. The control input enters the equations

Table 1.2: List of missions making use of solar radiation pressure

Property	IKAROS	ODISSEE	Mercury Orbiter
Mass	310 kg	100 kg	235 kg
Shape	Cylindrical satellite with square solar sail	Cuboid satellite; sail module connected using a 10m collapsible mast and a 2DOF actuator gimbal.	Cuboid satellite; sail module connected using a 10m collapsible mast and a 2DOF actuator gimbal.
Dimension	1.6 m x 0.8 m	60 cm x 60 cm x 80 cm	60 cm x 60 cm x 80 cm
Orbit	Low-thrust Venus fly-by	Geostationary transfer orbit	Sun-synchronous polar orbit
Apogee	NA	35883 km (at time of release after launch)	8790 km
Perigee	NA	620 km (at time of release after launch)	2640 km
Use of Solar blade/sail	Venus fly-by, followed by journey to the far side of Sun using SRP.	Perform attitude control by gimbaling the central mast to offset the CM to CP and generating external torque due to SRP	Low-thrust spiral transfer to Mercury
Dimension of solar blades/sail (L x W x H)	14 m x 14 m x 7.5 $\mu\text{m}$	40 m x 40 m x 7.5 $\mu\text{m}$ m	125 m x 125 m
Solar blade/sail material	Sail membrane is made of 7.5 $\mu\text{m}$ thick sheet of polyamide resin deposited with a thin-film of aluminium.	Carbon fibre reinforced plastic (CFRP) booms and sails made of 7.5 $\mu$ thick Kapton film, coated with 0.1 $\mu$ aluminium reflector on one side and 0.015 $\mu$ thick chrome emitter on the other.	CFRP booms and sails made of Kapton
Mission duration	6 months to reach Venus, and 3 years to reach the far side of the Sun	550 days Lunar polar flyby	1.8 years to reach Mercury

of motion as trigonometric functions of the orientation angles. Specifying the control input angles in closed-loop form presents a challenge.

[**PROB3**] *Model uncertainties and external disturbances:* In space applications, controllers designed based on nonlinear spacecraft models can also be imprecise due to unknown values of some physical parameters, disturbance models, etc. The resulting mismatch between the model and the real system is referred to as model uncertainty. The problem of disturbance rejection is particularly pronounced for spacecraft that operate in the altitude ranges where their dynamics is affected by various environmental and non-environmental disturbances.

[**PROB4**] *Orbit selection and formation design.* It is well known that SRP is the dominant environmental force in the high Earth orbits where as atmospheric drag is dominant in the low earth orbits. Hence orbit selection and formation trajectory generation becomes critical so that both the environmental forces can be utilized to its fullest possible manner.

## 1.4 Research Objectives

To address the problems presented, this dissertation concentrates on the development of nonlinear adaptive control laws for multiple satellite formation flying and attitude control. From practical viewpoint, the main objective is to design control algorithms that are globally stable and are able to achieve high precision pointing, fast slewing, and large maneuvers in the presence of external disturbances, and model uncertainties. The main objectives are identified as:

[**OBJ1**] **Control System Design:** In the proposed system, precise system modeling is not always possible due to the lack of exact knowledge of all the parameters associated with solar radiation pressure and aerodynamic drag. Hence a robust closed loop feedback control strategy based on adaptive control theory is developed (Fig.1.4). The adaptive control law reconfigures the control algorithm using the adaptive estimates of the unknown parameters. The objective of this control

methodology is to provide a reliable, and cost-effective control algorithm that simultaneously accounts for modeling uncertainties and external disturbances as well as provides the desired system performance.

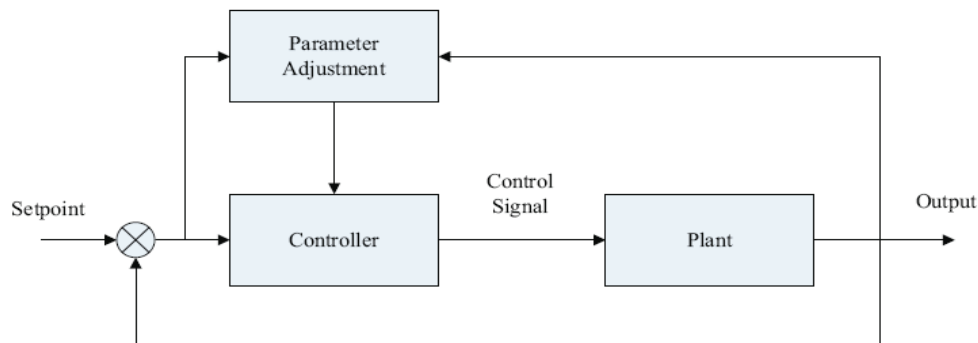


Figure 1.4: Block diagram representation of an Adaptive Control System

**[OBJ2] Validation:** Dynamic system analysis should be conducted to determine the effect of parameter uncertainties and external disturbances on the performance and flight-worthiness of the control system. Validation of the proposed control algorithms is conducted by means of conventional theoretical analysis, numerical simulation study, and real-time experimental testing. Principles of nonlinear control theory are used to demonstrate the AOCS performance and stability. Numerical simulation is performed to demonstrate the system performance, compliance with design requirements, and validate established theoretical framework. An important step involved in this stage of validation is the selection of feasible orbits and also finalizing the design parameters for the control flaps (aerodynamic drag plates as well as solar flaps). Final validation of the proposed control methodology is conducted by hardware-in-loop (HIL) simulations. Here, since we propose control of the satellite formation and attitude using maneuverable drag plates/solar flaps, we verify the proposed rotation

scheme by utilizing a satellite prototype with flat plates attached to its surface. This satellite prototype is connected in an hardware-in-loop (HIL) arrangement to verify the satellite formation control system.

## 1.5 Research Contributions

Acknowledging the advantages of using a passive AOCS, the core of this dissertation concentrates on the application of aerodynamic drag or SRP for satellite formation and attitude control. Nonlinear control laws that are able to incorporate the nonaffine, underactuated nature of the aerodynamic drag model or SRP model in its formulation are developed. And finally these robust control algorithms are shown to accomplish different formation configurations, perform attitude stabilization as well as maneuvering. The major contributions of this thesis are as follows:

1. **Satellite formation control using aerodynamic drag (Chapter 3)**

This dissertation begins by presenting a control methodology for satellite formation control using aerodynamic drag. Here control authority, achieved by the rotation of the drag plates, is available only in the along track direction. We make use of the coupling between the radial and along track direction to develop a nonlinear adaptive control algorithm that can control the satellite formation. Existing control formulation methods for such underactuated, nonaffine systems are based on linearized relative motion dynamics and hence work only for a sufficiently small neighborhood of the origin. A novel control algorithm for multiple satellite formation control using aerodynamic drag is also developed. This is significant because multiple satellite formation maneuvering for this SFF system is more challenging as the achievable levels of aerodynamic drag between each follower and the leader are mutually constrained. Numerical simulations accounting for different formation scenarios under realistic environmental conditions are carried out. To fully confirm the validity of the proposed methodology, the drag plate rotation scheme is validated in an HIL arrangement as well.

2. **Satellite formation control using solar radiation pressure (Chapter 4)**

The feasibility of using SRP for formation control in a geocentric orbit is investigated in this section. Here a nonlinear adaptive control algorithm based on higher order sliding mode control technique is developed. The system is essentially underactuated, hence an area control input is introduced. This additional input transforms the system to a fully actuated system. The performance of the proposed system in the presence of external disturbance, and parameter uncertainties is examined. Feasibility of multiple satellite formation flying using solar radiation pressure is also validated using numerical simulation.

### 3. Satellite attitude control using aerodynamic drag (Chapter 5))

Satellite attitude stabilization in the local vertical local horizontal (LVLH) frame using aerodynamic drag is examined in this chapter. Existing literature proposes only pitch and yaw control using aerodynamic drag. Roll stabilization is usually achieved by a separate actuator. By developing the control algorithm based on nonlinear theory, here we are able to achieve complete three axis attitude stabilization using aerodynamic drag. The proposed attitude control system demonstrated robust performance in the presence of uncertainties and disturbances.

### 4. Satellite attitude control using solar radiation pressure (Chapter 6)

Satellite attitude stabilization using solar radiation pressure is examined. An adaptive control algorithm is developed that is able to achieve complete three axis attitude stabilization. To date, variety of control methods using SRP has been proposed for attitude control, but it has been confined to the the control of satellite pitch motion. Here the efficacy of using SRP for three axis attitude control in the presence of uncertainties and perturbations is verified.

### 5. Fault Tolerant Satellite Attitude Control Using Solar Radiation Pressure / Aerodynamic Drag (Chapter 7)

The performance of the proposed satellite attitude control strategies in the presence of faults or failures of the drag plates or solar flaps is examined. First, the pitch attitude performance of the satellite in the presence of faults or failures in the solar flaps is evaluated. The fault scenarios considered include sudden failure of one of

the solar flaps, occurrence of an abrupt blockage or loss in effectiveness of one of the rotating solar flaps, and occurrence of a periodic actuator fault. This is followed by the evaluation of the performance of the system during three axis attitude control in the presence of similar failures.

## 1.6 Thesis Outline

This section outlines the structure of this dissertation. Chapter 2 outlines the dynamics of satellite formation flying system under the influence of solar radiation pressure, aerodynamic drag and other external perturbations. The formation flying equations are presented along with the desired reference trajectories for the leader satellite. A brief outline of sliding mode control technique is provided. An adaptive nonlinear control methodology for satellite formation flying using aerodynamic drag is presented in Chapter 3. Satellite formation flying using solar radiation pressure, based on control law developed using higher order sliding mode technique is presented in Chapter 4. Chapter 5 details the results of satellite attitude control using aerodynamic drag. This is followed by the results of satellite attitude control using solar radiation pressure in Chapter 6. Chapter 7 examines the satellite attitude system performance in the presence of faults/failures of drag plates or solar flaps. Chapter 8 concludes this thesis along with suggestions for future work.

## CHAPTER 2

# Satellite Formation Dynamics and Control Methodology

---

SATELLITE formation flying (SFF) is defined as two or more satellites flying in a cooperative manner in prescribed reference orbits at fixed separation distance for a given period of time. Centralized formation is one of the classifications based on the control architecture, wherein there is a leader satellite and all other satellites follow the leader satellite. This configuration is also known as *Leader-Follower* formation. The SFF system considered in this thesis is the Leader-Follower configuration. Depending on the purpose of the formation, different reference trajectories are designed to produce different formation geometries. In this chapter we derive the mathematical formulation of the SFF system, including the relations for the different reference trajectories, mathematical formulation of the perturbations affecting the SFF system and examine the effect of these perturbing forces on the SFF system.

The chapter is organized as follows: Section 2.1 introduces the equations of motion of the satellite formation flying system, including the linearized Hill's or Clohesy-Wiltshire equations. The mathematical relations of the different reference trajectories are derived in Section 2.2. Section 2.3 discusses and formulates the different external perturbations affecting the SFF system. Finally, the underlying concept of sliding mode control, the control strategy employed throughout this thesis is provided in Section 2.4.

## 2.1 SFF System Model

We start the mathematical formulation of the SFF system by assuming that the leader and follower satellites are point masses under the Earth's central gravitational force of attraction

(Fig. 2.1). The *leader satellite* is in an elliptical planar trajectory with the Earth's center at one of its foci and a *follower satellite* is moving in a desired relative trajectory about the leader satellite. The motion of the follower satellite is described relative to the leader satellite using a relative local vertical local horizontal (LVLH) frame  $S - xyz$  fixed at the center of the leader satellite with the  $x$ -axis pointing along the local vertical, the  $z$ -axis taken along normal to the orbital plane, and the  $y$ -axis representing the third axis of the right-handed  $S - xyz$  frame.  $\vec{\rho} \in \mathbb{R}^3$ ,  $\vec{\rho} \triangleq [x \ y \ z]^T$ , defines the relative position vector of the follower spacecraft from the origin of the leader spacecraft coordinate frame. Both,  $\vec{r}_l$  and  $\vec{r}_f$  are expressed in the LVLH frame. In this thesis, the motion along  $x$ ,  $y$ , and  $z$  are referred as *radial*, *along-track*, and *cross-track* motion, respectively.

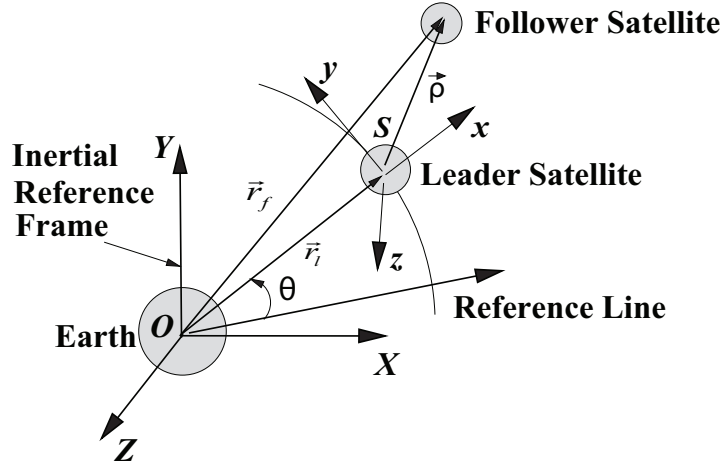


Figure 2.1: Geometry of orbit motion of leader and follower satellite. [Kumar 2006]

### 2.1.1 Equations of Motion

The position vector of the leader satellite in the  $S - xyz$  is given as

$$\vec{r}_l = r_l \hat{i} \quad (2.1)$$

and the position vector of the follower satellite in  $S - xyz$  frame is given as

$$\vec{r}_f = \vec{r}_l + \vec{\rho} \quad (2.2)$$

Now let us define  $\vec{\rho} = (x\hat{i} + y\hat{j} + z\hat{k})$  and  $\vec{r}_f = (r_l + x)\hat{i} + y\hat{j} + z\hat{k}$ . The velocity of the leader satellite is given as

$$\dot{\vec{r}}_l = \dot{r}_l\hat{i} + \vec{\omega} \times (r_l\hat{i}) = \dot{r}_l\hat{i} + r_l\dot{\theta}\hat{j} \quad (2.3)$$

The velocity of the follower satellite is given as

$$\dot{\vec{r}}_f = \dot{\vec{r}}_l + \dot{\vec{\rho}} = \dot{r}_l\hat{i} + r_l\dot{\theta}\hat{j} + (\dot{x}\hat{i} + \dot{y}\hat{j} + \dot{z}\hat{k}) + \dot{\theta}\hat{k} \times (x\hat{i} + y\hat{j} + z\hat{k}) \quad (2.4)$$

or

$$\dot{\vec{r}}_f = (\dot{r}_l + \dot{x} - \dot{\theta}y)\hat{i} + (r_l\dot{\theta} + \dot{y} + \dot{\theta}x)\hat{j} + \dot{z}\hat{k} \quad (2.5)$$

Now we use the Lagrange method of deriving the equations of motions, The kinetic energy of the leader satellite is given as,

$$T = \frac{1}{2}m_l\dot{\vec{r}}_l^2 = \frac{1}{2}m_l(\dot{r}_l^2 + \dot{\theta}^2r_l^2) \quad (2.6)$$

and the potential energy is given as

$$U = \frac{-\mu m_l}{\|r_l\|} = \frac{-\mu m_l}{r_l} \quad (2.7)$$

Now calculating  $L = T - U$ , we get

$$L = T - U = \frac{1}{2}m_l\dot{r}_l^2 + \frac{1}{2}m_l\dot{\theta}^2r_l^2 + \frac{\mu m_l}{r_l} \quad (2.8)$$

Now taking the partial derivatives of  $L$ , as follows,  $(\frac{d}{dt}(\frac{\partial L}{\partial \dot{r}_l}) - \frac{\partial L}{\partial r_l})$  and  $(\frac{d}{dt}(\frac{\partial L}{\partial \dot{\theta}}) - \frac{\partial L}{\partial \theta})$ , we get

$$\ddot{r}_l = \dot{\theta}^2r_l - \frac{\mu}{r_l^2} \quad (2.9)$$

$$r_l\ddot{\theta} = -2\dot{\theta}\dot{r}_l \quad (2.10)$$

These form the equations of motion of the leader satellite. Next we derive the relative equations of motion of the follower satellite in similar manner. First the kinetic energy is

calculated and is given as

$$T = \frac{1}{2} m_f \dot{r}_f^2 \quad (2.11)$$

and the potential energy is given as

$$U = \frac{-\mu m_f}{\|r_f\|} \quad (2.12)$$

Now taking the partial derivatives of  $L$  with respect to  $x$ ,  $y$ ,  $z$ ,  $\dot{x}$ ,  $\dot{y}$ , and  $\dot{z}$ , and performing some manipulations we get the relative equations of the follower satellite. The complete nonlinear relative equations of motion of the leader and follower satellites can now be written along with the force and disturbance terms as follows,

$$\ddot{r}_l - r_l \dot{\theta}^2 + \frac{\mu_e}{r_l^2} = 0 \quad (2.13)$$

$$r_l \ddot{\theta} + 2\dot{\theta} \dot{r}_l = 0 \quad (2.14)$$

$$m_f \ddot{x} - 2m_f \dot{\theta} \dot{y} - m_f (\dot{\theta}^2 x + \ddot{\theta} y) + m_f \mu_e \left( \frac{r_l + x}{r_f^3} - \frac{1}{r_l^2} \right) = f_x + f_{dtx} \quad (2.15)$$

$$m_f \ddot{y} + 2m_f \dot{\theta} \dot{x} + m_f (\ddot{\theta} x - \dot{\theta}^2 y) + m_f \frac{\mu_e}{r_f^3} y = f_y + f_{dty} \quad (2.16)$$

$$m_f \ddot{z} + m_f \frac{\mu_e}{r_f^3} z = f_z + f_{dtz} \quad (2.17)$$

where  $r_f = [(r_l + x)^2 + y^2 + z^2]^{1/2}$  is the position of the follower satellite,  $f_{dtj}$  is the net relative perturbations acting on the SFF system, and  $f_j$  are the components of the control input vector, for  $j = x, y, z$ . This mathematical model for SFF is also referred to as the “true model” [Vaddi 2003].

### 2.1.2 Hill-Clohessy-Wiltshire Equations

Satellite formation flying is principally concerned with the relative motion of the follower satellite with respect to the leader, most commonly expressed in the rotating Hill reference frame. Although the actual relative dynamics of the follower satellite are nonlinear as well as nonperiodic, a set of linearized ordinary differential equations which approximate the full dynamics and have periodic solutions can be derived. These are commonly referred

to as the Hill-Clohessy-Wiltshire (HCW) equations. The homogeneous form of the HCW equations is given as [Hill 1878, Clohessy & Wiltshire 1960]:

$$\begin{aligned}\ddot{x} - 2\dot{\theta}\dot{y} - 3\dot{\theta}^2x &= 0 \\ \ddot{y} + 2\dot{\theta}\dot{x} &= 0 \\ \ddot{z} + \dot{\theta}^2z &= 0\end{aligned}\tag{2.18}$$

The simplifying assumptions made during the derivation affects the accuracy of the HCW equations. The assumptions include no external perturbations, the leader is assumed to be in a circular orbit around the Earth, and also require that the relative distance between the leader and the follower is much smaller than that of the orbital radius of the leader. However, the HCW equations are useful in control algorithm design and their periodic solutions help in deriving basic reference trajectories for the controller to track during near circular formation flying.

## 2.2 Desired Formation Geometry

Formation flying guidance is defined as the generation of any reference trajectories used as a input for a formation member's relative state tracking control law [Scharf *et al.* 2004]. We consider three different formation flying designs. They are the along track formation, circular formation and the projected circular formations. In along track formation the follower satellite shares the same ground track as the leader satellite. The follower has to keep a constant desired along track separation with respect to the leader,. Mathematically it is represented as  $y_d = r_d$ , where  $r_d$  is the desired separation between the leader and follower satellites in the along track direction. Fig. 2.2 shows a pictorial representation of along track satellite formation.

The desired states,  $(x_d, \dot{x}_d, y_d, \dot{y}_d, z_d, \dot{z}_d)$ , of circular formation and projected circular formation are derived from Hill's equations analytically or geometrically [Sabot *et al.* 2001]. The mathematical formulation of the these two desired trajectories are as follows:

1. *Circular Formation*: In this formation, the leader and the follower satellite maintain a constant separation from each other in three-dimensional space and the formation is

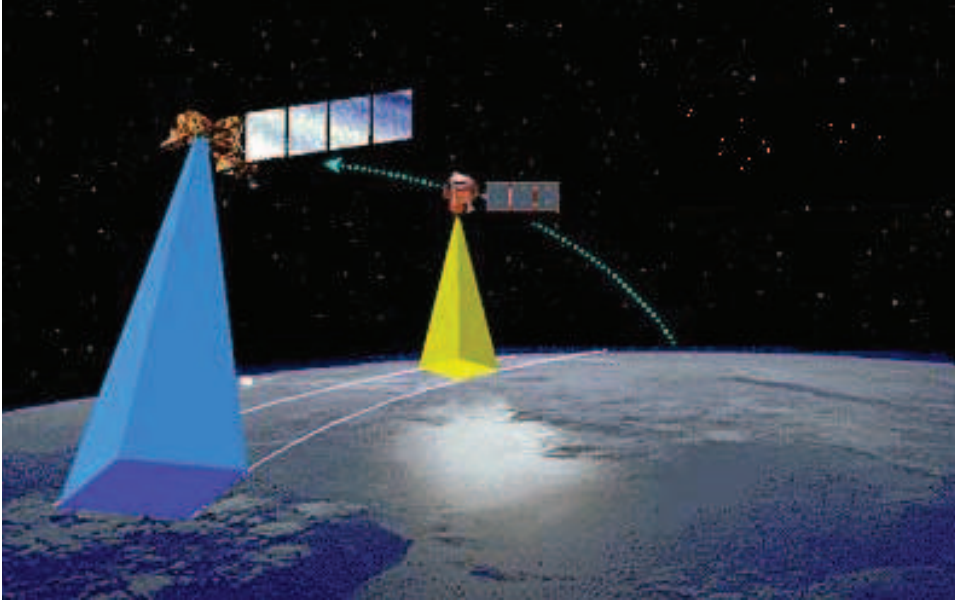


Figure 2.2: Along track formation (Courtesy of NASA)

mathematically defined as  $x^2 + y^2 + z^2 = r_d^2$ . The relative motion in the radial/along-track ( $x/y$ ) plane is fixed in eccentricity [Sabot *et al.* 2001]. The equations of desired circular trajectory are given as follows,

$$\begin{Bmatrix} x_d \\ y_d \\ z_d \end{Bmatrix} = \frac{r_d}{2} \begin{bmatrix} \sin(\dot{\theta}t + \phi) \\ 2 \cos(\dot{\theta}t + \phi) \\ \sqrt{3} \sin(\dot{\theta}t + \phi) \end{bmatrix} \quad (2.19)$$

where  $r_d$  is the formation size for circular and projected circular formations,  $\phi$  is the in-plane phase angle between the leader and the follower satellites, and  $\dot{\theta}$  is the mean angular velocity and equals to  $\sqrt{\mu_e/a_c^3}$  ( $\mu_e$  is the gravitational parameter of the Earth;  $a_c$  is the semi-major axis of the leader satellite) [Yan *et al.* 2009].

2. *Projected Circular Formation*: In this formation, the leader and the follower satellite maintains a fixed relative distance when the formation is projected onto the along-track/cross-track ( $y - z$ ) plane. This configuration finds applications for ground observing Synthetic Aperture Radar (SAR) missions. Since most SAR applications target objects on the surface of the Earth, it is desirable to achieve a formation plane

perpendicular to the radial vector in order to have a field of view that has its target on the Earth. Fig. 2.3 represents the projected circular formation scheme. Mathematically it is defined as  $y^2 + z^2 = r_d^2$ .

$$\begin{Bmatrix} x_d \\ y_d \\ z_d \end{Bmatrix} = \frac{r_d}{2} \begin{bmatrix} \sin(\dot{\theta}t + \phi) \\ 2 \cos(\dot{\theta}t + \phi) \\ 2 \sin(\dot{\theta}t + \phi) \end{bmatrix} \quad (2.20)$$

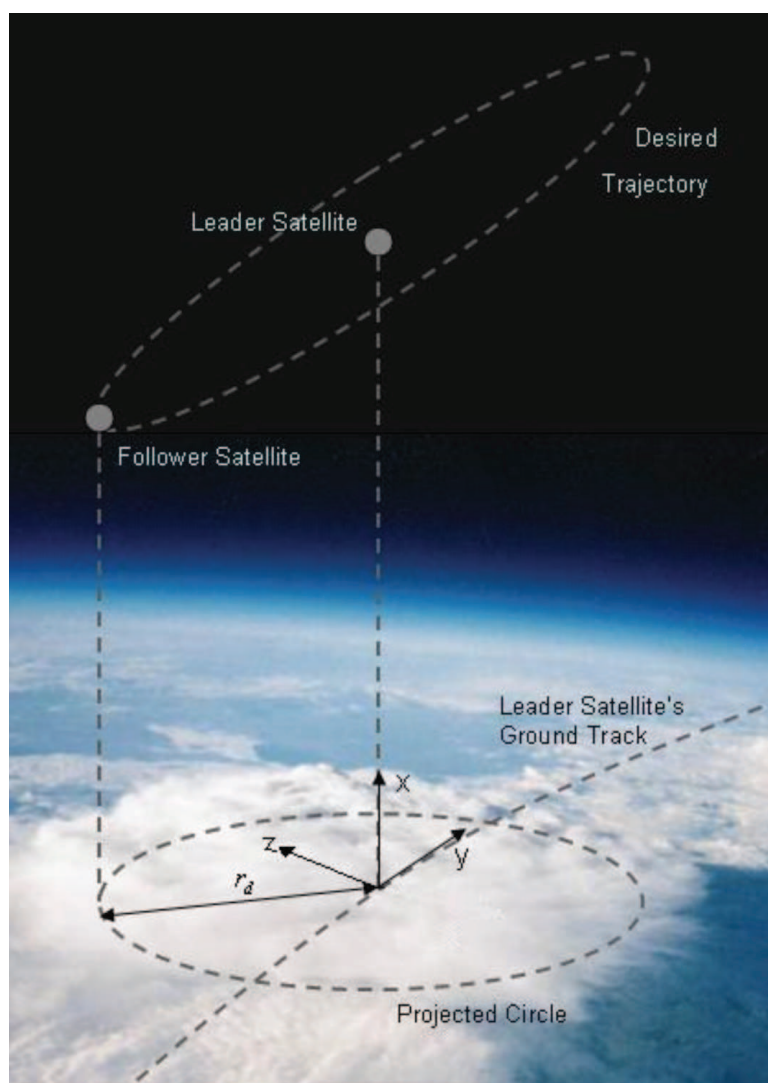


Figure 2.3: Projected circular formation.

## 2.3 External Perturbations

The disturbances terms in Eqs. (2.15)-(3.5),  $f_{dtj}$  for  $j = x, y, z$  constitute time-varying quantities attributed to gravitational field, solar radiation pressure, aerodynamic drag and third body perturbations. For a satellite in low Earth orbit, the second zonal harmonic ( $J_2$ ) of the oblate Earth's potential distribution is by far the most dominant perturbation force followed by aerodynamic drag and solar radiation pressure. The disturbance accelerations due to  $J_2$  are at least an order of magnitude larger than the other perturbations such as third-body gravitational effects, drag due to residual atmosphere, and solar radiation pressure [Sabol *et al.* 2001]. The effects of the Earth's oblateness on the formation geometry are: 1) precession of the orbital plane leading to differential changes in the right ascension of the ascending node, and 2) secular changes in the argument of perigee and mean anomaly due to rotation of the line of apsides in the orbital plane. Next, we derive the relative acceleration components due to  $J_2$  in the LVLH frame. The leader satellite ( $\vec{r}_l$ ) and follower satellite ( $\vec{r}_f$ ) positions in the LVLH frame are given by

$$\vec{r}_l = \begin{bmatrix} r_l & 0 & 0 \end{bmatrix}^T \quad \text{and} \quad \vec{r}_f = \begin{bmatrix} r_l + x & y & z \end{bmatrix}^T \quad (2.21)$$

and the transformation matrix,  $T_{IB}$  required to convert these positions from the relative frame to the Earth-centered inertial frame of reference is obtained by using the following rotation sequence

$$T_{IB} = T_3(\Omega_l) \times T_1(i_l) \times T_3(\omega_l + \theta) \quad (2.22)$$

Using the transformation matrix,  $T_{IB}$ , along with Eq. (2.21),

$$\vec{R}_l = T_{IB} \vec{r}_l \quad \text{and} \quad \vec{R}_f = T_{IB} \vec{r}_f \quad (2.23)$$

we obtain the positions of the leader satellite ( $\vec{R}_l = [X_l, Y_l, Z_l]^T$ ) and the follower satellite ( $\vec{R}_f = [X_f, Y_f, Z_f]^T$ ) in the ECI frame. The perturbations due to  $J_2$  in the ECI frame for

the leader and follower satellites are given by [Schaub & Junkins 2003]

$$\vec{J}_{2l} = -\frac{3\mu_e J_2 R_e^2}{2\|\vec{R}_l\|^5} \begin{bmatrix} \left\{ 1 - \frac{5Z_l^2}{\|\vec{R}_l\|^2} \right\} X_l \\ \left\{ 1 - \frac{5Z_l^2}{\|\vec{R}_l\|^2} \right\} Y_l \\ \left\{ 3 - \frac{5Z_l^2}{\|\vec{R}_l\|^2} \right\} Z_l \end{bmatrix} \quad \vec{J}_{2f} = -\frac{3\mu_e J_2 R_e^2}{2\|\vec{R}_f\|^5} \begin{bmatrix} \left\{ 1 - \frac{5Z_f^2}{\|\vec{R}_f\|^2} \right\} X_f \\ \left\{ 1 - \frac{5Z_f^2}{\|\vec{R}_f\|^2} \right\} Y_f \\ \left\{ 3 - \frac{5Z_f^2}{\|\vec{R}_f\|^2} \right\} Z_f \end{bmatrix} \quad (2.24)$$

where  $\mu_e$  is the Earth's gravitational parameter,  $R_e$  is the radius of the Earth, and  $J_2$  is second zonal gravitational coefficient,  $J_2 = 1.08263 \times 10^{-3}$ . The full effects of differential  $J_2$  can be added to the nonlinear relative mathematical model by transforming the disturbance forces from the Earth-centered inertial frame to the relative reference frame. Therefore, the external disturbance forces in Eqs. (2.15)-(3.5) is given by

$$\vec{F}_d = T_{IB}^{-1}[\vec{J}_{2f} - \vec{J}_{2l}] \quad (2.25)$$

Figure 2.4 shows the force profile of differential  $J_2$  acceleration acting on the follower satellite in a projected circular formation of size ( $r_d = 0.5$  km) around a leader satellite in a circular orbit at an altitude of 500 km with an orbital inclination,  $i_l$  of  $45^\circ$ . Figure 2.5 illustrates the growth in relative error (the difference between follower satellite's relative state and the desired state) due to the  $J_2$  perturbation acting on an uncontrolled 500 m projected circular formation. It can be observed from Figure 2.5 (a) that the secular drift occurs in all coordinates directions and Figure 2.5 (b) indicates the slow phase shift in the relative orbit.

### 2.3.1 Aerodynamic Drag Model

Next we study the aerodynamic drag models. Aerodynamic drag has substantial influence on the motion of the near-Earth satellites. There are two extremes when discussing how

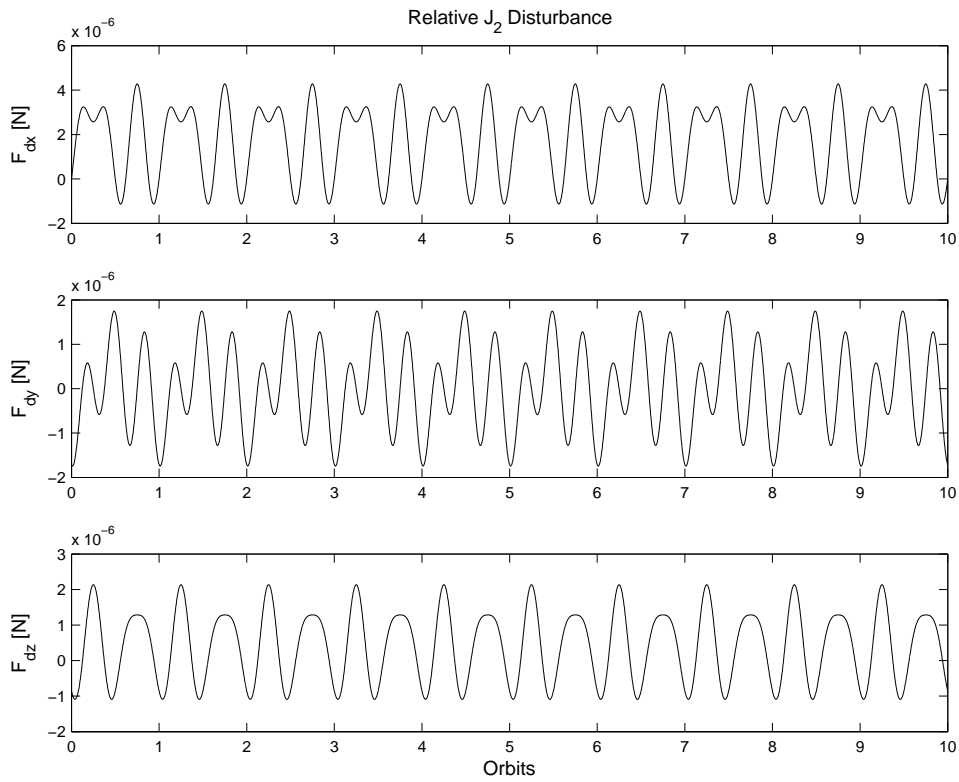
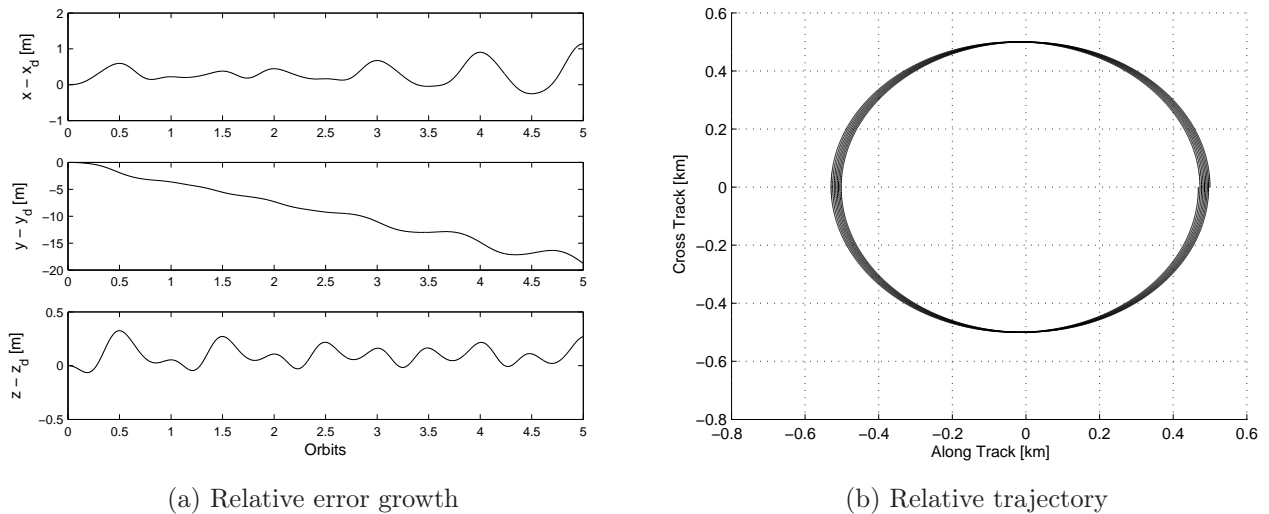


Figure 2.4: Relative  $J_2$  disturbance ( $r_p = 6878$  km and  $r_d = 0.5$  km,  $e=0$ ,  $\Omega_l = 0^\circ$ ,  $i_l = 45^\circ$ , and  $\omega_l = 0^\circ$ ).



(a) Relative error growth

(b) Relative trajectory

Figure 2.5: Relative error due to  $J_2$  disturbance.

particles impact a flat surface and how momentum is transferred from the collision of these particles. These are specular and diffuse. Under the specular reflection concept, each molecule bounces off the surface with no change in energy. The angle of reflection equals the angle of incidence. Momentum transfer therefore takes place normal to the surface. In practical situation very few molecules experience specular reflection, Most of the molecules becomes at least partially accommodated to the surface. Diffuse reflection suggests that all the incoming molecules are completely accommodated to the surface. Reality falls somewhere in between specular and diffuse reflection. Two of the commonly used aerodynamic models are the free-molecular aerodynamic force model and a more simplified aerodynamic force model

### 2.3.1.1 Simplified Aerodynamic Force Model

First we consider the simplified aerodynamic force model. It is expressed in terms of the drag, i.e. the force parallel to the satellite velocity direction. The vector equation for computing the drag force is given as [Kumar 2006],

$$\vec{F}_D = -\frac{1}{2}\rho C_D A V_{rel}^2 \hat{V}_{rel} \quad (2.26)$$

where  $C_D$  is the drag coefficient,  $\rho$  is the atmospheric density, and  $A$  is the projected area of the satellite normal to  $\vec{V}_{rel}$ .  $\vec{V}_{rel}$  is the relative velocity of the satellite with respect to the atmosphere. The relative velocity can be represented by

$$\vec{V}_{rel} = [1 - (\omega_E R/V) \cos i] \vec{V} \quad (2.27)$$

where  $\omega_E$  is the Earth's rotation rate,  $\hat{V}_{rel} = \frac{\vec{V}_{rel}}{V_{rel}}$  is the velocity vector of the surface element with respect to the atmosphere, and  $i$  is the orbit inclination. The drag force,  $\vec{F}_D$ , thus acts in the direction opposite to the relative velocity,  $\vec{V}_{rel}$ . The coefficient  $C_D$  is dependent on the geometry of the satellite and varies with altitude, and the satellite angle of attack. At orbital altitudes the large mean free path makes turbulent mixing of the

atmosphere ineffective, so the density distribution is governed by the relation:

$$\rho = \rho_0 \exp\left(-\frac{y - y_0}{H}\right) \quad (2.28)$$

where  $y$  is an altitude above a reference surface (Earth),  $y_0$  is the altitude at geocentric distance  $r_0$  which has density  $\rho_0$ , and  $H$  is the scale height given by

$$\frac{1}{H} = \frac{1}{h} - \frac{2}{r_0}, h = \frac{R_0 T}{Mg} \quad (2.29)$$

where  $T$  is the local atmospheric temperature,  $M$  is the molecular mass, and  $R_0$  is the universal gas constant. The density model given by Eq. (2.28) is also known as the exponential density model. The density scale height  $H$  governs the rate of decrease of density and has a firm temperature dependence. Most uncertain parameter in the aerodynamic force equation is the atmospheric density. Various density models are currently available, but the two of the most widely used density models are the exponential density model (Eq. 2.28) and the NRLMSISE-00(United States Naval Research Laboratory Mass Spectrometer and Incoherent Scatter Radar Exosphere) model [Picone *et al.* 2000]. NRLMSISE-00 model is one of the widely used empirically derived aerodynamic drag force models and considered to be more accurate especially at higher altitudes. The model utilizes atmospheric composition data from instrumented satellites and temperatures from ground-based radars as well as extensive set of parametric equations, of which the parameters have been determined using large historical data sets and also depend on latitude, local time, day of the year, solar activity index ( $F_{10.7}$ ) and geomagnetic activity index ( $A_p$ ) [Picone *et al.* 2000]. Figure (2.6) shows the variations in the density profiles of the exponential and NRLMSISE-00 model.

### 2.3.1.2 Free Molecular Aerodynamic Force Model

The second aerodynamic model is the free molecular aerodynamic force model. Based on the free-molecular force model, the force on a flat surface of area  $A$  is given by the vector equation [Kumar 2006],

$$\vec{F} = A \left[ -\hat{n}p + \left( \hat{n} \sin \alpha - \hat{V}_{rel} \right) \left( \frac{\tau}{\cos \alpha} \right) \right] \quad (2.30)$$

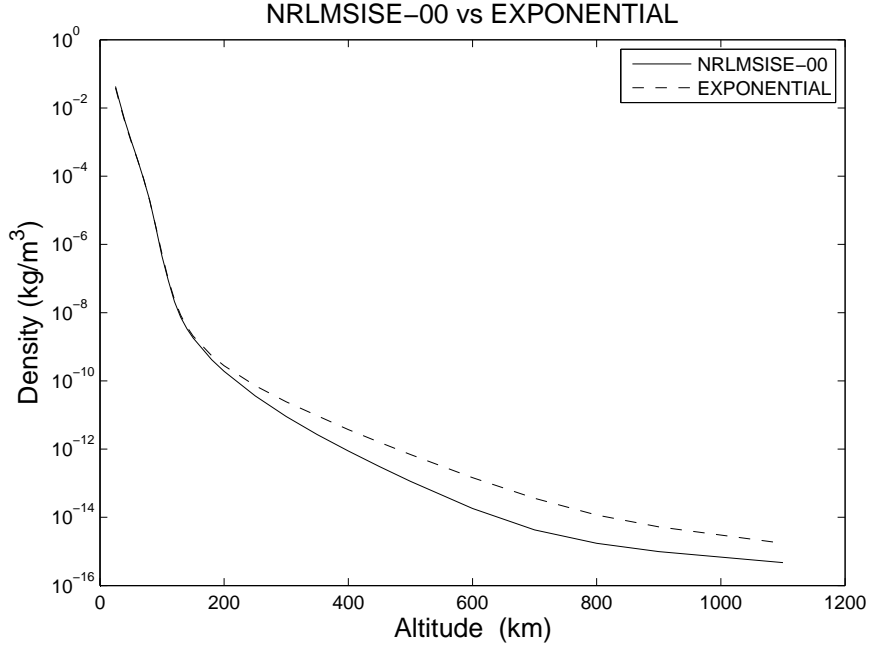


Figure 2.6: Variation of density with altitude.

where  $p$  is the total pressure,  $\tau$  is the shearing stress,  $\hat{V}_{rel} = \frac{\vec{V}_{rel}}{V_{rel}}$  is the velocity vector of the surface element with respect to the atmosphere and  $\hat{n}$  is the outward pointing unit normal vector. The total pressure  $p$  and the shearing stress  $\tau$  are given by [Gombosi 1994]

$$\begin{aligned} \frac{p}{q_\infty} &= \left\{ \left[ \frac{2 - \sigma_n}{\sqrt{\pi}} \right] \sin \zeta + \frac{\sigma_n}{2s} \sqrt{\frac{T_s}{T_a}} \right\} \left\{ \frac{1}{s} e^{-s^2 \sin^2 \zeta} + \sqrt{\pi} [1 + \operatorname{erf}(s \sin \zeta)] \sin \zeta \right\} \\ &\quad + \left[ \frac{2 - \sigma_n}{2s^2} \right] [1 + \operatorname{erf}(s \sin \zeta)] \\ \frac{\tau}{q_\infty} &= \sigma_t \left\{ \frac{1}{s\sqrt{\pi}} e^{-s^2 \sin^2 \zeta} + [1 + \operatorname{erf}(s \sin \zeta)] \sin \zeta \right\} \end{aligned} \quad (2.31)$$

where  $\sigma_n$  and  $\sigma_t$  are the normal and tangential accommodation coefficients,  $T_s$  is the absolute temperature of the satellite surface,  $T_a$  is the atmospheric temperature,  $q_\infty$  is the dynamic pressure given by  $q_\infty = \frac{1}{2} \rho V_{rel}^2$ , and  $\operatorname{erf}(x)$  is the error function defined by  $\operatorname{erf}(x) = \frac{2}{\sqrt{\pi}} \int_0^x e^{-y^2} dy$  and  $s$  is the air speed nondimensionalized by the mean molecular speed of the atmosphere.

As mentioned earlier, the satellite orbit contracts under the influence of aerodynamic

drag. The effect on the satellite altitude is less in the higher orbits, but the orbit is appreciably affected by drag at lower orbits. Figure (2.7) illustrates the orbital decay of a 10 kg satellite at an initial orbit of 500 km and with an exposed surface area of  $1 \text{ m}^2$ . The Solar Radio Flux ( $F_{10.7}$ ) index is set to 120 and the Geomagnetic Index ( $A_p$ ) has a value of 3. It can be observed that initially there is a linear decay rate, but at lower orbits the decay rate demonstrates exponential increase. Figure (2.8) shows the decay rate over the satellite life time.

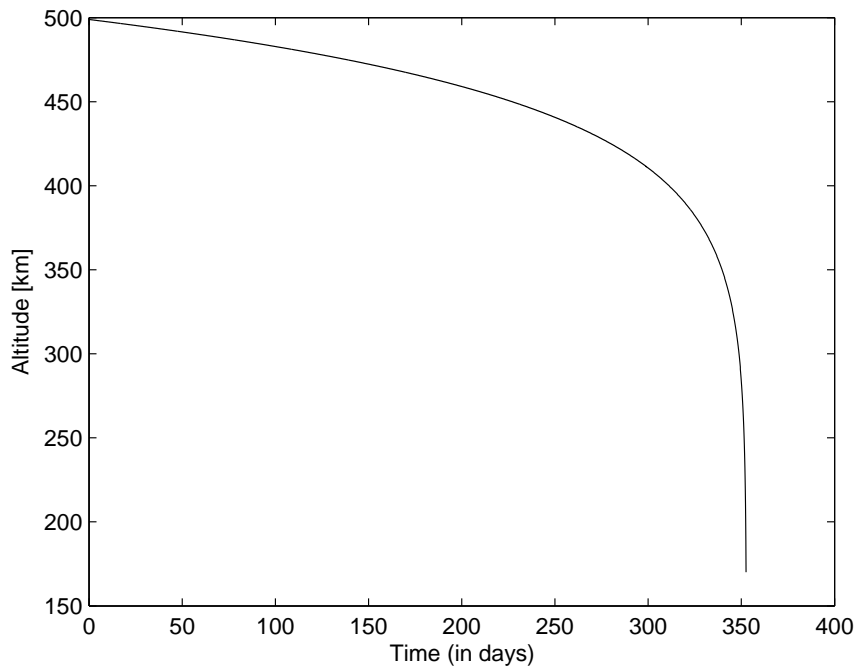


Figure 2.7: Orbit decay under the influence of aerodynamic drag.

In this dissertation, we propose the use of differential force to maintain the SFF system. In the case of aerodynamic drag, this differential force is created by maneuvering the drag plates attached to the leader and follower satellites in the formation. The differential force is given as  $(\vec{F}_{Df} - \vec{F}_{Dl})$ , where  $\vec{F}_{Df}$  and  $\vec{F}_{Dl}$  represents the force due to aerodynamic drag on the follower and leader satellites respectively. Figure (2.9) shows the error in the relative position of the follower satellite under the influence of the differential aerodynamic drag in a projected circular formation of size  $0.5 \text{ km}$ .

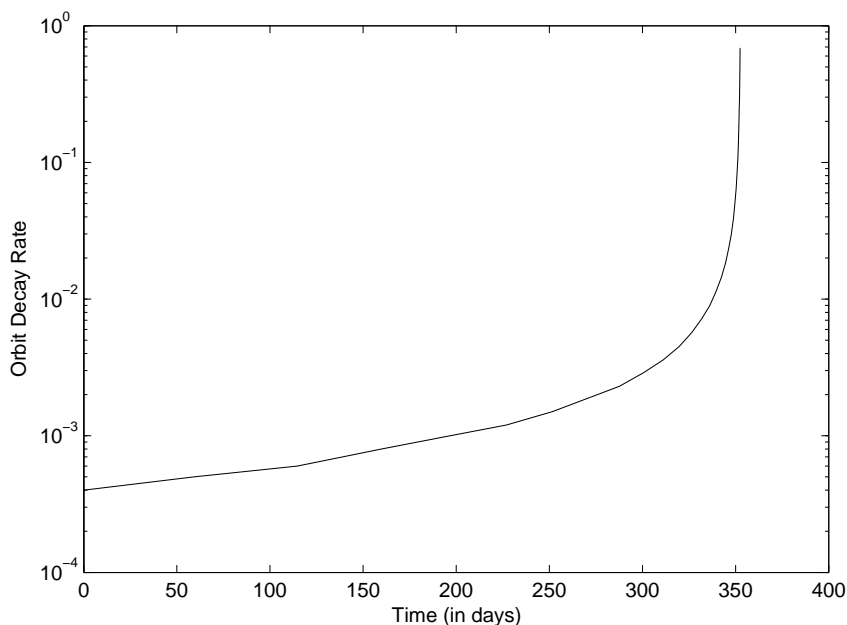


Figure 2.8: Orbit decay rate under the influence of aerodynamic drag.

In addition to the aerodynamic drag, which acts in a direction opposite to the satellite's motion, there is also an aerodynamic lift force acting in a direction perpendicular to the satellite's motion. The value of the lift force depends on the orientation of the satellite, geometry and angle of attack. According to Karr [Karr & Cleland 1975], for an energy accommodation factor of 0.9, the value of the lift to drag ratio for a flat plate is less than 0.1 and hence the effects of lift is neglected.

### 2.3.2 Solar Radiation Pressure Model

The solar radiation pressure force is the largest perturbation acting on high Earth orbit satellites next to the gravitational perturbations from the Earth, Sun, and Moon, and it is the cause of largest error in the modeling of satellite orbital dynamics. The more traditionally developed optical force model assumes that the solar flaps are flat and includes the optical and thermal properties of the surface of the flaps. Here the force exerted on a non-perfect solar flap is obtained by considering reflection, absorption and re-radiation by the flap and is also parameterized by a number of coefficients representing the optical

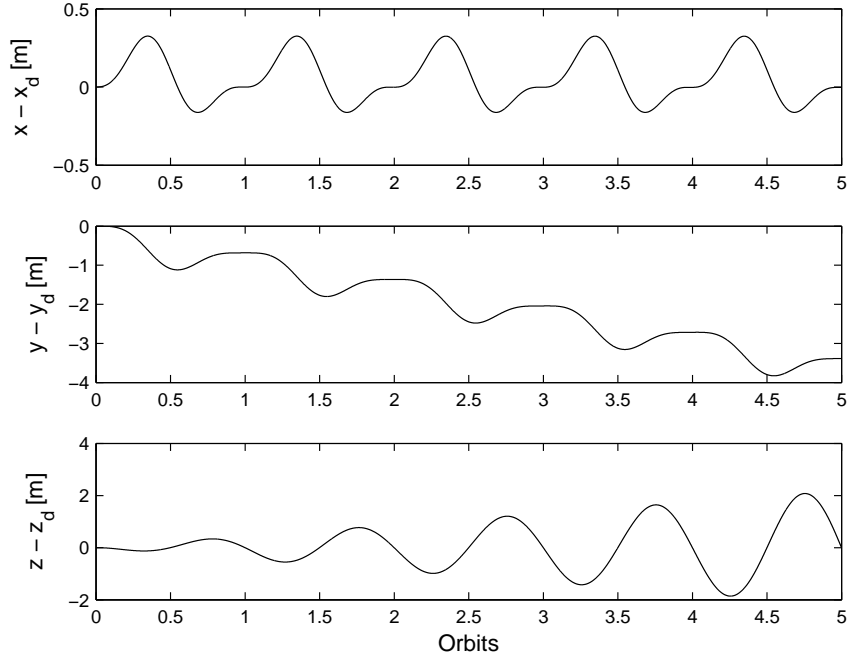


Figure 2.9: Relative positions of a follower satellite under the influence of differential aerodynamic drag with formation size  $r_d = 0.5$  km

properties of the flap. Considering the reflectance, absorption, and emissivity of the flap, the total force exerted due to SRP can be written as

$$f = f_r + f_a + f_e \quad (2.32)$$

where  $f_r$  is the force due to reflection,  $f_a$  is the force due to absorption, and  $f_e$  is the force due to emission due to re-radiation. From Fig. (2.10) it can be observed that, the SRP force acting on a flat surface in terms of normal and transverse components is given by

$$\vec{F} = F_n \hat{i} + F_t \hat{j} \quad (2.33)$$

$$\frac{F_n}{pA} = (1 + \rho_r \rho_s) \cos^2 \alpha + B_f \rho_r (1 - \rho_s) \cos \alpha + \frac{e_f B_f - e_b B_b}{e_f + e_b} (1 - \rho_r) \cos \alpha \quad (2.34)$$

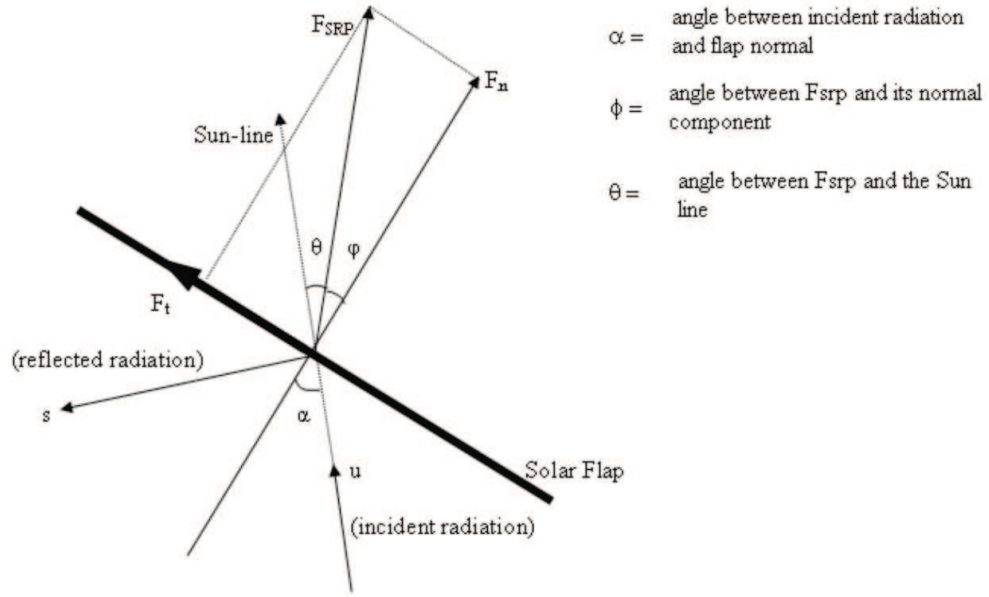


Figure 2.10: Force on a non-perfectly reflecting solar flap.

$$\frac{F_t}{pA} = (1 - \rho_r \rho_s) \cos \alpha \sin \alpha \quad (2.35)$$

Here  $B_f$  and  $B_b$  are non-Lambertian coefficients for front and back surfaces,  $e_f$  and  $e_b$  are front and back surface emission coefficients,  $\rho_r$  is the reflectivity of the front surface,  $\rho_s$  is the specular reflection coefficient, and  $\alpha$  is the pitch angle of the solar flap relative to the Sun-line. Due to optical absorption, the realistic solar flap has a center-line angle, which is the angle between the force vector and the flap normal and is given by

$$\tan \varphi = \frac{F_t}{F_n} \quad (2.36)$$

Two material property parameters which totally account for the effects of absorption, specular and diffuse reflection and thermal emission on thrust and moments are,  $\gamma = \rho_r \rho_s$ , the fraction of the incident flux that is specular reflected and  $\beta$  given by

$$\beta = B_f \rho_r (1 - \rho_s) + \frac{e_f B_f - e_b B_b}{e_f + e_b} (1 - \rho_r) \quad (2.37)$$

which is the fraction of the incident flux that contributes to thrust from diffuse reflection and thermal re-emission. Based on JPL calculations for comet Halley rendezvous study [Wright 1992], the optical parameters for an ideal and non-ideal solar flap are shown in Table 2.1. Assuming that the surface is ideal, the force due to SRP acting on an ideal

Table 2.1: Optical Coefficients.

	$\rho_r$	$\rho_s$	$e_f$	$e_b$	$B_f$	$B_b$
Ideal	1	1	0	0	2/3	2/3
Non-Ideal	0.88	0.94	0.05	0.55	0.79	0.55

reflecting surface simplifies to a force acting normal to the flap given as,

$$F = F_n = 2pA\cos^2\alpha \quad (2.38)$$

Fig. (2.11) shows the error in the relative position of the follower satellite under the influence of the differential SRP in a projected circular formation of size 10 km.

## 2.4 Control Methodology

It is evident from Figs. (2.9) and (2.11), that the formation system is adversely affected by differential aerodynamic drag and SRP. Hence, a suitable control technique is required to make use of these differential forces to control the relative states of the formation. In this thesis, we consider sliding mode control (SMC) technique. SMC is a subset of the variable structure control (VSC) technique. Here a control algorithm is derived such that it is deliberately altered during the control process based on predefined rules which depend on the state of the system. For the purpose of illustration consider the following linear time-invariant system in state-space form ([Edwards & Spurgeon 1998b]):

$$\begin{bmatrix} \dot{X}_1 \\ \dot{X}_2 \end{bmatrix} = \begin{bmatrix} 0 & 1 \\ 0 & 0 \end{bmatrix} \begin{bmatrix} X_1 \\ X_2 \end{bmatrix} + \begin{bmatrix} 0 \\ 1 \end{bmatrix} U \quad (2.39)$$

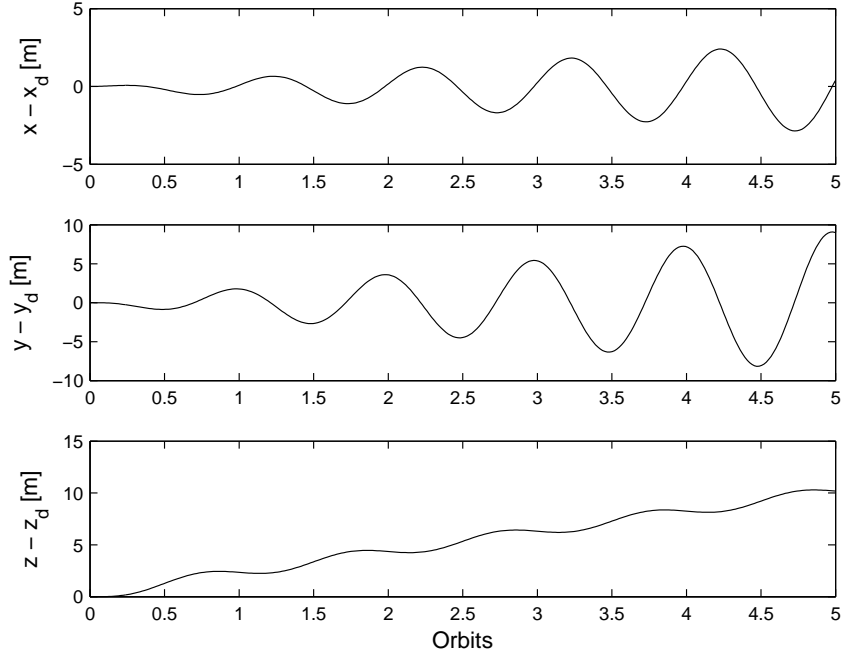


Figure 2.11: Relative positions of a follower satellite under the influence of  $J_2$  and differential SRP with formation size  $r_d = 10$  km.

where  $X \in \mathbb{R}^2 = [X_1, X_2]^T$  is the state vector, and  $U$  is a scalar control input. Next, define a linear sliding surface given by

$$S = X_2 + p X_1 \quad (2.40)$$

where  $p$  is a positive design scalar. Consider the VSC control law given by

$$U = -\eta \operatorname{sgn}(S) = \begin{cases} -\eta & \text{if } S > 0 \\ \eta & \text{if } S < 0 \end{cases} \quad (2.41)$$

where  $\eta$  is a positive design scalar that has a direct effect on the rate at which the sliding surface can be reached. The expression given by Eq. (2.41) is used to control the double integrator given by Eq. (2.39). The phase portrait of the closed-loop system obtained from using the control law given by Eq. (2.41) with  $p = 1$  and  $\eta = 2$  and different initial conditions is shown in Fig. (2.12). The inclined line ( $S = X_2 + p X_1$ ) in Fig. 2.12 represents the set of points for which  $S = 0$ ; in this case a straight line through the origin of gradient

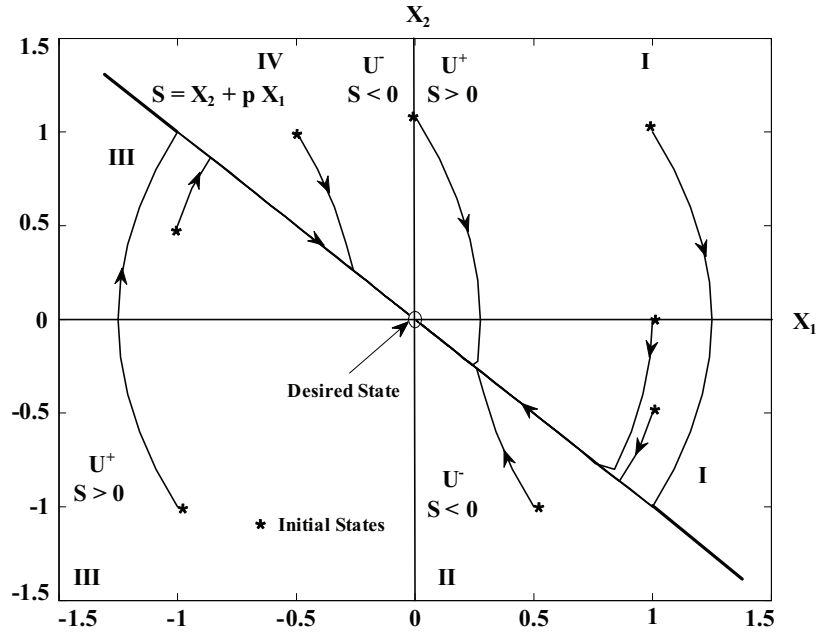


Figure 2.12: Phase portrait of the double integrator under VSC.

$-p$ . This line divides the phase plane into four regions given by

$$\begin{aligned} \text{I: } X_1 > 0, S > 0 \quad \text{and} \quad \text{II: } X_1 > 0, S < 0 \\ \text{III: } X_1 < 0, S < 0 \quad \text{and} \quad \text{IV: } X_1 < 0, S > 0 \end{aligned} \quad (2.42)$$

For a given initial state, the control input  $U$  drives the system trajectory towards the line  $S = 0$ . For values of  $X_2$  satisfying the inequality  $p|X_2| < \eta$ ,

$$S \dot{S} = S[p X_2 - \eta \operatorname{sgn}(S)] < |S|(p|X_2| - \eta) < 0$$

Therefore,

$$\lim_{S \rightarrow 0^+} \dot{S} < 0 \quad \text{and} \quad \lim_{S \rightarrow 0^-} \dot{S} > 0 \quad (2.43)$$

Consequently, when  $p|X_2| < \eta$  the system trajectories on either side of the line  $S = 0$  point towards the line. This is demonstrated in Fig. 2.12 which shows the phase portraits intercepting the line  $S = 0$  from different initial conditions. The condition given by  $S \dot{S} < 0$  is referred to as the *reachability condition*. The trajectory of the system confined to the sliding surface,  $S = 0$ , satisfies the differential equation obtained from rearranging the

terms in Eq. (2.40) for  $S = 0$ .

$$\dot{X}_1 = -p X_1 \quad (2.44)$$

This represents a first-order decay and the trajectories of the system will ‘slide’ along the line  $S = 0$  to the origin. Such dynamical behavior is described as an *ideal sliding mode* and the line  $S = X_2 + p X_1$  is termed the *sliding surface*. During sliding motion, lower-order dynamics dominate the behavior of the system independent of the control. Therefore, the control action only ensures that the sliding surface is reached and the conditions given by Eq. (2.43) are satisfied. The dynamic performance of the system is governed by the choice of the parameter  $p$  in the sliding surface. The finite-time ( $t_r$ ) convergence of the system trajectories to the sliding surface (*reaching time*) can be shown by recalling that

$$S \dot{S} \leq -\eta |S| \quad (2.45)$$

Dividing by  $|S|$  and integrating both sides of Eq. (2.45) between 0 and  $t_r$  gives

$$\int_0^{t_r} \frac{S}{|S|} \dot{S} d\tau \leq - \int_0^{t_r} \eta d\tau$$

$$|S(t_r)| - |S(0)| \leq -\eta t_r \quad (2.46)$$

Since  $|S(t_r)| = 0$ , the reaching time is given by

$$t_r \leq \frac{|S(0)|}{\eta} \quad (2.47)$$



## CHAPTER 3

# Satellite Formation Control Using Aerodynamic Drag

---

**F**EASIBILITY of achieving robust satellite formation control using aerodynamic drag is explored in this chapter. The recently launched TanDEM-X with TerraSAR-X [Krieger & Zink 2007], Tango and Mango of the PRISMA mission [SSC 2010] and Earth Observing Satellite-1 with Landsat-7 [Folta & Hawkins 1996], constitute the only three occasions when satellite formation flying was performed. On both occasions, along track formation was carried out. The main challenge in such SFF mission involves controlling the relative positions of the satellites in the presence of external disturbances i.e., gravitational perturbation (including the Earth's oblateness ( $J_2$ -effect)), aerodynamic drag, solar radiation pressure, and third body perturbations. The effect of these external disturbances were analyzed in Chapter 2. In this chapter, a methodology to achieve coordinated multiple satellite formation flying using differential aerodynamic drag is proposed. The satellite's relative orbit is controlled by rotating the drag plates attached to the satellites and thereby varying the aerodynamic drag experienced by each satellite. This in turn generates relative differential accelerations among the satellites in the formation. A control algorithm based on sliding mode control (SMC) technique is used to develop the steering law for the drag plates. The proposed method can only be used in low Earth orbit (LEO) missions.

The chapter is organized as follows: Section 3.1 introduces the nonlinear mathematical model of the SFF system. Control laws along with the observer design are described in Section 3.2. For a detailed assessment of the system performance under the proposed control strategies, the results of numerical simulations incorporating different formation scenarios are presented in Section 3.3. The conclusions of the present study are summarized in Section 3.4.

### 3.1 SFF Model and Systems Equations of Motion

The investigation is initiated by formulating the nonlinear equations of motion of the SFF system.

#### 3.1.1 Coordinate Frames and Equations of Motion

The SFF system comprises a leader satellite and a follower satellite as shown in Fig.2.1. To initiate the study, we recall the assumptions from Chapter 2, i.e., the leader satellite is in a reference orbit that is assumed to be planer and defined by a radial distance from the center of the Earth and a true anomaly, and the follower satellite is moving in a relative trajectory about the leader satellite. The orientation of the relative frame that is fixed at the leader satellite is such that the  $x$ -axis points along the local vertical, the  $z$ -axis is taken along normal to the orbital plane, and the  $y$ -axis represents the third axis of this right-handed frame. The equations of motion of the follower satellite reproduced here. The orbital equations of motion for the leader satellite is given by Eqs.(3.1) and (3.2), and the relative equations of motion in the radial, along track and cross track directions are given by Eqs.(3.3) and (3.5):

$$\ddot{r}_l - r_l \dot{\theta}^2 + \frac{\mu_e}{r_l^2} = 0 \quad (3.1)$$

$$r_l \ddot{\theta} + 2\dot{\theta}\dot{r}_l = 0 \quad (3.2)$$

$$m_f \ddot{x} - 2m_f \dot{\theta} \dot{y} - m_f (\dot{\theta}^2 x + \ddot{\theta} y) + m_f \mu_e \left( \frac{r_l + x}{r_f^3} - \frac{1}{r_l^2} \right) = f_x + f_{dtx} \quad (3.3)$$

$$m_f \ddot{y} + 2m_f \dot{\theta} \dot{x} + m_f (\ddot{\theta} x - \dot{\theta}^2 y) + m_f \frac{\mu_e}{r_f^3} y = f_y + f_{dty} \quad (3.4)$$

$$m_f \ddot{z} + m_f \frac{\mu_e}{r_f^3} z = f_z + f_{dtz} \quad (3.5)$$

where  $r_l$  is the radial distance from the center of the Earth, and  $r = [(r_l + x)^2 + y^2 + z^2]^{\frac{1}{2}}$ .  $f_j$  and  $f_{dtj}$  denote the control and disturbance forces along the  $j$ -axis,  $j = x, y, z$ , respectively. However, in this study, control force is available only in the  $y$ -axis. This force,  $f_y$ , is created by the drag plates on the satellites while the disturbance force,  $f_{dtj}$ , is attributed

to gravitational perturbation, solar radiation pressure, aerodynamic drag, third body perturbations and the Earth's oblateness effect. Since aerodynamic drag is considered as the control input, only disturbing effect from that will be the variation in atmospheric density.

### 3.1.2 Aerodynamic Drag Model

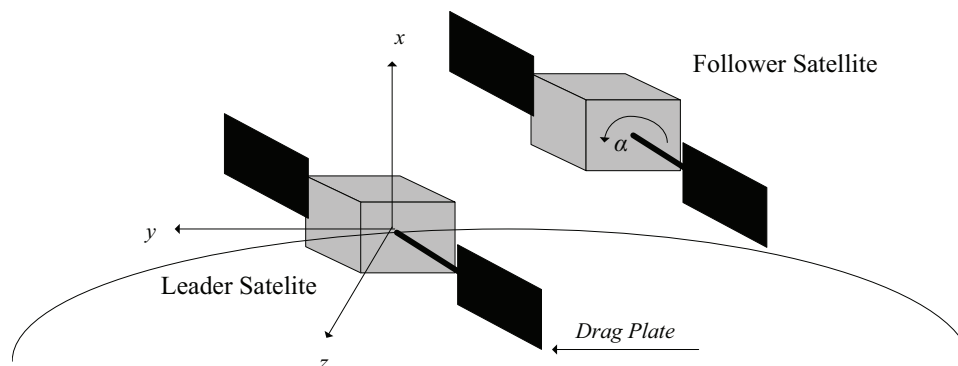


Figure 3.1: Pictorial representation of the formation system.

The aerodynamic drag has a substantial influence on the motion of the near-Earth satellites. The aerodynamic force in continuum flow can be expressed in terms of the drag, i.e. the force parallel to the atmospheric velocity direction. The vector equation for computing the drag force is

$$\vec{F}_D = -\frac{1}{2}\rho C_D A |\vec{V}_{rel}|^2 \hat{V}_{rel} \quad (3.6)$$

where  $C_D$ , is the drag coefficient,  $\rho$ , is the atmospheric density, and  $A$  is the projected area of the satellite normal to  $\vec{V}_{rel}$ .  $\vec{V}_{rel}$ , is the relative velocity of the satellite with respect to the atmosphere and  $\hat{V}_{rel}$  is a unit vector in the direction of the satellite's velocity. The drag force,  $\vec{F}_D$ , thus acts in the direction opposite to the relative velocity,  $\vec{V}_{rel}$ . The coefficient  $C_D$  is dependent on the geometry of the satellite and varies with altitude, and the angle of attack. The differential drag created by the drag plates attached to the satellites in the formation can be formulated using Eq. (3.6), and the force ( $f_y$ ) in Eq.(3.4) acting on the follower satellite is given by

$$f_y = F_{D_f} - F_{D_l}$$

$$f_y = -\frac{1}{2}\rho_f C_d V_{frel}^2 A_f \sin \alpha_f - \left( -\frac{1}{2}\rho_l C_d V_{lrel}^2 A_l \sin \alpha_l \right) \quad (3.7)$$

where  $\rho_j$ ,  $V_{jrel}$ ,  $A_j$ ,  $\alpha_j$ , for  $j = f, l$  correspond to the local atmospheric density, the relative velocity of the satellite with the local atmosphere, the area of the drag plate for the follower and leader satellites, respectively. The drag plates are assumed to be of negligible thickness. A pictorial representation of the system is shown in Fig.3.1. Similar satellite formation control with only along-track force has been considered in previous works ([Kumar *et al.* 2007c],[Starin *et al.* 2001]).

## 3.2 Design of Control Law

The control objective here is to determine the orientation of the drag plates ( $\alpha_f, \alpha_l$ ) which will drive the follower satellite to the desired formation trajectory with respect to the leader satellite in the presence of external disturbances and initial deployment errors. We develop a control law based on SMC technique. Considering the mathematical formulation of the leader follower SFF model and aerodynamic drag model presented in the previous section, we define the relative state vector and the desired relative trajectory as,  $X(t)$ ,  $X_d(t) \in \mathbb{R}^4$  respectively. The performance measure is defined as the tracking error,  $e(t) \in \mathbb{R}^4$ ,

$$e(t) \triangleq X(t) - X_d(t) \quad (3.8)$$

The objective is to develop a control algorithm for Eqs.(3.3) and (3.4) in the SFF system such that the control force  $f_y$  drives the relative states of the system to the desired relative trajectories as  $t \rightarrow \infty$ , and thereby the tracking errors, Eq.(3.8), converges to zero.

In order to simplify the control law design, we consider  $\alpha_f = \alpha_0 + \delta\alpha/2$  and  $\alpha_l = \alpha_0 - \delta\alpha/2$ , where  $\alpha_0$  is the initial orientation of the drag plates. Assuming the first order approximation for the differential drag plate's orientation  $\delta\alpha$ , and considering the parameters  $\rho_j$ ,  $V_{jrel}$ ,  $A_j$ , for  $j = f, l$  are same for both the leader and follower satellites ( $\rho_j = \rho$ ,  $V_{rj} = V_r$ ,  $A_j = A$ , for  $j = f, l$ ) into Eq.(3.7), we have

$$f_y = -\frac{1}{2}\rho C_d V_{rel}^2 A \cos \alpha_0 \delta\alpha \quad (3.9)$$

Please note that these assumptions on the aerodynamic drag system parameters are applied only during the control law formulation but not considered during the numerical simulations.

Next we present the design procedure to implement SMC for changing  $\delta\alpha$  to achieve satellite formation control. The overall design can be divided into two main steps. (i) A stable sliding surface/manifold is designed such that this surface will ensure that the follower satellite dynamics precisely tracks the desired trajectory once the system is restricted to that manifold. (ii) A feedback control algorithm that can drive the relative states to the sliding manifold in finite time and maintain it on the manifold is derived. The sliding manifold should be designed such that not only the closed loop system stability is guaranteed in the presence of unmatched perturbations, but also the desired dynamic behaviour should be exhibited when the dynamics of the system is on the sliding manifold.

### 3.2.1 Design of Sliding Manifold

The sliding manifold is designed using the linear representation of the nonlinear system equations of motion Eqs.(3.3) and (3.4),(i.e., Hill's Equations [Hill 1878] or the Clohessy-Wiltshire equations (HCW) [Clohessy & Wiltshire 1960]), that can be represented in terms of new coordinates  $p_1 \in \mathbb{R}^{3 \times 1}$  and  $p_2 \in \mathbb{R}$  as follows:

$$\begin{bmatrix} \dot{p}_1 \\ \dot{p}_2 \end{bmatrix} = \begin{bmatrix} A_{11} & A_{12} \\ A_{21} & A_{22} \end{bmatrix} \begin{bmatrix} p_1 \\ p_2 \end{bmatrix} + \begin{bmatrix} 0 \\ B \end{bmatrix} U \quad (3.10)$$

where  $p_1 = [x, y, \dot{x}]$ , is the state vector associated with the states that are not under explicit control authority called the unactuated states,  $p_2 = \dot{y}$ , is the system state under explicit control authority called the actuated state,  $U = \delta\alpha$ , and

$$A_{11} = \begin{bmatrix} 0 & 0 & 1 \\ 0 & 0 & 0 \\ 3\dot{\theta}^2 & 0 & 0 \end{bmatrix}; \quad A_{12} = \begin{bmatrix} 0 \\ 1 \\ 2\dot{\theta} \end{bmatrix}; \quad A_{21} = \begin{bmatrix} 0 & 0 & -2\dot{\theta} \end{bmatrix}$$

$$A_{22} = \begin{bmatrix} 0 \end{bmatrix}; \quad B = \begin{bmatrix} -\frac{\rho}{2} C_d V_{rel}^2 A \cos \alpha_0 \end{bmatrix} \quad (3.11)$$

Note  $\dot{\theta}$  is a constant given by  $\sqrt{\mu/a_c^3}$ . Carrying out a similar transformation on the desired trajectory relations, Eqs.(2.19) and (2.20), we have  $X_d = [p_1^d, p_2^d]^T$ . Thus, the desired trajectory after the transformation can be obtained as,

$$\begin{bmatrix} \dot{p}_1^d \\ \dot{p}_2^d \end{bmatrix} = \begin{bmatrix} A_{11}^d & A_{12}^d \\ A_{21}^d & A_{22}^d \end{bmatrix} \begin{bmatrix} p_1^d \\ p_2^d \end{bmatrix} \quad (3.12)$$

Based on Eqs.(3.11) and (3.12), the following error dynamics can be formulated:

$$\begin{aligned} \dot{e}_1 &= A_{11}e_1 + A_{12}e_2 + \bar{A}_{11}p_1^d + \bar{A}_{12}p_2^d \\ \dot{e}_2 &= A_{21}e_1 + A_{22}e_2 + BU + \bar{A}_{21}p_1^d + \bar{A}_{22}p_2^d \end{aligned} \quad (3.13)$$

where  $\bar{A}_{i,j} = A_{i,j} - A_{i,j}^d$  or  $i, j=1,2$  and  $e_i = p_i - p_i^d$ . By utilizing the coupling between the actuated and the unactuated states, the sliding surface,  $S$  can be defined as a function of the tracking errors and the desired states as follows:

$$S = \{e_1 \in \mathbb{R}^{3 \times 1}, e_2 \in \mathbb{R} : e_2 + Ke_1 = 0\} \quad (3.14)$$

where  $K \in \mathbb{R}^{1 \times 3}$  is a weighting matrix. The sliding motion starts as soon as the system reaches the sliding surface,  $S = 0 \forall t > t_r$ , where  $t_r$  is the reaching time and the system dynamics is governed by the following relation

$$e_2 = -Ke_1 \quad (3.15)$$

From Eq.(3.15) it can be observed that the error state  $e_2$  manifests as a control signal to stabilize  $e_1$  during ideal sliding mode behaviour, i.e.,  $S = 0$ . Furthermore, Eq.(3.15) holds only on the sliding surface and substituting this relation to the reduced order system in Eq.(3.13) yields

$$\dot{e}_1 = (A_{11} - A_{12}K)e_1 + \bar{A}_{11}p_1^d + \bar{A}_{12}p_2^d \quad (3.16)$$

As per the preceding Eq.(3.16), the choice of sliding surface is governed by the suitable selection of weighting matrix  $K$  which affects the dynamics of the reduced order system. The weighting matrix  $K$  can be determined by any classical control methods such that

Eq.(3.16) is Hurwitz. Here the weighting matrix  $K$  is designed using the linear quadratic regulator method.

### 3.2.2 Control Formulation

Here an adaptive control algorithm that will manoeuvre the system trajectories to the sliding manifold is designed. In the SFF system controlled by aerodynamic drag, parameter uncertainties such as aerodynamic density, relative velocity and drag coefficient can adversely affect the performance of the system if not appropriately addressed. In the adaptive control methodology the unknown or slowly time-varying parameters are estimated online and these estimated quantities are used in place of the uncertain parameters in the feedback control law. In order to design control algorithm, the equations of motion that are of interest in this study Eqs.(3.3) and (3.4) are rewritten in the form:

$$\dot{X} = AX + E(X) + CU + DF_{dt} \quad (3.17)$$

where

$$X = \begin{bmatrix} x \\ y \\ \dot{x} \\ \dot{y} \end{bmatrix}; A = \begin{bmatrix} 0 & 0 & 1 & 0 \\ 0 & 0 & 0 & 1 \\ 3\dot{\theta}^2 & 0 & 0 & 2\dot{\theta} \\ 0 & 0 & -2\dot{\theta} & 0 \end{bmatrix}; E(X) = \begin{bmatrix} 0 \\ 0 \\ \mu \left( \frac{1}{r_c^2} - \frac{(r_c+x)}{r^3} \right) - 2\dot{\theta}^2 x \\ \dot{\theta}^2 y - \frac{\mu y}{r^3} \end{bmatrix}$$

$$C = \begin{bmatrix} 0 \\ 0 \\ 0 \\ B \end{bmatrix}; D = \begin{bmatrix} 0 & 0 \\ 0 & 0 \\ 1 & 0 \\ 0 & 1 \end{bmatrix}$$

Here the nonlinear terms in the equations of motion have been lumped into  $E(X)$ ,  $A$  represents the linear part of the system,  $C$  is the control matrix, where  $B$  is as shown in Eq.(3.11),  $U$  is the control input, and  $F_{dt}$  the differential perturbation forces. The control law is derived such that, the system response during the transient phase is improved and the closed loop system is maintained on the sliding surface at all time. Next we make use

of the estimates on the upper-bound of the uncertainties and perturbation on the system to design the control algorithm. It is assumed that the nonlinear component,  $E(X)$ , in the equations of motion are bounded and the choice of the desired reference trajectories,  $X_d$ , impose the following constraint given by,

$$\|E(X)\| \leq d_2 \|X\| \text{ and } \|X_d\| \leq d_1 \quad (3.18)$$

where  $d_1 > 0$  and  $d_2$  is the Lipschitz constant of the nonlinear vector field associated with  $E(X)$ . This information is found by varying the formation disc size from 1 km to 150 km and choosing the maximum value, i.e.,  $\max(\|E(X)\| / \|X\|)$  [Vaddi 2003]. All the external perturbations such as  $J_2$ , solar perturbations, and magnetic forces, are assumed to be bounded as well and included in the following chosen uncertainty bound (with scalar constants  $d_3, d_4 > 0$ ).

$$\|F_{dt}\| \leq d_3 \|X\| + d_4 \quad (3.19)$$

Next the adaptive control algorithm is derived. Here the parameter  $B$  given in Eq.(3.11), is assumed as an unknown quantity and is hence estimated online and then used in the control algorithm. The sliding manifold derived in Eq.(3.14) is rewritten as

$$S = \{e \in \mathbb{R}^{4 \times 1} : \Lambda e = 0\} \quad (3.20)$$

where  $\Lambda = [K \ 1] = [K_1 \ K_2 \ K_3 \ 1]$  and  $e_i = p_i - p_i^d$  for  $j = 1, 2$ . Its derivative is obtained as

$$\dot{S} = \Lambda \dot{e} \quad (3.21)$$

Now consider the Lyapunov candidate function defined as follows,

$$V = \frac{1}{2} S^T S + \frac{1}{2\gamma} \tilde{B}^T \tilde{B} \quad (3.22)$$

where  $V > 0$  and  $\gamma$  is a positive constant. Taking the derivative of  $V$  along its trajectories yields,

$$\dot{V} = S^T \dot{S} + \frac{\tilde{B} \dot{\tilde{B}}}{\gamma} \quad (3.23)$$

Substituting Eq.(3.21), in Eq.(3.23) and expanding we get,

$$\dot{V} = S^T \Lambda \dot{e} + \frac{\tilde{B} \dot{\hat{B}}}{\gamma} \quad (3.24)$$

or

$$\dot{V} = S^T \left[ \Lambda AX + BU + \Lambda (E(X) + DF_{dt}) - \Lambda \dot{X}_d \right] + \frac{\tilde{B} \dot{\hat{B}}}{\gamma} \quad (3.25)$$

Taking the parameter estimation error as  $\tilde{B} = \hat{B} - B$  (estimate - true value), and expanding Eq.(3.25), we have

$$\dot{V} = S^T \left[ \Lambda AX + (\hat{B} - \tilde{B})U + \Lambda (E(X) + DF_{dt}) - \Lambda \dot{X}_d \right] + \frac{\tilde{B} \dot{\hat{B}}}{\gamma} \quad (3.26)$$

Rearranging the preceding Eq.(3.26) yields,

$$\dot{V} = S^T \left[ \Lambda AX + \hat{B}U + \Lambda (E(X) + DF_{dt}) - \Lambda \dot{X}_d \right] - S^T \tilde{B}U + \frac{\tilde{B} \dot{\hat{B}}}{\gamma} \quad (3.27)$$

Now the bounds on the uncertainties and nonlinear components, given by Eqs.(3.18) and (3.19), can be combined together and written as

$$\|L\| \leq (d_3 + d_2) \|X\| + (d_4 + d_1) \leq d(1 + \|X\|) \quad (3.28)$$

where

$$L = \Lambda (E(X) + DF_{dt}) - \Lambda \dot{X}_d$$

Therefore Eq.(3.27) can be written as

$$\dot{V} = S^T \left[ \Lambda AX + \hat{B}U + \|L\| \right] - S^T \tilde{B}U + \frac{\tilde{B} \dot{\hat{B}}}{\gamma} \quad (3.29)$$

Now in order to make  $\dot{V}$  negative, choose the adaptive law as

$$\dot{\hat{B}} = \gamma S^T U \quad (3.30)$$

Also let

$$\Lambda AX + \hat{B}U = -\eta \text{sgn}(S) \quad (3.31)$$

where  $\eta$  is a positive constant and  $\eta \gg \sup \|L\|$ . Substituting Eqs.(3.31) and (3.30) into Eq.(3.29) we have,

$$\dot{V} = S^T [-\eta \text{sgn}(S) + \|L\|] \quad (3.32)$$

Thus,  $\dot{V}$  is negative and hence the reaching condition is satisfied. Using Theorem-3 of LaSalle's principle [LaSalle 1960] it is proved that the system is completely stable and hence the system states converge onto the sliding surface which is the invariant set here. Next, Eq.(3.31) is rearranged to derive the control law as,

$$U = -\frac{1}{\hat{B}} [\eta \text{sgn}(S) + \Lambda AX] \quad (3.33)$$

It is to be mentioned that the system states are driven to the sliding surface by the discontinuous part in the control law (i.e.,  $\eta \text{sgn}(S)$ ). The orientation of the drag plates ( $\alpha_f, \alpha_l$ ) can now be determined and used in computing the differential drag, Eq.(3.7). This is then used in the numerical simulations, Eq.(3.4). Though sliding mode control is a robust control technique, chattering is a major drawback because of the discontinuous control nature. This problem, however, can be solved by replacing the nonlinear signum function with a suitable boundary layer of nonlinear saturation function. Using this approach, the phase trajectory oscillates within the sliding surface without switching controller action. Hence, the control law, Eq.(3.33) can be rewritten incorporating the boundary layer function as

$$U = -\frac{1}{\hat{B}} \left[ \eta \left( \frac{S}{|S| + \tau} \right) + \Lambda AX \right] \quad (3.34)$$

where  $\tau$ , the width of the boundary layer is a positive constant.

### 3.2.3 Dynamic System Stability Analysis

Next we examine the robustness of the system during the sliding regime. It is well known that the system states are insensitive to matched disturbances, i.e., once on the sliding surface, the uncertainties and perturbations do not affect the explicitly actuated states. But

the unmatched disturbances do affect the closed loop system performance. To evaluate this we apply Shyu's stability criterion [Shyu *et al.* 1998] together with the procedure detailed in Spurgeon et.al.[Spurgeon & Davies 1993],[Edwards & Spurgeon 1998a] for the reduced order systems with unmatched disturbances. Consider the error dynamics of the SFF system on the sliding surface referring to Eq.(3.13) in conjunction with uncertainties or disturbances,

$$\begin{aligned}\dot{e}_1 &= A_{11}e_1 + A_{12}e_2 + \bar{A}_{11}p_1^d + \bar{A}_{12}p_2^d + f_{um}(X) \\ \dot{e}_2 &= A_{21}e_1 + A_{22}e_2 + B_2U + \bar{A}_{21}p_1^d + \bar{A}_{22}p_2^d + f_{ma}(X)\end{aligned}\quad (3.35)$$

where  $f_{um}(X) \in \mathbb{R}^3$  and  $f_{ma}(X) \in \mathbb{R}$  are the bounded terms representing unmatched and matched uncertainties or disturbances in the system, respectively. The unmatched uncertainties are assumed to be bounded  $\|f_{um}(X)\| \leq 1 + d_5 \|X\|$ . The equation representing the error dynamics on the sliding surface, obtained by substituting  $S = 0$  in Eq.(3.35), is given as

$$\dot{e}_1 = (A_{11} - A_{12}K) e_1 + f_{um}(X) \quad (3.36)$$

To verify the stability of the system in the presence of unmatched uncertainties we propose the following theorem.

**Theorem 3.1:** *For a reduced order system with uncertainty, described by*

$$\dot{x}_1 = (A_{11} - A_{12}K) x_1 + \bar{f}(x_1) \quad (3.37)$$

where  $\bar{f}(x_1)$  is the unmatched uncertainty and which satisfies the uniform Lipschitz condition  $\|f_{um}(x_1^1) - f_{um}(x_1^2)\| \leq k \|x_1^1 - x_1^2\|$ , the uncertain system on the sliding surface  $S = 0$  is asymptotically stable. Here range of  $k$  is given by  $0 < k < 0.5\lambda_{\min}(\bar{Q}) / \|\bar{P}\|$  with  $P$  and  $Q \in \mathbb{R}^{(n-m) \times (n-m)}$ .  $P$  and  $Q$  are symmetric, positive-definite matrices satisfying the Lyapunov equation  $(A_{11})^T \bar{P} + \bar{P} (A_{11}) = -\bar{Q}$ .

**Proof:** Consider a candidate Lyapunov function

$$\dot{V} = \dot{e}_1^T \bar{P} e_1 + e_1^T \bar{P} \dot{e}_1 \quad (3.38)$$

Substituting Eq.(3.37) into Eq.(3.38) yields,

$$\begin{aligned}\dot{V} &= e_1 [(A_{11} - A_{12}K) + (A_{11} - A_{12}K)] \bar{P}e_1^T + 2\bar{P}e_1^T f_{um}(X) \\ &\leq -e_1^T \bar{Q}e_1 + 2\bar{P}e_1^T f_{um}(X)\end{aligned}\quad (3.39)$$

Now by using Eq.(3.39) in conjugation with the Rayleigh principle, we have

$$e_1^T \bar{Q}e_1 \geq \lambda_{\min} \bar{Q} \|e_1\|^2 \text{ and } \|\bar{P}f_{um}(X)\| \leq k \|\bar{P}\| \|e_1\| \quad (3.40)$$

Therefore, this yields

$$\dot{V} \leq -\lambda_{\min} \bar{Q} \|e_1\|^2 + 2k \|\bar{P}\| \|e_1\|^2 \quad (3.41)$$

Hence  $\dot{V}$  is negative. This shows that the system is insensitive to the unmatched disturbances and all the states reach the sliding surface and remain bounded.  $\square$

### 3.2.4 Observer Design

From previous sections on control algorithm design, it is clear that state variables are required in the feedback control formulation. These can be measured or estimated for the tracking control. A Carrier-phase Differential GPS (CD Global Positioning System) receiver could be used to obtain the relative positions of the satellites. Here it is considered that only the relative position vector is readily available. We either use numerical differentiation to obtain the velocities or use an observer to estimate the states. Here an observer is designed for estimating the velocities to be used in the feedback control law. The observer is based on the modified second order sliding mode super twisting algorithm [Davila *et al.* 2005], [M'Sirdi *et al.* 2008]. This particular sliding mode observer formulation is used due to its finite time convergence to the true value of the observed states, robustness with respect to uncertainties and also requires smaller gain values and is more accurate in terms of estimation [Davila *et al.* 2005]. Considering the state variables  $x_1 = x$ ,  $x_2 = \dot{x}$ ,  $y_1 = y$ ,  $y_2 = \dot{y}$  and  $z_1 = z$ , the nonlinear equations of motion of the system given by Eq.(3.17) can

be rewritten without considering any external disturbance terms as follows.

$$\begin{aligned}
 \dot{x}_1 &= x_2 \\
 \dot{y}_1 &= y_2 \\
 \dot{x}_2 &= f_1(x_1, y_2) + \xi_1(x_1, y_1, z_1) \\
 \dot{y}_2 &= f_2(x_2, f_y) + \xi_2(x_1, y_1, z_1, f_y)
 \end{aligned} \tag{3.42}$$

where  $f_1(x_1, y_2)$  and  $f_2(x_2, f_y)$  represent the known nominal functions, while  $\xi_1(x_1, y_1, z_1)$  and  $\xi_2(x_1, y_1, z_1, f_y)$  represent the terms involving uncertainties. Consider the observer as

$$\begin{aligned}
 \dot{\hat{x}}_1 &= \hat{x}_2 + \delta_1 |x_1 - \hat{x}_1|^{\frac{1}{2}} \text{sgn}(x_1 - \hat{x}_1) \\
 \dot{\hat{y}}_1 &= \hat{y}_2 + \delta_2 |y_1 - \hat{y}_1|^{\frac{1}{2}} \text{sgn}(y_1 - \hat{y}_1) \\
 \dot{\hat{x}}_2 &= f_1(x_1, \hat{y}_2) + \beta_1 \text{sgn}(x_1 - \hat{x}_1) \\
 \dot{\hat{y}}_2 &= f_2(\hat{x}_2, f_y) + \beta_2 \text{sgn}(y_1 - \hat{y}_1)
 \end{aligned} \tag{3.43}$$

where  $\hat{x}_1, \hat{x}_2, \hat{y}_1$  and  $\hat{y}_2$  are the state estimates,  $\delta_j$  and  $\beta_j, j = 1, 2$  are design constants and  $\delta_1 |x_1 - \hat{x}_1|^{\frac{1}{2}} \text{sgn}(x_1 - \hat{x}_1), \delta_2 |y_1 - \hat{y}_1|^{\frac{1}{2}} \text{sgn}(y_1 - \hat{y}_1), \beta_1 \text{sgn}(x_1 - \hat{x}_1)$  and  $\beta_2 \text{sgn}(y_1 - \hat{y}_1)$  are the output injections. In order to ensure the convergence of the observer, initial values of the estimates are taken  $\hat{x}_1 = x_1, \hat{y}_1 = y_1, \hat{x}_2 = 0$  and  $\hat{y}_2 = 0$ . Denoting the state estimation errors as  $\tilde{x}_1 = x_1 - \hat{x}_1, \tilde{x}_2 = x_2 - \hat{x}_2, \tilde{y}_1 = y_1 - \hat{y}_1$  and  $\tilde{y}_2 = y_2 - \hat{y}_2$ , the state estimation error equations are obtained from Eqs.(3.42) and (3.43) as follows.

$$\begin{aligned}
 \dot{\tilde{x}}_1 &= \tilde{x}_2 - \delta_1 |\tilde{x}_1|^{\frac{1}{2}} \text{sgn}(\tilde{x}_1) \\
 \dot{\tilde{y}}_1 &= \tilde{y}_2 - \delta_2 |\tilde{y}_1|^{\frac{1}{2}} \text{sgn}(\tilde{y}_1) \\
 \dot{\tilde{x}}_2 &= F(x_1, y_1, z_1, y_2, \hat{y}_2) - \beta_1 \text{sgn}(\tilde{x}_1) \\
 \dot{\tilde{y}}_2 &= F(x_1, y_1, z_1, x_2, \hat{x}_2) - \beta_2 \text{sgn}(\tilde{y}_1)
 \end{aligned} \tag{3.44}$$

where  $F(x_1, y_1, z_1, y_2, \hat{y}_2) = f_1(x_1, y_2) - f_1(x_1, \hat{y}_2) + \xi_1(x_1, y_1, z_1)$  and  $F(x_1, y_1, z_1, x_2, \hat{x}_2) = f_2(x_2, f_y) - f_2(\hat{x}_2, f_y) + \xi_2(x_1, y_1, z_1, f_y)$ . Assuming that the system states and the control input,  $f_y$ , are bounded then the existence of constants  $f_1^+$  and  $f_2^+$  are ensured such that

$$|F(x_1, y_1, z_1, y_2, \hat{y}_2)| < f_1^+ \text{ and } |F(x_1, y_1, z_1, x_2, \hat{x}_2)| < f_2^+ \quad (3.45)$$

Let,  $\beta_1 > f_1^+$  and  $\beta_2 > f_2^+$

$$\beta_1 > \sqrt{\frac{2}{\alpha_1 - f_1^+} \frac{(\alpha_1 + f_1^+)(1+p)}{(1-p)}} \text{ and } \beta_2 > \sqrt{\frac{2}{\alpha_2 - f_2^+} \frac{(\alpha_2 + f_2^+)(1+p)}{(1-p)}} \quad (3.46)$$

where  $p$  is a constant in the range  $0 < p < 1$ . It has been proved in Davila [Davila *et al.* 2005] that if the observer parameters  $\beta_j$  and  $\delta_j$ ,  $j = 1, 2$  are chosen in accordance with Eq.(3.46) and if the condition in Eqs.(3.45) holds for the set of the system equations of motion, then the variables of the observer will converge in finite time to the actual system states, i.e.,  $(\hat{x}_1, \hat{x}_2, \hat{y}_1, \hat{y}_2) \rightarrow (x_1, x_2, y_1, y_2)$ . The separation principle is also satisfied, thereby allowing the design of the observer and the control law separately.

### 3.3 Performance Evaluation

In order to examine the effectiveness and performance of the proposed formation control strategy, the detailed response is numerically simulated using the set of governing equations of motion Eqs.(3.1) - (3.4) along with Eq.(3.7) in conjunction with the proposed control law given by Eq.(3.34), and the adaptation law, Eq.(3.30). The velocity of the follower satellite is derived using the SMC observer given in Eq.(3.43). The integration is carried out in Matlab using the fourth order Runge-Kutta solver with a fixed step size of 0.1 sec. The desired states of the system are given by the types of formation, as per Eqs.(2.19) - (2.20). The SFF systems parameters and the orbital parameters used in the numerical simulation are listed in Table 3.1. The controller and observer design parameters are presented in Table 3.2. It should be noted here that in the development of the control law it is assumed that the leader is in an unperturbed reference orbit. However, numerical simulation is conducted on the system model that considers the leader satellite under  $J_2$ -effect, variation in atmospheric density with position, and variation in orientation of the drag plates. The atmospheric density and the relative velocity in Eq.(3.7) are updated depending on the

Table 3.1: Orbital and system parameters

Parameters	Value
$m_f$ (kg)	10
$\mu(km^3s^{-2})$	398600
$r_p$ (km)	6878
$e$	0.001
$\Omega, \omega$ (deg)	0
$i$ (AF)(deg)	97.44
$i$ (PCF)(deg)	45
$C_d$	2.0
$F_{10.7}$	150
$A_p$	3
$A$ ( $m^2$ )	1.0
$\phi$ (deg)	0

satellite position during the simulation. The Matlab function ATMOSNRLMSISE00 is used in the calculation of the atmospheric density based on NRLMSISE-00 scheme.

Table 3.2: Controller and observer parameters

Parameters	Value(s)
$\eta$	0.00001
$\tau$	0.002
$[K_1, K_2, K_3]$	[0.0434 19.4337 -0.0200]
Initial estimate of density, $\hat{\rho}_0$ ( $kg/m^3$ )	$1.454 \times 10^{-13}$
Initial estimate of drag coefficient, $\hat{C}_d$	1.8
Initial estimate of Area, $\hat{A}$ ( $m^2$ )	0.5
Initial Mass, $\hat{m}_f$ (kg)	2.5
Initial angle estimate, $\hat{\alpha}_0$ (deg)	0
$\gamma$	$10^{-4}$
$\delta_1, \delta_2$	1 , 1
$\beta_1, \beta_2$	2 , 2

The control law development refers to the exponential atmospheric density model given by  $\rho(h) = \rho_0 e^{-(\frac{h-h_0}{H})}$ . Here  $h$  is the actual altitude above the Earth's surface,  $\rho_0$  is the reference density,  $h_0$  is the reference altitude and  $H$  is the scale height. Table 8-4 in [Vallado 2004] is used to obtain the density values. The adaptive control algorithm makes

use only of an initial estimate of the atmospheric density. Here the initial value of  $\rho_0$  is taken as  $1.454 \times 10^{-13} \text{kg/m}^3$ , which corresponds to the density for an altitude between 600-700 km. The SFF system is in an orbit of 350 km altitude. This bias in the initial estimate is used to examine the efficacy of the control algorithm in a more realistic environment.

With regard to the observer data, it is assumed that errors in the available position measurements are of the order of 5 cm. This is simulated by adding white noise to the position vector such that the variance for the relative position is  $\left(\frac{5}{3}\right)^2$ . This will generate biased position vectors with maximum error of 5 cm [Bevilacqua *et al.* 2009].

### 3.3.1 Projected circular formation and Circular formation

First we examine the performance of the proposed SFF system in maintaining a projected circular formation. The phase angle ( $\phi$ ) between the leader and the follower satellites is assumed to be zero degree with a desired formation radius,  $r_d = 0.5$  km with the leader satellite in an orbit of inclination,  $i = 45^\circ$ . In *PCF*, the leader and the follower satellite maintain a fixed relative distance on the  $y$ - $z$  plane. But due to the lack of control on the  $z$ -axis, the *PCF* will deteriorate over time due to the influence of the  $J_2$  perturbation. Hence we make use of the iterative scheme given in [Damaren 2007] to derive the initial conditions to reduce the effect of  $J_2$  on  $z$ -axis. These initial conditions are derived based on the nonlinear equations of motion rather than the *HCW* equations and yield relative orbits that are nearly periodic in the presence of  $J_2$  perturbation, and hence ascertain the validity of performing projected circular formation with differential aerodynamic drag. Such special initial conditions are also derived in [Sabatini *et al.* 2008]. Fig. (3.2), shows the relative error plots for the follower in the proposed SFF system for one day in orbit using the following initial state vector given by,

$$X = [0 \ 0.5 \ 0 \ 0.00286 \ -0.00319 \ 0.00055]^T \quad (3.47)$$

The relative position errors remain bounded to less than  $-2$  m in the radial direction and to within  $-5$  m in the along track direction. Relative error in the cross track direction remains bounded between  $\pm 20$  m.

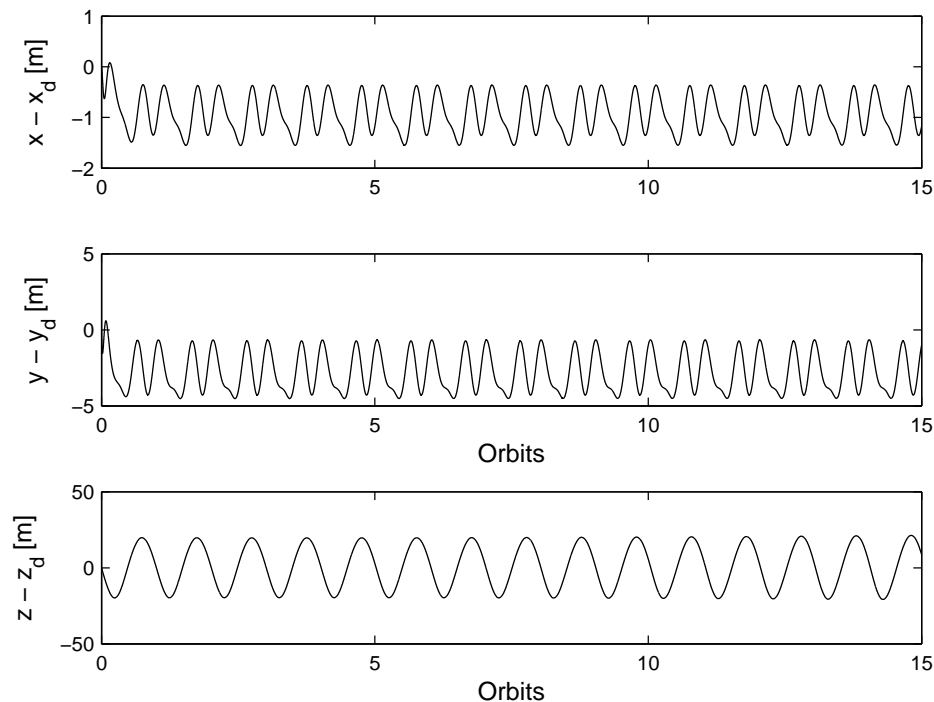


Figure 3.2: Relative position errors in project circular formation for one day ( $r_d = 0.5$  km).

Next we examine the performance of the proposed SFF system in the presence of an additional disturbance in the form of an initial offset error of 50 m in the radial and along track direction. It can be observed from Fig. 3.3, that these relative states converge to the desired states in one orbit with the relative position errors remain bounded to less than  $-1$  m and  $-2$  m in the radial and along track directions, respectively. The corresponding maximum drag plate orientation,  $(\alpha_F)$  is 28.5 deg during the transient state while in the steady state, it oscillates within  $\pm 0.4$  deg, which is required to cancel the  $J_2$  disturbance and nonlinearities. It can be observed that the orientation of the drag plate changes in a smooth and continuous manner. The value of  $\tau$ , the boundary layer constant in Eq.(3.34), decides this delay in change in orientation of the drag plates.

The adaptive parameter converges to  $-5.72 \times 10^{-8}$ . Fig. 3.4 shows the convergence of the observed states  $(\hat{x}, \hat{y})$  to its true values  $(x, y)$ . The convergence is rapid and takes place within 0.1 orbit.

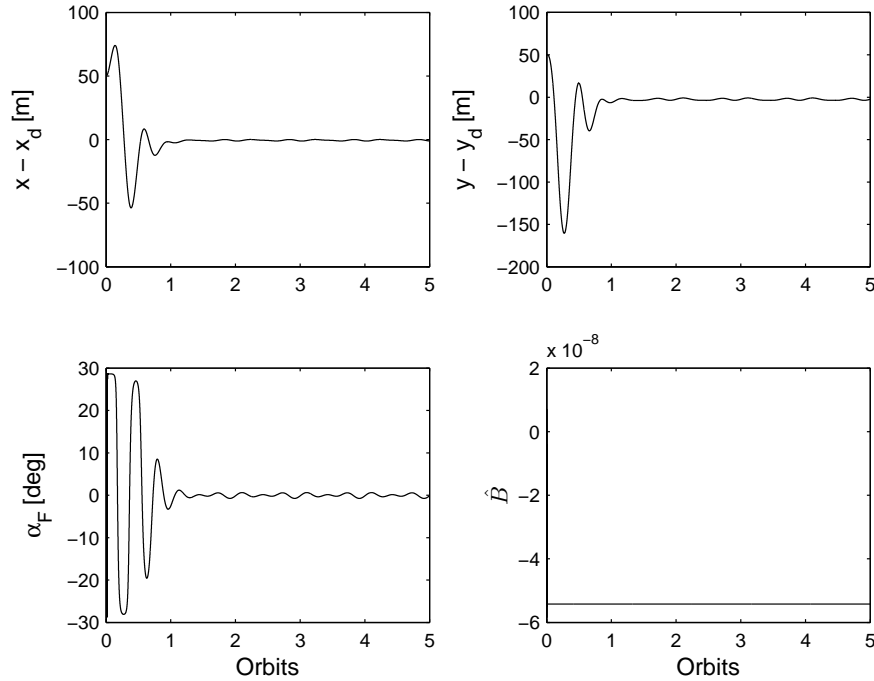


Figure 3.3: Relative position errors control input and adaptive parameter for projected circular formation ( $r_d = 0.5$  km, initial offset errors of 50 m).

Formation reconfiguration is another important requirement of the SFF missions, and is studied next. The projected circular formation of size 0.5 km is reconfigured into a circular formation of 1 km. From Fig. 3.5 it can be observed that reconfiguration is possible with the proposed control methodology, and the steady state errors remain bounded within and in the radial and along track directions, respectively. The estimated parameter  $\hat{B}$ , after reconfiguration, converges to  $-3.86 \times 10^{-9}$ . During the reconfiguration phase the control input oscillates between  $\pm 29.1$  deg, and during the steady state the orientation oscillates within  $\pm 1.0$  deg. The increase in the steady state errors and the corresponding control input can be attributed to the increase in the formation size. Thus, the proposed adaptive controller can successfully handle the parameter uncertainties and maintain the desired formation as well as perform formation reconfiguration by the continuous rotation of the drag plates. The  $y$ - $z$  view of the formation reconfiguration scenario is shown in Fig. 3.6.

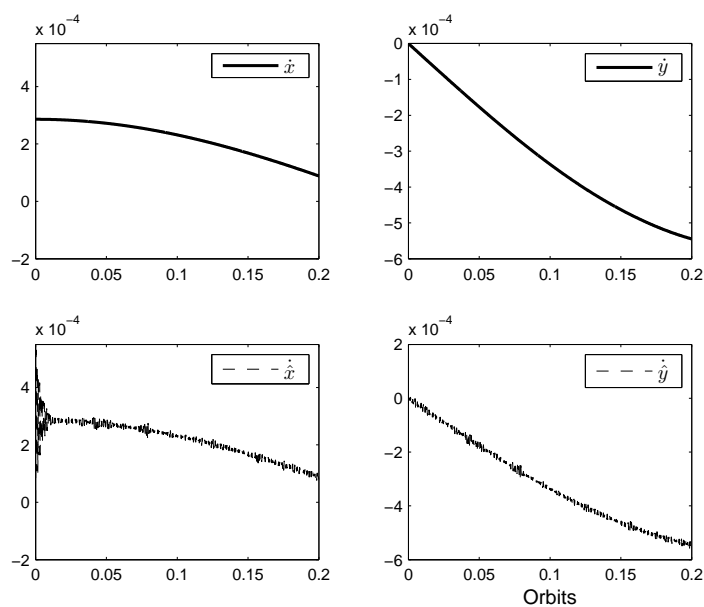


Figure 3.4: Observed states for projected circular formation ( $r_d = 0.5$  km, initial offset errors of 50 m).

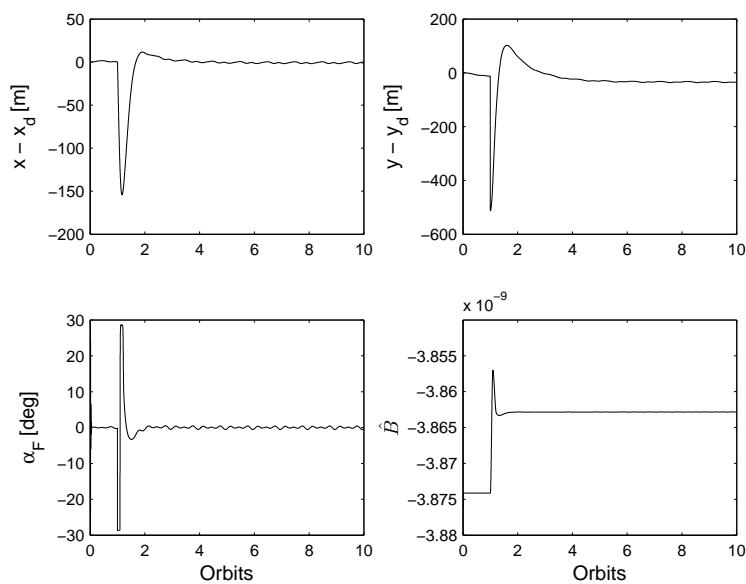


Figure 3.5: Relative position errors, control input and adaptive parameter for formation reconfiguration from PCF ( $r_d = 0.5$  km) to CF ( $r_d = 1.0$  km).

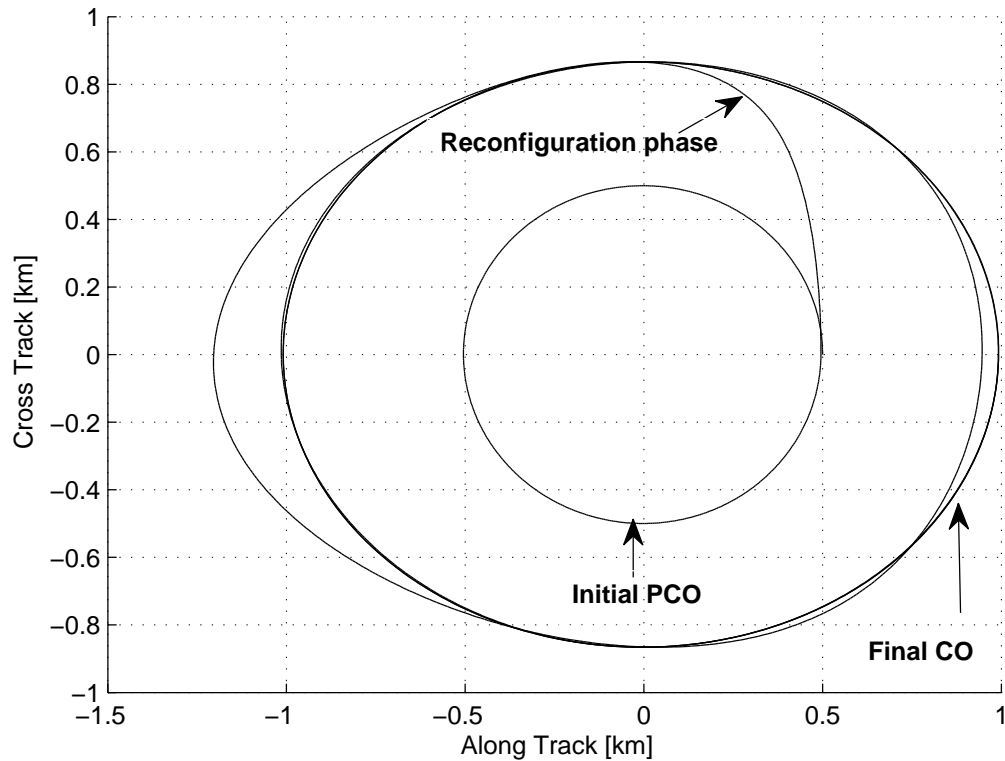


Figure 3.6: Formation reconfiguration from projected circular formation ( $r_d = 0.5$  km) to circular formation ( $r_d = 1.0$  km).

### 3.3.2 Along-track formation

The desired relative motion in this type of formation flying is to maintain a constant separation between the leader and follower in the along track direction. Examples of such formation includes the TanDEM-X [Krieger & Zink 2007] and JC2Sat [Mierlo 2009] missions. The desired separation distance is taken as 0.5 km and the leader satellite is considered to be in a Sun synchronous orbit with inclination of  $i = 97.44$  deg. Fig. 3.7 shows the response of relative position errors in the radial and along track directions, along with the drag plate orientation ( $\alpha_F$ ) when the SFF system is subjected to  $J_2$  disturbance and has an initial offset error of 50 m. It is observed that the relative states converge to the desired states in less than an orbit with the relative position errors being bounded within  $\pm 0.3$  m and  $\pm 0.8$  m in the radial and along track directions, respectively. The corresponding maximum

drag plate orientation is  $\pm 29.1$  deg during the transient state while in the steady state, it oscillates within  $\pm 0.4$  deg.

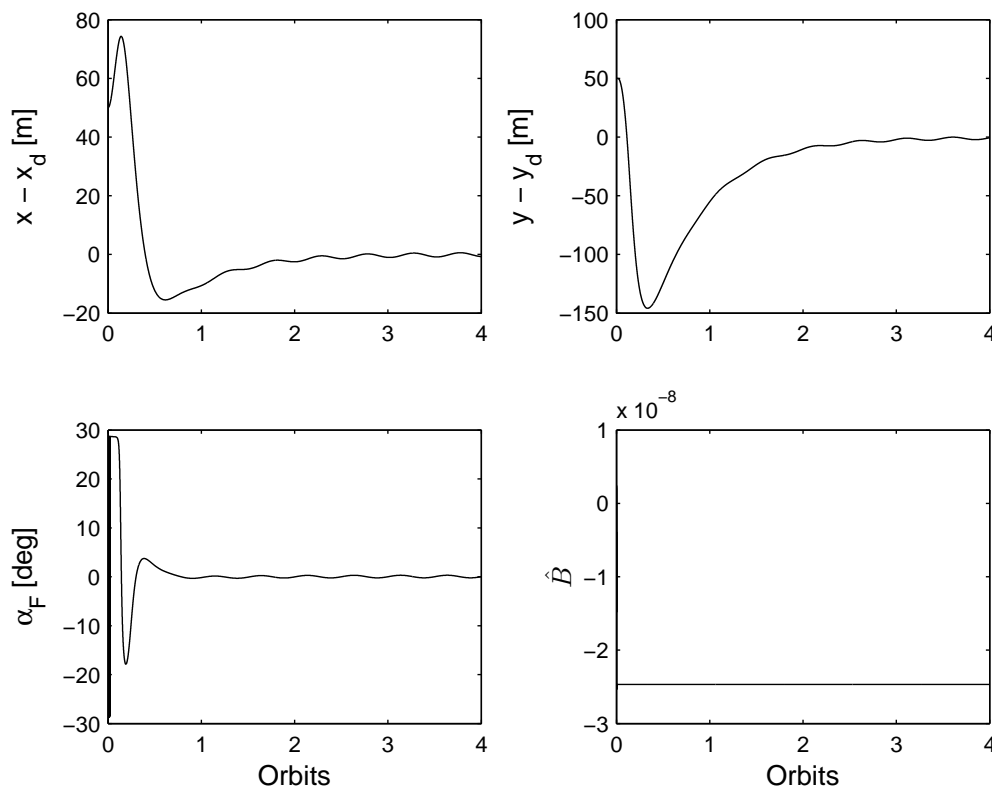


Figure 3.7: Relative position errors control angle and adaptive parameter for along track formation ( $r_d = 0.5$  km, initial offset errors of 50 m).

Reconfiguration in the case of along track formation is also studied. Reconfiguration from the initial formation size of  $r_d = 0.5$  km to the final formation of  $r_d = 5$  km (Fig. 3.8) is performed from the first orbit. It can be observed that the formation is successfully reconfigured in 3 orbits using the proposed control strategy and the steady state errors remain bounded within  $\pm 15$  m and  $\pm 25$  m in the radial and along track directions, respectively. The estimated parameter,  $\hat{B}$ , after reconfiguration, converges to  $-3.55 \times 10^{-9}$ . During the reconfiguration phase the drag plate orientation oscillates between  $\pm 29.1$  deg, and during the steady state the control wing orientation oscillates within  $\pm 3.8$  deg. The increase in the steady state errors and the corresponding control input can be attributed

to a large increase in the formation size (i.e., by 10 folds compared to the case of Fig. 3.7).

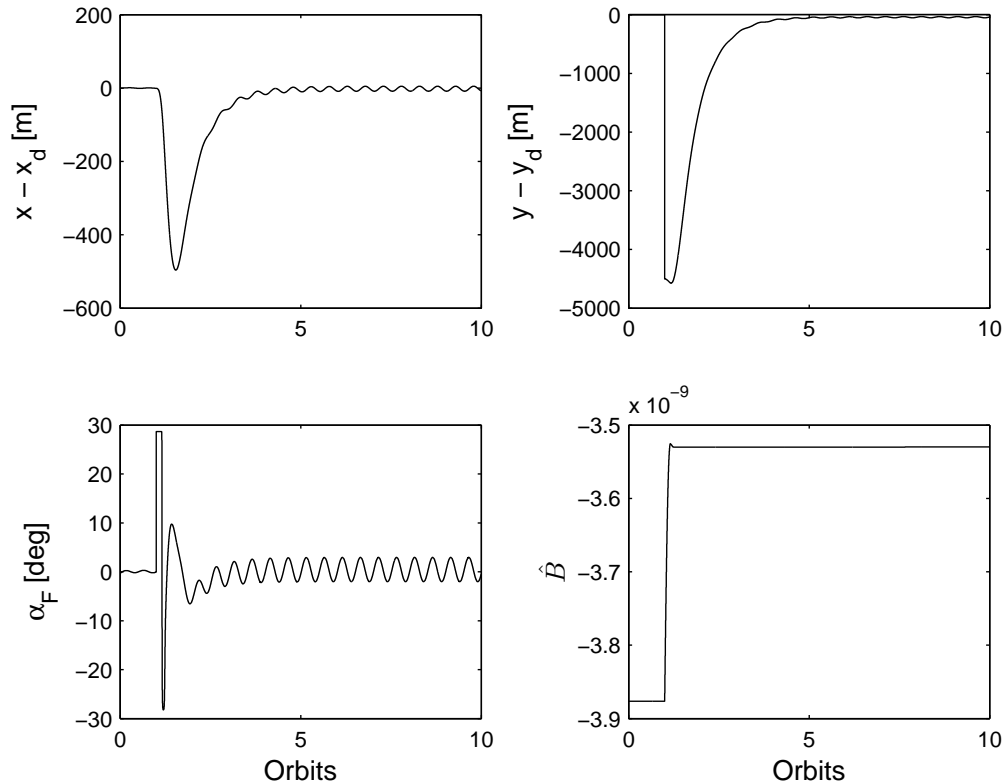


Figure 3.8: Relative position errors control angle and adaptive parameter for along track reconfiguration from  $r_d = 0.5$  km to  $r_d = 5.0$  km.

These results demonstrate the efficacy of the control algorithm for formation maintenance and formation reconfiguration in the presence of initial errors and external perturbations.

### 3.3.3 Multiple Satellite Formation

Feasibility of multiple satellite formation flying and reconfiguration is investigated in this section. The projected circular formation is examined in the multiple reconfiguration problem. The problem of multiple satellite formation maneuvering for the proposed SFF system is more challenging as the achievable levels of differential drag between each follower and the leader are mutually constrained. A heuristic algorithm is developed to analyze this sce-

nario and is tested in a configuration of four followers with the phase angles of the followers at 0 deg, 90 deg, 180 deg and 270 deg, respectively. The algorithm is stated as follows:

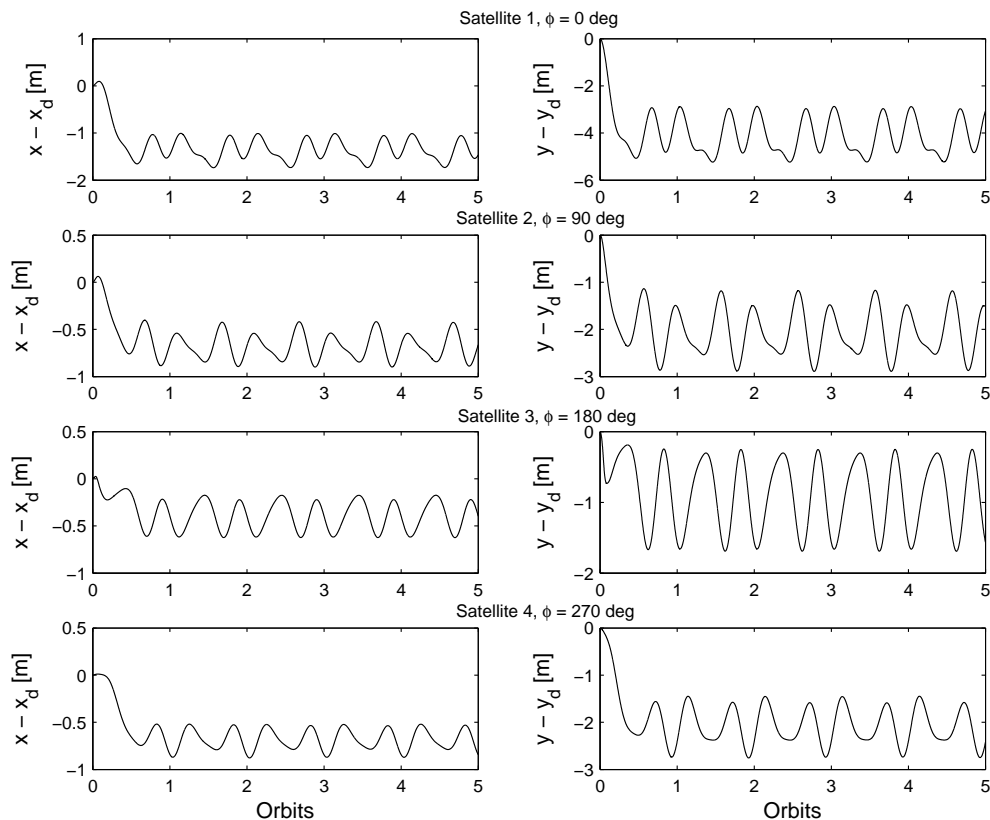


Figure 3.9: Relative position errors during multiple satellite formation flying in projected circular formation ( $r_d = 0.5$  km)

During each orbit the drag plate orientation required for each individual leader-follower satellite configuration for maintaining the projected circular formation of size,  $r_d = 0.5$  km, is calculated based on the proposed control methodology. The followers align their corresponding drag plates with this calculated orientation. In the first orbit, the drag plates on the leader satellite are oriented with the calculated value with respect to the follower with phase angle 0 deg. This yields the required differential drag for the follower (Satellite 1 with phase = 0 deg). In the next orbit the same procedure of calculation of the required wing orientation is performed, but the drag plates on the leader is oriented according to the follower satellite with phase 90 deg (Satellite 2). This method is continued for the

successive orbits with the orientation of the drag plates on the leader satellite switching between the four follower satellites. The differential drag achieved by the other three follower satellites in each orbit may not be the same as required by each individual follower satellite in relation to the leader satellite. But it is found during simulation that with the proposed  $\alpha$  algorithm the projected circular formation is maintained with reasonable relative errors (Fig. 3.9). The control input response is shown in Fig. 3.10. The switching after each successive orbit can be seen in Fig. 3.10 as well.

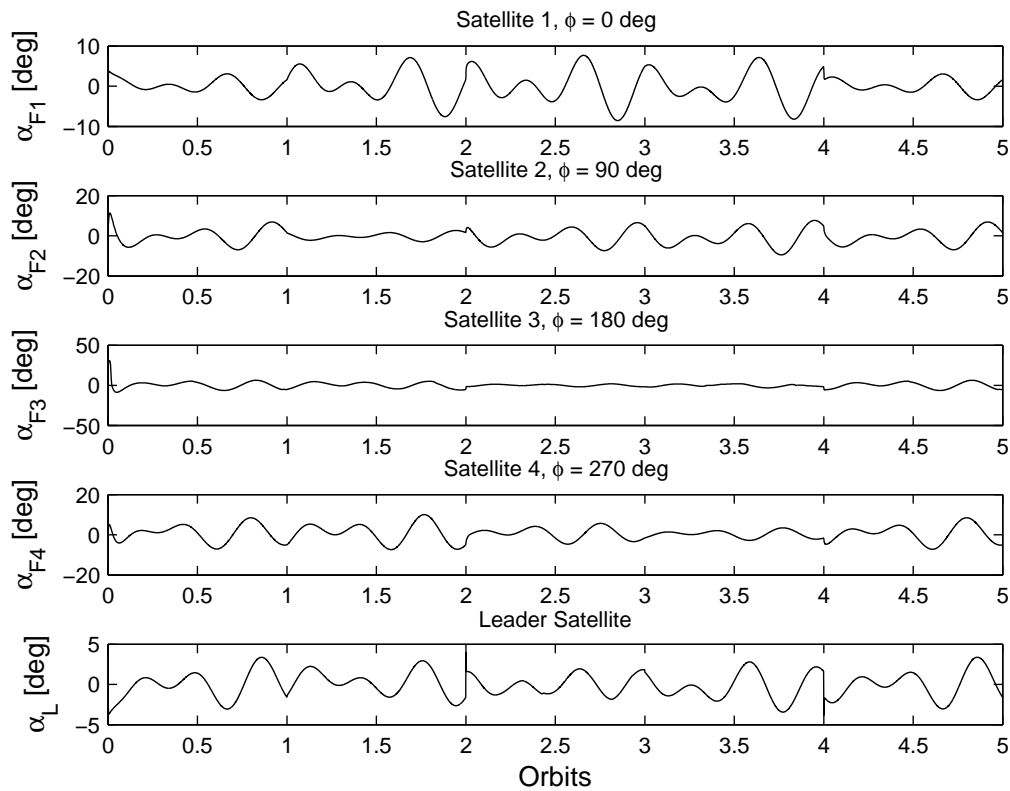


Figure 3.10: Aerodynamic drag plate orientation during multiple satellite formation flying.

Another important feature to be checked is the performance of the proposed algorithm in the case where the mass and surface areas of the four followers are different. The mass and area are selected as in Table 3.3. The mass and surface area of the leader satellite is not changed. Fig. 3.11 shows the relative position errors in the radial and along track directions over a day for the four follower satellites in a projected circular formation. As

expected the relative errors decreases with increase in the resultant acceleration due to aerodynamic drag.

Table 3.3: Additional parameters for multiple satellite formation flying

Parameters	Value(s)
Area, ( $A_1 - A_4$ ) ( $m^2$ )	0.4, 0.45, 0.5, 0.55
Mass, ( $m_{f1} - m_{f4}$ ) (kg)	5, 10, 12, 15

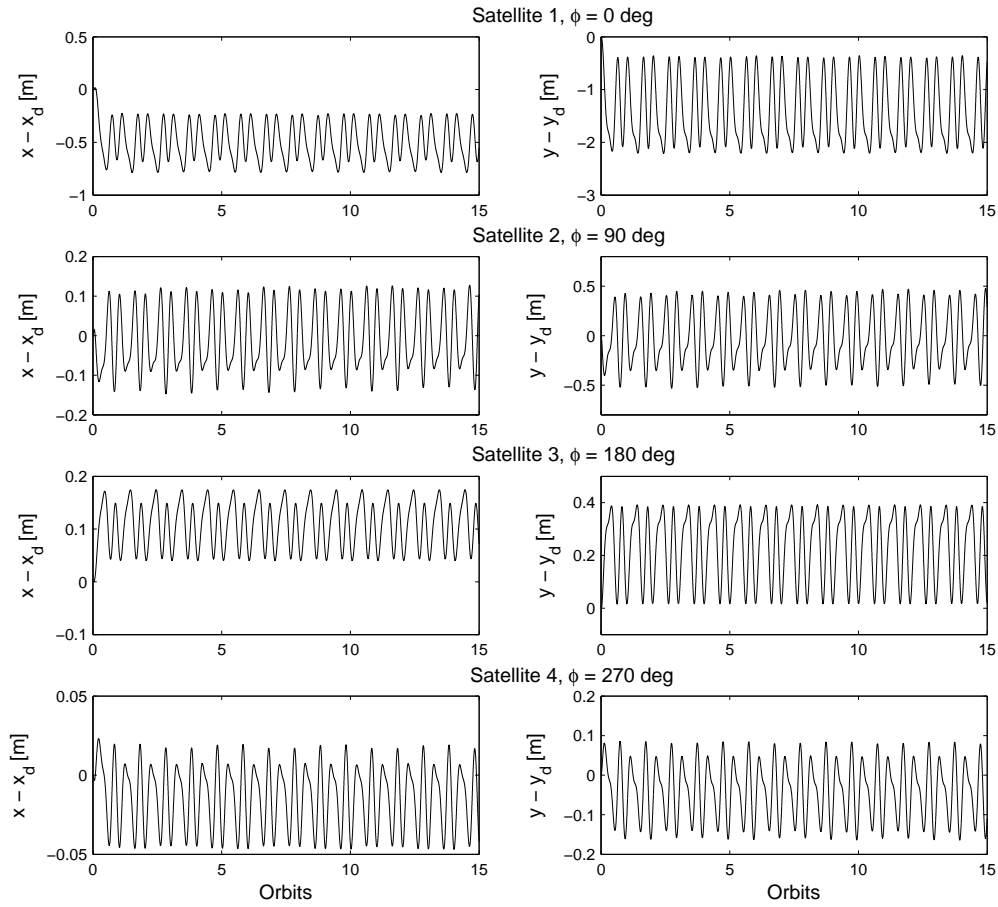


Figure 3.11: Relative position errors during multiple satellite formation flying in projected circular formation for one day.

Next we consider the case of multiple satellite reconfiguration using the proposed heuristic algorithm. This could be for a variety of reasons; especially in a multiple formation flying

system where in a new follower satellite may need to be inserted into the cluster or a faulty follower may need to be replaced with a new satellite. Here two satellites in a projected circular formation of initial formation size,  $r_d = 0.25$  km and  $r_d = 0.5$  km with the phase angle of each equal to 0 deg, are reconfigured to final formation sizes of  $r_d = 0.5$  km and  $r_d = 0.75$  km, respectively (Fig. 3.12). A smooth reconfiguration is achieved with the application of the heuristic algorithm.

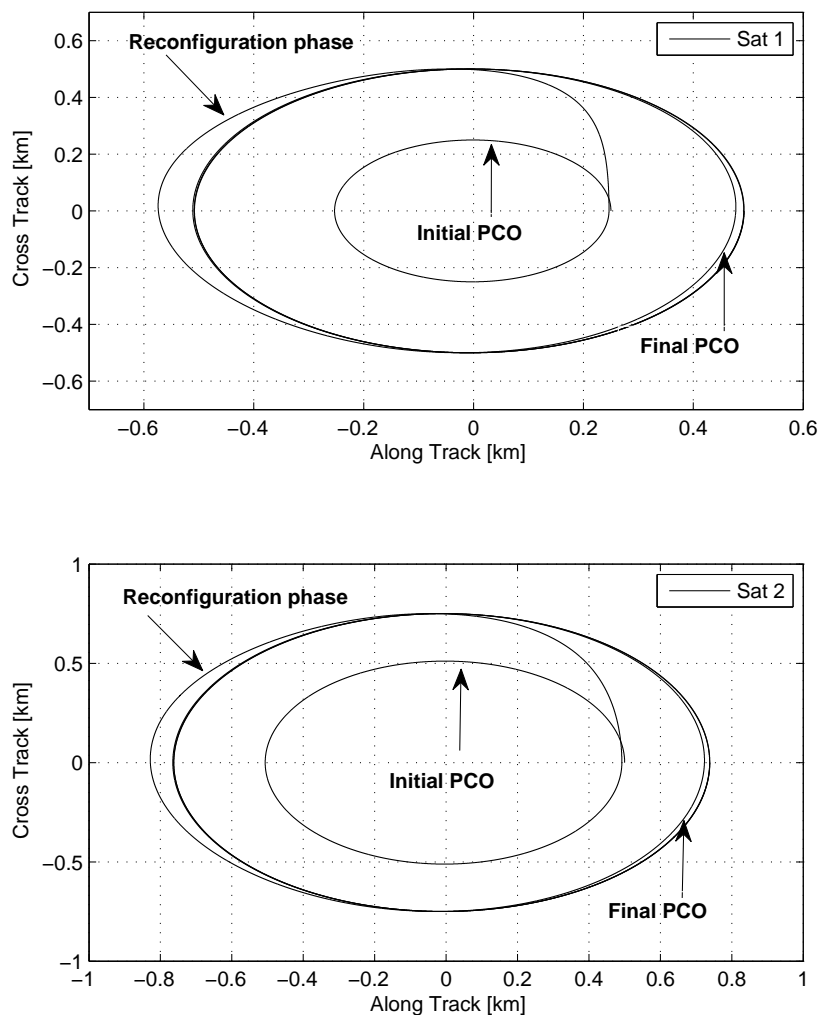


Figure 3.12: System response during multiple satellite reconfiguration in PCF (Sat-1:  $r_d = 0.25$  km to  $r_d = 0.5$  km; Sat-2:  $r_d = 0.5$  km to  $r_d = 0.75$  km).

Finally to analyze the robustness of the proposed heuristic algorithm, Monte Carlo simulation is carried out. The effect of different initial conditions on the proposed methodology is evaluated by 1000 simulation runs. Four follower satellites in a projected circular formation are considered. Different initial conditions are generated by varying the desired formation size,  $r_d$ , from 0.5 km to 5 km. Each simulation is run for 5 orbits and the mean value of relative error in the  $x$ -axis and  $y$ -axis is calculated and plotted against the corresponding value of  $r_d$  (Fig. 3.13). Here '+' indicates the mean value of  $e_x$  and '.' indicates that of  $e_y$ . It can be observed that the relative errors in both the axes remain bounded within  $\pm 8$ m.

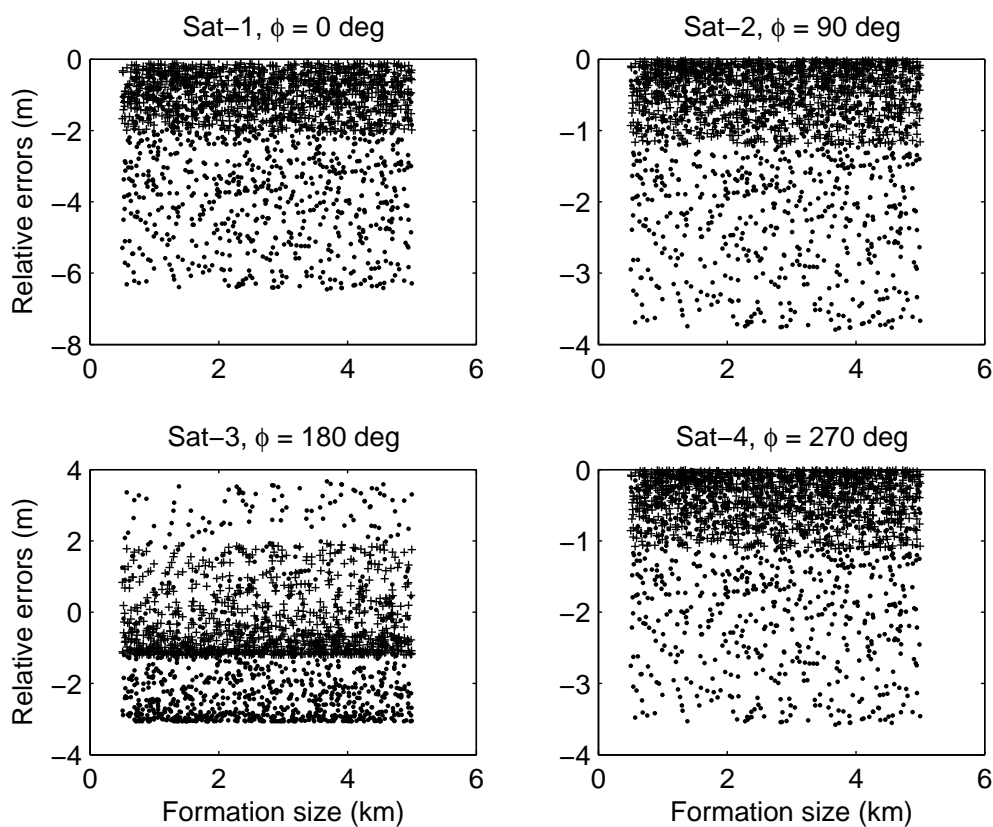


Figure 3.13: Variation of mean relative error in  $x$  and  $y$ - axis for the four follower satellites over a 1000 numerical simulation runs.

Next, the performance of the proposed SFF system in the case of the leader in a low eccentric orbit is evaluated. Fig. 3.14 and Fig. 3.15 shows the relative errors in the case of

the leader in a low eccentric orbits of  $e = 0.001$  and  $e = 0.01$  respectively. The relative errors are larger than the circular case, but remain bounded. The orbital elements corresponding

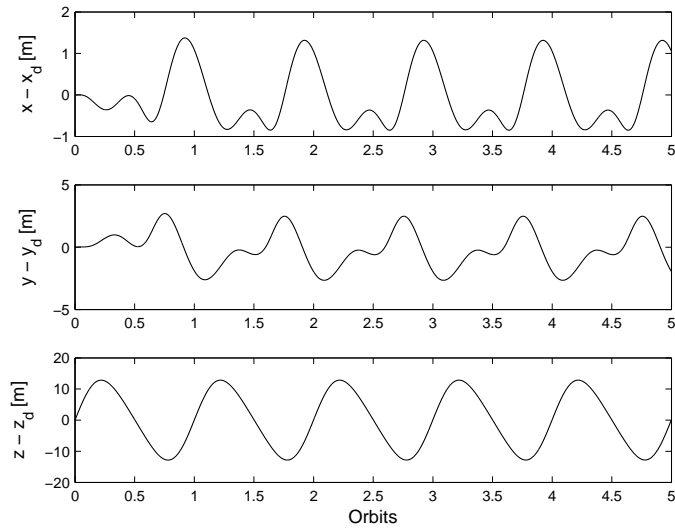


Figure 3.14: Relative position errors along track formation with  $e = 0.001$ .

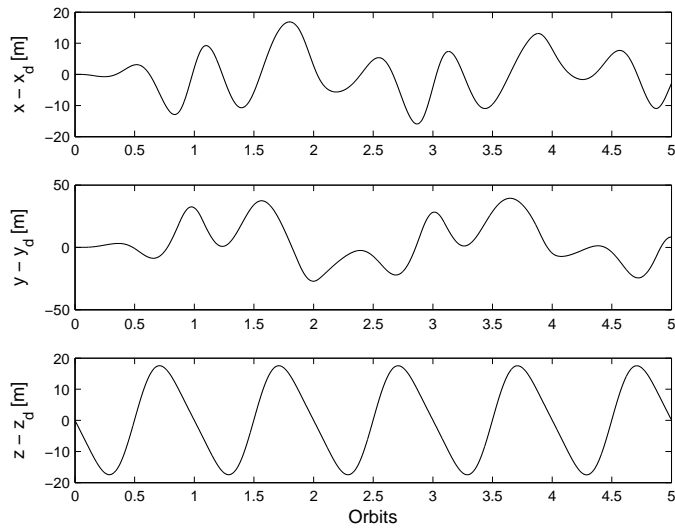


Figure 3.15: Relative position errors along track formation with  $e = 0.01$ .

to the leader satellite is examined.

To understand the effect of aerodynamic drag and external disturbances on the leader satellite and its subsequent effect on the formation system, the proposed system is evaluated on a high fidelity model. The equations of motion describing the leader satellite is given by

$$\ddot{X}_L = -\frac{\mu}{r^3}X_L - \frac{3\mu J_2 R_e^2}{2r^5} \left[ 1 - \frac{5Z^2}{r^2} \right] X_L + Ft_x \quad (3.48)$$

$$\ddot{Y}_L = -\frac{\mu}{r^3}Y_L - \frac{3\mu J_2 R_e^2}{2r^5} \left[ 1 - \frac{5Z^2}{r^2} \right] Y_L + Ft_y \quad (3.49)$$

$$\ddot{Z}_L = -\frac{\mu}{r^3}Z_L - \frac{3\mu J_2 R_e^2}{2r^5} \left[ 3 - \frac{5Z^2}{r^2} \right] Z_L + Ft_z \quad (3.50)$$

where  $r = \sqrt{X_L^2 + Y_L^2 + Z_L^2}$  and  $Ft_j$  for  $j = x, y, z$  represent the aerodynamic drag and external disturbances affecting the system. The relative equations can be written as

$$\ddot{\vec{Q}}_r = \ddot{\vec{r}}_F - \ddot{\vec{r}}_L = f(X_j, Y_j, Z_j) + U, \quad j = F, L \quad (3.51)$$

where  $F$  and  $L$  represent the leader and follower satellite respectively and  $U$  is the control input required to maintain the desired formation. A projected circular formation scenario is examined with  $i = 45^\circ$  and  $e = 0.001$ . Fig. 3.16 shows the orbital elements ( $a$ ,  $e$ ,  $i$  and  $\dot{\theta}$ ) of the leader satellite over a period of one day. As expected the semimajor axis of the leader satellite is affected by the aerodynamic drag and it decreases over the course of each orbit. Fig. 3.17 shows the 3 –  $D$  plot of the leader satellite under the influence of aerodynamic drag. The corresponding performance of the follower satellite, Fig. 3.18, shows a bounded system response.

### 3.3.4 Qualitative Analysis

Next a quantitative analysis in terms of the differential aerodynamic drag generated with respect to drag plate area and altitude of the satellite is carried out. This analysis will provide required surface area of the drag plate for achieving desired satellite formation. Here, the projected circular formation examined earlier is considered for different altitudes ranging from 350 km to 650 km from the Earth's surface. The maximum drag plate area is assumed to be  $2m^2$  as a realistic assumption. As expected, it can be observed from Fig.

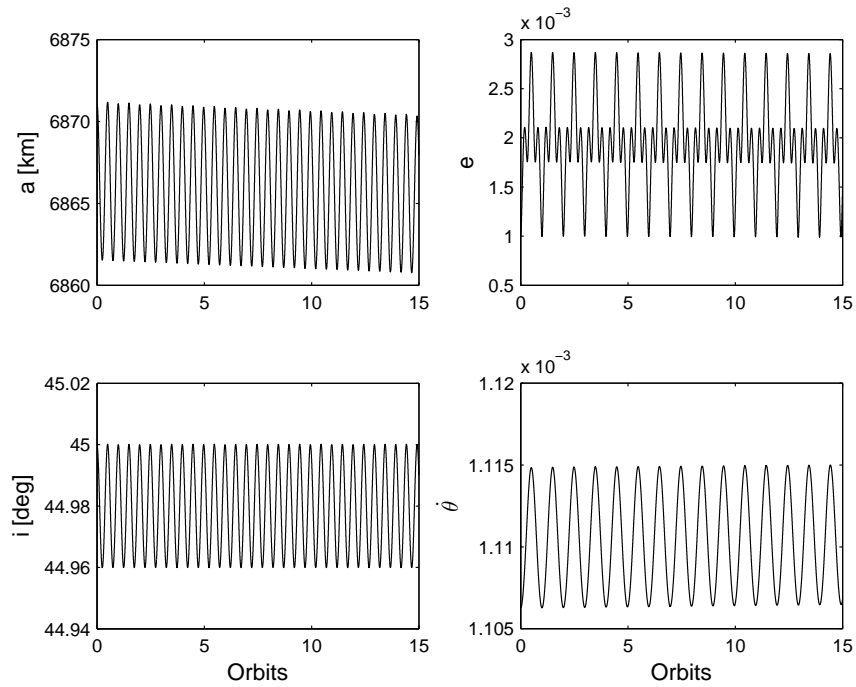


Figure 3.16: Leader satellite under the influence of aerodynamic drag

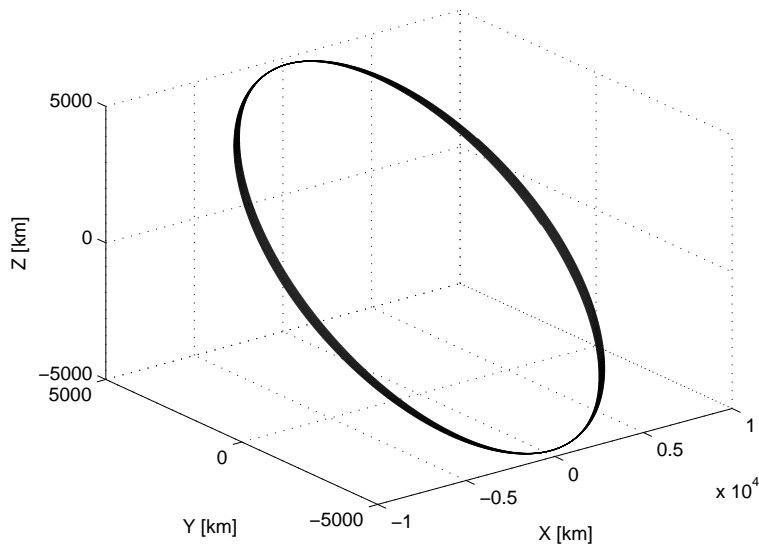


Figure 3.17: Leader satellite under the influence of aerodynamic drag (3-D plot)

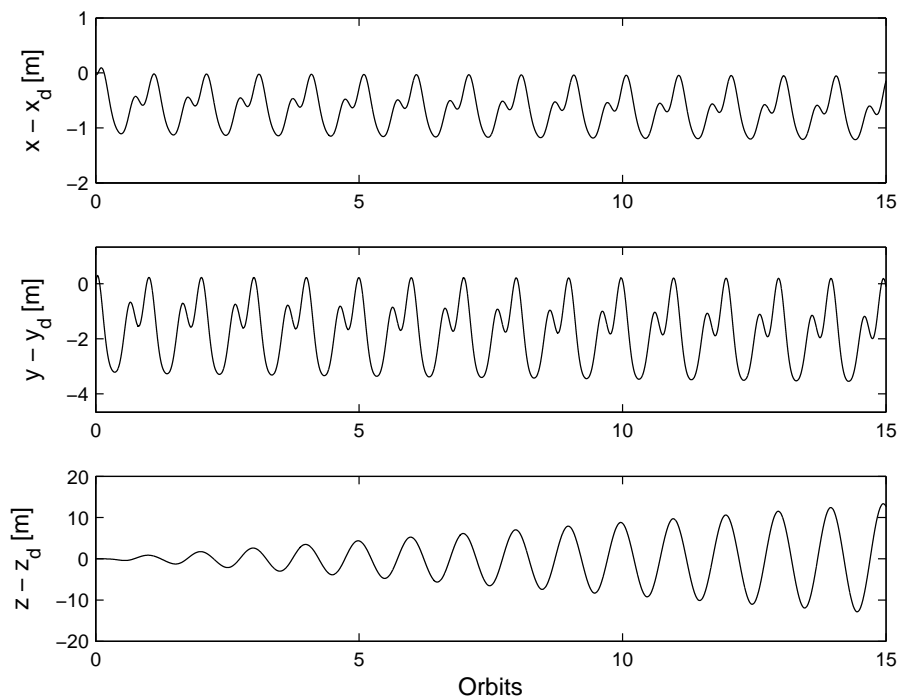


Figure 3.18: Relative position errors in projected circular formation with  $i = 45^\circ$ ,  $e = 0.001$ .

(3.19) that the drag force increases with increase in projected area as well as decrease in altitude. Formation reconfiguration at lower altitude is achieved with a smaller projected area compared to the required projected area at higher altitudes. It is observed that to maintain a projected circular at an altitude of 650 km, a projected area of  $1.78m^2$  is required. All the cases examined above suggest that use of differential aerodynamic drag is a viable alternative for multiple satellite formation.

### 3.3.5 Hardware-In-Loop (HIL) testing

The validity of the control scheme is evaluated through Hardware-In-Loop (HIL) simulation using a prototype model. The HIL arrangement is shown in Fig. (3.20). The satellite prototype is attached with plates as shown in Fig. (3.20). These plates with servo motors are attached to the satellite body. The computer running Matlab/Simulink simulates the leader follower satellite formation flying system. The control algorithm calculates the

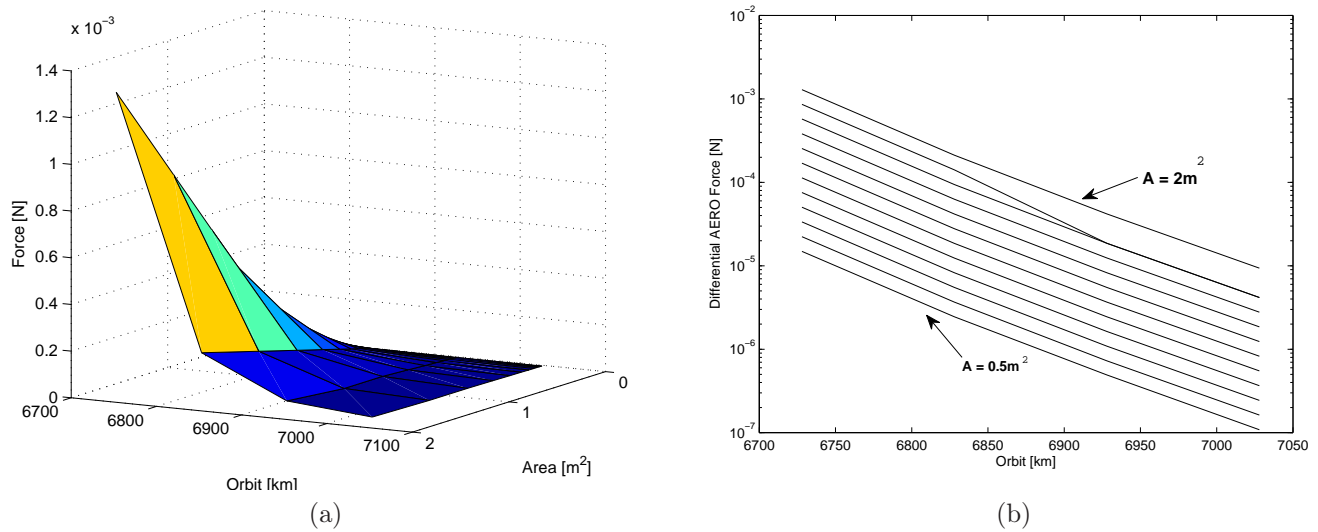


Figure 3.19: Variation of aerodynamic force with respect to projected area and altitude.

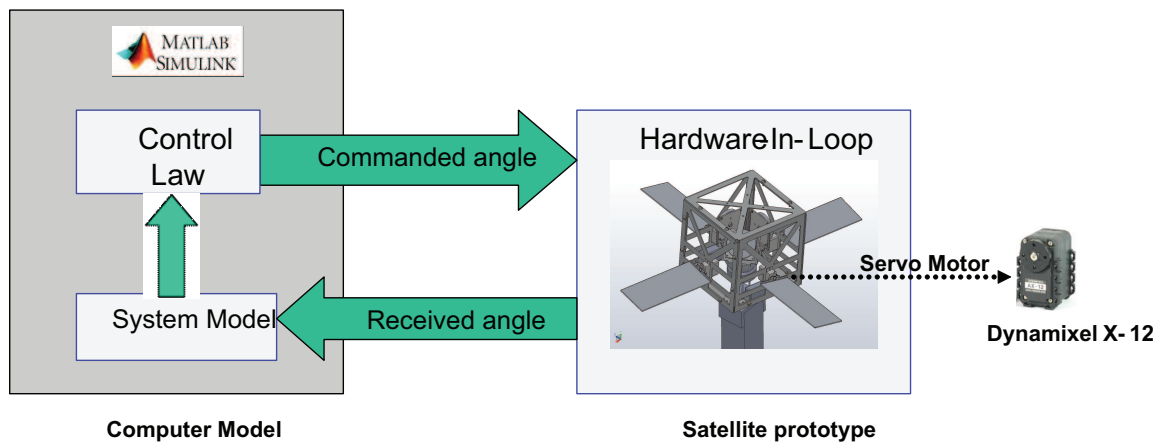


Figure 3.20: Block diagram of HIL testing.

required orientation of the wings to maintain the formation in different scenarios. The desired orientation is transmitted from the computer to the servos motor attached on the prototype. The orientation achieved by the servo is then fed back to the computer and this information is used in propagating the equations of motion in Simulink. By this experiment the real world scenario with respect to panel rotation is created. Comparison of the HIL test results with the numerical simulation results showed similar system response with respect to the relative error convergence. Fig. (3.21) shows the system response in

the HIL test for performing formation reconfiguration in the along track direction. The relative errors in the  $x$  and  $y$  axes and the commanded angle to the servo motor are shown in the Fig. (3.21). Next projected circular formation maintenance and reconfiguration

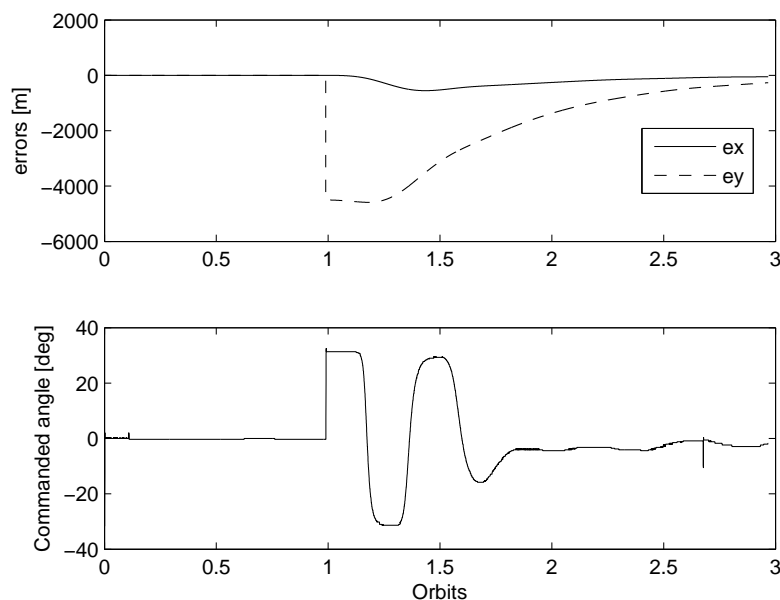


Figure 3.21: Relative position errors and commanded angle during along track formation flying.

is examined. Projected circular formation of size 0.5 km with initial offset error of 50 m (Fig. 3.22) as well as formation reconfiguration (Fig. 3.23) is tested. In both the cases the formation is successfully maintained with relative errors converging rapidly. The results show the feasibility of using the proposed control methodology of varying the orientation of the wings mounted on the satellite for formation maintenance.

### 3.4 Summary

In this chapter we examined the use of differential aerodynamic drag for multiple satellite formation flying. Differential aerodynamic drag is created by the desired rotation of drag plates attached to the leader and follower satellites. The orientation of the drag plates are governed by the control law developed based on adaptive sliding mode which accounts for

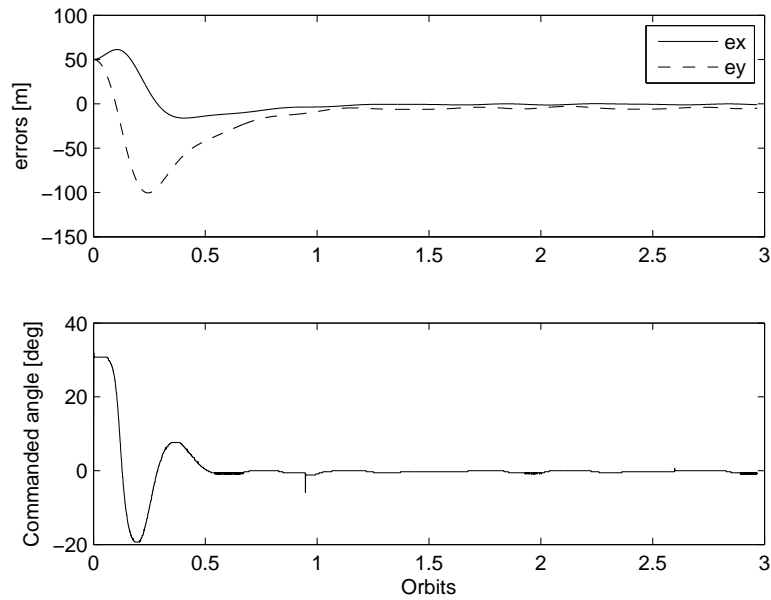


Figure 3.22: Relative position errors and commanded angle during projected circular formation flying.

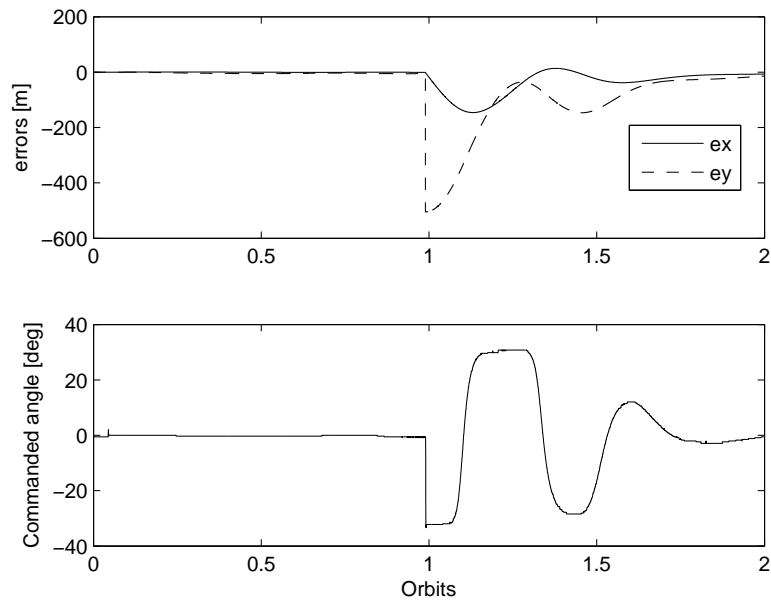


Figure 3.23: Relative position errors and commanded angle during projected circular formation reconfiguration.

the various uncertainties associated with aerodynamic drag. Numerical simulation results confirm the viability of performing different formation scenarios in the presence of differential  $J_2$  effect, navigation errors and initial offset errors using the proposed technique. The relative errors in the along track and radial direction converged within half an orbit and remained bounded to within a maximum of  $\pm 5$  m. These relative errors are reasonable for certain applications like monitoring of cloud formation, terrestrial imaging. In the case of formation reconfiguration, smooth reconfiguration is achieved within an orbit. For a multiple satellite formation such as a four follower satellite formation with different mass and projected area, the simulation results show that the desired formation is maintained with the relative errors bounded to within a maximum of  $\pm 8$  m. The robustness of the control methodology for the multiple satellite formation system is validated by performing Monte Carlo analysis. Compared to existing literature on this topic, major contributions include *a)* nonlinear control algorithm development based on adaptive sliding mode control. *b)* development of an heuristic control methodology for multiple satellite formation flying using aerodynamic drag. *c)* validation of the proposed system in the presence of parameter uncertainties like variation in the density and altitude and navigation and initial offset errors. Overall, the theoretical and numerical results suggest that the use of differential aerodynamic drag is a viable alternative for multiple satellite formation.



## CHAPTER 4

# Satellite Formation Control Using Solar Radiation Pressure

---

SATELLITE formation flying (SFF) in low Earth orbit (LEO) using differential aerodynamic drag was studied in the previous chapter. Application of LEO formation flying mainly addresses Earth observation missions. Here we examine the feasibility of using solar radiation pressure (SRP) for maintaining and maneuvering satellite formation system in geostationary orbits. Such a formation system has the advantage of continuous regional navigation and also act as a positioning system [Hui *et al.* 2006]. Here we proposes a method based on differential solar radiation pressure to achieve coordinated control of multiple satellites flying in formation. The relative orbit is controlled by varying the level of solar radiation pressure experienced by the solar flaps mounted on each satellite and thereby generating relative differential accelerations among the satellites in the formation. Solar radiation pressure provides control authority in both in-plane as well as out-of-plane direction thereby allowing for complete control of the formation system as compared to control using aerodynamic drag. Sliding mode control (SMC) theory is used to develop an adaptive control algorithm for maneuvering the solar flaps to maintain the satellite formation.

This chapter is organized as follows: Section 4.1 revisits the nonlinear mathematical model of the SFF system. Development of the adaptive control algorithm is described in Section 4.2. For a detailed assessment of the system performance under the proposed control strategies, the results of numerical simulations incorporating different formation scenarios are presented in Section 4.3. The conclusions of the study are summarized in Section 4.4.

## 4.1 SFF System Model and Equations of Motion

The leader follower system shown in Fig.2.1 is used to describe the SFF system. The assumptions stated in Chapter 3, Section 3.1.1 holds here as well and is not repeated for brevity. The mathematical model of the SFF presented in Chapter 2: Section 2.1 is reproduced here. Eqs.(4.1) and (4.2) describe the orbital equations of motion for the leader satellite while Eqs.(4.3) through (4.5) are the relative equations of motion of the follower satellite:

$$\ddot{r}_l - r_l \dot{\theta}^2 + \frac{\mu_e}{r_l^2} = 0 \quad (4.1)$$

$$r_l \ddot{\theta} + 2\dot{\theta} \dot{r}_l = 0 \quad (4.2)$$

$$m_f \ddot{x} - 2m_f \dot{\theta} \dot{y} - m_f (\dot{\theta}^2 x + \ddot{\theta} y) + m_f \mu_e \left( \frac{r_l + x}{r_f^3} - \frac{1}{r_l^2} \right) = f_x + f_{dtx} \quad (4.3)$$

$$m_f \ddot{y} + 2m_f \dot{\theta} \dot{x} + m_f (\ddot{\theta} x - \dot{\theta}^2 y) + m_f \frac{\mu_e}{r_f^3} y = f_y + f_{dty} \quad (4.4)$$

$$m_f \ddot{z} + m_f \frac{\mu_e}{r_f^3} z = f_z + f_{dtz} \quad (4.5)$$

where  $r_f = [(r_l + x)^2 + y^2 + z^2]^{1/2}$  is the position of the follower spacecraft,  $f_{dtj}$  is the net relative perturbations acting on the SFF system, and  $f_j$  are the components of the control input vector, for  $j = x, y, z$ . Here the control forces,  $f_j$  for  $j = x, y, z$ , is created by the rotation of the solar flaps on the satellites.

### 4.1.1 Solar Radiation Pressure Model

In geostationary orbits, SRP is the most dominant external force acting on a satellite. The Earth's oblateness effect has a very reduced effect at these orbits. The mathematical model of SRP is given as

$$\vec{F}_{SRP} = C_{srp} (\vec{s} \cdot \vec{n}) \{b_1 \vec{s} + [b_2 (\vec{s} \cdot \vec{n}) + b_3] \vec{n}\} \quad (4.6)$$

where  $\vec{s}$  represents the Sun vector,  $\vec{n}$ , is the solar flap normal vector,  $\zeta_s$ , is the specular reflection factor, and other coefficients are given by,

$$b_1 = \frac{1}{2}(1 - \zeta_s \rho_s) \quad (4.7)$$

$$b_2 = \zeta_s \rho_s \quad (4.8)$$

$$b_3 = \frac{1}{2} \left[ B_f(1 - \zeta_s) \rho_s + (1 - \rho_s) \frac{e_f B_f - e_b B_b}{e_f + e_b} \right] \quad (4.9)$$

$C_{srp}$  is the solar flap characteristic acceleration and is given by

$$C_{srp} = \frac{2p_0 A_0}{m} \quad (4.10)$$

where the nominal SRP force is  $p_0 = 1.04 \times 10^{17} \text{ N/m}^2$ ,  $A_0$  is the sail reference area and  $m$  is the satellite mass. Referring to Fig.4.1, the flap normal  $\vec{n}$ , specified by the two orientation

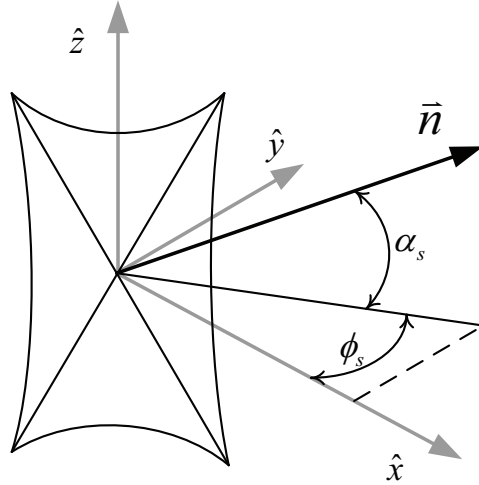


Figure 4.1: Orientation of the solar flap

angles  $\phi_s$  and  $\alpha_s$  are defined as,

$$\hat{n} = \begin{bmatrix} \cos \alpha_s \cos \phi_s \\ \cos \alpha_s \sin \phi_s \\ \sin \alpha_s \end{bmatrix} \quad (4.11)$$

## 4.2 Design of Control Law

The control objective is to determine the orientation of the solar flaps  $(\alpha_{sj}, \phi_{sj})$ , for  $j = F, L$  where  $F$  stands for the follower satellite and  $L$  stands for the leader satellite. A control algorithm based on SMC technique is developed to drive the follower satellite to the desired formation trajectory with respect to the leader satellite in the presence of external disturbances and initial deployment errors. Considering the mathematical formulation of the leader follower SFF model and SRP model presented in the previous section, the relative state vector and the desired relative trajectory can be defined as,  $X(t)$ , and  $X_d(t) \in \mathbb{R}^6$  respectively. The performance measure is defined as the tracking error,  $e(t) \in \mathbb{R}^6$ ,

$$e(t) \triangleq X(t) - X_d(t) \quad (4.12)$$

The resultant control forces  $f_j$  for  $j = x, y, z$  in Eqs. (4.3) - (4.5) will drive the relative states of the SFF system to the desired trajectories as  $t \rightarrow \infty$  and thereby the tracking errors, Eq. (4.12), converge to zero. Control algorithm development is simplified by the following assumptions on the SRP model. The solar flap is assumed to be an ideal highly reflective surface with only specular reflection and no absorption, and the Sun vector is defined as  $\vec{s} = [1, 0, 0]^T$ . This yields the SRP force relation to be written as,

$$F = C_{srp}(\vec{s} \cdot \vec{n})^2 \vec{n} \quad (4.13)$$

The transformation of this force equation to the orbital frame from the Sun centered inertial frame is given as  $F_s = C^{B/I} \cdot C^{I/S} \cdot F$ . Here,  $C^{B/I}$  represents the transformation matrix from the geocentric inertial to the orbital frame given by,

$$\begin{bmatrix} c(ot)c(\Omega) - s(ot)s(\Omega)c(i-\varepsilon) & -s(ot)c(\Omega) - c(ot)s(\Omega)\cos(i-\varepsilon) & s(\Omega)s(i-\varepsilon) \\ c(ot)s(\Omega) + s(ot)c(\Omega)c(i-\varepsilon) & -s(ot)s(\Omega) + c(ot)c(\Omega)\cos(i-\varepsilon) & -c(\Omega)s(i-\varepsilon) \\ s(ot)s(i-\varepsilon) & c(ot)s(i-\varepsilon) & c(i-\varepsilon) \end{bmatrix}$$

where  $ot$  represents  $(\omega + \theta)$ ,  $\varepsilon$  is the angle between the ecliptic and equatorial plane,  $c()$  and  $s()$  represents  $\cos()$  and  $\sin()$  respectively.  $C^{I/S}$  represents the transformation from

the Sun centered inertial to the geocentric inertial frame as follows,

$$\begin{bmatrix} \cos \psi & -\sin \psi & 0 \\ \sin \psi & \cos \psi & 0 \\ 0 & 0 & 1 \end{bmatrix}$$

where  $\psi$  is the solar aspect angle. Following these modifications, the differential SRP force can be expressed as,

$$f_j = F_{sjF} - F_{sjL} \quad for j = x, y, z \quad (4.14)$$

With respect to the solar flaps on the leader and follower satellites in Eq.(4.14), we assume that the leader and follower spacecraft are both equipped with solar sails having the same area to mass ratio, also we assume  $\zeta_s = 1$  and  $\varepsilon_f B_f = \varepsilon_b B_b$ . With these simplifications, the equations used for control law design are written in the following form,

$$\dot{X} = AX + E(X) + g(U) + F_{dt} \quad (4.15)$$

where

$$X = \begin{bmatrix} x \\ y \\ z \\ \dot{x} \\ \dot{y} \\ \dot{z} \end{bmatrix}; \quad A = \begin{bmatrix} 0 & 0 & 0 & 1 & 0 & 0 \\ 0 & 0 & 0 & 0 & 1 & 0 \\ 0 & 0 & 0 & 0 & 0 & 1 \\ 3\dot{\theta}^2 & 0 & 0 & 0 & 2\dot{\theta} & 0 \\ 0 & 0 & 0 & -2\dot{\theta} & 0 & 0 \\ 0 & 0 & -\dot{\theta}^2 & 0 & 0 & 0 \end{bmatrix}; \quad E(X) = \begin{bmatrix} 0 \\ 0 \\ 0 \\ \mu\left(\frac{1}{r_l^2} - \frac{(r_l+x)}{r_f^3}\right) - 2\dot{\theta}^2 x \\ \dot{\theta}^2 y - \frac{\mu y}{r_f^3} \\ \dot{\theta}^2 z - \frac{\mu z}{r_f^3} \end{bmatrix}$$

$$g(U) = \begin{bmatrix} f_x \\ f_y \\ f_z \end{bmatrix}; \quad F_{dt} = \begin{bmatrix} f_{dtx} \\ f_{dty} \\ f_{dtz} \end{bmatrix}$$

The nonlinear terms in the equations of motion have been lumped into  $E(X)$ ,  $A$  represents the linear part of the SFF system,  $g(U)$  is the control matrix, and  $F_{dt}$  the differential

perturbation forces. The control forces  $f_j$  for  $j = x, y, z$  is given by

$$\begin{aligned}
 f_x &= (C_{SRP} + \delta a) (\cos \alpha_{sF} \cos \phi_{sF})^2 (\cos(\theta - \psi) \cos \alpha_{sF} \cos \phi_{sF} + \sin(\theta - \psi) \sin \alpha_{sF} \cos \phi_{sF}) \\
 &\quad - (C_{SRP}) (\cos \alpha_{sL} \cos \phi_{sL})^2 (\cos(\theta - \psi) \cos \alpha_{sL} \cos \phi_{sL} + \sin(\theta - \psi) \sin \alpha_{sL} \cos \phi_{sL}) \\
 f_y &= (C_{SRP} + \delta a) (\cos \alpha_{sF} \cos \phi_{sF})^2 (-\sin(\theta - \psi) \cos \alpha_{sF} \cos \phi_{sF} + \cos(\theta - \psi) \sin \alpha_{sF} \cos \phi_{sF}) \\
 &\quad - C_{SRP} (\cos \alpha_{sL} \cos \phi_{sL})^2 (-\sin(\theta - \psi) \cos \alpha_{sL} \cos \phi_{sL} + \cos(\theta - \psi) \sin \alpha_{sL} \cos \phi_{sL}) \\
 f_z &= (C_{SRP} + \delta a) (\cos \alpha_{sF} \cos \phi_{sF})^2 \sin \phi_{sF} - C_{SRP} (\cos \alpha_{sL} \cos \phi_{sL})^2 \sin \phi_{sL}
 \end{aligned}$$

The control angles  $\alpha_s$  and  $\phi_s$  are augmented by an additional control input  $\delta a$ , this new variable represents the change in the characteristic acceleration of the solar flap brought about by the change in the solar flap area. By the addition of this extra control input, the system becomes fully actuated with control authority equalling the number of degrees of freedom. It can be observed that, the orientation of the solar flaps, ( $\alpha_s$  and  $\phi_s$ ) appears in non-affine nature in the system formulation. Hence a nonlinear control algorithm based on higher order sliding mode is developed. Increasing the order of the system helps in extracting the angular rates of the solar flaps ( $\dot{\alpha}_s$  and  $\dot{\phi}_s$ ) and  $\dot{\delta a}$  from 4.15. The corresponding angular orientation of the solar flaps is obtained by integration of these angular rates. This information is then used in the system dynamics to calculate the force due to solar radiation pressure.

### 4.2.1 Adaptive Control Formulation and Stability Analysis

First we define the higher order sliding manifold given by

$$\sigma = \dot{S} + \xi S \quad (4.16)$$

where  $\xi$  is a positive constant. The lower order sliding plane,  $S$  is given by

$$S = \Lambda e \quad (4.17)$$

where

$$\Lambda = \begin{bmatrix} k_1 & 0 & 0 & k_2 & 0 & 0 \\ 0 & k_3 & 0 & 0 & k_4 & 0 \\ 0 & 0 & k_5 & 0 & 0 & k_6 \end{bmatrix} \quad \text{and} \quad e = X - X_d$$

In the adaptive control law,  $C_{srp}$  is taken as the unknown quantity due to the presence of uncertainty in the its associated parameters. Consider the candidate Lyapunov function defined as

$$V = \frac{1}{2}\sigma^T\sigma + \frac{1}{2\zeta}\tilde{C}_{srp}^T\tilde{C}_{srp} \quad (4.18)$$

where  $V > 0$  and  $\zeta$  is a positive constant. Taking the derivative along the trajectory gives,

$$\dot{V} = \sigma^T\dot{\sigma} + \frac{\tilde{C}_{srp}\dot{\tilde{C}}_{srp}}{\zeta} \quad (4.19)$$

where  $\tilde{C}_{srp} = \hat{C}_{srp} - C_{srp}$  (estimate - true value) and  $\dot{\sigma} = \ddot{S} + \xi\dot{S}$ .  $\ddot{S}$  represents the derivative of the equations of motion given by Eq. (4.15). Substituting for  $\dot{\sigma}$  in Eq. (4.19), and expanding we get

$$\dot{V} = \sigma^T(\ddot{S} + \xi\dot{S}) + \frac{\tilde{C}_{srp}\dot{\tilde{C}}_{srp}}{\zeta} \quad (4.20)$$

Before we proceed with the control algorithm design, we make use of the estimates on the upper bound of the uncertainties and perturbation on the system. The upper bounds introduced in Chapter 3: Section 3.2.2 are applicable here as well and the overall bound on the external disturbances is given as

$$L = \Lambda(E(X) + DF_{dt}) - \Lambda\dot{X}_d \quad (4.21)$$

Now Eq. (4.20) can be rewritten as

$$\dot{V} = \sigma^T \left[ \Lambda A \dot{X} + C_{srp} \frac{\partial g(U)}{\partial U} \dot{U} + \xi \dot{S} \right] + \frac{\tilde{C}_{srp}\dot{\tilde{C}}_{srp}}{\zeta} \quad (4.22)$$

Taking the parameter estimation error as  $\tilde{C}_{srp} = \hat{C}_{srp} - C_{srp}$ , and expanding Eq.(4.22), we have

$$\dot{V} = \sigma^T \left[ \Lambda A \dot{X} + \left( \hat{C}_{srp} - \tilde{C}_{srp} \right) \frac{\partial g(U)}{\partial U} \dot{U} + \xi \dot{S} \right] + \frac{\tilde{C}_{srp}\dot{\tilde{C}}_{srp}}{\zeta} \quad (4.23)$$

Rearranging the preceding Eq.(4.23) yields,

$$\dot{V} = \sigma^T \left[ \Lambda A \dot{X} + \hat{C}_{srp} \frac{\partial g(U)}{\partial U} \dot{U} \right] - \sigma^T \tilde{C}_{srp} \frac{\partial g(U)}{\partial U} \dot{U} + \frac{\tilde{C}_{srp} \dot{\hat{C}}_{srp}}{\zeta} \quad (4.24)$$

Now in order to make  $\dot{V}$  negative, choose the adaptive law as

$$\dot{\hat{C}}_{srp} = \zeta \sigma^T \frac{\partial g(U)}{\partial U} \dot{U} \quad (4.25)$$

Also let

$$\Lambda A \dot{X} + \hat{C}_{srp} \frac{\partial g(U)}{\partial U} \dot{U} = -\eta \operatorname{sgn}(\sigma) \quad (4.26)$$

where  $\eta$  is a positive constant. Substituting Eqs.(4.26) and (4.25) into Eq.(4.24) we have,

$$\dot{V} = \sigma^T [-\eta \operatorname{sgn}(\sigma)] = -\eta |\sigma| \quad (4.27)$$

Thus,  $\dot{V}$  is negative and hence the reaching condition is satisfied. Using Theorem-3 of LaSalle's principle [LaSalle 1960] it is proved that the system is completely stable and hence the system states converge onto the sliding surface. Next, Eq.(4.26) is rearranged to derive the control law that is capable of formation maneuvering and maintenance is given as,

$$\dot{U} = -\frac{1}{\hat{C}_{srp} \frac{\partial g(U)}{\partial U}} \left[ \eta \operatorname{sgn}(\sigma) + \Lambda A \dot{X} \right] \quad (4.28)$$

where  $\dot{U} = [\delta \dot{a} \quad \dot{\alpha}_s \quad \dot{\phi}_s]^T$  and  $U = \int \dot{U} dt$ . The discontinuous  $\operatorname{sgn}(\sigma)$  operator in Eq. (4.28), is replaced by a boundary layer to remove instantaneous switching and it is given by,

$$\dot{U} = -\frac{1}{\hat{C}_{srp} \frac{\partial g(U)}{\partial U}} \left[ \eta \left( \frac{\sigma}{|\sigma| + \delta} \right) + \Lambda A \dot{X} \right] \quad (4.29)$$

### 4.3 Performance Evaluation

In order to examine the effectiveness of the proposed formation control strategy, the detailed system response is numerically simulated using the set of governing equations of motion

Eqs. (4.1) - (4.5) along with Eq. (4.6) in conjunction with the proposed control algorithm given by Eq. (4.29), and the adaptation law, given by Eq. (4.25). The integration is carried out in Matlab using the fourth order Runge-Kutta solver with a fixed step size of 0.1 sec. The desired states of the system are given by the types of formation, as per Eqs.(2.19) and (2.20). The SFF systems parameters and the orbital parameters used in the numerical simulation are listed in Table 4.1. The controller and parameters are presented in Table 4.2. It should be noted here that in the development of the control law it is assumed that the leader is in an unperturbed reference orbit. However, numerical simulation is conducted on the system model that considers the leader satellite under  $J_2$ -effect, and variation in orientation of the solar flaps. A satellite in the geostationary orbit is considered here and hence the Earth shadow effect is assumed to be negligible as its effect is experienced for only about 5% of the orbital period [Kumar 2006].

Table 4.1: Orbital and system parameters

Parameters	Value
$m_f$ (kg)	10
$\mu(km^3s^{-2})$	398600
$r_p(km)$	42378
$\Omega, \omega$ (deg)	0
$i$ (deg)	45
$e$	0
$\phi$ (deg)	0
$A$ ( $m^2$ )	2.0
$\psi$ (deg)	45
$p$ ( $N/m^2$ )	$4.563 \times 10^{-6}$
$[\rho, s, \varepsilon_f, \varepsilon_b, B_f, B_b]$	[0.88, 0.94, 0.05, 0.55, 0.79, 0.55]

### 4.3.1 Projected circular formation and Circular formation

First we examine the performance of the proposed SFF system in maintaining a projected circular formation. The phase angle  $\phi$  between the leader and the follower satellites is assumed to be zero degree with a desired formation radius,  $r_d = 10km$  with the leader satellite in an orbit of inclination,  $i=45$ . The relative position errors remain bounded to

Table 4.2: Controller parameters

Parameters	Value(s)
$\eta$	0.00001
$\tau$	0.002
$[K_1, K_2, K_3, K_4, K_5, K_6]$	[1.0 2.5 2.5 4 2.5 4]
Initial estimate of Area, $\hat{A}$ ( $m^2$ )	0.5
Initial estimate of p, $\hat{p}$ ( $N/m^2$ )	$4.563 \times 10^{-6}$
Initial Mass, $\hat{m}_f$ (kg)	2.5
$\zeta$	$10^{-2}$

less than 1 m in the radial direction and to within 5 m in the along track and cross track direction (Fig. 4.2). The in-plane ( $\phi$ ) and out-of plane ( $\alpha$ ) orientations of the solar flaps have a maximum deflection of  $7^\circ$  (Fig. 4.3) and the maximum area change is less than  $1 m^2$ . Next we examine the performance of the proposed SFF system in the presence of an

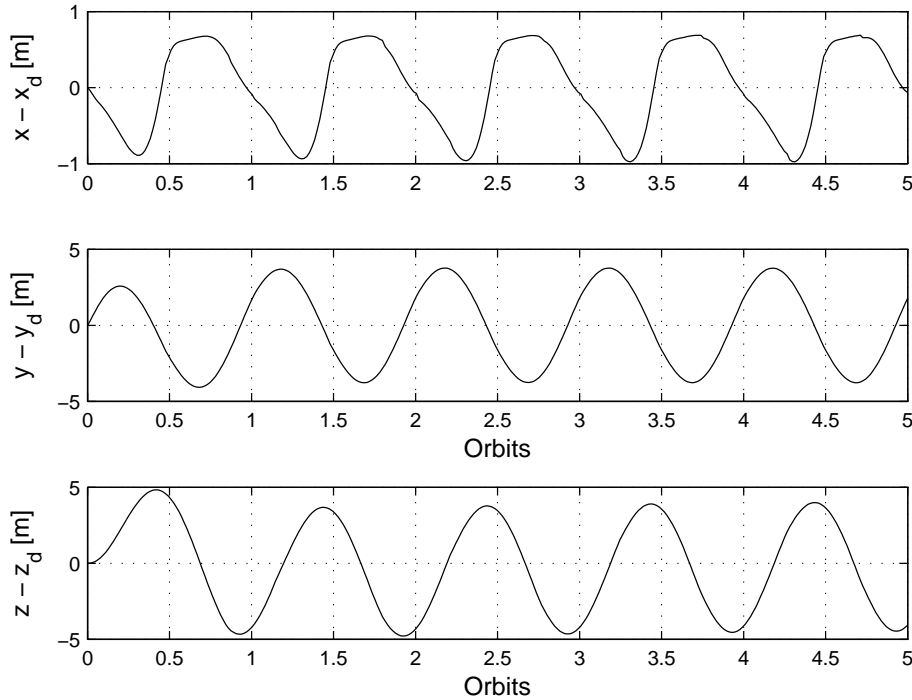


Figure 4.2: Relative position errors of the follower satellite in projected circular formation ( $r_d = 10\text{km}$ ).

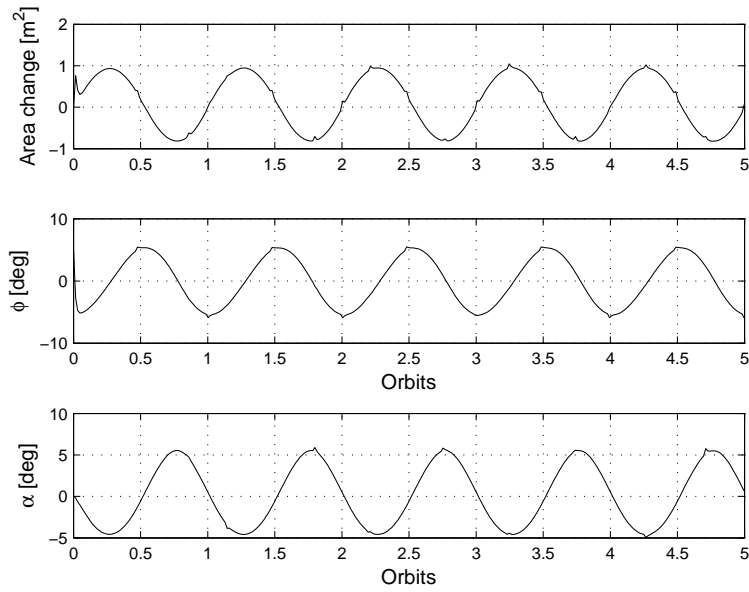


Figure 4.3: Area change and control angle orientation of the solar flaps on the follower satellite in a projected circular formation ( $r_d = 10\text{km}$ ).

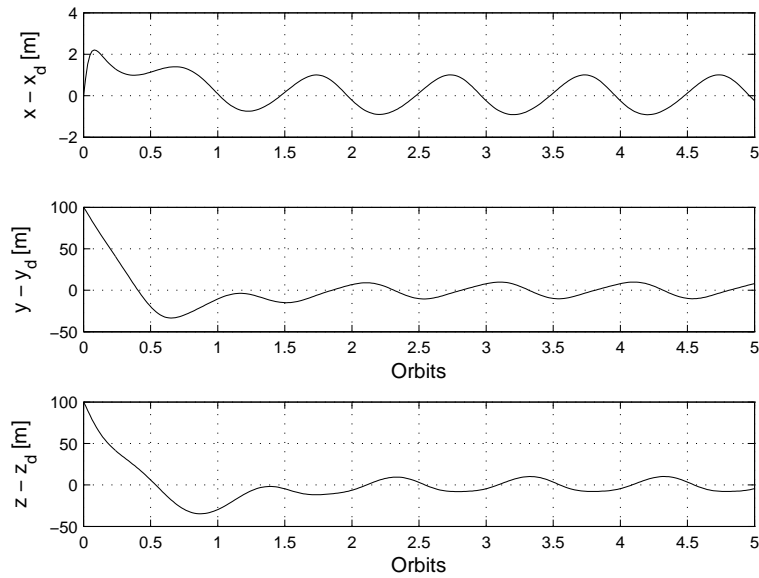


Figure 4.4: Relative position errors of the follower satellite in projected circular formation ( $r_d = 10\text{km}$ ) with initial offset error of 100 m.

additional disturbance in the form of an initial offset error of 100 m in the along track and cross track direction. It can be observed from Fig. (4.4), that the relative states converge to the desired states in less than one orbit with the relative position errors being bounded to less than 10m in all three directions. The corresponding maximum solar flap orientation (Fig. 4.5), in the in-plane direction ( $\phi$ ) is  $-12.5^\circ$  and  $-17.5^\circ$  in the out-of plane direction during the transient state while in the steady state, it oscillates within  $\pm 5^\circ$ . Formation

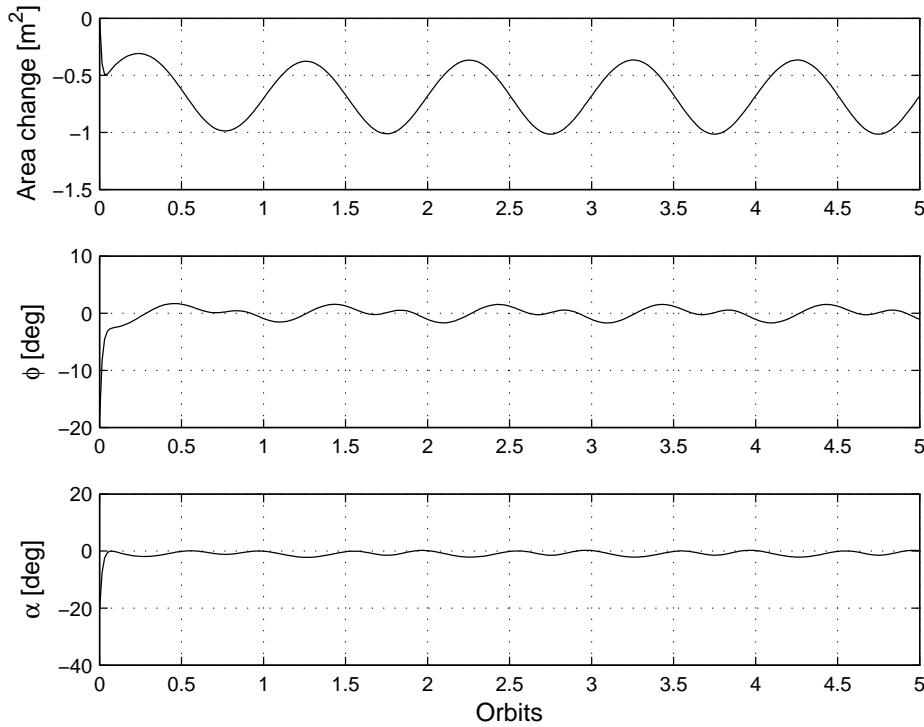


Figure 4.5: Area change and control angle orientation of the solar flaps on follower satellite in projected circular formation ( $r_d = 10\text{km}$ ) with initial offset error of 100 m.

reconfiguration is another important requirement of the SFF missions, and is studied next. The projected circular formation of size 10 km is reconfigured into a circular formation of 15 km after 1 orbit. From Fig. (4.6) it can be observed that reconfiguration is possible with the proposed control methodology, and the steady state errors remain bounded. A smooth reconfiguration is established with the solar flaps deflecting to a maximum orientation of  $24^\circ$  in the in-plane and  $10^\circ$  in the out-of-plane directions during the reconfiguration phase (Fig. 4.7).

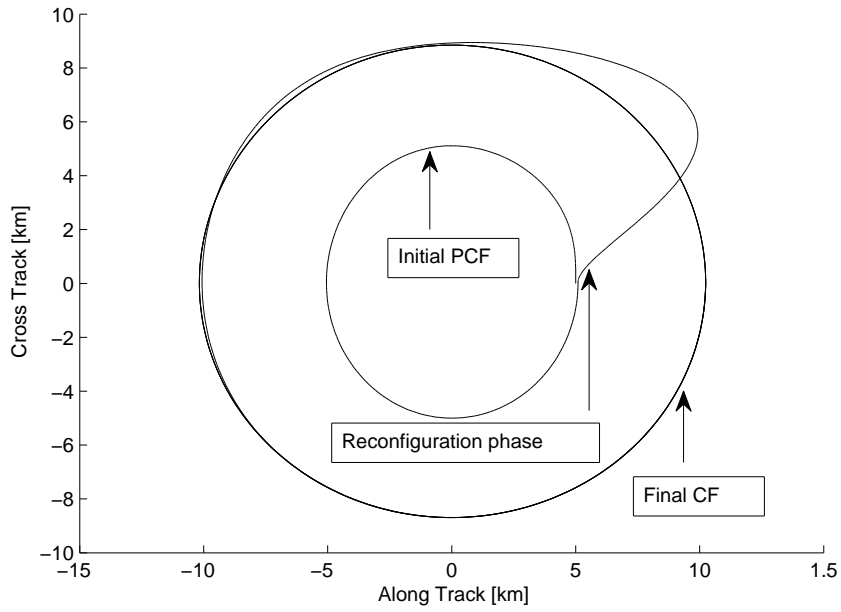


Figure 4.6: Reconfiguration of follower satellites from a projected circular formation (PCF) of  $r_d = 5$  km to a circular formation (CF) of  $r_d = 10$  km.

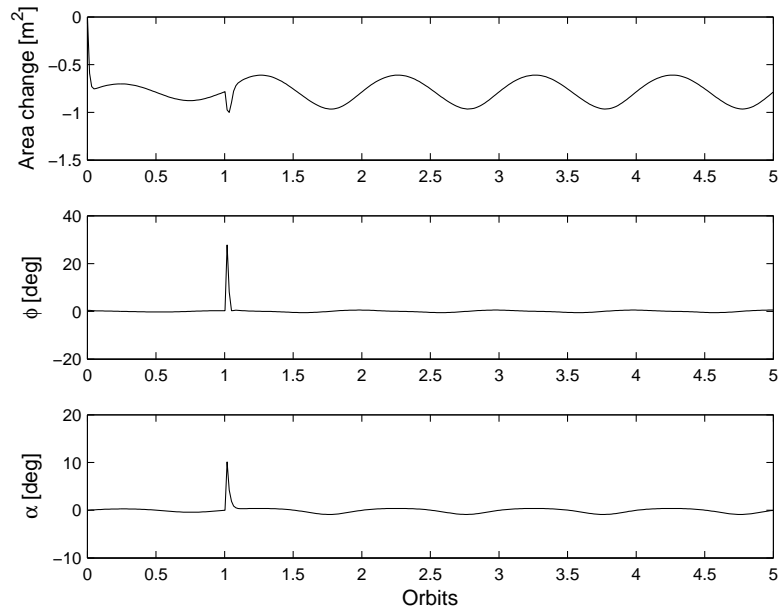


Figure 4.7: Area change and control angle orientation of the solar flaps on the follower satellite during formation reconfiguration.

### 4.3.2 Along-track Formation

Next, along-track formation using solar radiation pressure is evaluated. The constant separation is desired to be 10 km. Fig. 4.8 shows the relative errors in the radial and along track direction during along-track formation flying with an initial offset error of 100 m.

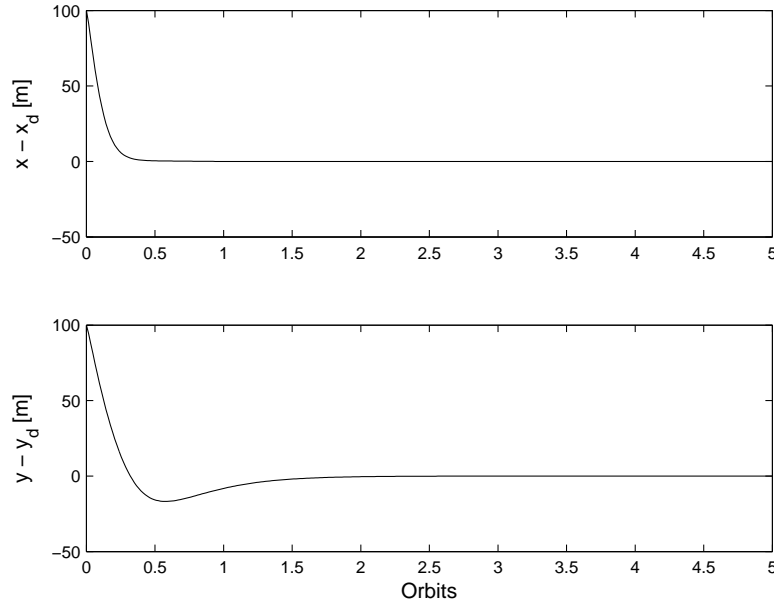


Figure 4.8: Relative position errors of the follower satellite in the radial and along-track direction during along track formation flying with  $r_d = 10$  km.

### 4.3.3 Multiple Satellite Formation

Feasibility of multiple satellite formation flying and reconfiguration using SRP is investigated in this section. The projected circular formation is examined in the multiple reconfiguration problem. Similar to the multiple satellite formation flying using aerodynamic drag, the constraint on the level of differential SRP achievable between each follower and the leader makes this problem equally challenging. The heuristic algorithm proposed in the previous chapter is rewritten here for clarity, and is tested in a configuration of two followers with the phase angles of the followers at  $0^\circ$ , and  $180^\circ$ , respectively. The algorithm is given as: During each orbit the solar flap orientation required for each individual leader-

follower satellite configuration for maintaining the projected circular formation of size,  $r_d = 5$  km, is calculated based on the proposed control methodology. The followers align their corresponding solar flaps with this calculated orientation. In the first orbit, the solar flap on the leader satellite is oriented with the calculated value with respect to the follower with phase angle  $0^\circ$ . This yields the required differential solar radiation pressure for the follower (Satellite 1 with phase  $\phi = 0^\circ$ ). In the next orbit the same procedure of calculation of the required solar flap orientation is performed, but the flap on the leader is oriented according to the follower satellite with phase  $180^\circ$  (Satellite 2). This method is continued for the successive orbits with the orientation of the solar flaps on the leader satellite switching between the two follower satellites. Eventhough, the differential force achieved by the follower satellites in each orbit may not be the same as required by each individual follower satellite in relation to the leader satellite, it is found during simulation that with the proposed algorithm, the projected circular formation is maintained with reasonable relative errors (Fig. 4.9). Next we consider the case of multiple satellite reconfigurations using the

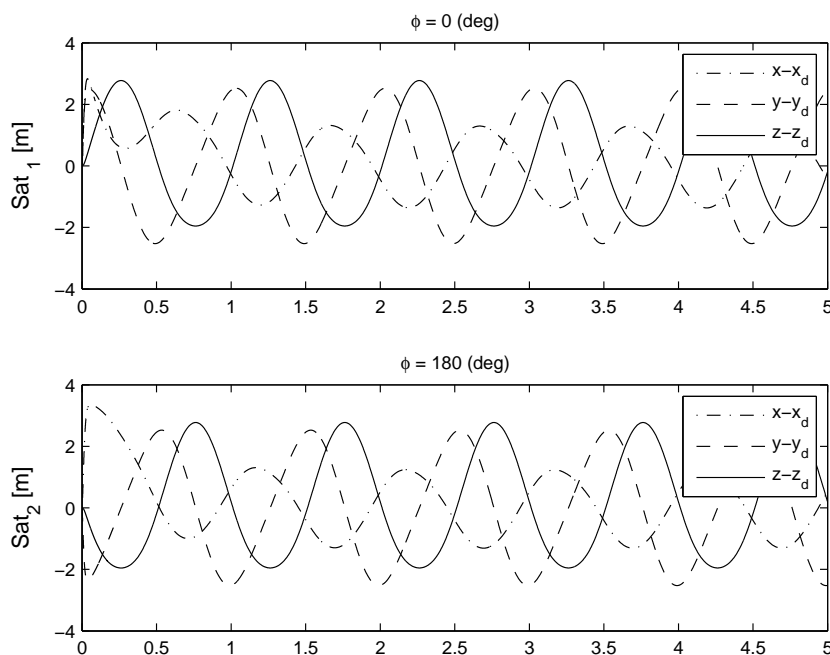


Figure 4.9: Relative position errors of the follower satellite during multiple satellite formation flying in PCF of size,  $r_d = 10$  km.

proposed heuristic algorithm. Here two satellites in a projected circular formation of initial formation size,  $r_d = 5$  km and phase angles of  $0^\circ$  and  $180^\circ$  respectively, are reconfigured to a final formation size of  $r_d = 20$  km (Fig. 4.10). A smooth reconfiguration is achieved with the application of the proposed heuristic algorithm.

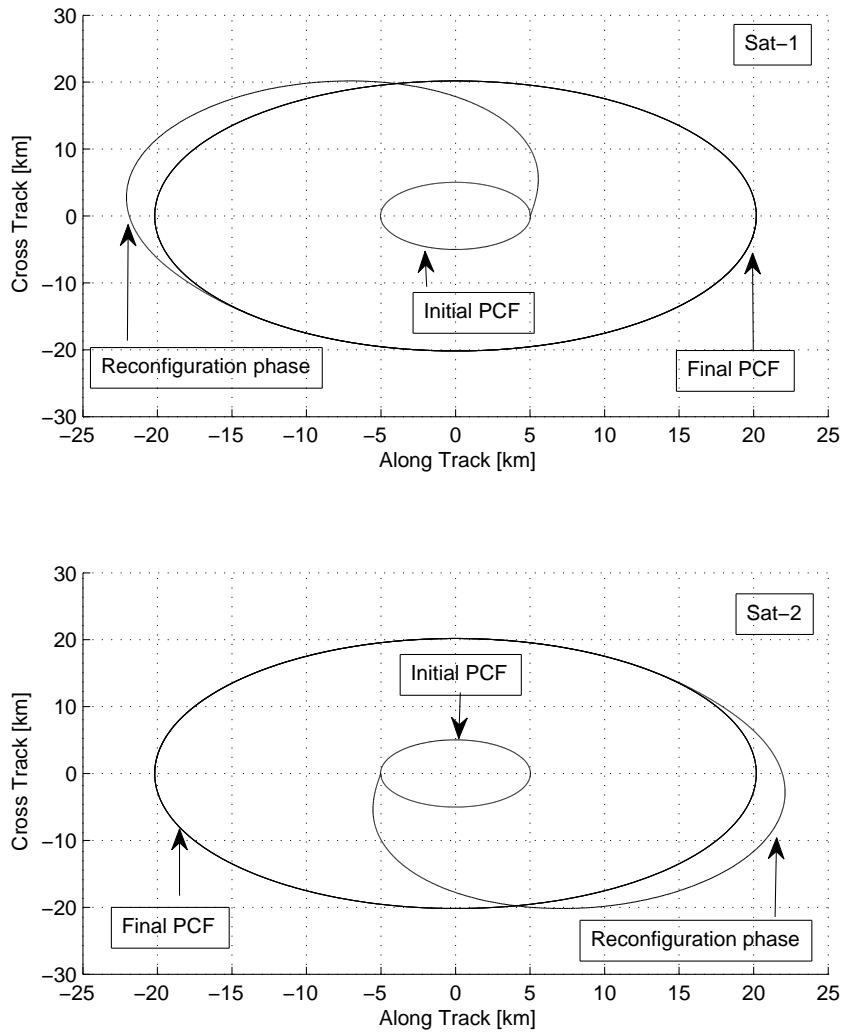


Figure 4.10: Multiple satellite formation reconfiguration.

## 4.4 Summary

This chapter examines the feasibility of using differential solar radiation pressure for multiple satellite formation flying. Differential solar radiation pressure is created by the desired rotation of solar flaps attached to the satellites and this rotation is governed by the control law developed based on the application of adaptive sliding mode control technique. The performance of the proposed satellite formation flying system in maintaining and reconfiguring various formations is evaluated including the performance of the formation system in the presence of initial offset errors. The relative errors in the satellite formation system remained bounded within  $\pm 5$  m in all the three axes for all test scenarios considered. The maximum deflection of the solar flaps is observed during the transient state, with the maximum flap orientation limited to within  $\pm 8^\circ$  in the steady state. The viability of multiple satellite formation is also confirmed in the study. Multiple satellite formation reconfiguration is also examined with excellent results. The theoretical and numerical results suggest that the use of differential SRP is a suitable alternative to multiple satellite formation even in the presence of external disturbances.



## CHAPTER 5

# Satellite Attitude Control Using Aerodynamic Drag

---

IN Chapter 3 and Chapter 4, the feasibility of performing satellite formation flying using either aerodynamic drag or solar radiation pressure was studied and evaluated. The satellite attitude dynamics was not considered and attitude was assumed stabilized. The attitude control system provides the satellite with the maneuvering, tracking and pointing capability. For many Earth orbiting satellite three axis attitude stabilization is essential to meet the nadir pointing requirement of the mission. This chapter looks to expand upon the previous efforts on the use of aerodynamic drag for passive satellite attitude control. Existing literature proposes the combined use of aerodynamic and magnetic torquing [Psiaki 2004], control of the two of principal axes using torque due to aerodynamic drag [Pande & Venkatachalam 1979], [Modi & Shrivastava 1973], or using an additional yaw stabilizer along with the drag plates [Chen *et al.* 2000] for achieving three axis satellite attitude control. The proposed system comprises of a satellite with two pairs of oppositely placed drag plates, and the satellite attitude is controlled by the suitable rotation of these drag plates. This arrangement of the drag plates results is an inherently underactuated system with the number of available control inputs less than the degree of freedom to be controlled. To compensate for unknown disturbances and parameter uncertainties, an adaptive nonlinear control design based on the theory of sliding mode is proposed as the control technique for satellite attitude control.

The chapter is organized as follows: Section 5.1 introduces the nonlinear equations of motion of an Earth orbiting satellite. The adaptive control algorithm based on sliding mode technique is formulated with the corresponding stability conditions for robustness against uncertainties and disturbances in Section 5.2. The detailed numerical simulation of

the governing system equations of motion under the proposed control strategy, including the effects of various system parameters on the controller performance is given in Section 5.3. Conclusions are stated in Section 5.4.

## 5.1 Proposed System Model

We start the study by formulating the nonlinear equations of motion of the rigid body satellite. The proposed system consists of a *rigid body satellite* in an elliptical planar trajectory with the Earth's center at one of its foci.

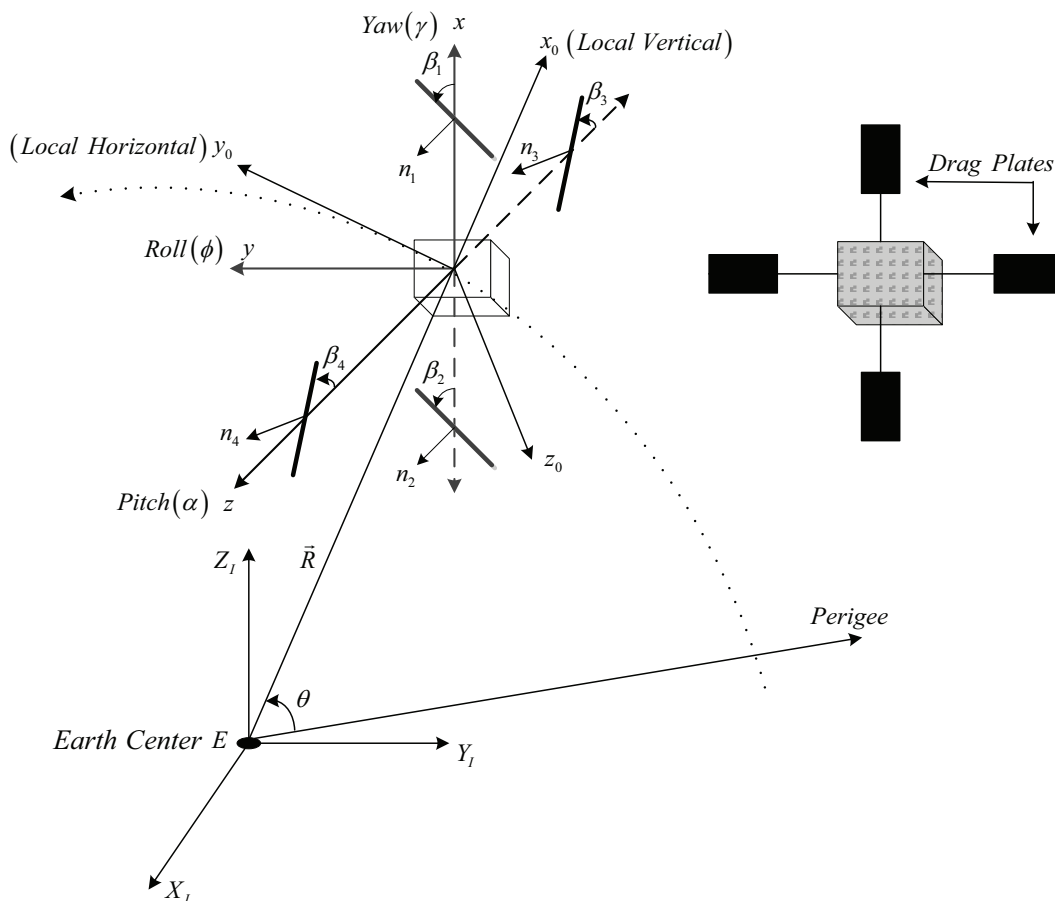


Figure 5.1: Geometry of orbit motion of rigid satellite.

### 5.1.1 Coordinate Frames

Fig.5.1 shows the *Earth centered inertial* (ECI) frame, denoted by  $E - X_I Y_I Z_I$ , with its origin located at the center of the Earth. The axes are defined such that the  $Z_I$ -axis is passing through the celestial North pole, the  $X_I$ -axis is directed towards the vernal equinox, and the  $Y_I$ -axis completes the right-handed triad. The local vertical local horizontal (LVLH) orbital reference frame,  $\mathfrak{L} - x_0 y_0 z_0$ , has its origin fixed at the center of mass of the satellite. The  $x_0$ -axis points along the local vertical,  $z_0$ -axis is normal to the orbital plane, and the  $y_0$ -axis points along the orbit direction. The corresponding principal body-fixed coordinate axes of the satellite are denoted by  $\mathfrak{B} - x y z$  as shown in the figure. The nodal line represents the reference line in orbit for the measurement of the true anomaly (eccentric orbit) or angle  $\theta$  (circular orbit).

Satellite attitude is represented using the Euler angles,  $(\alpha, \phi, \gamma)$ . The Euler angles describe the attitude orientation of the body-fixed reference frame,  $\mathfrak{B} - x y z$ , relative to the LVLH reference frame,  $\mathfrak{L} - x_0 y_0 z_0$ , by a set of three successive rotations. The rotations can occur about any of the three orthogonal axes, provided two successive rotations about the same axis are not performed. This results in 12 sets of possible Euler angles for such successive rotations about the body-fixed axis. The most commonly used rotation sequence is the (3 – 2 – 1) set of Euler angles, with  $\alpha$  (pitch) about the  $z$ -axis (3),  $\phi$  (roll) about the new  $y$ -axis (2), and finally  $\gamma$  (yaw) about the resulting  $x$ -axis (1).

However, Euler angles exhibit singularities whenever the roll angle ( $\phi$ ) has a value of  $\pm \frac{\pi}{2}$ . But singularity does not reflect any physical limitations of the rigid satellite rather it is an *inherent* property of the Euler angle representation. The orientation of the body-fixed reference frame,  $\mathfrak{B} - x y z$ , with respect to the LVLH reference frame,  $\mathfrak{L} - x_0 y_0 z_0$  using the (3 – 2 – 1) rotation sequence is described by the direction cosine matrix  $C^{B/L} = R_1(\gamma)R_2(\phi)R_3(\alpha) = R_x(\gamma)R_y(\phi)R_z(\alpha)$ .

$$C^{B/L} = \begin{bmatrix} c\phi c\alpha & c\phi s\alpha & -s\phi \\ s\gamma s\phi c\alpha - c\gamma s\alpha & s\gamma s\phi s\alpha + c\gamma c\alpha & s\gamma c\phi \\ c\gamma s\phi c\alpha + s\gamma s\alpha & c\gamma s\phi s\alpha - s\gamma c\alpha & c\gamma c\phi \end{bmatrix} \quad (5.1)$$

where  $c\phi = \cos \phi$  and  $s\phi = \sin \phi$ ,  $R_x(\gamma)$  denotes the rotation matrix for  $\gamma$  rotation about

the  $x$ -axis,  $R_y(\phi)$  denotes the rotation matrix for  $\phi$  rotation about the  $y$ -axis, and  $R_z(\alpha)$  denotes the rotation matrix for  $\alpha$  rotation about the  $z$ -axis.

Here  $\beta_p$  for  $p = 1, 2$  represents the orientation of the drag plates with its normal initially aligned with the  $y$ -axis rotated about the  $z$ -axis and  $\beta_p$  for  $p = 3, 4$  represents the orientation of the pair of drag plates with its normal initially aligned with the  $y$ -axis, and then rotated about the  $x$ -axis.

### 5.1.2 Satellite Angular Velocity

Let the unit vectors associated with the reference frames  $\mathfrak{B} - x y z$  and  $\mathfrak{L} - x_0 y_0 z_0$ , be represented as  $\{\hat{i}, \hat{j}, \hat{k}\}$  and  $\{\hat{i}_0, \hat{j}_0, \hat{k}_0\}$  respectively. Using the (3-2-1) rotation sequence, the transformation from the  $\mathfrak{L} - x_0 y_0 z_0$  orbital frame to the body-fixed frame  $\mathfrak{B} - x y z$  is given by,

$$\begin{bmatrix} \hat{i} \\ \hat{j} \\ \hat{k} \end{bmatrix} = \begin{bmatrix} c\phi c\alpha & c\phi s\alpha & -s\phi \\ s\gamma s\phi c\alpha - c\gamma s\alpha & s\gamma s\phi s\alpha + c\gamma c\alpha & s\gamma c\phi \\ c\gamma s\phi c\alpha + s\gamma s\alpha & c\gamma s\phi s\alpha - s\gamma c\alpha & c\gamma c\phi \end{bmatrix} \begin{bmatrix} \hat{i}_0 \\ \hat{j}_0 \\ \hat{k}_0 \end{bmatrix} \quad (5.2)$$

For a rigid satellite in a circular orbit around the Earth, the angular velocity of the body-fixed frame  $\mathfrak{B}$  relative to the ECI frame  $E$  is given by

$$\vec{\omega}^{B/I} = \vec{\omega}^{B/L} + \vec{\omega}^{L/I} \quad (5.3)$$

where  $\vec{\omega}^{B/L}$  is the angular velocity of  $\mathfrak{B}$  relative to the orbital frame  $\mathfrak{L}$ , and  $\vec{\omega}^{L/I}$  is the angular velocity of the orbital frame with respect to the ECI frame. From Fig. (5.1), the angular velocity of  $\mathfrak{L}$  relative to  $E$  is

$$\vec{\omega}^{L/I} = \dot{\theta} \hat{k}_0 \quad (5.4)$$

where  $\dot{\theta}$  is the orbital rate of the satellite. Here,  $\dot{\theta} = \frac{\sqrt{\mu p}}{R^2}$ , where  $\mu$  represents the gravitational parameter of the Earth,  $p$  is the semi-latus rectum, and  $R$  is the distance of the

satellite from the center of the Earth. From Eq. (5.2) we have

$$\begin{bmatrix} \hat{i}_0 \\ \hat{j}_0 \\ \hat{k}_0 \end{bmatrix} = \begin{bmatrix} c\phi c\alpha & s\gamma s\phi c\alpha - c\gamma s\alpha & c\gamma s\phi c\alpha + s\gamma s\alpha \\ c\phi s\alpha & s\gamma s\phi s\alpha + c\gamma c\alpha & c\gamma s\phi s\alpha - s\gamma c\alpha \\ -s\phi & s\gamma c\phi & c\gamma c\phi \end{bmatrix} \begin{bmatrix} \hat{i} \\ \hat{j} \\ \hat{k} \end{bmatrix} \quad (5.5)$$

Substituting for  $\hat{k}_0$  from Eq. (5.5) into Eq. (5.4) yields,

$$\vec{\omega}^{L/I} = \dot{\theta} \begin{bmatrix} -\sin\phi \\ \sin\gamma \cos\phi \\ \cos\gamma \cos\phi \end{bmatrix} \quad (5.6)$$

The angular velocity of the satellite with respect to the orbital frame  $\mathcal{L}$  is given by

$$\begin{aligned} \vec{\omega}^{B/L} &= \omega_x^{BL} \hat{i} + \omega_y^{BL} \hat{j} + \omega_z^{BL} \hat{k} \\ &= \dot{\alpha} \hat{k}_0 + \dot{\phi} \hat{j}_1 + \dot{\gamma} \hat{i} \end{aligned} \quad (5.7)$$

where  $\dot{\alpha}$  is about the  $k_0$  axis in the frame  $\mathcal{L} - x_0 y_0 z_0$ , followed by  $\dot{\phi}$  about the  $j_1$  axis in the intermediate frame  $S - x_1 y_1 z_1$ , and finally  $\dot{\gamma}$  about the  $i$  axis in the frame  $\mathfrak{B} - x y z$ . This can also be written as

$$\vec{\omega}^{B/O} = \begin{bmatrix} \hat{i} & \hat{j} & \hat{k} \end{bmatrix} \begin{bmatrix} \dot{\gamma} \\ 0 \\ 0 \end{bmatrix} + \begin{bmatrix} \hat{i}_1 & \hat{j}_1 & \hat{k}_1 \end{bmatrix} \begin{bmatrix} 0 \\ \dot{\phi} \\ 0 \end{bmatrix} + \begin{bmatrix} \hat{i}_0 & \hat{j}_0 & \hat{k}_0 \end{bmatrix} \begin{bmatrix} 0 \\ 0 \\ \dot{\alpha} \end{bmatrix} \quad (5.8)$$

The unit vectors are related to each other based on rotation matrices as follows

$$\begin{aligned} \begin{bmatrix} \hat{i}_1 & \hat{j}_1 & \hat{k}_1 \end{bmatrix}^T &= [R_x(\gamma)R_y(\phi)]^{-1} \begin{bmatrix} \hat{i} & \hat{j} & \hat{k} \end{bmatrix}^T \\ \begin{bmatrix} \hat{i}_0 & \hat{j}_0 & \hat{k}_0 \end{bmatrix}^T &= [R_x(\gamma)R_y(\phi)R_z(\alpha)]^{-1} \begin{bmatrix} \hat{i} & \hat{j} & \hat{k} \end{bmatrix}^T \end{aligned} \quad (5.9)$$

Using Eqs. (5.7)-(5.9), the angular velocity of the satellite with respect to the orbital reference frame can now be expressed as

$$\begin{aligned} \begin{bmatrix} \omega_x^{BL} \\ \omega_y^{BL} \\ \omega_z^{BL} \end{bmatrix} &= \begin{bmatrix} \dot{\gamma} \\ 0 \\ 0 \end{bmatrix} + R_x(\gamma)R_y(\phi) \begin{bmatrix} 0 \\ \dot{\phi} \\ 0 \end{bmatrix} + R_x(\gamma)R_y(\phi)R_z(\alpha) \begin{bmatrix} 0 \\ 0 \\ \dot{\alpha} \end{bmatrix} \\ &= \begin{bmatrix} 1 & 0 & -\sin \phi \\ 0 & \cos \gamma & \sin \gamma \cos \phi \\ 0 & -\sin \gamma & \cos \gamma \cos \phi \end{bmatrix} \begin{bmatrix} \dot{\gamma} \\ \dot{\phi} \\ \dot{\alpha} \end{bmatrix} \end{aligned} \quad (5.10)$$

Finally, using Eqs. (5.6) and (5.10) in Eq. (5.3), the angular velocity of the satellite relative to the ECI frame  $E$  expressed in the body frame  $\mathfrak{B}$  is

$$\begin{bmatrix} \omega_x \\ \omega_y \\ \omega_z \end{bmatrix} = \begin{bmatrix} 1 & 0 & -\sin \phi \\ 0 & \cos \gamma & \sin \gamma \cos \phi \\ 0 & -\sin \gamma & \cos \gamma \cos \phi \end{bmatrix} \begin{bmatrix} \dot{\gamma} \\ \dot{\phi} \\ \dot{\alpha} \end{bmatrix} + \dot{\theta} \begin{bmatrix} -\sin \phi \\ \sin \gamma \cos \phi \\ \cos \gamma \cos \phi \end{bmatrix} \quad (5.11)$$

### 5.1.3 Free Molecular Aerodynamic Drag Model

The free-molecular aerodynamic drag model introduced in Chapter 2 is reproduced here

$$\vec{F} = A \left[ -\hat{n}p + \left( \hat{n} \sin \zeta - \hat{V}_{rel} \right) \left( \frac{\tau}{\cos \zeta} \right) \right] \quad (5.12)$$

where  $p$  is the total pressure and  $\tau$  is the shearing stress,  $\hat{V}_{rel} = \frac{\vec{V}_{rel}}{\|\vec{V}_{rel}\|}$  is the velocity unit vector of the surface element with respect to the atmosphere and  $\hat{n}$  is the outward-pointing unit normal vector. The total pressure  $p$  and shearing stress  $\tau$  are given by [Gombosi 1994]

$$\begin{aligned} \frac{p}{q_\infty} &= \left\{ \left[ \frac{2 - \sigma_n}{\sqrt{\pi}} \right] \sin \zeta + \frac{\sigma_n}{2s} \sqrt{\frac{T_s}{T_a}} \right\} \left\{ \frac{1}{s} e^{-s^2 \sin^2 \zeta} + \sqrt{\pi} [1 + \operatorname{erf}(s \sin \zeta)] \sin \zeta \right\} \\ &\quad + \left[ \frac{2 - \sigma_n}{2s^2} \right] [1 + \operatorname{erf}(s \sin \zeta)] \\ \frac{\tau}{q_\infty} &= \sigma_t \left\{ \frac{1}{s\sqrt{\pi}} e^{-s^2 \sin^2 \zeta} + [1 + \operatorname{erf}(s \sin \zeta)] \sin \zeta \right\} \end{aligned} \quad (5.13)$$

Here  $\sigma_n$  and  $\sigma_t$  are the normal and tangential accommodation coefficients,  $T_s$  is the absolute temperature of the surface,  $T_a$  is the atmospheric temperature,  $q_\infty$  is the dynamic pressure given by

$$q_\infty = \frac{1}{2}\rho V_{rel}^2 \quad (5.14)$$

$$\operatorname{erf}(x) = \frac{2}{\sqrt{\pi} \int_0^x e^{-y^2} dy} \quad (5.15)$$

and  $s$  is the air speed, nondimensionalized by the mean molecular speed of the atmosphere and given by

$$s = \sqrt{\frac{M_a V_{rel}^2}{2R^* T_a}} \quad (5.16)$$

where  $M_a$  is the mean molar mass of the atmosphere and  $R^*$  is the universal gas constant.  $M_a$  and  $T_a$  vary with altitude and can be obtained from the 1976 U.S. Standard Atmospheric model. The accommodation coefficients  $\sigma_n$  and  $\sigma_t$ , represent the fact that some impinging air molecules come to thermal equilibrium with the surface and then get re-emitted thermally while others reflect specularly. Specular reflection means that the angle of incidence equals the angle of reflection and that the relative speed remains unchanged. The values  $\sigma_n = \sigma_t = 0$  implies specular reflection of all the impinging air molecules, while  $\sigma_n = \sigma_t = 1$  implies full thermal accommodation of all the impinging air molecules. Eventhough there are no reliable data for these coefficients, typical values of  $\sigma_n$  and  $\sigma_t$  lie between 0.85 and 1, which means that most of the air molecules get re-emitted thermally. It is to be noted that  $\sin \zeta = \hat{n}^T \hat{V}_{rel}$ .

The outward-pointing unit normal vectors are given as

$$n_p = \left[ -\sin \beta_p \hat{i} + \cos \beta_p \hat{j} \right] \quad p = 1, 2 \quad (5.17)$$

$$n_p = \left[ \cos \beta_p \hat{j} + \sin \beta_p \hat{k} \right] \quad p = 3, 4 \quad (5.18)$$

Another aspect to be considered is the effect of shading, which refers to the situation where one aerodynamic surface lies directly upstream of another aerodynamic surface causing re-incidence of emitted air molecules. This can perturb the incident velocity distributions that

have been used to derive Eqs. (5.13). However, as can be observed from Fig. (5.1) we can neglect this phenomenon because the drag plates do not cause shading in this arrangement. The resultant torque on the surface can be calculated using the equations for pressure and shearing stress Eqs. (5.13) in conjunction with the unit vectors  $\hat{n}$  and  $\hat{V}_{rel}$ . The net torque can then be computed by summing the moments over all the four surfaces, given by

$$\vec{T}_a = \sum_{i=1}^4 \vec{r}_i \times \vec{F}_{a_i} \quad (5.19)$$

where  $\vec{r}_j$  is the position vector of the geometric center of the individual drag plates measured from the satellite center of mass. For the proposed system configuration, it can be inferred that  $\vec{T}_a$  will have components only along the  $x$  and  $z$  direction, i.e.,  $T_{a\alpha}$  and  $T_{a\gamma}$  respectively. Considering Eq. (5.19) it can be written as follows:

$$\vec{T}_{a\alpha} = \vec{T}_{a_1} + \vec{T}_{a_2} \quad (5.20)$$

$$\vec{T}_{a\gamma} = \vec{T}_{a_3} + \vec{T}_{a_4} \quad (5.21)$$

#### 5.1.4 Equations of Motion

The governing nonlinear coupled differential equations of motion of the system are obtained as

$$\begin{bmatrix} \ddot{\alpha} \\ \ddot{\phi} \\ \ddot{\gamma} \end{bmatrix} = \begin{bmatrix} N_{11} & N_{12} & N_{13} \\ N_{21} & N_{22} & N_{23} \\ N_{31} & N_{32} & N_{33} \end{bmatrix} \left\{ \begin{bmatrix} F_\alpha \\ F_\phi \\ F_\gamma \end{bmatrix} + \begin{bmatrix} T_{a\alpha} \\ T_{a\phi} \\ T_{a\gamma} \end{bmatrix} \right\} \quad (5.22)$$

where  $F_\alpha$ ,  $F_\phi$ , and  $F_\gamma$  are the nonlinear terms given by

$$\begin{aligned} F_\alpha &= p_\alpha \cos \phi \cos \gamma + p_\phi \cos \phi \sin \gamma - p_\gamma \sin \gamma \\ F_\phi &= -p_\alpha \sin \gamma + p_\phi \cos \gamma \\ F_\gamma &= p_\gamma \end{aligned} \quad (5.23)$$

The coefficients  $p_\alpha$ ,  $p_\phi$ , and  $p_\gamma$  in the preceding Eq. (5.23) are given by,

$$p_\alpha = [(1 - k_{xz} + k_{yz})(\dot{\theta} + \dot{\alpha})\dot{\phi} \sin \phi \cos \gamma] - (k_{xz} - k_{yz})(\dot{\theta} + \dot{\alpha})^2 \sin \phi \cos \phi \sin \gamma + (1 + k_{xz} - k_{yz})[(\dot{\theta} + \dot{\alpha})\dot{\gamma} \cos \phi \sin \gamma + \dot{\phi}\dot{\gamma} \cos \gamma] - 3(k_{xz} - k_{yz})(\cos \alpha \sin \phi \sin \gamma - \sin \alpha \cos \gamma) \cos \alpha \cos \phi$$

$$p_\phi = [(1 - k_{xz} + k_{yz})(\dot{\theta} + \dot{\alpha})\dot{\gamma} \sin \phi \sin \gamma] - (1 - k_{xz})(\dot{\theta} + \dot{\alpha})^2 \sin \phi \cos \phi \cos \gamma + (1 - k_{xz} - k_{yz})[(\dot{\theta} + \dot{\alpha})\dot{\gamma} \cos \phi \cos \gamma - \dot{\phi}\dot{\gamma} \sin \gamma] + 3(1 - k_{xz})(\cos \alpha \sin \phi \cos \gamma + \sin \alpha \sin \gamma) \cos \alpha \cos \phi$$

$$p_\gamma = [k_{xz} - (1 - k_{yz}) \cos 2\gamma](\dot{\theta} + \dot{\alpha})\dot{\phi} \cos \phi - (1 - k_{yz})[(\dot{\theta} + \dot{\alpha})^2 \cos^2 \phi - \dot{\phi}^2] \sin \gamma \cos \gamma + 3(1 - k_{yz})(\cos \alpha \sin \phi \cos \gamma + \sin \alpha \sin \gamma) (\cos \alpha \sin \phi \sin \gamma - \sin \alpha \cos \gamma)$$

The elements of the matrix  $N$  in Eq. (5.22) are given by

$$N_{11} = \frac{\sin^2 \gamma + k_{yz} \cos^2 \gamma}{k_{yz} \cos^2 \phi}, \quad N_{12} = \frac{(1 - k_{yz}) \sin \gamma \cos \gamma}{k_{yz} \cos \phi}$$

$$N_{13} = N_{11} \sin \phi, \quad N_{21} = N_{12}, \quad N_{22} = \frac{\cos^2 \gamma + k_{yz} \sin^2 \gamma}{k_{yz}}$$

$$N_{23} = N_{12} \sin \phi, \quad N_{31} = N_{13}, \quad N_{32} = N_{23}, \quad N_{33} = N_{11} \sin^2 \phi + \frac{1}{k_{xz}}$$

The dimensionless parameters representing the principal moment of inertia ratios of the satellite are defined as

$$k_{xz} = \frac{I_x}{I_z} = \frac{1 - k_1}{1 - k_1 k_2} \quad \text{and} \quad k_{yz} = \frac{I_y}{I_z} = \frac{1 - k_2}{1 - k_1 k_2} \quad (5.24)$$

$$k_1 = \frac{I_z - I_x}{I_y} \quad \text{and} \quad k_2 = \frac{I_z - I_y}{I_x} \quad (5.25)$$

For a specific orbit, the orbital radius  $R$  is given by

$$R = \frac{a(1 - e^2)}{1 + e \cos \theta} = \frac{\mu^{1/3}(1 - e^2)}{\Omega^{2/3}(1 + e \cos \theta)} \quad (5.26)$$

and the orbital rate,  $\dot{\theta}$ , is obtained by

$$\dot{\theta} = \frac{\sqrt{\mu a(1 - e^2)}}{R^2} \quad (5.27)$$

Since the true anomaly  $\theta(t)$  is implicitly known from the Kepler's equation, it is convenient to replace  $t$  with  $\theta$  as the independent variable. The corresponding derivatives with respect to  $\theta$  are represented as

$$\dot{q} = \dot{\theta} q' = \frac{\sqrt{\mu a(1 - e^2)}}{R^2} q' \quad (5.28)$$

$$\ddot{q} = \frac{\mu}{R^3} [(1 + e \cos \theta) q'' - 2q' e \sin \theta] \quad (5.29)$$

where  $q$  is given as  $q \in \mathbb{R}^3 = [\alpha, \phi, \gamma]^T$ . After carrying out algebraic manipulation and nondimensionalization, the governing nonlinear equations of motion of the system can be written in the matrix notation as follows

$$q'' = M(q, k_{xz}, k_{yz}) [F(q, q', e, k_{xz}, k_{yz}) + \hat{T}_f] \quad (5.30)$$

where  $M(q, k_{xz}, k_{yz}) \in \mathbb{R}^{3 \times 3}$  and  $F(q, q', e, k_{xz}, k_{yz}) \in \mathbb{R}^{3 \times 1}$  are matrices containing nonlinear functions, and  $\hat{T}_f \in \mathbb{R}^3 = [\hat{T}_{a\alpha}, \hat{T}_{a\phi}, \hat{T}_{a\gamma}]^T$  corresponds to the dimensionless control torques. The nondimensionalized torque due to aerodynamic drag is given by,

$$\hat{T}_{aq} = \frac{(1 - e^2)^3}{(1 + e \cos \theta)^3} \left( \frac{T_{aq}}{I_z \Omega^2} \right) = \frac{(1 - e^2)^3}{(1 + e \cos \theta)^3} \begin{bmatrix} \hat{T}_{a\alpha} \\ \hat{T}_{a\phi} \\ \hat{T}_{a\gamma} \end{bmatrix}$$

In this proposed system configuration, the control torques  $\hat{T}_{a\alpha}$  and  $\hat{T}_{a\gamma}$  are obtained using aerodynamic drag as given by Eqs.(5.20) and (5.21), but the torque component  $\hat{T}_{a\phi}$  is zero.

## 5.2 Design of Control Law

In this section, a nonlinear control algorithm that makes use of torque due to aerodynamic drag to stabilize the satellite is developed. Taking into account the parameter uncertainty associated with aerodynamic drag, the control law is made to be adaptive in nature. As stated in Section 5.1, the control inputs are the orientation of the two sets of drag plates attached to the satellite. From Eqs. (5.12) - (5.19), it is evident that it is difficult to extract the angular rotations of the drag plates from the highly nonlinear coupled equations of motion. Hence we use a simpler representation of the aerodynamic drag model to design the control algorithm. In this simplified aerodynamic drag model it is assumed that the energy of the impinging molecules are totally absorbed on impact with the satellite surface. The force due to aerodynamic drag in this case is represented as follows

$$F_a = -\frac{1}{2}C_D A \rho V_{rel}^2 (\hat{n} \cdot \hat{v}_b) \hat{v}_b \quad (5.31)$$

where  $\hat{n}$  is the outward normal, and  $\hat{v}_b$  is the unit vector in the direction of the translational velocity. The torque due to aerodynamic drag is obtained by computing the moments over the drag plate surface, given by

$$T_a = B \sum_{i=1}^4 \vec{r}_i \times (\hat{n}_i \cdot \hat{v}_b) \hat{v}_b \quad (5.32)$$

where  $B = -\frac{1}{2}C_D A \rho V_{rel}^2$ . Here again, the torques along the pitch and yaw axes are given as

$$T_{a\alpha} = T_{a_1} + T_{a_2} \quad (5.33)$$

$$T_{a\gamma} = T_{a_3} + T_{a_4} \quad (5.34)$$

To facilitate the control law design, the state space representation of the system can be formulated as follows:

$$\begin{bmatrix} x_{11}' \\ x_2' \end{bmatrix} = \begin{bmatrix} \bar{A}_{11} & \bar{A}_{12} \\ \bar{A}_{21} & \bar{A}_{22} \end{bmatrix} \left\{ \begin{bmatrix} F_1 \\ F_2 \end{bmatrix} + \begin{bmatrix} 0 \\ U \end{bmatrix} + \begin{bmatrix} d_1 \\ d_2 \end{bmatrix} \right\} \quad (5.35)$$

Here  $x'_1 = \phi'$ ,  $x'_2 = [\alpha', \gamma']$ ,  $F_1 = F_\phi$ ,  $F_2 = [F_\alpha, F_\gamma]^T$ ,  $d_1$  and  $d_2$  represent the external disturbances, and  $\bar{A}$  matrix constitutes the nonlinear terms and is given by

$$\bar{A}_{11} = \frac{\cos^2 \gamma + k_{yz} \sin^2 \gamma}{k_{yz}} \quad \text{and} \quad \bar{A}_{21} = \begin{bmatrix} \frac{(1 - k_{yz}) \sin \gamma \cos \gamma}{k_{yz} \cos \phi} \\ \frac{(1 - k_{yz}) \sin \gamma \cos \gamma \sin \phi}{k_{yz} \cos \phi} \end{bmatrix} \quad (5.36)$$

$$\bar{A}_{12} = \begin{bmatrix} \frac{(1 - k_{yz}) \sin \gamma \cos \gamma}{k_{yz} \cos \phi} & \frac{(1 - k_{yz}) \sin \gamma \cos \gamma \sin \phi}{k_{yz} \cos \phi} \end{bmatrix} \quad (5.37)$$

$$\bar{A}_{22} = \begin{bmatrix} \frac{\sin^2 \gamma + k_{yz} \cos^2 \gamma}{k_{yz} \cos^2 \phi} & \frac{\sin \phi (\sin^2 \gamma + k_{yz} \cos^2 \gamma)}{k_{yz} \cos^2 \phi} \\ \frac{\sin \phi (\sin^2 \gamma + k_{yz} \cos^2 \gamma)}{k_{yz} \cos^2 \phi} & \frac{\sin^2 \phi (\sin^2 \gamma + k_{yz} \cos^2 \gamma)}{k_{yz} \cos^2 \phi} + \frac{1}{k_{xz}} \end{bmatrix} \quad (5.38)$$

The control torques,  $U \in \mathbb{R}^{2 \times 1} = [\hat{T}_{a\alpha}, \hat{T}_{a\gamma}]^T$  is in dimensionless form and is given as  $\hat{T}_{aq} = \left( \frac{T_{aq}}{I_z \Omega^2} \right)$  for  $q = \alpha, \gamma$ . To simplify the control algorithm development, the following assumptions are made with respect to the orientation of the drag plates. It is assumed that  $\beta_2 = -\beta_1$  and  $\beta_4 = -\beta_3$ . Eq. (5.35), is rewritten in the following form,

$$M(q) q'' = F(q, q') + U_a(\beta_1, \beta_3) \quad (5.39)$$

where  $q \in \mathbb{R}^3 = [\phi \ \alpha \ \gamma]^T$ ,  $M(q) \in \mathbb{R}^{3 \times 3}$ ,  $F(q, q')$ ,  $D \in \mathbb{R}^3$ , and  $U_a(\beta_1, \beta_3) = [0 \ \hat{T}_{a\alpha}, \hat{T}_{a\gamma}]^T$ .  $F(q, q')$  represents the vector containing all the nonlinear terms including the Coriolis and centrifugal contributions and is described in Eq. (5.22), and  $M$  is the mass matrix.

Next, we present the design procedure to implement an adaptive sliding mode control for changing the orientation of the drag plates in order to achieve satellite attitude control. The design can be divided into two main steps. First, we design a stable sliding surface and this is followed by the development of the feedback control algorithm that drives the system dynamics to this sliding surface in finite time.

### 5.2.1 Design of Sliding Manifold

The control inputs i.e., the orientation of the drag plates,  $(\beta_i, \text{ for } i = 1 - 4)$ , appears in non-affine nature in the system formulation. A nonlinear control algorithm based on

higher order sliding mode is developed to calculate the orientation of the drag plates. This increase in the order of the system helps in deriving the control law that can extract the angular rates of the drag plates ( $\beta'_i$ ,  $i = 1 - 4$ ) from Eq. (5.39). The corresponding angular orientation of the drag plates can then be obtained by integration of these angular rates. This information is then used in the system dynamics to calculate the torque due to aerodynamic drag. First a sliding surface with order less than the system dynamics is introduced; it is given as

$$S = K_A M \tilde{q}' + K_B \tilde{q} \quad (5.40)$$

where  $\tilde{q}' = q' - q'_d$ , and  $\tilde{q} = q - q_d$  are the state error variables and  $K_A$  and  $K_B$  are positive constants given by

$$K_A = \begin{bmatrix} 0 & P_2 & 0 \\ P_5 & 0 & P_6 \end{bmatrix} \quad \text{and} \quad K_B = \begin{bmatrix} 0 & P_1 & 0 \\ P_3 & 0 & P_4 \end{bmatrix} \quad (5.41)$$

Now a higher order sliding manifold is defined combining  $S$  and its derivative, i.e,  $S'$ , it is given as

$$\sigma = S' + \xi S \quad (5.42)$$

where  $S' = K_A M \tilde{q}'' + (K_A M' + K_B) \tilde{q}'$

### 5.2.2 Adaptive Control Formulation and Stability Analysis

The next stage is the adaptive control law formulation based on Lyapunov stability theorem. The control law that drives the states to be along the sliding manifold,  $\sigma = 0$  for all  $t > t_r$ , can be derived by choosing the Lyapunov candidate function defined as follows:

$$V = \frac{1}{2} \sigma^2 + \frac{1}{2\zeta} \tilde{B}^2 \quad (5.43)$$

where  $V > 0$  and  $\zeta$  is a positive constant. Taking the derivative along the trajectory gives

$$V' = \sigma \sigma' + \frac{\tilde{B} \hat{B}'}{\zeta} \quad (5.44)$$

where  $\sigma' = S'' + \xi S'$ . The control algorithm design is simplified by expressing the system nonlinearities and external disturbances present in system dynamics by using its worst case upper-bound in the controller design. This assumption gives us the following relation:

$$L = K_A F'(q, q') + [K_A M' + K_B] q'' + K_A M'' q' \quad (5.45)$$

It is to be noted that  $L$  contains all the terms including the system nonlinearities, parameter uncertainties and external disturbances, and the upper bound of this lumped disturbances is given by

$$\|L\| \leq d_1 + d_2 \|q\| + d_3 \|q'\| \leq d \quad (5.46)$$

Now, expanding  $\sigma'$  in Eq. 5.44 yields

$$\sigma' = K_A [M q''' + M' q''] + [K_A M' + K_B] q'' + K_A M'' q' \quad (5.47)$$

Here,  $q'''$  represents the derivative of the equations of motion [Eq. 5.39] along its trajectories given by

$$q''' = F'(q, q') + B U'_a \begin{bmatrix} \beta'_1 \\ \beta'_3 \end{bmatrix} \quad (5.48)$$

where  $U'_a = [T'_{a\alpha} \quad T'_{a\gamma}]$ . Substituting for this in Eq. 5.47, we get,

$$\sigma' = K_A B U'_a + K_A F'(q, q') + [K_A M' + K_B] q'' + K_A M'' q' \quad (5.49)$$

Now substituting the preceding equation in Eq. (5.44), along with the consideration on the bounds given in Eq. (5.46), we get

$$V' = \sigma (K_A B U'_a \beta' + \|L\|) + \frac{\tilde{B} \hat{B}'}{\zeta} \quad (5.50)$$

Now considering the parameter estimation error in  $B$  as

$$\tilde{B} = \hat{B} - B \quad (5.51)$$

and expanding Eq. (5.50), we have

$$V' = \sigma \left[ K_A \left( \widehat{B} - \widetilde{B} \right) U'_a \beta' + \|L\| \right] + \frac{\widetilde{B} \widehat{B}'}{\zeta} \quad (5.52)$$

Rearranging the preceding Eq. (5.52) yields

$$V' = \sigma \left[ K_A \widehat{B} U'_a \beta' + \|L\| \right] - \sigma K_A \widetilde{B} U'_a \beta' + \frac{\widetilde{B} \widehat{B}'}{\zeta} \quad (5.53)$$

Now in order to make  $V'$  negative, choose the adaptive law as

$$\widehat{B}' = \zeta \sigma K_A U'_a \beta' \quad (5.54)$$

where  $\zeta$  is the adaptation gain. Also let

$$K_A \widehat{B} U'_a \beta' = -\eta \operatorname{sgn}(\sigma) \quad (5.55)$$

where  $\eta$  is a positive constant and  $\eta \gg \sup \|L\|$ . Substituting Eq. (5.55) and Eq. (5.54) into Eq. (5.53), we have

$$V' = \sigma [-\eta \operatorname{sgn}(\sigma)] = -\eta |\sigma| \quad (5.56)$$

Eq. (5.56) is semi-negative definite, but by using Theorem-3 of LaSalle's principle [LaSalle 1960] it is proved that the system is completely stable and hence the system states converge onto the sliding surface which is the invariant set here. For a system satisfying Eq. (5.56), it can be proved that the time taken ( $t_r$ ) by the state trajectory to move towards and reach the sliding surface is governed by the relation  $|\sigma(t=0)|/c$ , where  $c = (\eta - d)$  and  $d$  is assumed to be a bounded value. From the fact that  $V$  is positive and  $V'$  is negative, it can be stated that  $V$  is decreasing and lower bounded by zero, i.e.,  $V \in L_\infty$ . Hence, it can be inferred from Eq. (5.43) that  $\sigma, \widetilde{B} \in L_\infty$ . Let us define  $\widetilde{B} U'_a \beta' = D$ . Since all the states remain bounded we can conclude that  $\|D\| < d$ . Eq. (5.56) can now be rewritten as

$$V' = \sigma (\sigma' + D) = -\eta |\sigma| \quad (5.57)$$

Two possible cases are to be considered here:  $\sigma(t=0) < 0$  and  $\sigma(t=0) > 0$ . For the first case of  $\sigma(t=0) < 0$ , Eq. (5.57) reduces to

$$\sigma' \geq c \quad (5.58)$$

where  $c = \eta - d$ . The reaching time ( $t_r$ ) in this case is derived as

$$\frac{\sigma(t=t_r) - \sigma(t=0)}{t_r} \leq c \Rightarrow t_r \leq \frac{-\sigma(t=0)}{c} \quad (5.59)$$

where  $\sigma(t=t_r) = 0$  as per the definition. For the second case of  $\sigma(t=0) > 0$ , Eq. (5.57) yields

$$\sigma' \leq c \quad (5.60)$$

Hence, the reaching time ( $t_r$ ) in this case is obtained as

$$\frac{\sigma(t=t_r) - \sigma(t=0)}{t_r} \leq c \Rightarrow t_r \leq \frac{\sigma(t=0)}{c} \quad (5.61)$$

Combining both the cases and referring to Eqs. (5.59) and (5.61), the reaching time, ( $t_r$ ), is given by

$$t_r \leq \frac{|\sigma(t=0)|}{c} \quad (5.62)$$

Next, Eq. (5.55) is rearranged to derive the control law as

$$\beta' = -\frac{1}{K_A \hat{B} U'_a} [\eta \operatorname{sgn}(\sigma)] \quad (5.63)$$

A boundary layer is introduced in the control input, Eq. (5.63), formulation to remove the instantaneous discontinues switching and it is given by

$$\beta' = -\frac{1}{K_A \hat{B} U'_a} \eta \left[ \frac{\sigma}{|\sigma| + \delta} \right] \quad (5.64)$$

where  $\delta$  is the width of the boundary layer.

**Remark 5.1:** The Euler angles  $\gamma$ ,  $\phi$ , and  $\alpha$  are limited to the ranges  $-\pi < \gamma < \pi$ ,

$-\frac{\pi}{2} < \phi < \frac{\pi}{2}$ , and  $-\pi < \alpha < \pi$ . Therefore, the Lyapunov analysis guarantees stability for any initial condition that avoids singularities due to  $\phi = \pm\frac{\pi}{2}$ .

## 5.3 Performance Evaluation

To study the effectiveness and performance of the proposed adaptive controller, the detailed system response is numerically simulated using the set of governing equations of motion, given by Eq.(5.30) along with proposed adaptive control law given by Eq.(5.64). The integration is carried out Matlab using the fourth order Runge-Kutta solver. The simulation parameters used are shown in Table 5.1.

Based on the values of the satellite moment of inertias, the nondimensional parameters  $k_1$  and  $k_2$  given in Eqs. (5.25) has values of 0.3 and 0.2 respectively. The control law is developed based on these values. The effect of varying satellite moments of inertia are examined by implementing the changes in the moments only in the satellite dynamic model.

### 5.3.1 Nominal Performance

The first case to be evaluated is the stabilization of the satellite in a circular orbit from the large initial disturbances about its three axes given by

$$\begin{aligned}\alpha_0 &= \phi_0 = \gamma_0 = 60 \text{ deg} \\ \alpha'_0 &= \phi'_0 = \gamma'_0 = 2.5 \text{ deg / sec}\end{aligned}\tag{5.65}$$

Fig. 5.2 illustrates the satellite attitude response subjected to large initial errors. It can be observed that the adaptive controller performs very well with no overshoot. The Euler angles asymptotically approach zero from the non-zero initial conditions, and the maximum deflection of the drag plates of nearly  $15^\circ$  can be observed during the transient stage.

Fig. 5.3 shows the angular rates and the adaptive parameter  $\hat{B}$ . The adaptive parameter and the angular velocities, except for  $\omega_z$ , converge to zero as the satellite reaches steady state. The angular velocity of the satellite about the  $z$ -axis converges to a value equal to  $0.0011 \text{ rad/sec}$ , which is the orbital frequency of the satellite about the Earth.

Table 5.1: System parameters.

Parameters	Values
Moment of Inertia $[I_{xx} \ I_{yy} \ I_{zz}]$ (kg m <sup>2</sup> )	[15 17 20]
Orbital Parameters	
$R$ (km)	6878
$\mu$ (km <sup>3</sup> /s <sup>2</sup> )	$3.986 \times 10^5$
$\rho$ (kg/m <sup>3</sup> )	$6.967 \times 10^{-13}$
Free Molecular Aerodynamic Model Parameters	
$s$	5
$\sigma_n$	0.85
$\sigma_t$	0.9
$T_a$ (K)	1000
$T_s$ (K)	300
$C_D$	2.0
$A$ (m <sup>2</sup> )	1.0
$r$ (m)	0.5
Control Parameters	
$[P_1 \ P_2 \ P_3]$	[4.5 4.5 4.5]
$[P_4 \ P_5 \ P_6]$	[-2.1 1.5 -2.5]
$\eta$	0.5
$\delta$	0.01
$\zeta$	200
Initial Estimates	
$\rho_0$ (kg/m <sup>3</sup> )	$1.454 \times 10^{-13}$
$C_{D_0}$	1.8
$A_0$ (m <sup>2</sup> )	0.5

### 5.3.2 Variations in Mass Moment of Inertia

In the nominal case the the values of both  $k_1$  and  $k_2$  were positive, signifying the stable gravity gradient configuration. Now, the performance of the proposed adaptive control algorithm in the presence of variations on the satellite moments of inertia is examined. First, a satellite in an axially symmetric configuration is considered, then the performance of the proposed system as affected by the product of inertia terms ( $I_{xy}$ ,  $I_{xz}$ ,  $I_{yz}$ ) is evaluated, and finally the efficacy of the adaptive control algorithm for a satellite in an unstable gravity gradient configuration is examined. The inertia matrix for the first and second cases is as

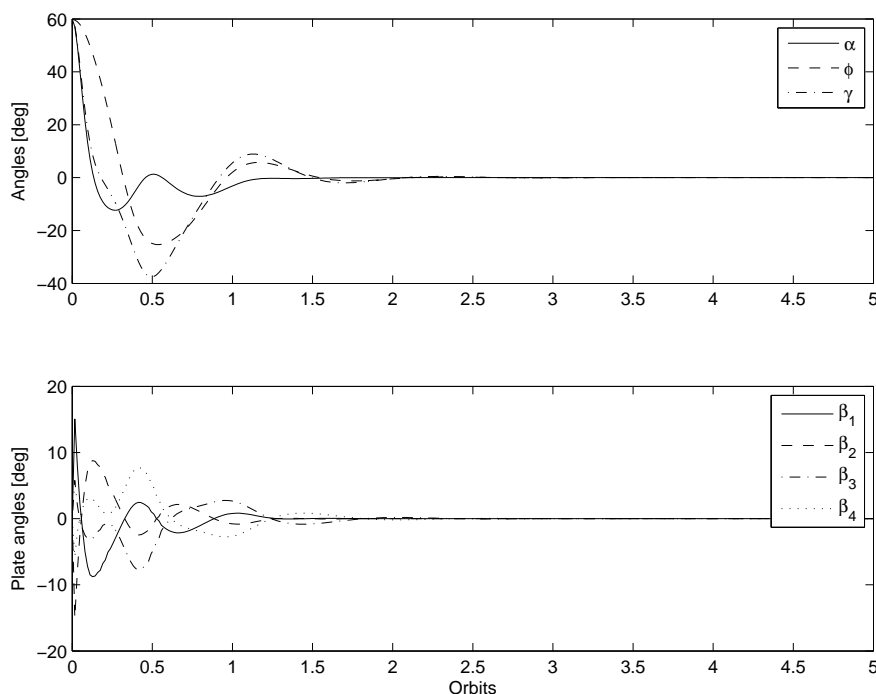


Figure 5.2: Performance of the adaptive sliding mode controller during attitude stabilization,  $k_1 = 0.3$ ,  $k_2 = 0.2$ .

Table 5.2: Variations in satellite moments of inertia

Axisymmetric	Products of Inertia
$\begin{bmatrix} 17 & 0 & 0 \\ 0 & 17 & 0 \\ 0 & 0 & 20 \end{bmatrix}$	$\begin{bmatrix} 15 & 0.5 & 0.9 \\ 0.5 & 17 & 2 \\ 0.9 & 2 & 20 \end{bmatrix}$

shown in Table 5.2.

The system performance for an axis-symmetric satellite is shown in Fig. (5.4). The attitude response converges asymptotically and remains identical to the previous case. Fig. (5.5) shows the corresponding angular rates and the adaptive parameter  $\hat{B}$ .

We next examine the performance of the proposed control technique on a satellite model containing the product of inertia terms. The attitude of the satellite is stabilized (Fig. 5.6) It can be observed that the product of inertia terms does have an adverse effect on the satellite as the steady state satellite attitude is non zero.

The performance of the control method for a satellite in an unstable gravity gradient

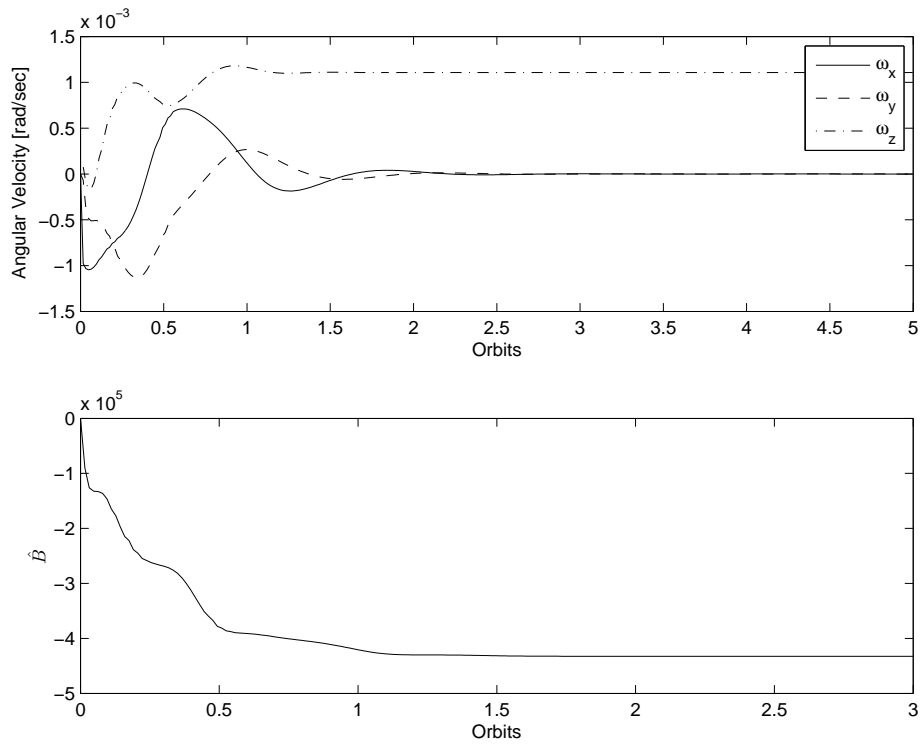


Figure 5.3: Response of angular velocity and estimated adaptive parameter,  $k_1 = 0.3$ ,  $k_2 = 0.2$ .

configuration is now evaluated. The values of the nondimensional parameters are taken as  $k_1 = 0.1$  and  $k_2 = -0.2$  for an inertia matrix in this configuration given by

$$I = \begin{bmatrix} 15 & 0 & 0 \\ 0 & 20 & 0 \\ 0 & 0 & 17 \end{bmatrix} \quad (5.66)$$

Figure (5.7) illustrates the effectiveness of the proposed control methodology in stabilizing the attitude of a satellite in an unstable configuration. The attitude is stabilized without any overshoot and the drag plates exhibits the maximum deflection of  $10^\circ$  during the transient stage. It is to be noted that, these variations in the inertia of the satellite is unknown to the the control law which is developed based on the nominal value.

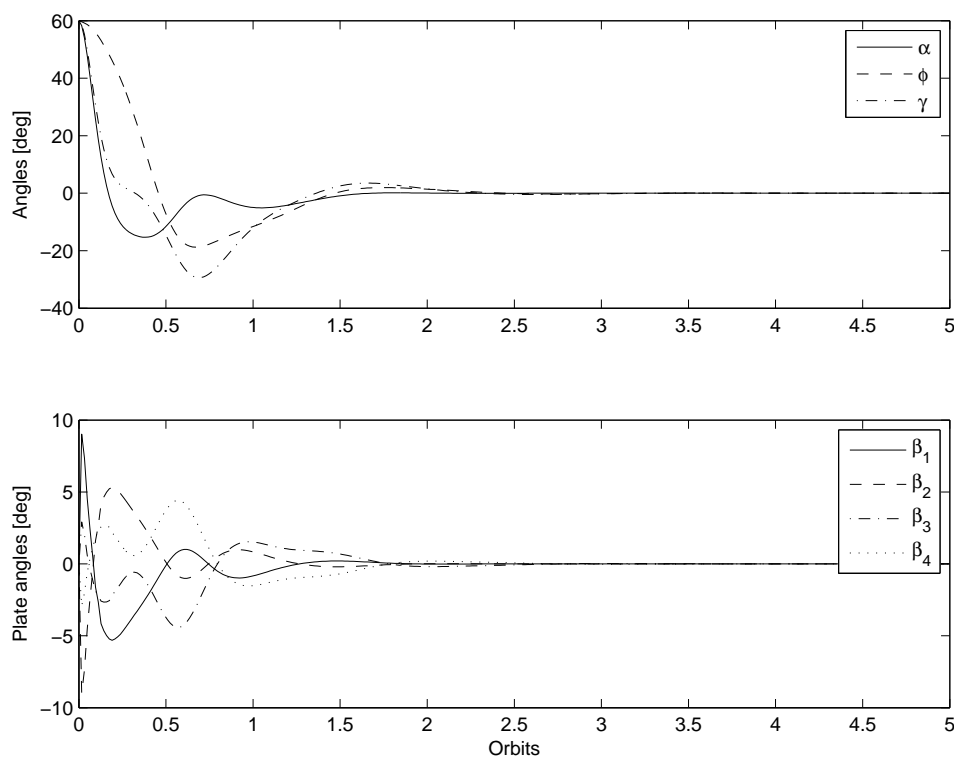


Figure 5.4: Performance of the adaptive sliding mode controller during attitude stabilization,  $k_1 = 0.177$ ,  $k_2 = 0.177$ .

### 5.3.3 Eccentricity and External Disturbances

First, the effectiveness of the control strategy for satellite in an elliptical orbit is studied. The orbital eccentricity is increased from  $e = 0.01$  (Fig. 5.8) to  $e = 0.1$  (Fig. 5.9). The

state error in the pitch axis is bounded by  $|\alpha|_{\max} = 0.51^\circ$ , roll axis by  $|\phi|_{\max} = 0.15^\circ$  and the yaw axis by  $|\gamma|_{\max} = 0.065^\circ$ . The maximum deterioration is observed in the pitch response as compared to the previous numerical results. This is expected as the orbital eccentricity directly affects the pitch motion of the satellite. The drag plates in the pitch axis continuously maneuvers to counter this disturbance due to eccentricity. The maximum deflection of the drag plates is observed in the transient stage and the steady state deflection is nearly  $5^\circ$ . Overall the satellite attitude remains stabilized within reasonable limits even in elliptic orbits using the proposed methodology.

Finally, the effect of external disturbance on the performance of the system is verified. The system may experience external disturbance torques due to several factors including

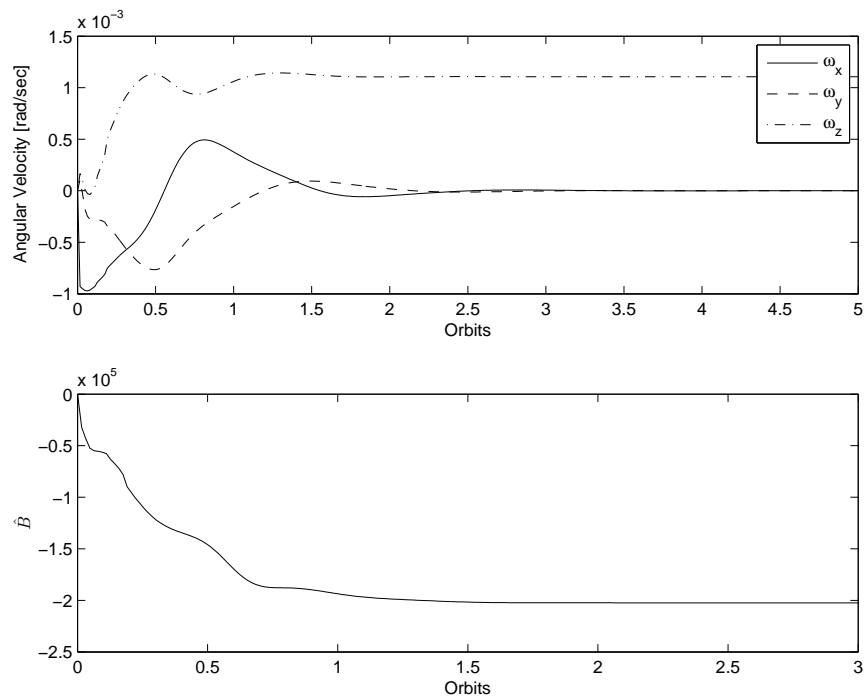


Figure 5.5: Response of angular velocity and estimated adaptive parameter,  $k_1 = 0.177$ ,  $k_2 = 0.177$ .

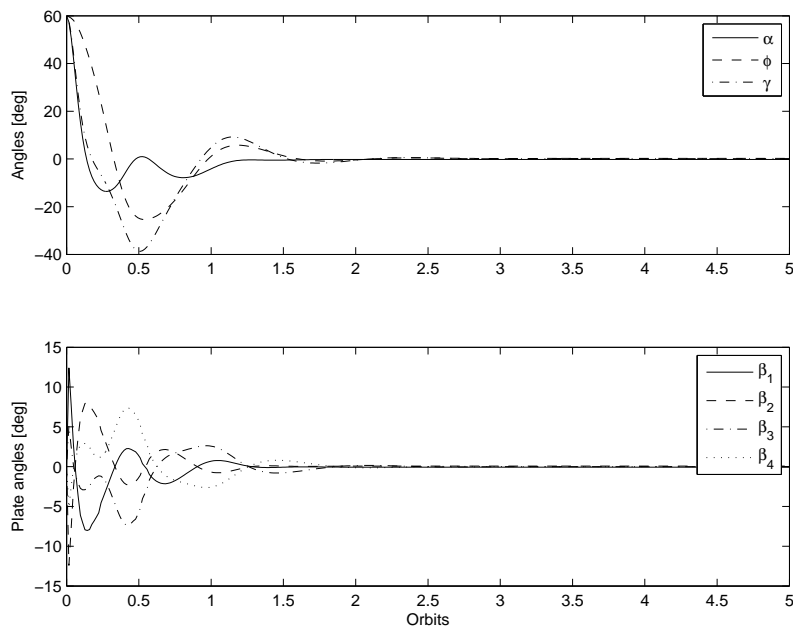


Figure 5.6: Performance of the adaptive sliding mode controller during attitude stabilization,  $k_1 = 0.3$ ,  $k_2 = 0.2$  with product of inertia terms.

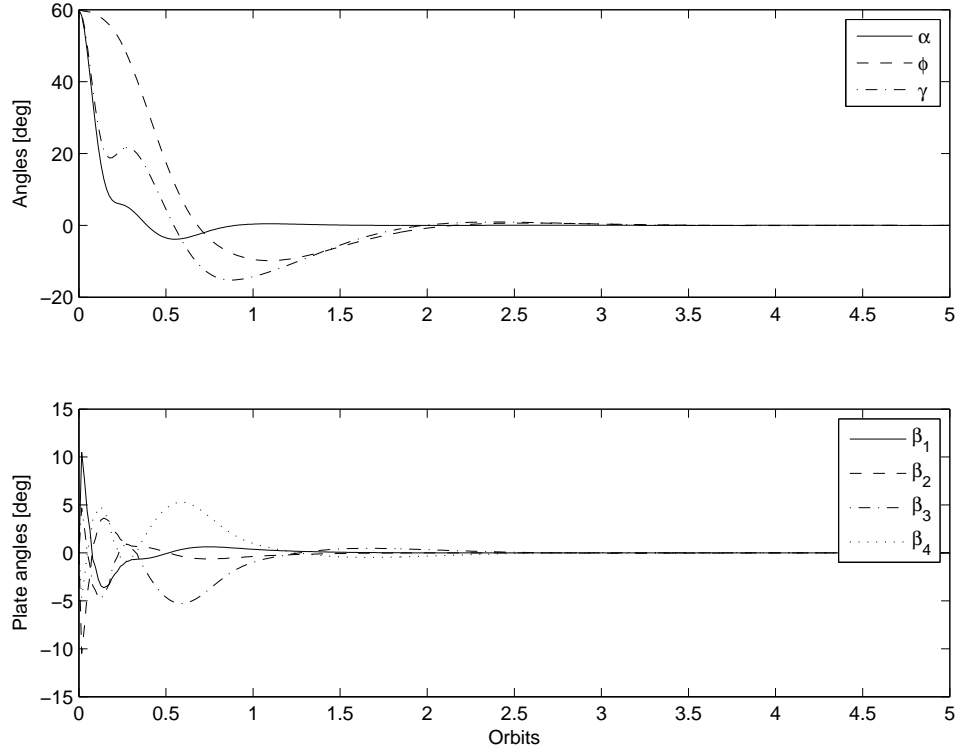


Figure 5.7: Response of angular velocity and estimated adaptive parameter,  $k_1 = 0.1$ ,  $k_2 = -0.2$ .

solar radiation pressure and other environmental forces. The disturbances due to solar radiation pressure is more significant and can be expressed as (in Nm) [Kaplan 1976]

$$\begin{bmatrix} T_{s\alpha} \\ T_{s\phi} \\ T_{s\gamma} \end{bmatrix} = S_f \begin{bmatrix} (1 \times 10^{-4}) \cos(\dot{\theta}t) \\ (2 \times 10^{-5})[1 - 2 \sin(\dot{\theta}t)] \\ (5 \times 10^{-5}) \cos(\dot{\theta}t) \end{bmatrix} \quad (5.67)$$

Here  $T_{s_j}$  for  $j = \alpha, \phi, \gamma$  represents the disturbance torque due to solar radiation pressure. It can be observed from Fig. (5.10) that the controller is able to regulate the satellite attitude by the maneuvering of the drag plates, and hence establishes the robustness of the proposed methodology to time varying disturbances external disturbance. The above results bring out the powerful features of the proposed adaptive control algorithm. The performance of the controller does not deteriorate even when the system parameters are changing and yet provides excellent attitude response.

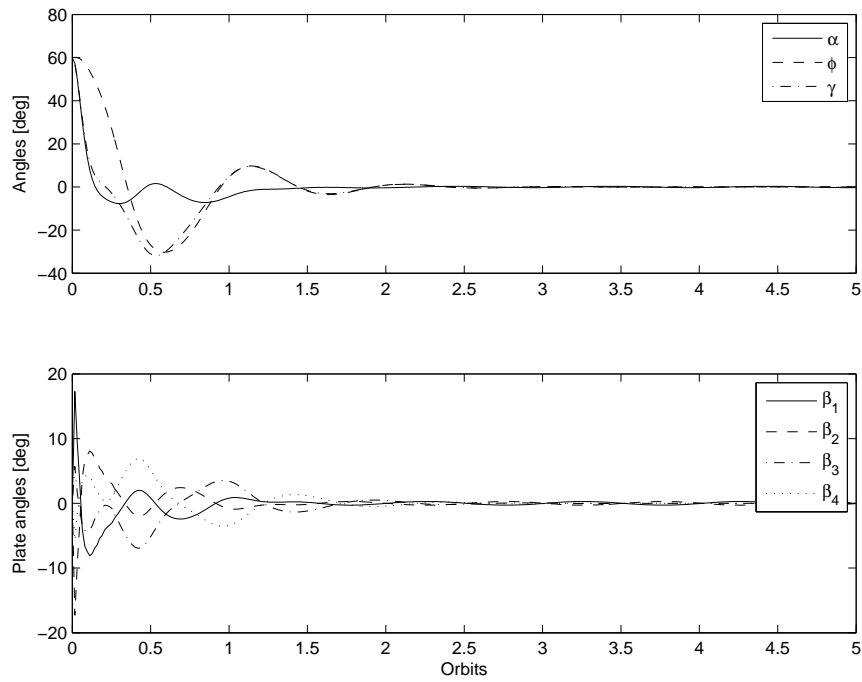


Figure 5.8: Performance of the adaptive sliding mode controller during attitude stabilization,  $e=0.01$

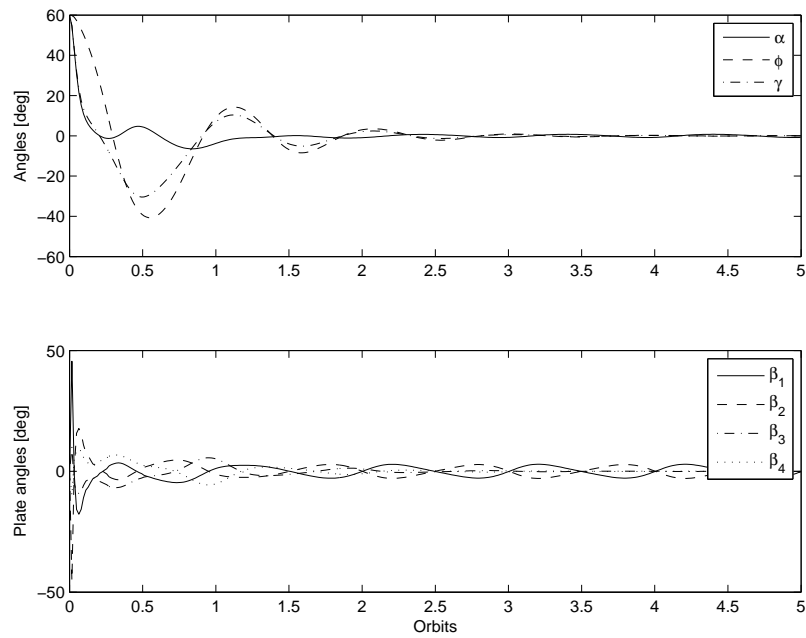


Figure 5.9: Performance of the adaptive sliding mode controller during attitude stabilization,  $e=0.1$

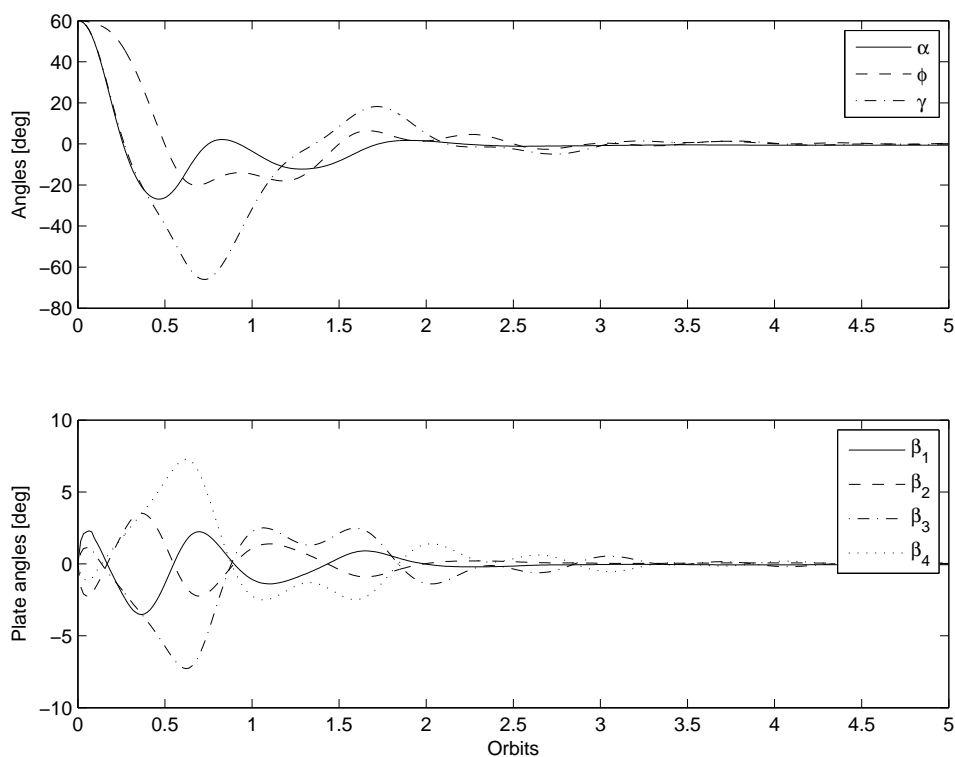


Figure 5.10: Performance of the adaptive sliding mode controller during attitude stabilization in the presence of external disturbances

## 5.4 Summary

This chapter examines the feasibility of three axis satellite attitude control using aerodynamic drag. The proposed system configuration consists of a satellite with two pairs of oppositely placed drag plates. Attitude maneuvering and stabilization are accomplished by suitable rotation of these drag plates. Such a configuration has not been proposed in the existing literature. This system configuration provides explicit control authority only along its two principal axes, i.e., the pitch and yaw axes. Complete three axis attitude control using aerodynamic drag is achieved by the application of the control law developed based on sliding mode theory. The controller enables the satellite to achieve any arbitrary orientation. The performance of the control strategy in attitude stabilization is examined in detail using high-fidelity nonlinear system model. Unlike earlier results on the use of aerodynamic drag for satellite attitude control, numerical simulation results were obtained under many scenarios including presence of external disturbances, high initial attitude rates

and uncertainty in the mass moments of inertia and the the proposed control scheme illustrated excellent performance in successfully regulating the satellite attitude motion in each case. The satellite attitude was observed to be stabilized within  $0.2^\circ$  in all the cases except for the elliptic orbit ( $e = 0.1$ ) and stands as a good candidate for use in future space missions.

## CHAPTER 6

# Satellite Attitude Control Using Solar Radiation Pressure

---

**I**N Chapter 5, the feasibility of performing satellite attitude control using aerodynamic drag was studied and evaluated. In this chapter three axis satellite attitude control using solar radiation pressure is analyzed. An adaptive nonlinear control design based on the theory of sliding mode is proposed to control the attitude of a satellite using solar radiation pressure. The system comprises of a satellite with two pairs of oppositely placed solar flaps. The nonlinear analytical model describing the system is used to derive an adaptive control law, based on Lyapunov stability theorem, in the presence of unknown, slow-varying external disturbances. This control law suitably rotates the solar flaps to achieve desired satellite attitude performance. The detailed numerical simulation of the governing nonlinear system equations of motion including the effects of various system parameters on the controller performance establishes the feasibility of the proposed control strategy. The numerical results show the robustness of the proposed adaptive control scheme in controlling the satellite attitude in the presence of uncertainties and external disturbances.

The system model and its equations of motion are presented in Section 6.1. Section 6.2 presents the closed-loop nonlinear control law based on SMC along with the stability analysis of the closed-loop system. In Section 6.3 numerical simulation is carried out for a detailed assessment of the proposed attitude control strategy. The effects of various system parameters on the performance of the controller are examined and the effectiveness of the proposed controller in the presence of parameter uncertainties and external disturbances is studied. Finally, the findings of the present study are summarized in Section 6.4.

## 6.1 Proposed System Model and Equations of Motion

The nonlinear equations of motion of the rigid body satellite derived in Section 5.1 is discussed here in brief for clarity. The system model comprises of a satellite with two pairs of oppositely placed light-weight solar flaps along the  $y$  and  $z$  axes of the satellite as shown in Fig. (6.1). The system center of mass lies on the center of mass of the satellite. The LVLH orbital reference frame,  $\mathcal{L} - x_0 y_0 z_0$ , has its origin fixed at the center of mass of the satellite. The  $x_0$ -axis points along the local vertical, the  $z_0$ -axis is normal to the orbital plane, and the  $y_0$ -axis points along the orbit direction. The corresponding principal body-fixed coordinate frame of the satellite is denoted by  $O - x y z$ . The nodal line represents the reference line in orbit for the measurement of the true anomaly (eccentric orbit) or angle  $\theta$  (circular orbit). For the solar flaps along the  $y$ -axis, its normal considered initially aligned with the  $x$ -axis is rotated by an angle  $\beta$  about the  $z$ -axis (normal to the orbit plane); and for the pair of solar flaps along the  $z$ -axis with its normal initially aligned with the  $x$ -axis is rotated by an angle  $\varsigma$  about the  $y$ -axis.

### 6.1.1 Solar Radiation Pressure Model

The force acting on the solar flap- $j$ ,  $j = 1-4$  due to SRP is given by

$$\vec{F}_{SRP} = 2pA_j |(\vec{s} \cdot \vec{n})| \{b_1 \vec{s} + [b_2 (\vec{s} \cdot \vec{n}) + b_3] \vec{n}\} \quad (6.1)$$

where  $\vec{s}$  represents the Sun vector,  $\vec{n}$ , is the solar flap normal vector,  $\zeta_s$ , is the specular reflection factor, and other coefficients are given by,

$$b_1 = \frac{1}{2}(1 - \zeta_s \rho_s) \quad (6.2)$$

$$b_2 = \zeta_s \rho_s \quad (6.3)$$

$$b_3 = \frac{1}{2} \left[ B_f(1 - \zeta_s) \rho_S + (1 - \rho_s) \frac{e_f B_f - e_b B_b}{e_f + e_b} \right] \quad (6.4)$$

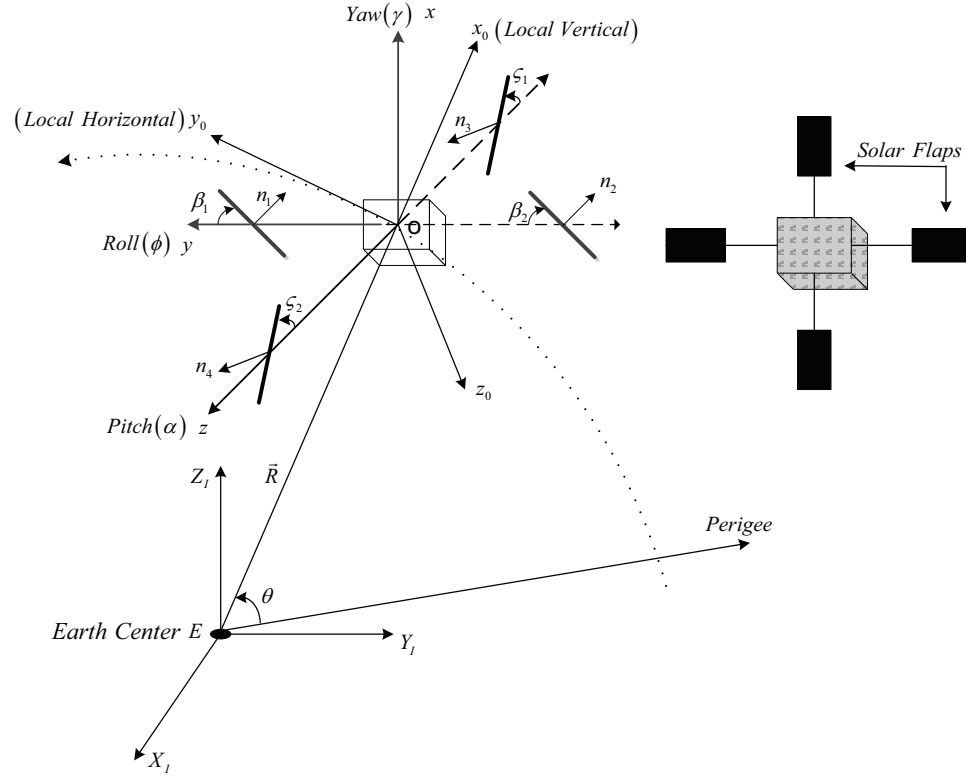


Figure 6.1: Configuration of the proposed solar controller.

Assuming that the Sun is fixed in the inertial space, the Sun vector,  $\vec{s}$ , on the solar flaps, is obtained in the satellite body fixed reference frame, S-XYZ, as

$$\vec{s} = s_x \hat{i} + s_y \hat{j} + s_z \hat{k} \quad (6.5)$$

From Fig. (6.2), the transformation to the body fixed frame from the Sun centered inertial frame is obtained as  $[s_x \ s_y \ s_z]^T = C^{B/L} \cdot C^{B/I} \cdot C^{I/S}$ . Here,  $C^{B/L}$  represents the transformation matrix from the orbital frame to the body fixed frame and is given by Eq. 5.1,  $C^{B/I}$  represents the transformation matrix from the geocentric inertial to the orbital frame given by,

$$\begin{bmatrix} c(ot) c(\Omega) - s(ot) s(\Omega) c(i - \varepsilon_s) & -s(ot) c(\Omega) - c(ot) s(\Omega) \cos(i - \varepsilon_s) & s(\Omega) s(i - \varepsilon_s) \\ c(ot) s(\Omega) + s(ot) c(\Omega) c(i - \varepsilon_s) & -s(ot) s(\Omega) + c(ot) c(\Omega) \cos(i - \varepsilon_s) & -c(\Omega) s(i - \varepsilon_s) \\ s(ot) s(i - \varepsilon_s) & c(ot) s(i - \varepsilon_s) & c(i - \varepsilon_s) \end{bmatrix}$$

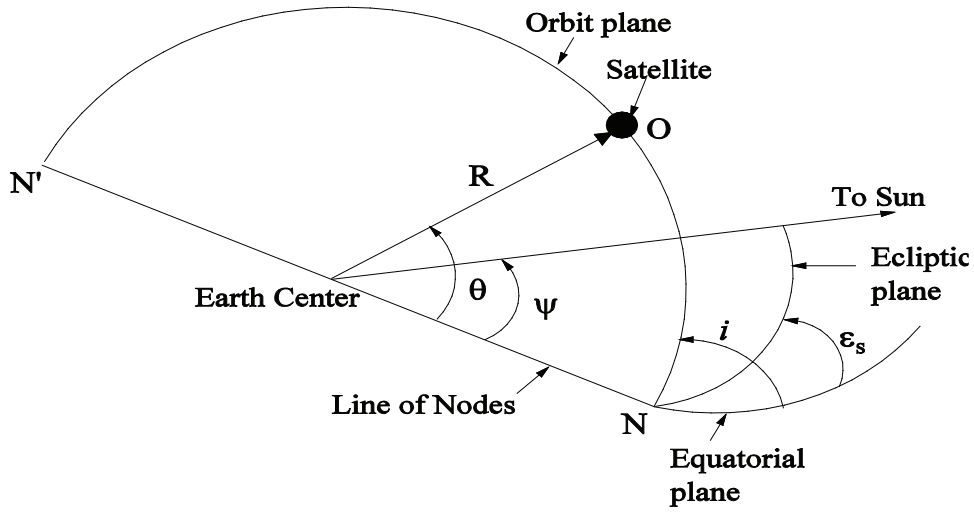


Figure 6.2: Geometry of orbit motion of rigid satellite.

where  $ot$  represents  $(\omega + \theta)$ ,  $c()$  and  $s()$  represents  $\cos()$  and  $\sin()$  respectively.  $C^{I/S}$  represents the transformation from the Sun centered inertial to the geocentric inertial frame as follows,

$$\begin{bmatrix} \cos \psi & -\sin \psi & 0 \\ \sin \psi & \cos \psi & 0 \\ 0 & 0 & 1 \end{bmatrix}$$

where  $\psi$  is the solar aspect angle. The vector normal to the solar flap- $j$ ,  $\vec{n}_j$  is given by

$$\vec{n}_j = [\cos \beta_j] \hat{i} + [\sin \beta_j] \hat{j}, \quad j = 1, 2 \quad (6.6)$$

$$\vec{n}_j = [\cos \varsigma_j] \hat{i} + [\sin \varsigma_j] \hat{k}, \quad j = 3, 4 \quad (6.7)$$

Here  $\beta$  and  $\varsigma$  represents the orientation of the solar flaps. Thus, the torque exerted by the solar flap- $j$  on the satellite is obtained as

$$\vec{T}_{sj} = \vec{r}_j \times \vec{F}_{sj} = r_j \hat{j} \times \vec{F}_{sj}, \quad j = 1, 2 \quad (6.8)$$

$$\vec{T}_{sj} = \vec{r}_j \times \vec{F}_{sj} = r_j \hat{k} \times \vec{F}_{sj}, \quad j = 3, 4 \quad (6.9)$$

Considering the proposed system configuration along with the Eqs. (6.8) and (6.9), it can be inferred that control torques available only about the pitch ( $T_{s\alpha}$ ) and roll ( $T_{s\phi}$ ) axes. But we make use of the coupling between the roll and yaw axes to achieve complete three axis satellite attitude control. Next we look at the formulation of the complete equations of motion of the proposed system.

### 6.1.2 Equations of Motion

The governing nonlinear coupled differential equations of motion of the system are obtained as

$$\begin{bmatrix} \ddot{\alpha} \\ \ddot{\phi} \\ \ddot{\gamma} \end{bmatrix} = \begin{bmatrix} N_{11} & N_{12} & N_{13} \\ N_{21} & N_{22} & N_{23} \\ N_{31} & N_{32} & N_{33} \end{bmatrix} \left\{ \begin{bmatrix} F_{\alpha} \\ F_{\phi} \\ F_{\gamma} \end{bmatrix} + \begin{bmatrix} T_{s\alpha} \\ T_{s\phi} \\ T_{s\gamma} \end{bmatrix} \right\} \quad (6.10)$$

The nonlinear terms in the matrix  $N$  and  $F_q$ , for  $q = [\alpha, \phi, \gamma]$ , were provided in the previous chapter [Eq. (5.23)] and are not repeated here for brevity. Following a similar approach of nondimensionalization as in the previous chapter, the governing nonlinear equations of motion of the system can be written in the matrix notation as follows

$$q'' = M(q, k_{xz}, k_{yz})[F(q, q', e, k_{xz}, k_{yz}) + \hat{T}_f] \quad (6.11)$$

where  $M(q, k_{xz}, k_{yz}) \in \mathbb{R}^{3 \times 3}$  and  $F(q, q', e, k_{xz}, k_{yz}) \in \mathbb{R}^{3 \times 1}$  are matrices containing nonlinear functions, and  $\hat{T}_f \in \mathbb{R}^3 = [\hat{T}_{s\alpha}, \hat{T}_{s\phi}, \hat{T}_{s\gamma}]^T$  corresponds to the dimensionless control torques. The nondimensionalized torque due to SRP is given by,

$$\hat{T}_{sq} = \frac{(1 - e^2)^3}{(1 + e \cos \theta)^3} \left( \frac{T_{sq}}{I_z \Omega^2} \right) = \frac{(1 - e^2)^3}{(1 + e \cos \theta)^3} \begin{bmatrix} \hat{T}_{s\alpha} \\ \hat{T}_{s\phi} \\ \hat{T}_{s\gamma} \end{bmatrix}$$

In this proposed system configuration, the control torques  $\hat{T}_{s\alpha}$  and  $\hat{T}_{s\phi}$  are obtained using SRP as given by Eqs.(6.8) and (6.9), but the torque component  $\hat{T}_{s\gamma}$  equals to zero.

## 6.2 Design of Control Law

In this section, an adaptive control law based on sliding mode technique is designed. Parameter uncertainties are associated with the SRP stabilized system, and these uncertainties can cause numerous problems in the control tasks and lead to inaccuracy and instability of the control system. Hence an adaptive control methodology is required to achieve consistent stable performance. The unknown parameters are estimated online and used in the feedback control law. The control inputs are the orientation of the two sets of solar flaps attached to the satellite. Considering Eqs. (6.1) through (6.9) and (6.10), it is evident that it is difficult to extract the angular rotations of the solar flaps from the coupled equations of motion. But if we choose the angular rates as the control inputs, the corresponding angular orientation of the solar flaps can be obtained by integrating the angular rates. Hence, to facilitate the control law design, the state space representation of the system can be formulated as follows,

$$\begin{bmatrix} x_1' \\ x_2' \end{bmatrix} = \begin{bmatrix} \bar{A}_{11} & \bar{A}_{12} \\ \bar{A}_{21} & \bar{A}_{22} \end{bmatrix} \left\{ \begin{bmatrix} F_1 \\ F_2 \end{bmatrix} + \begin{bmatrix} 0 \\ U_a \end{bmatrix} + \begin{bmatrix} d_1 \\ d_2 \end{bmatrix} \right\} \quad (6.12)$$

Here  $x_1 = \gamma'$ ,  $x_2 = [\alpha', \phi']$ ,  $U_a \in \mathbb{R}^{2 \times 1} = [\hat{T}_{s\alpha}, \hat{T}_{s\phi}]^T$ ,  $d_1$  and  $d_2$  represents the external disturbances,  $F_1 = F_\gamma$  and  $F_2 = [F_\alpha, F_\phi]^T$ .

$$\bar{A}_{11} = \frac{\sin^2 \phi (\sin^2 \gamma + k_{yz} \cos^2 \gamma)}{k_{yz} \cos^2 \phi} + \frac{1}{k_{xz}} \quad \text{and} \quad \bar{A}_{12} = \begin{bmatrix} \frac{\sin \phi (\sin^2 \gamma + k_{yz} \cos^2 \gamma)}{k_{yz} \cos^2 \phi} & \frac{(1 - k_{yz}) \sin \gamma \cos \gamma \sin \phi}{k_{yz} \cos \phi} \end{bmatrix}$$

$$\bar{A}_{12} = \bar{A}_{21}^T \quad \text{and} \quad \bar{A}_{22} = \begin{bmatrix} \frac{\sin^2 \gamma + k_{yz} \cos^2 \gamma}{k_{yz} \cos^2 \phi} & \frac{(1 - k_{yz}) \sin \gamma \cos \gamma}{k_{yz} \cos \phi} \\ \frac{(1 - k_{yz}) \sin \gamma \cos \gamma}{k_{yz} \cos \phi} & \frac{\cos^2 \gamma + k_{yz} \sin^2 \gamma}{k_{yz}} \end{bmatrix}$$

To simplify the control algorithm development, the following assumptions are made with respect to the orientation of the solar flaps. It is assumed that  $\beta_2 = -\beta_1$  and  $\varsigma_2 = -\varsigma_1$ , also we assume that the cross-sectional area of the solar flaps and the distance between the system center of mass O and the center of pressure for both sets of solar flaps are the same (i.e.  $A_j = A$ ,  $r_j = r$  for  $j = 1, 2, 3, 4$ ). Now assuming the solar flaps to be highly reflective surface (i.e.,  $\rho_d = 0$ ; no absorption, specular reflection only,  $\rho_t = 0$ , no transitivity as well),

the force on the flaps due to SRP can be written as

$$\vec{F}_s = 2\rho_s p A |\vec{s} \cdot \vec{n}| (\vec{s} \cdot \vec{n}) \vec{n} \quad (6.13)$$

The corresponding torque due to SRP can be expressed as

$$\vec{T}_{sj} = \vec{r}_j \times \vec{F}_{sj} = r_j \hat{j} \times 2\rho_s p A (|\vec{s} \cdot \vec{n}| (\vec{s} \cdot \vec{n}) \vec{n}), \quad j = 1, 2 \quad (6.14)$$

$$\vec{T}_{sj} = \vec{r}_j \times \vec{F}_{sj} = r_j \hat{k} \times 2\rho_s p A (|\vec{s} \cdot \vec{n}| (\vec{s} \cdot \vec{n}) \vec{n}), \quad j = 3, 4 \quad (6.15)$$

The torque equations are then converted into dimensionless form by making use of  $C_{srp} = \frac{2\rho_s p A r}{I_z \Omega^2}$ . Now, Eq. (6.12) is rewritten in the following form,

$$M(q) q'' = F(q, q') + U_a(\beta_1, \varsigma_1) \quad (6.16)$$

where  $q \in \mathbb{R}^3 = [\gamma \ \alpha \ \phi]^T$ ,  $M(q) \in \mathbb{R}^{3 \times 3}$ ,  $F(q, q') \in \mathbb{R}^3$ , and  $U_a(\beta_1, \varsigma_1) = [0 \ \hat{T}_{s\alpha} \ \hat{T}_{s\phi}]^T$ .  $F(q, q')$  represents the vector containing all the nonlinear terms including the Coriolis and centrifugal contributions, and  $M$  is the mass matrix. The basic objectives for the design of the control law are a) To drive the system errors to zero without oscillations or overshoots; b) To compensate external disturbances from the beginning.

First we design the linear sliding manifold which guarantees the desired dynamic behavior for the nominal system in the presence of uncertainties and disturbances, and this is followed by design of the sliding mode control law such that the system states are driven to this sliding plane and the system remains stable.

### 6.2.1 Design of Sliding Manifold

For the proposed system given by Eq. (6.16), the orientation of the solar flaps, ( $\beta_i$  and  $\varsigma_i$ , for  $i = 1, 2$ ), are the control inputs and appear in non-affine nature in the system formulation. Hence a nonlinear control algorithm based on higher order sliding mode is developed. Increasing the order of the system helps in extracting the angular rates of the solar flaps ( $\beta'_i, \varsigma'_i$ ,  $i = 1, 2$ ) from Eq. 6.16. The corresponding angular orientation of the

solar flaps is obtained by integration of these angular rates. These control inputs are then used in the system dynamics to calculate the torque due to SRP. First a sliding surface with order less than the system dynamics is introduced, it is given as

$$S = K_A M \tilde{q}' + K_B \tilde{q} \quad (6.17)$$

where  $\tilde{q}' = q' - q'_d$ , and  $\tilde{q} = q - q_d$  are the state error variables and  $K_A$  and  $K_B$  are positive constants given by

$$K_A = \begin{bmatrix} 0 & P_2 & 0 \\ P_5 & 0 & P_6 \end{bmatrix} \quad \text{and} \quad K_B = \begin{bmatrix} 0 & P_1 & 0 \\ P_3 & 0 & P_4 \end{bmatrix} \quad (6.18)$$

Now a higher order sliding manifold is defined combining  $S$  and its derivative, i.e,  $S'$ ; it is given as,

$$\sigma = S' + \xi S \quad (6.19)$$

where  $S' = K_A M \tilde{q}'' + (K_A M' + K_B) \tilde{q}'$ .

### 6.2.2 Adaptive Control Formulation and Stability Analysis

In this section the adaptive control algorithm is formulated and its stability is analyzed. The time varying and uncertain parameter is the the solar parameter  $C_{srp}$ , hence it is assumed to be unknown and is estimated online and then used in the control algorithm. Using Lyapunov stability theorem, the control law that drives the system states to be along the sliding manifold,  $\sigma = 0$  for all  $t > t_r$ , is derived. Consider the Lyapunov candidate function defined as follows,

$$V = \frac{1}{2} \sigma^2 + \frac{1}{2\zeta} \tilde{C}_{srp}^2 \quad (6.20)$$

where  $V > 0$  and  $\zeta$  is a positive constant.  $\tilde{C}_{srp} = \hat{C}_{srp} - C_{srp}$  which is the true value - estimate value. Taking the derivative along the trajectory gives,

$$V' = \sigma \sigma' + \frac{\tilde{C}_{srp} \hat{C}'_{srp}}{\zeta} \quad (6.21)$$

where  $\sigma' = S'' + \xi S'$ . Next, the system nonlinearities and external disturbances present in system dynamics are expressed using its worst case upper-bound in the controller design, leading to the following relation,

$$\|L\| \leq d_1 + d_2\|q\| + d_3\|q'\| \leq d \quad (6.22)$$

Now, expanding  $\sigma'$  in Eq. (6.21) yields,

$$\sigma' = K_A[Mq''' + M'q''] + [K_A M' + K_B]q'' + K_A M''q' \quad (6.23)$$

where  $q'''$  represents the derivative of the equations of motion, Eq. (6.16) along its trajectories given by

$$q''' = F'(q, q') + C_{srp} U'_a \begin{bmatrix} \beta'_1 \\ \varsigma'_1 \end{bmatrix} \quad (6.24)$$

where  $U'_a = \begin{bmatrix} \hat{T}'_{s\alpha} & \hat{T}'_{s\gamma} \end{bmatrix}$ . Substituting Eq. (6.24) in Eq. (6.23), we get,

$$\sigma' = K_A C_{srp} U'_a [\beta'_1, \varsigma'_1]^T + K_A F'(q, q') + [K_A M' + K_B]q'' + K_A M''q' \quad (6.25)$$

Now, substituting  $\sigma'$ , from the from preceding equation in Eq. (6.21), along with the consideration on the bounds given in Eq. (6.22) we get

$$V' = \sigma \left( K_A C_{srp} U'_a [\beta'_1, \varsigma'_1]^T + \|L\| \right) + \frac{\tilde{C}_{srp} \hat{C}_{srp}}{\zeta} \quad (6.26)$$

Now considering the parameter estimation error in  $B$  as

$$\tilde{C}_{srp} = \hat{C}_{srp} - C_{srp} \quad (6.27)$$

and expanding Eq. (6.26), we have

$$V' = \sigma \left[ K_A \left( \hat{C}_{srp} - \tilde{C}_{srp} \right) U'_a [\beta'_1, \varsigma'_1]^T + \|L\| \right] + \frac{\tilde{C}_{srp} \hat{C}_{srp}}{\zeta} \quad (6.28)$$

Rearranging the preceding Eq. (6.28) yields

$$V' = \sigma \left[ K_A \hat{C}_{srp} U'_a [\beta'_1 \ \varsigma'_1]^T + \|L\| \right] - \sigma K_A \tilde{C}_{srp} U'_a [\beta'_1 \ \varsigma'_1]^T + \frac{\tilde{C}_{srp} \hat{C}'_{srp}}{\zeta} \quad (6.29)$$

Now in order to make  $V'$  negative, choose the adaptive law as

$$\hat{C}'_{srp} = \zeta \sigma K_A U_a [\beta'_1 \ \varsigma'_1] \quad (6.30)$$

where  $\zeta$  is the adaptation gain. Also let

$$K_A \hat{C}_{srp} U'_a [\beta'_1, \ \varsigma'_1] = -\eta \operatorname{sgn}(\sigma) \quad (6.31)$$

where  $\eta$  is a positive constant and  $\eta \gg \sup \|L\|$ . Substituting Eq. (6.31) and Eq. (6.30) into Eq. (6.29), we have

$$V' = \sigma [-\eta \operatorname{sgn}(\sigma)] = -\eta |\sigma| \quad (6.32)$$

Now, we can prove that the system is completely stable using theorem-3 of LaSalle's principle [LaSalle 1960], and hence the system states converge onto the sliding surface. The reaching time,  $(t_r)$ , for adaptive sliding mode derived in Chapter 5 holds in this case as well. It is given as  $|\sigma(t=0)|/c$ , where  $c = (\eta - d)$  and  $d$  is assumed to be a bounded value. Next, Eq. (6.31) is rearranged to derive the control law as

$$[\beta'_1, \ \varsigma'_1] = -\frac{1}{K_A \hat{C}_{srp} U'_a} [\eta \operatorname{sgn}(\sigma)] \quad (6.33)$$

And the control law with the introduction of the boundary layer in Eq. (6.33), is given by,

$$[\beta'_1, \ \varsigma'_1] = -\frac{1}{K_A \hat{C}_{srp} U'_a} \eta \left[ \frac{\sigma}{|\sigma| + \delta} \right] \quad (6.34)$$

where  $\delta$  is the width of the boundary layer.

**Remark 6.1:** The Euler angles  $\gamma$ ,  $\phi$  and  $\alpha$  are limited to the ranges  $-\pi < \gamma < \pi$ ,  $-\frac{\pi}{2} < \phi < \frac{\pi}{2}$ , and  $-\pi < \alpha < \pi$ . Therefore, the Lyapunov analysis guarantees stability for

any initial condition that avoids singularities due to  $\phi = \pm \frac{\pi}{2}$ .

## 6.3 Performance Evaluation

To study the effectiveness and performance of the proposed adaptive controller, the detailed system response is numerically simulated using the set of governing equations of motion given by Eq. (6.10) along with proposed adaptive control law given by Eq. (6.34). The integration is carried out Matlab using the fourth order Runge-Kutta solver. The simulation parameters used are shown in Table 6.1.

Table 6.1: System parameters.

Parameters	Values
Moment of Inertia $[I_{xx} \ I_{yy} \ I_{zz}]$ (kg m <sup>2</sup> )	[15 17 20]
System Parameters	
$R$ (km)	42378
$\mu$ (km <sup>3</sup> /s <sup>2</sup> )	$3.986 \times 10^5$
$p$ (N/m <sup>2</sup> )	$4.563 \times 10^{-6}$
$\varepsilon$ (deg)	23.5
$i$ (deg)	0
$\psi$ (deg)	45
$r$ (m)	0.5
$A$ (m <sup>2</sup> )	1.0
Control Parameters	
$[P_1 \ P_2 \ P_3]$	[4.5 4.5 4.5]
$[P_4 \ P_5 \ P_6]$	[-2.1 1.5 -2.5]
$\eta$	0.5
$\delta$	0.01
$\zeta$	200
Initial Estimates	
$\rho_{s0}$	0.7
$p_0$ (N/m <sup>2</sup> )	$4.563 \times 10^{-6}$
$r_0$ (m)	0.25
$A_0$ (m <sup>2</sup> )	0.25

Similar to Chapter 5, the nondimensional parameters  $k_1$  and  $k_2$  based on the values of the satellite mass moment of inertia, have values of 0.3 and 0.2 respectively. The control

law is developed based on these values. The effect of variations in satellite mass moment of inertia is examined by implementing the changes in the mass moment of inertia only in the satellite dynamic model.

### 6.3.1 Nominal Performance

First, we evaluate stabilization of the satellite in a circular orbit from the large initial disturbances about its three axes given by

$$\begin{aligned}\alpha_0 &= -60 \text{ deg}; \phi_0 = 50 \text{ deg}; \gamma_0 = 60 \text{ deg} \\ \alpha'_0 &= \phi'_0 = \gamma'_0 = 2.5 \text{ deg / sec}\end{aligned}\tag{6.35}$$

Fig. (6.3) illustrates the satellite attitude response subjected to the large initial errors. It can be observed that the adaptive controller successfully stabilizes the satellite. The Euler angles asymptotically approach zero and the maximum deflection of the solar flaps  $|\beta|_{\max}(|\zeta|_{\max})$  is  $28^\circ$  ( $9^\circ$ ), observed during the transient state. Fig. (6.4) shows the angular rates and the adaptive parameter  $\hat{C}_{srp}$ .

### 6.3.2 Variations in Mass Moment of Inertia

The performance of the proposed adaptive control algorithm in the presence of variations on the satellite mass moment of inertia is examined next. A satellite in an axially symmetric configuration is considered, then the performance of the proposed system as affected by the product of inertia terms ( $I_{xy}, I_{xz}, I_{yz}$ ) is evaluated, and finally the efficacy of the adaptive control algorithm for a satellite in an unstable gravity gradient configuration is examined. The inertia matrix for the first and second cases is chosen same as shown in Table 5.2 in Chapter 5. The system performance for an axisymmetric satellite is shown in Fig. (6.5). The attitude response converges asymptotically. Fig. (6.6) shows the corresponding angular rates and the adaptive parameter  $\hat{C}_{srp}$ . Next, the effect of incorporating product of inertia terms in the satellite model is evaluated. The attitude of the satellite is stabilized within one and half orbits (Fig. 6.7). The steady state error is non-zero, as expected from the addition of the product of inertia terms. The performance of the control method for

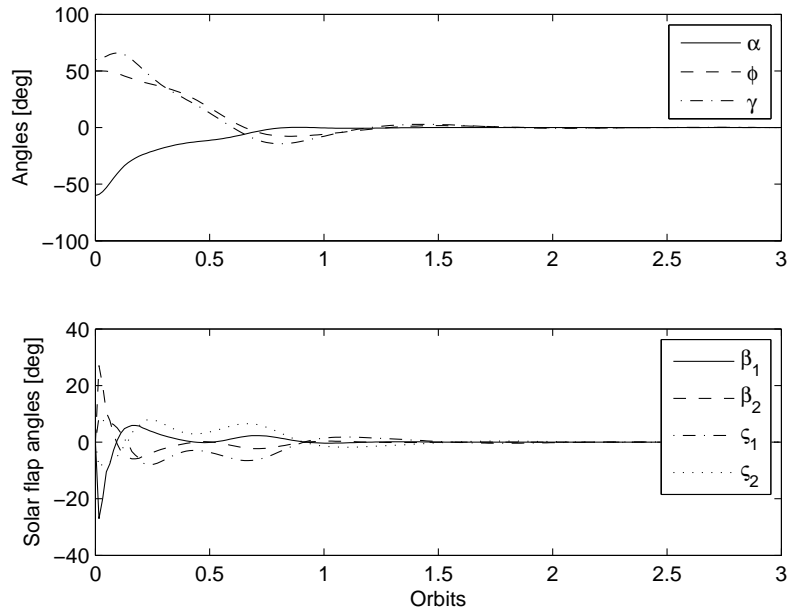


Figure 6.3: Performance of the adaptive sliding mode controller during attitude stabilization,  $k_1 = 0.3$ ,  $k_2 = 0.2$ .

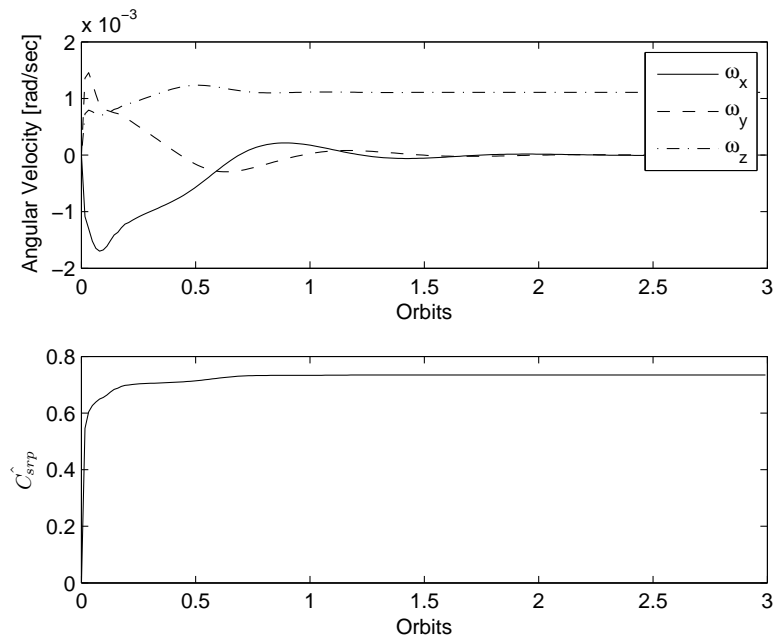


Figure 6.4: Response of angular velocity and estimated adaptive parameter,  $k_1 = 0.3$ ,  $k_2 = 0.2$ .

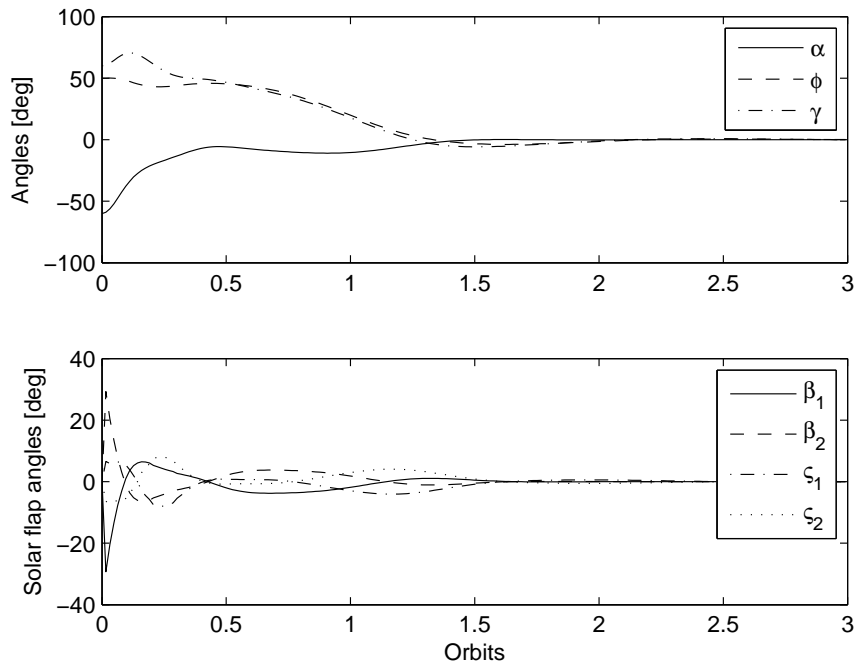


Figure 6.5: Performance of the adaptive sliding mode controller during attitude stabilization,  $k_1 = 0.177$ ,  $k_2 = 0.177$ .

a satellite in an unstable gravity gradient configuration is now evaluated. The values of the nondimensional parameters are taken as  $k_1 = -0.1$  and  $k_2 = 0.2$  corresponding to the unstable configuration of a satellite with no control in its yaw axis. Fig. 6.8 illustrates the effectiveness of the proposed control methodology. The attitude is stabilized within one and half orbit and the solar flaps exhibit the maximum deflection of  $30^\circ$  during the transient state.

### 6.3.3 Effect of System Parameters

Fig. (6.8) shows the effect of the solar aspect angle  $\psi$  on the proposed controller. Satellite attitude response remains virtually unaffected as the value of  $\psi$  is changed from  $45^\circ$  to  $135^\circ$ . However the solar flap deflection changes with changes in  $\psi$ . The maximum deflection in the solar flap,  $|\beta|_{\max} (|\zeta|_{\max})$  is  $28^\circ$  ( $9^\circ$ ), during the transient state for  $\psi = 45^\circ$ . In the case of  $\psi = 135^\circ$ , the maximum deflection in solar flaps are  $|\beta|_{\max} (|\zeta|_{\max})$  is  $28^\circ$  ( $11^\circ$ ).

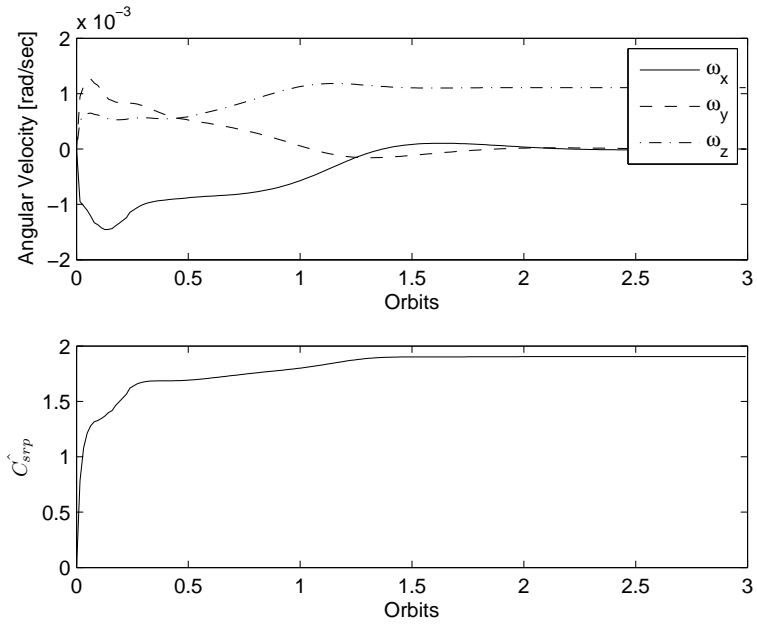


Figure 6.6: Response of angular velocity and estimated adaptive parameter,  $k_1 = 0.177$ ,  $k_2 = 0.177$ .

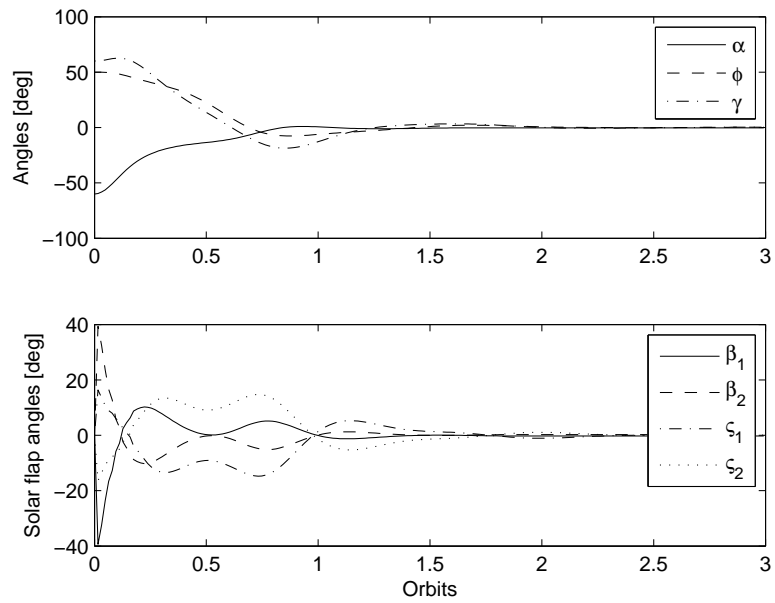


Figure 6.7: Performance of the adaptive sliding mode controller during attitude stabilization,  $k_1 = 0.3$ ,  $k_2 = 0.2$  with product of inertia terms.

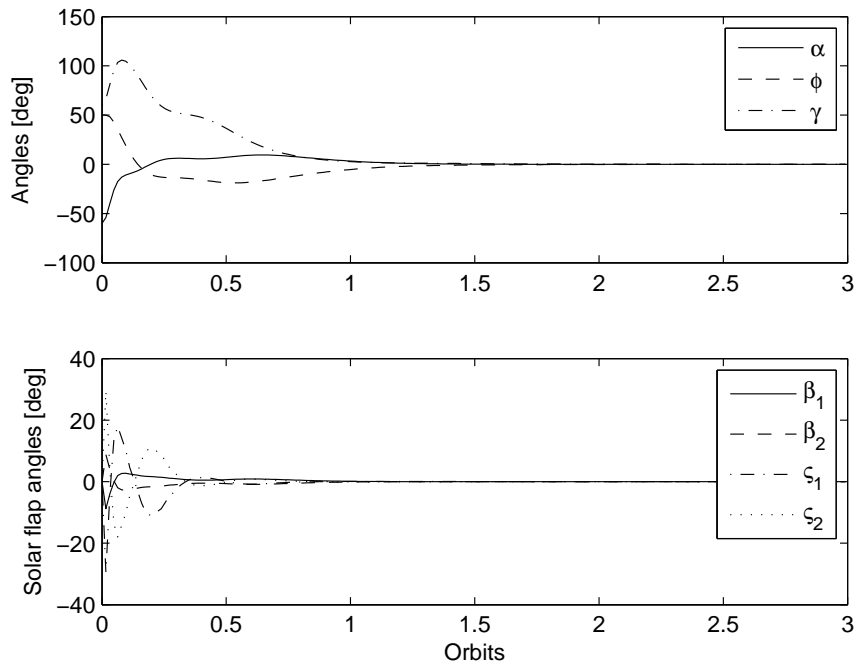


Figure 6.8: Response of angular velocity and estimated adaptive parameter,  $k_1 = -0.1$ ,  $k_2 = 0.2$ .

### 6.3.4 Eccentricity and External Disturbances

The effectiveness of the control methodology for a satellite in an elliptical orbit is examined next. The performance of the system for an orbital eccentricity of  $e = 0.1$  is shown in Fig. (6.10). The state error in the pitch axis is bounded by  $|\alpha|_{\max} = 0.1^\circ$ , roll axis by  $|\phi|_{\max} = 0.15^\circ$  and the yaw axis by  $|\gamma|_{\max} = 0.25^\circ$ . The solar flaps continuously maneuver to counter this disturbance due to eccentricity, and the maximum deflection of the solar flaps is observed in the transient state and the maximum deflection in the steady state deflection is nearly  $5^\circ$ . The satellite attitude remains stabilized within reasonable limits even in an orbit with an eccentricity of 0.1 using the proposed methodology.

Finally, the effect of external disturbance on the performance of the system is verified. The system may experience external disturbance torques due to several factors including SRP modeling errors (i.e.  $\rho_d \neq 1$ ), solar flap misalignment and other environmental forces. The satellite model is subjected to disturbance of a periodic nature, and the performance of the controller is evaluated. It can be observed from Fig. (6.11) that the controller

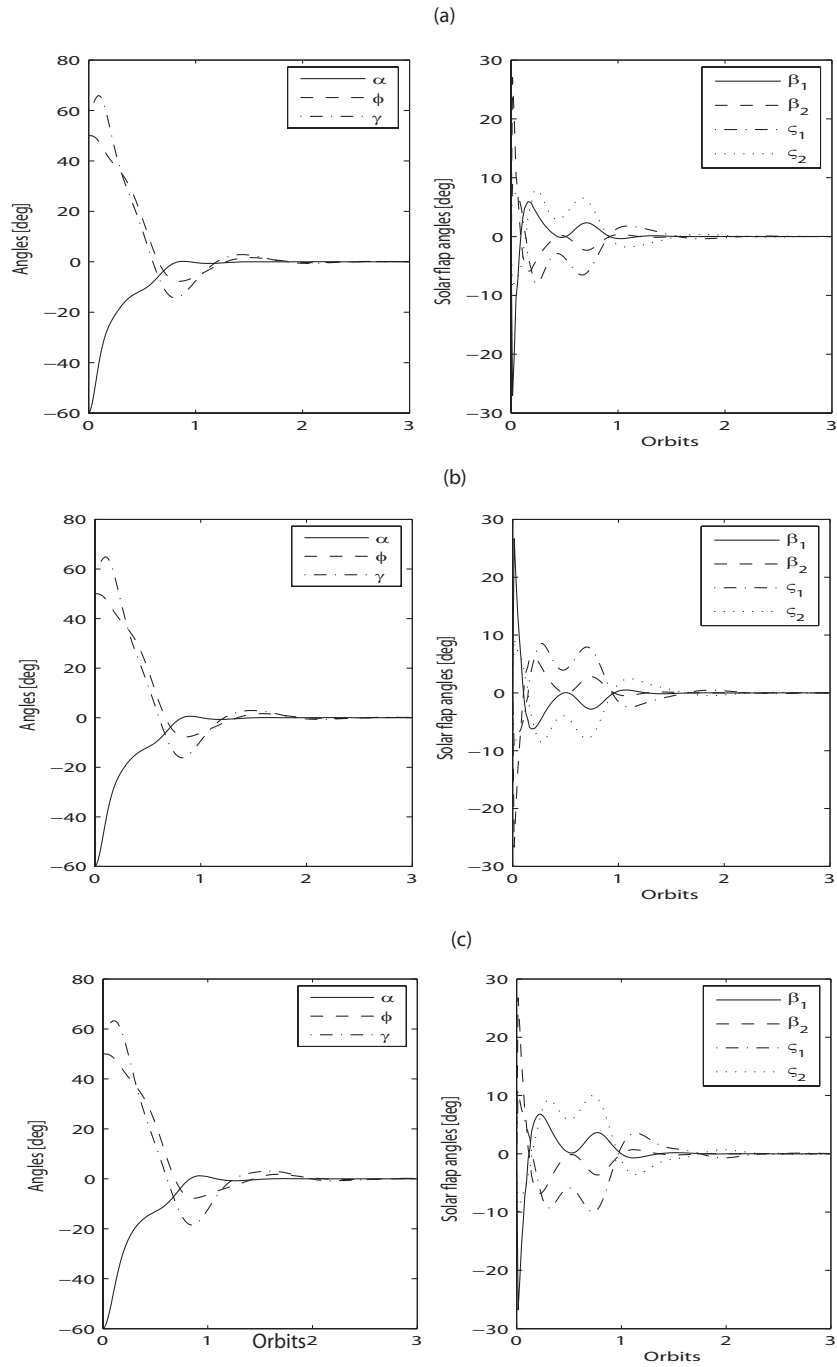


Figure 6.9: Effect of solar aspect angle  $\psi$  on solar flap deflection and attitude tracking: (a)  $\psi = 45^\circ$ , (b)  $\psi = 90^\circ$ , (c)  $\psi = 135^\circ$ .

maneuvers the solar flaps and is able to regulate the satellite attitude successfully. Thus, this establishes the robustness of the proposed methodology to time varying external dis-

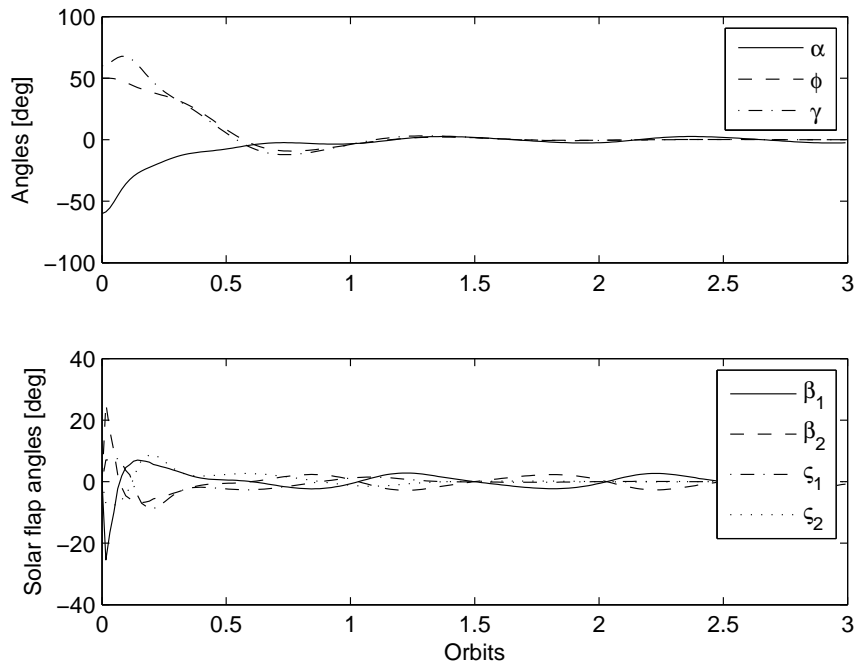


Figure 6.10: Performance of the adaptive sliding mode controller during attitude stabilization,  $e=0.1$

turbance. Furthermore, the above results bring out the powerful features of SRP based three axis satellite attitude control using the proposed adaptive control methodology. The performance of the controller does not deteriorate even when the system parameters are changing and yet provides excellent attitude response.

## 6.4 Summary

This chapter examines the feasibility of three axis satellite attitude control using solar radiation pressure. A satellite with two sets of oppositely placed light weight solar flaps is proposed. This configuration provides explicit control only on two of the axes, the pitch and roll axis. But, three axis attitude maneuvering and maintenance is accomplished by rotating the solar flaps with accordance to the control law developed based on sliding mode theory. The performance of the control strategy in attitude stabilization is examined in the detail including its performance in the presence of external disturbances, variation in the solar

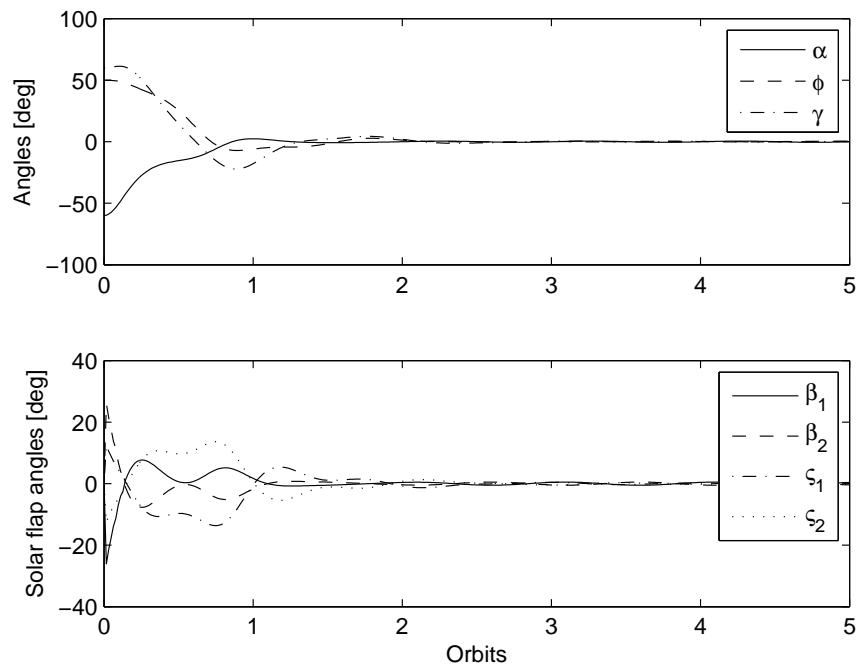


Figure 6.11: Performance of the adaptive sliding mode controller during attitude stabilization in the presence of external disturbances

aspect angle  $\psi$ , high initial attitude rates and uncertainty in the mass moment of inertias. The satellite attitude was observed to be stabilized within  $0.1^\circ$  in all the cases. Thus, the proposed nonlinear adaptive controller is feasible in achieving high attitude performance as required by future satellite missions.



## CHAPTER 7

# Fault Tolerant Satellite Attitude Control Using Solar Radiation Pressure / Aerodynamic Drag

---

**I**N Chapters 5 and Chapter 6, the feasibility of achieving robust satellite attitude control using maneuverable drag plates and solar flaps respectively were demonstrated. This chapter evaluates the performance of this control strategy in the presence of faults or failures of the drag plates or solar flaps. The adaptive nonlinear control design employed in the previous chapters is extended to handle the presence of such faults or failures. First, the pitch attitude performance of the satellite in the presence of faults or failures in the solar flaps is evaluated. The fault scenarios considered include sudden failure of one of the solar flaps, occurrence of an abrupt blockage or loss in effectiveness of one of the rotating solar flaps, and occurrence of a periodic actuator fault. Next, performance of the system during three axis attitude control scenario in the presence of similar failures is examined.

The system model and its equations of motion in the case of pitch attitude control using solar radiation pressure is presented in Section 7.1. In section 7.2, the nonlinear adaptive sliding mode control law is derived. In Section 7.4 numerical simulation is carried out for a detailed assessment of the proposed attitude control strategy, and the effects of different failure scenarios on the controller performance is examined. Next, in section 7.5, the controller performance in the case of three axis attitude control using either aerodynamic drag or solar radiation pressure is evaluated in the presence of faults and failures. Finally, the findings of the present study are summarized in Section 7.6.

## 7.1 Proposed System Model and Equations of Motion for Pitch Attitude Control

The system model consists of a satellite with two-oppositely placed light-weight solar flaps along the satellite Y-axis and its center of mass  $O$  moving in a circular orbit about the Earth's center  $E$  (Fig.7.1). The system center of mass  $O$  lies on the center of mass of the satellite. The mass of the solar flaps and other accessories are assumed to be negligible. For the system under consideration, an orbital reference frame  $O-X_oY_oZ_o$  is selected such that the  $Y_o$ -axis always points along the local vertical, the  $X_o$ -axis lies normal to the orbital plane, and the  $Z_o$ -axis represents the third axis of this right handed frame taken. The body-fixed coordinate frame is represented by  $O - XYZ$ . For solar flap-j, we consider its axis  $n_j$  initially aligned with the  $Z$ -axis is rotated by an angle  $\beta_j$  about the  $X$ -axis (normal to the orbit plane  $Y-Z$ ). The solar flaps are considered to be made of a highly reflective surface (i.e.,  $\rho_d = 0$ ; no absorption, specular reflection only). The distances between the system center of mass  $O$  and the center of pressure for both the solar flaps are assumed to be the same and their cross-sectional areas facing the Sun are equal.

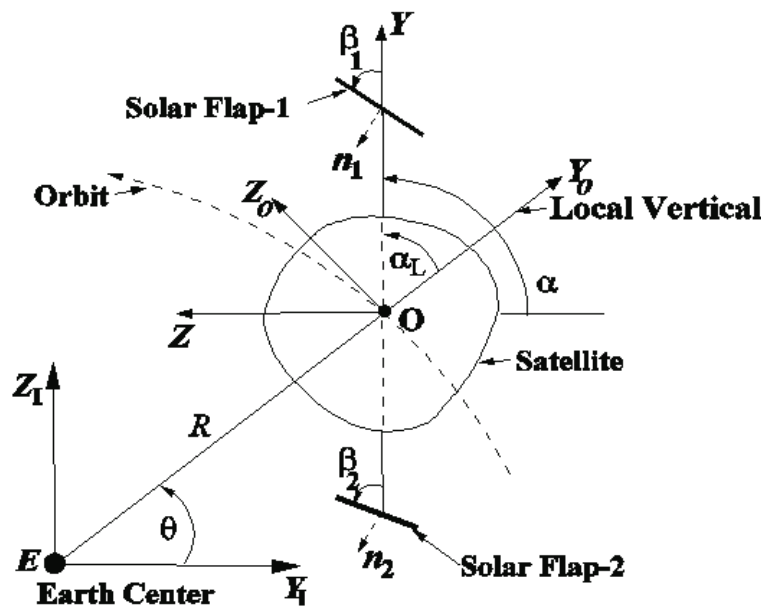


Figure 7.1: Configuration of the proposed solar controller.

Using Euler's method the governing equation of motion of the system is written as

$$I_x (\ddot{\theta} + \ddot{\alpha}_L) = \tau_g + \tau_s + \tau_d \quad (7.1)$$

where  $\tau_d$  is the disturbance torque,  $\tau_g$  is the gravity gradient torque given by

$$\tau_g = -\frac{3\mu}{2R^3} (I_y - I_z) \sin 2\alpha_L \quad (7.2)$$

and  $\tau_s$  denotes the torque due to solar radiation pressure and it is derived as follows: Considering a highly reflective surface (i.e.,  $\rho_d = 0$ ; no absorption, specular reflection only,  $\rho_t = 0$ , no transitivity as well), the force acting on the flap-j due to SRP is given by

$$\vec{F}_{s_j} = 2\rho_s p A_j |\vec{s}_j \cdot \vec{n}_j| (\vec{s}_j \cdot \vec{n}_j) \vec{n}_j, \quad j = 1, 2 \quad (7.3)$$

Here  $\vec{s}_j$  is the unit vector of the incoming light from the Sun on the solar flap-j and is expressed in the satellite body-fixed reference frame as

$$\begin{aligned} \vec{s}_j = & [\sin \psi \sin (i - \varepsilon_s)] \hat{i} + [-\cos \psi \cos (\theta + \alpha_L) - \sin \psi \cos (i - \varepsilon_s) \sin (\theta + \alpha_L)] \hat{j} \\ & + [\cos \psi \sin (\theta + \alpha_L) - \sin \psi \cos (i - \varepsilon_s) \cos (\theta + \alpha_L)] \hat{k} \end{aligned} \quad (7.4)$$

The vector normal to the solar flap-j,  $\vec{n}_j$  is given by

$$\vec{n}_j = [-\sin \beta_j] \hat{j} + [\cos \beta_j] \hat{k}, \quad j = 1, 2 \quad (7.5)$$

Thus, the torque exerted by the solar flap-j on the satellite is obtained as

$$\vec{\tau}_{s_j} = \vec{r}_j \times \vec{F}_{s_j} = (-1)^{j+1} 2\rho_s p A_j r_j |\vec{s}_j \cdot \vec{n}_j| (\vec{s}_j \cdot \vec{n}_j) [\cos \beta_j] \hat{i}, \quad j = 1, 2 \quad (7.6)$$

Assuming that the cross-sectional area of the flap and the distance between the system center of mass S and the center of pressure for both the solar flaps are the same (i.e.  $A_j = A$ ,  $r_j = r$ ), the components of the total solar torque about the satellite body axes

can be written as

$$\tau_s = \tau_{s_1} + \tau_{s_2} = 2\rho_s p A r [|\vec{s}_1 \cdot \vec{n}_1| (\vec{s}_1 \cdot \vec{n}_1) \cos \beta_1 - |\vec{s}_2 \cdot \vec{n}_2| (\vec{s}_2 \cdot \vec{n}_2) \cos \beta_2] \quad (7.7)$$

Let  $\alpha$  be the orientation of the satellite with respect to the inertial axis  $Y_1$  (Fig.7.1). We have the following relation

$$\alpha = \alpha_L + \theta \quad (7.8)$$

where  $\theta = \Omega t$  is the orbital angle, and  $\Omega = \mu/R^3$  is the orbital rate. Substituting,  $\alpha_L = \alpha - \theta$ , in  $\tau_g$  and  $\tau_s$  in Eq. (7.2) and Eq. (7.7), respectively, and expressing the derivatives with respect to  $\theta$  and using following relations:

$$\begin{aligned} \dot{\alpha} &= \Omega \alpha' \\ \ddot{\alpha} &= \Omega^2 \alpha'' \end{aligned} \quad (7.9)$$

the resulting governing equation of motion of the system is obtained as follows:

$$\alpha'' = T_g + T_s \quad (7.10)$$

where

$$\begin{aligned} T_g &= -\frac{3}{2} K \sin 2(\alpha - \theta) \\ T_s &= C_1 \sigma \sin^2(\alpha + \gamma + \beta_1) \Delta_1 \cos \beta_1 - C_2 \sigma \sin^2(\alpha + \gamma + \beta_2) \Delta_2 \cos \beta_2 \\ \sigma &= 1 - \sin^2 \psi \sin^2(i - \varepsilon_s) \\ \gamma &= -\tan^{-1}(\tan \psi \cos(i - \varepsilon_s)) \\ \Delta_j &= \text{sgn}(\sin(\alpha + \gamma + \beta_j)), \quad j = 1, 2 \\ K &= \frac{I_y - I_z}{I_x}, \quad C_1 = \frac{2\rho_s p A_1 r_1}{I_x \Omega^2}, \quad C_2 = \frac{2\rho_s p A_2 r_2}{I_x \Omega^2}, \end{aligned}$$

Here  $\text{sgn}(f)$  denotes signum function. Also the solar aspect angle ( $\psi$ ) is a function of  $\theta$  and varies from 0 to  $2\pi$  radians in one year.

## 7.2 Design of Control Law

In this section, an adaptive sliding mode control law is derived. Adaptive control methodology is employed to deal with the uncertainties due to unknown or slowly time-varying parameters. Here the solar parameters  $C_1$  and  $C_2$  and the satellite mass distribution parameter  $K$  are assumed to be unknown and are estimated online and then used in the control law.

## 7.3 Adaptive Control Law Design

The nonlinear and nonautonomous system equation of motion, Eq. (7.10), can be represented in state space form. The following state vector is defined

$$x = \begin{bmatrix} \alpha & \alpha' & \beta_1 & \beta_2 \end{bmatrix}^T \quad (7.11)$$

A state space representation of the system, with a selected controlled output variable  $y = \alpha$ , is given by

$$\begin{aligned} \dot{x} &= f(x) + g u \\ y &= \alpha \end{aligned} \quad (7.12)$$

where

$$\begin{aligned} f(x) &= \begin{bmatrix} \alpha' & T_{gs}(\alpha, \alpha', \gamma, \beta_i, \theta) & 0 & 0 \end{bmatrix}^T \\ \mathbf{u} &= \begin{bmatrix} \beta'_1 & \beta'_2 \end{bmatrix}^T \\ g &= \begin{bmatrix} g_1 & g_2 \end{bmatrix} \\ g_1 &= \begin{bmatrix} 0 & 0 & 1 & 0 \end{bmatrix}^T \\ g_2 &= \begin{bmatrix} 0 & 0 & 0 & 1 \end{bmatrix}^T \end{aligned}$$

where  $T_{gs} = T_g + T_s$

Next, the sliding plane is chosen as

$$S = \tilde{\alpha}'' + \lambda_2 \tilde{\alpha}' + \lambda_1 \tilde{\alpha} \quad (7.13)$$

where  $\tilde{\alpha}'' = \alpha'' - \alpha_d''$ ,  $\tilde{\alpha}' = \alpha' - \alpha_d'$ ,  $\tilde{\alpha} = \alpha - \alpha_d$  are the state error variables,  $\lambda_1$  and  $\lambda_2$  are positive constants. The basic idea is to alter the system dynamics along the sliding surface such that the trajectory of the system is steered onto the sliding manifold described by  $S = 0$ . Subsequently, control laws based on the Lyapunov stability theorem is derived. The control law that forces the motion of the states to be along the sliding manifold  $S = 0$  can be derived by choosing the Lyapunov candidate function defined as follows.

$$V = \frac{1}{2}S^2 + \frac{1}{2\gamma_1}\tilde{K}^2 + \frac{1}{2\gamma_2}\tilde{C}_1^2 + \frac{1}{2\gamma_3}\tilde{C}_2^2 \quad (7.14)$$

where  $V > 0$  and  $\gamma_1$ ,  $\gamma_2$  and  $\gamma_3$  are positive constants. Taking the derivative along the trajectory gives,

$$V' = SS' + \frac{\tilde{K}\tilde{K}'}{\gamma_1} + \frac{\tilde{C}_1\tilde{C}_1'}{\gamma_2} + \frac{\tilde{C}_2\tilde{C}_2'}{\gamma_3} \quad (7.15)$$

where  $S' = \tilde{\alpha}''' + (\lambda_2\tilde{\alpha}'' + \lambda_1\tilde{\alpha}')$ . Here

$$\alpha''' = \frac{\partial T_{gs}}{\partial \alpha}\alpha' + \frac{\partial T_{gs}}{\partial \theta}\theta' + \frac{\partial T_s}{\partial \beta_1}u_1 + \frac{\partial T_s}{\partial \beta_2}u_2 \quad (7.16)$$

and

$$\frac{\partial T_{gs}}{\partial \alpha} = -3K \cos [2(\alpha - \theta)] + \left\{ \begin{array}{l} C_1\sigma \sin 2(\alpha + \gamma + \beta_1) \Delta_1 \cos \beta_1 - \\ C_2\sigma \sin 2(\alpha + \gamma + \beta_2) \Delta_2 \cos \beta_2 \end{array} \right\} \quad (7.17)$$

$$\begin{aligned} \frac{\partial T_{gs}}{\partial \theta} = 3K \cos 2(\alpha - \theta) + \left\{ \begin{array}{l} C_1\sigma \sin 2(\alpha + \gamma + \beta_1) \Delta_1 \cos \beta_1 - \\ C_2\sigma \sin 2(\alpha + \gamma + \beta_2) \Delta_2 \cos \beta_2 \end{array} \right\} & \left\{ -\frac{\cos(i - \varepsilon_s) \sec^2 \psi}{1 + \tan^2 \psi \cos^2(i - \varepsilon_s)} \right\} \\ + \left\{ \begin{array}{l} C_1\sigma \sin^2(\alpha + \gamma + \beta_1) \Delta_1 \cos \beta_1 - \\ C_2\sigma \sin^2(\alpha + \gamma + \beta_2) \Delta_2 \cos \beta_2 \end{array} \right\} & \left\{ -\sin 2(\psi) \sin^2(i - \varepsilon_s) \right\} \end{aligned} \quad (7.18)$$

$$\frac{\partial T_s}{\partial \beta_1} = C_1\sigma\Delta_1 [\sin 2(\alpha + \gamma + \beta_1) \cos \beta_1 - \sin^2(\alpha + \gamma + \beta_1) \sin \beta_1] \quad (7.19)$$

$$\frac{\partial T_s}{\partial \beta_2} = C_2\sigma\Delta_2 [-\sin 2(\alpha + \gamma + \beta_2) \cos \beta_2 + \sin^2(\alpha + \gamma + \beta_2) \sin \beta_2] \quad (7.20)$$

Rearranging Eq. (7.16), we have

$$\alpha''' = K f_0 + C_1 f_1 + C_2 f_2 + C_1 g_1 u_1 + C_2 g_2 u_2 \quad (7.21)$$

where

$$f_0 = -3K \cos [2 (\alpha - \theta)] \alpha' + 3K \cos [2 (\alpha - \theta)] \quad (7.22)$$

$$\begin{aligned} f_1 = & [\sigma \sin 2 (\alpha + \gamma + \beta_1) \Delta_1 \cos \beta_1] \alpha' \\ & + [\sigma \sin 2 (\alpha + \gamma + \beta_1) \Delta_1 \cos \beta_1] \left[ -\frac{\cos (i - \varepsilon_s) \sec^2 \psi}{1 + \tan^2 \psi \cos^2 (i - \varepsilon_s)} \right] \\ & + [\sin^2 (\alpha + \gamma + \beta_1) \Delta_1 \cos \beta_1] [-\sin 2 (\psi) \sin^2 (i - \varepsilon_s)] \end{aligned} \quad (7.23)$$

$$\begin{aligned} f_2 = & [(-\sigma \sin 2 (\alpha + \gamma + \beta_2) \Delta_2 \cos \beta_2) \alpha'] \\ & + [-\sigma \sin 2 (\alpha + \gamma + \beta_2) \Delta_2 \cos \beta_2] \left[ -\frac{\cos (i - \varepsilon_s) \sec^2 \psi}{1 + \tan^2 \psi \cos^2 (i - \varepsilon_s)} \right] \end{aligned} \quad (7.24)$$

$$+ [-\sin^2 (\alpha + \gamma + \beta_2) \Delta_2 \cos \beta_2] [-\sin 2 (\psi) \sin^2 (i - \varepsilon_s)] \quad (7.25)$$

$$g_1 = \sigma \Delta_1 [\sin 2 (\alpha + \gamma + \beta_1) \cos \beta_1 - \sin^2 (\alpha + \gamma + \beta_1) \sin \beta_1] \quad (7.26)$$

$$g_2 = \sigma \Delta_2 [-\sin 2 (\alpha + \gamma + \beta_2) \cos \beta_2 + \sin^2 (\alpha + \gamma + \beta_2) \sin \beta_2] \quad (7.27)$$

Substituting  $\alpha'''$  from into Eq. (7.15) yields

$$\begin{aligned} V' = & S [K f_0 + C_1 f_1 + C_2 f_2 + C_1 g_1 \beta'_1 + C_2 g_2 \beta'_2 - \alpha'''_d + (\lambda_2 \tilde{\alpha}'' + \lambda_1 \tilde{\alpha}')] \\ & + \frac{\tilde{K} \hat{K}'}{\gamma_1} + \frac{\tilde{C}_1 \hat{C}'_1}{\gamma_2} + \frac{\tilde{C}_2 \hat{C}'_2}{\gamma_3} \end{aligned} \quad (7.28)$$

Taking the parameter estimation errors as

$$\tilde{K} = \hat{K} - K \quad \tilde{C}_1 = \hat{C}_1 - C_1 \quad \tilde{C}_2 = \hat{C}_2 - C_2 \quad (7.29)$$

and expanding Eq. (7.28), we have

$$V' = S \left[ \left( \hat{K} - \tilde{K} \right) f_0 + \left( \hat{C}_1 - \tilde{C}_1 \right) f_1 + \left( \hat{C}_2 - \tilde{C}_2 \right) f_2 + \left( \hat{C}_1 - \tilde{C}_1 \right) g_1 \beta'_1 + \left( \hat{C}_2 - \tilde{C}_2 \right) g_2 \beta'_2 - \alpha''_d + (\lambda_2 \tilde{\alpha}'' + \lambda_1 \tilde{\alpha}') \right] + \frac{\tilde{K} \hat{K}'}{\gamma_1} + \frac{\tilde{C}_1 \hat{C}'_1}{\gamma_2} + \frac{\tilde{C}_2 \hat{C}'_2}{\gamma_3} \quad (7.30)$$

Now in order to make  $V'$  negative choose the adaptive laws as

$$\hat{K}' = \gamma_1 S f_0 \quad \hat{C}'_1 = \gamma_2 S (f_1 + g_1 \beta'_1) \quad \hat{C}'_2 = \gamma_3 S (f_2 + g_2 \beta'_2) \quad (7.31)$$

where  $\gamma_1, \gamma_2$  and  $\gamma_3$  are the adaptation gains. Also let

$$\hat{K} f_0 + \hat{C}_1 f_1 + \hat{C}_2 f_2 + \hat{C}_1 g_1 \beta'_1 + \hat{C}_2 g_2 \beta'_2 - \alpha''_d + (\lambda_2 \tilde{\alpha}'' + \lambda_1 \tilde{\alpha}') = -\eta \operatorname{sgn}(S) \quad (7.32)$$

Substituting Eq. (7.31) and Eq. (7.32) into Eq. (7.30), we have

$$V' = S [-\eta \operatorname{sgn}(S)] = -\eta |S| \quad (7.33)$$

Next, Eq. (7.32) is rearranged to derive the control laws as,

$$u_1 = \frac{\hat{C}_1 g_1}{\left( \hat{C}_1 g_1 \right)^2 + \left( \hat{C}_2 g_2 \right)^2} \left\{ \alpha''_d - \hat{K} f_0 - \hat{C}_1 f_1 - \hat{C}_2 f_2 - (\lambda_2 \tilde{\alpha}'' + \lambda_1 \tilde{\alpha}') - \eta \operatorname{sgn}(S) \right\} \quad (7.34)$$

$$u_2 = \frac{\hat{C}_2 g_2}{\left( \hat{C}_1 g_1 \right)^2 + \left( \hat{C}_2 g_2 \right)^2} \left\{ \alpha''_d - \hat{K} f_0 - \hat{C}_1 f_1 - \hat{C}_2 f_2 - (\lambda_2 \tilde{\alpha}'' + \lambda_1 \tilde{\alpha}') - \eta \operatorname{sgn}(S) \right\} \quad (7.35)$$

Using a similar approach the control law based on sliding mode without adaptation can be derived. Assuming a candidate Lyapunov function,  $V = \frac{1}{2} S^2$ , the control laws for sliding mode without adaptation was obtained as

$$u_1 = \frac{C_1 g_1}{\left( C_1 g_1 \right)^2 + \left( C_2 g_2 \right)^2} \left\{ \alpha''_d - K f_0 - C_1 f_1 - C_2 f_2 - (\lambda_2 \tilde{\alpha}'' + \lambda_1 \tilde{\alpha}') - \eta \operatorname{sgn}(S) \right\} \quad (7.36)$$

$$u_2 = \frac{C_2 g_2}{(C_1 g_1)^2 + (C_2 g_2)^2} \{ \alpha''_d - K f_0 - C_1 f_1 - C_2 f_2 - (\lambda_2 \tilde{\alpha}'' + \lambda_1 \tilde{\alpha}') - \eta \operatorname{sgn}(S) \} \quad (7.37)$$

The adaptation laws, Eq. (7.31), provide the estimate of the unknown parameters  $\hat{K}$ ,  $\hat{C}_1$  and  $\hat{C}_2$  which are used in the control laws, Eq. (7.34) and (7.35). For the existence of the control laws,  $(\hat{C}_1 g_1)^2 + (\hat{C}_2 g_2)^2$  must be non-zero in the region of interest. This region  $\Omega_s$  ( $\Omega_{s1} \cap \Omega_{s2}$ ) of singularity is given by

$$\begin{aligned} \Omega_{s1} &= \left( \hat{C}_1 g_1 \right)^2 = \left\{ \hat{C}_1 \sigma \Delta_1 \left[ \sin 2(\alpha + \gamma + \beta_1) \cos \beta_1 - \sin^2(\alpha + \gamma + \beta_1) \sin \beta_1 \right] \right\}^2 = 0 \\ &= \left[ 2 \sin(\alpha + \gamma + \beta_1) \cos(\alpha + \gamma + \beta_1) \cos \beta_1 - \sin^2(\alpha + \gamma + \beta_1) \sin \beta_1 \right]^2 = 0 \end{aligned} \quad (7.38)$$

$$= \sin(\alpha + \gamma + \beta_1) \cos(\alpha + \gamma + \beta_1) \cos \beta_1 [2 - \tan(\alpha + \gamma + \beta_1) \tan \beta_1] = 0 \quad (7.39)$$

$$\Rightarrow (\alpha + \gamma + \beta_1) = 2n\pi, \quad \text{or} \quad [\tan(\alpha + \gamma + \beta_1) \tan \beta_1] = 2 \quad (7.40)$$

Similarly for  $\Omega_{s2}$ , we have

$$(\alpha + \gamma + \beta_2) = 2n\pi, \quad \text{or} \quad [\tan(\alpha + \gamma + \beta_2) \tan \beta_2] = 2 \quad (7.41)$$

Note that the control law is well defined as long as the trajectory of the system does not enter the region  $\Omega_s$ .

### 7.3.1 Pitch trajectory tracking

A specific trajectory is assumed for the purpose of attitude tracking. A simple polynomial based trajectory to achieve final attitude orientation is considered.

#### 7.3.1.1 Hurwitz filter trajectory

The following fourth order polynomial is adopted since the control law requires a third order desired pitch response.

$$\alpha_d'''' + 4\mu_d \alpha_d'''' + 6\mu_d^2 \alpha_d'' + 4\mu_d^3 \alpha_d' + \mu_d^4 \alpha_d = \mu_d^4 \alpha^* \quad (7.42)$$

where  $\mu_d$  is a positive real number and  $\alpha^*$  is the target pitch angle. The general closed form solution of Eq. (7.42) can be obtained as,

$$\alpha_d(\theta) = \alpha_f + k_1 e^{-\mu_d \theta} + \theta k_2 e^{-\mu_d \theta} + \theta^2 k_3 e^{-\mu_d \theta} + \theta^3 k_4 e^{-\mu_d \theta} \quad (7.43)$$

where  $k_1, k_2, k_3,$  and  $k_4$  can be obtained from initial conditions  $\alpha_d(0), \alpha_d^{(i)}(0), i = 1, 2, 3.$  Eq. (7.43) can be differentiated with respect to  $\theta$  to obtain  $\alpha_d'(\theta), \alpha_d''(\theta),$  and  $\alpha_d'''(\theta).$  Since we require that the tracking error converge to zero without oscillations, the characteristic polynomial given by the sliding plane (Eq. (7.13)) must be critically damped and it should have two real roots. This would ensure that oscillations or overshoots do not take place neither before nor after the sliding plane is reached. The condition for critically damped second order system is given by

$$\lambda_2 = 2\sqrt{\lambda_1} \quad (7.44)$$

and the parameters  $\lambda_1$  and  $\lambda_2$  must be strictly positive constants to make the system stable in the sliding manifold.

### 7.3.1.2 Closed-Loop Error Dynamics

The system given by Eq. (7.10) can be rewritten as

$$\alpha'' = T_{gs} + \tau_d \quad (7.45)$$

where  $\tau_d$  represent a bounded external disturbance. By differentiating Eq. (7.45) and using Eqs. (7.21), (7.34) and (7.35) yield

$$(\tilde{\alpha}''' + \lambda_2 \tilde{\alpha}'' + \lambda_1 \tilde{\alpha}' + \eta \operatorname{sgn}(S)) \frac{(C_1 \hat{C}_1 g_1^2 + C_2 \hat{C}_2 g_2^2)}{(\hat{C}_1 g_1)^2 + (\hat{C}_2 g_2)^2} + A_d = 0 \quad (7.46)$$

where  $A_d$  is the adaptive parameter estimation error given by

$$A_d = f_0 \left\{ \frac{\hat{K}}{\left(\hat{C}_1 g_1\right)^2 + \left(\hat{C}_2 g_2\right)^2} \left(C_1 \hat{C}_1 g_1^2 + C_2 \hat{C}_2 g_2^2\right) - K \right\} + \frac{1}{\left(\hat{C}_1 g_1\right)^2 + \left(\hat{C}_2 g_2\right)^2} \left(\hat{C}_1 f_1 + \hat{C}_2 f_2\right) \left(C_1 \hat{C}_1 g_1^2 + C_2 \hat{C}_2 g_2^2\right) - (C_1 f_1 + C_2 f_2) \quad (7.47)$$

The estimation error  $A_d$  will converge to zero as the estimated parameters converge to their original value. The preceding Eq. (7.46) is a third order linear differential equation of error dynamics and it does not contain any external disturbance term. This error equation is asymptotically stable as  $\theta \rightarrow \infty$ , and the tracking error  $\tilde{\alpha}(\theta) \rightarrow 0$ . Furthermore, the term  $\eta \operatorname{sgn}(S)$  forces the error dynamics to stay onto the sliding plane which makes the system insensitive to system parameter uncertainty and disturbances.

## 7.4 Performance Evaluation-Pitch Attitude Control

To study the effectiveness and performance of the proposed adaptive controller, the detailed system response is numerically simulated using the set of governing equations of motion, Eq. (7.10) in conjugation with the proposed control laws given by Eq. (7.34) and (7.35). The integration is carried out using International Mathematical and Statistical Library (IMSL) routine DDASPG based on the Petzold-Gear BDF method. Here we studied the attitude manoeuvre of the satellite starting from the initial attitude  $\alpha_0 = 110^\circ$  to the final desired attitude  $\alpha_d = 0^\circ$  with an initial tracking error of 100. The simulation parameters used are shown in Table 7.1. A satellite in the geostationary orbit is considered here and hence the Earth shadow effect is assumed to be negligible as its effect is experienced for only about 5% of the orbital period [Kumar *et al.* 2006].

### 7.4.1 Nominal performance

Fig.7.2 presents the response of the system to pitch trajectory tracking. It is found that the adaptive controller performs very well with no overshoot. The maximum solar flap

Table 7.1: Simulation parameters

Parameters	Values
<i>Mass distribution, <math>K</math></i>	0.5
<i>Solar parameter, <math>(C_1, C_2)</math></i>	(15, 15)
<i>Sliding mode gains, <math>(\lambda_1, \lambda_2)</math></i>	(6, 9)
<i><math>\eta, \phi, \mu_d</math></i>	(0.5, 0.5, 2.0)
<i>Adaptive gains, <math>(\gamma_1, \gamma_2, \gamma_3)</math></i>	(30, 6, 6)
<i>Initial estimate – Mass distribution, <math>\hat{K}_0</math></i>	0.05
<i>Initial estimate – Solar parameter, <math>(\hat{C}_{10}, \hat{C}_{20})</math></i>	(3, 3)
<i><math>(\alpha_0, \alpha'_0, \beta_1, \beta_2) (m^2)</math></i>	(110°, 0°, 0°, 0°)

deflection angle is 10° in the transient period and 6° in the steady state period. The flap deflection in the steady state is to counter the periodic gravity gradient torque  $T_g$ . Fig.7.2 also shows the estimates of the satellite mass distribution parameter and solar parameters  $\hat{K}$ ,  $\hat{C}_1$  and  $\hat{C}_2$  respectively. The estimated parameters converge to  $\hat{K} = 0.08$ ,  $\hat{C}_1 = 2.49$  and  $\hat{C}_2 = 2.52$ . The satellite pitch attitude tracking remains unaffected proving the robustness of the adaptive control scheme. The maximum solar flaps deflection ( $|\beta_j|_{\max}$ ) remains less than 6°.

### 7.4.2 Solar flap failure

Next the performance of the system when one of the solar flaps fails, say solar flap 2 (i.e.,  $C_2 = 0$ ), is studied (Fig.7.3). Failure is simulated to occur at 0.3 orbit. But this failure information is not passed onto the controller. The defective solar flap then fails to generate any useful torque. Referring to Fig.7.3, the operational flap, flap 1, compensates this failure by increasing the angle of rotation to achieve the desired trajectory and to maintain the attitude of the satellite. The satellite pitch attitude tracking remains unaffected. Note in this case the system using sliding mode control without adaptation fails to meet the desired pitch attitude and the solar flap deflection deviates to unreasonable orientations (Fig.7.4).

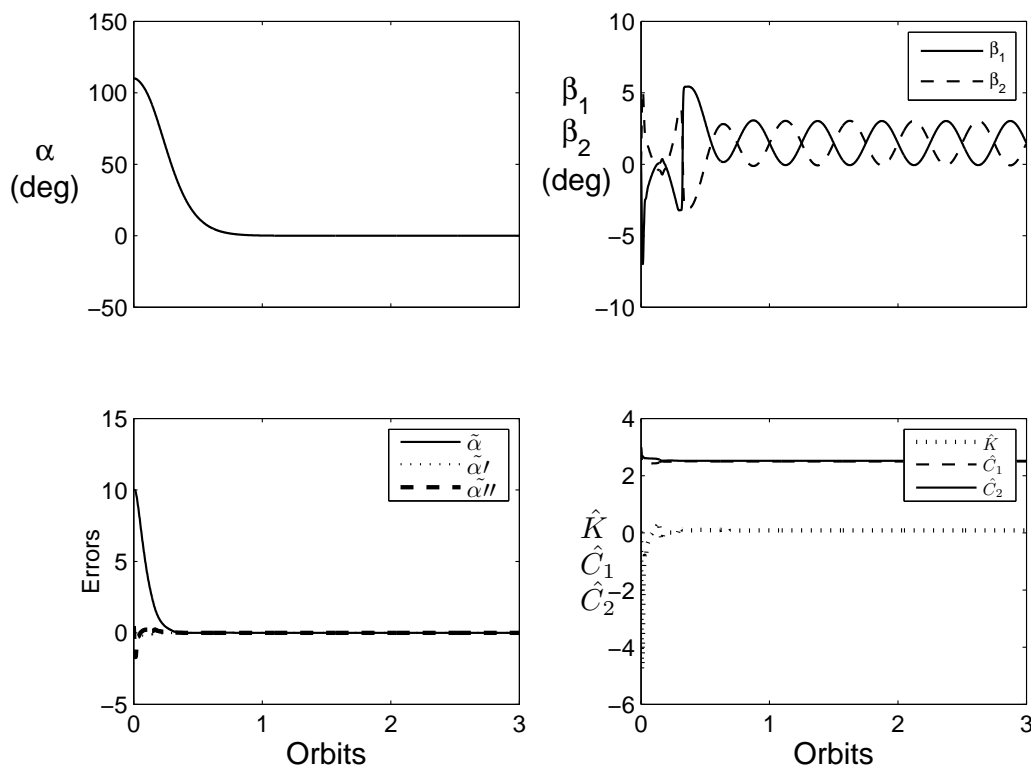


Figure 7.2: Performance of the adaptive sliding mode controller under attitude tracking.

### 7.4.3 Actuator stuck fault

Next, we consider a fault scenario in which the actuator gets stuck at a particular position, i.e., the solar flap 2 stops abruptly at 0.3 orbit (Fig.7.5). It is found that  $\beta_1$  compensates for the fault by overshooting to a maximum value of  $40^\circ$  as soon as  $\beta_2$  is jammed. But  $\beta_1$  eventually settles with a maximum deflection of  $17^\circ$  after the satellite pitch attitude reaches the desired angle. Thus, even when one of the actuators is stuck in position, the proposed fault-tolerant controller demonstrated excellent performance in providing desired satellite attitude control.

In the case of sliding mode without adaptation, the actuator stuck fault degrades the system performance and is unable to provide the desired response (Fig.7.6). The advantage of using an adaptive sliding mode control is very much evident in the presence of actuator fault and failures.

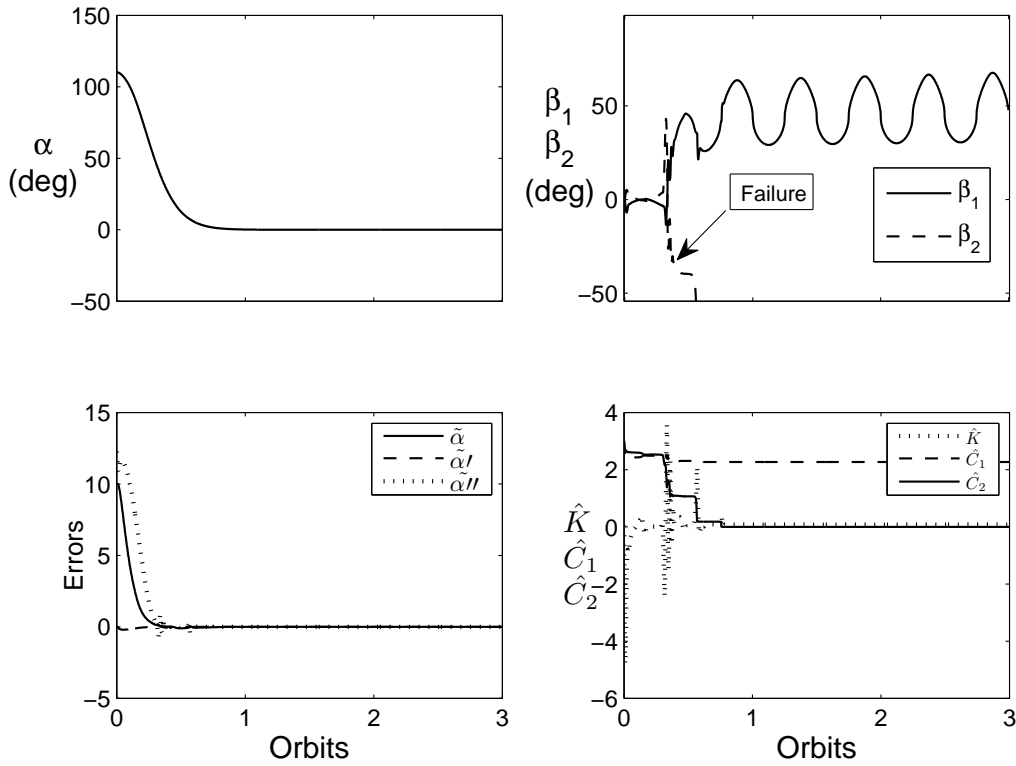


Figure 7.3: Performance of the adaptive sliding controller under solar flap failure at 0.3 orbit.

#### 7.4.4 Actuator loss of effectiveness

In this fault scenario, the actuator has a loss of its control effectiveness (i.e., impaired control surfaces). As a result of this fault, while executing manoeuvres, the torque produced by the defective solar panel is considerably less than its nominal value. Here we have simulated an actuator performance degradation of 90% in solar flap 1 (Fig.7.7). The operational solar flap 2 compensates for this loss in effectiveness of solar flap 1 by increased deflection to maintain the desired satellite attitude. The maximum deflection in solar flap 2,  $|\beta_2|_{\max}$ , is  $13.5^\circ$ . Furthermore the pitch tracking remains unaffected.

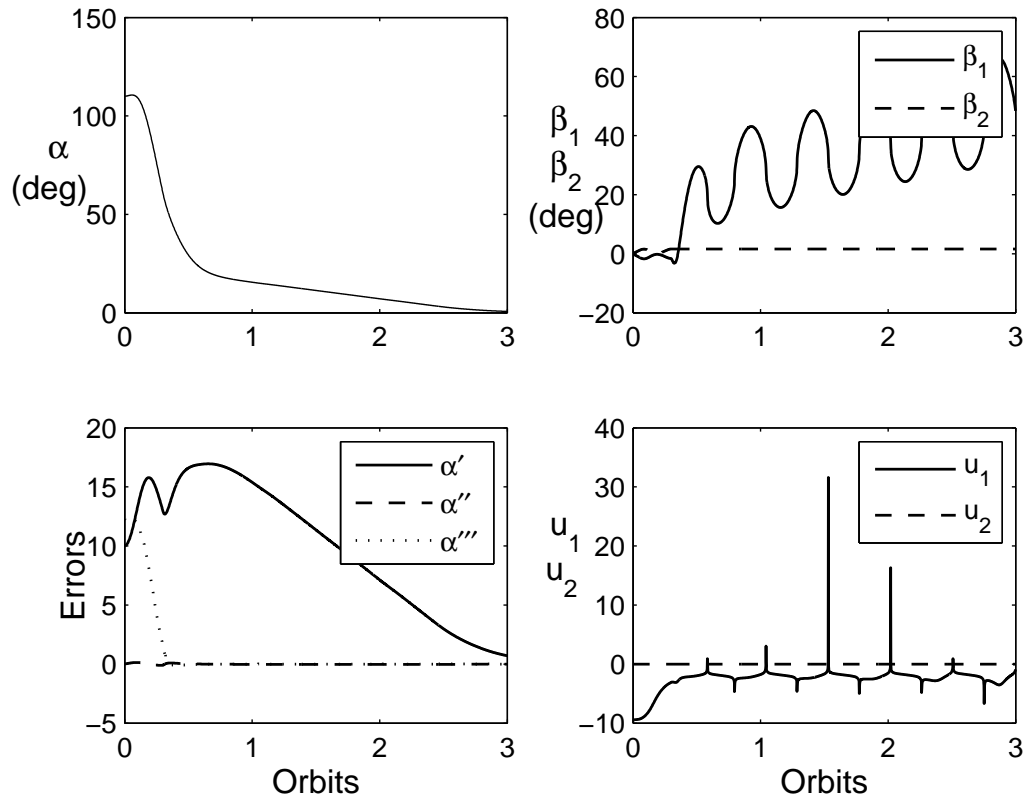


Figure 7.4: Performance of the sliding controller under solar flap failure at 0.3 orbit.

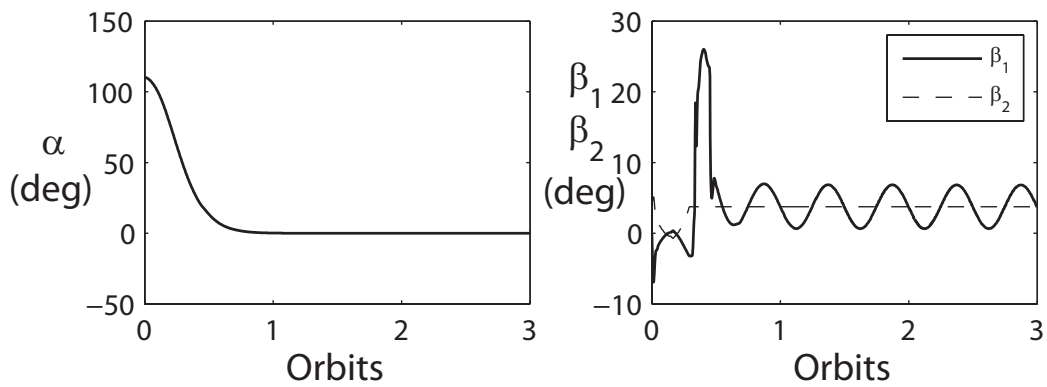


Figure 7.5: Performance of the adaptive sliding controller under actuator stuck fault from 0.3 orbit.

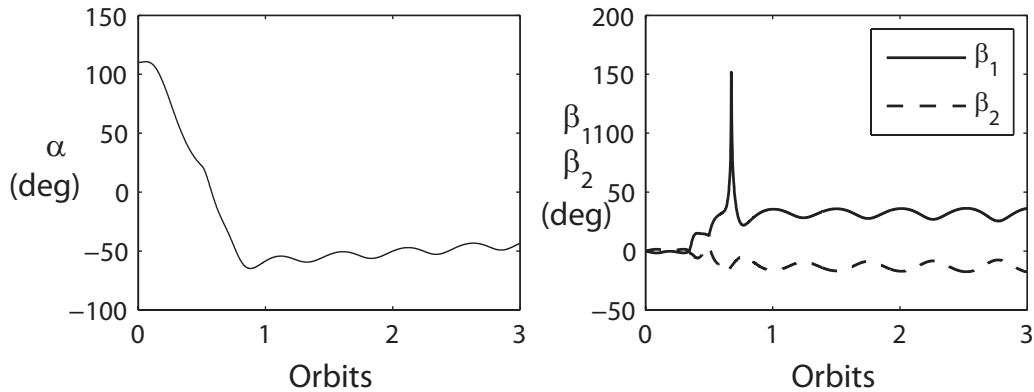


Figure 7.6: Performance of the sliding controller under actuator stuck fault from 0.3 orbit.

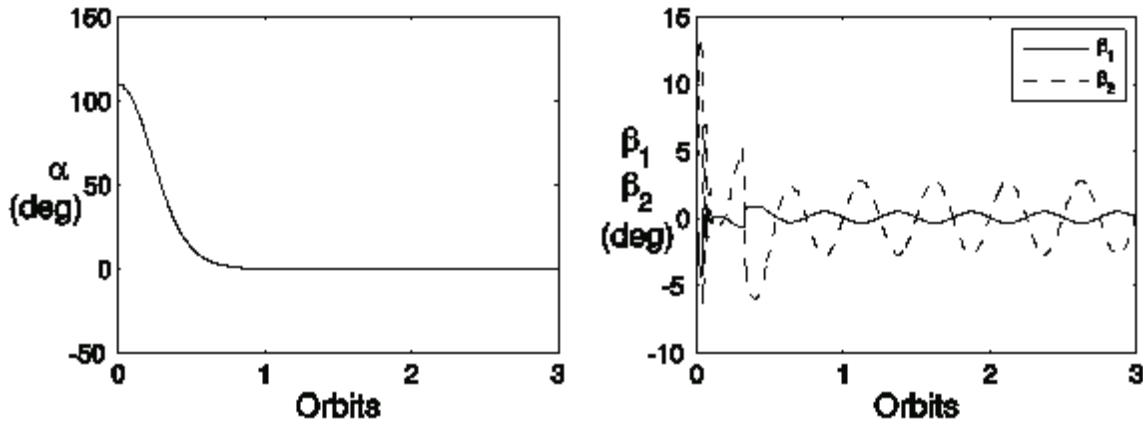


Figure 7.7: Performance of the adaptive sliding controller under actuator degradation (90%) fault.

### 7.4.5 Time varying actuator fault

Next, we consider a fault scenario in which the actuator has a time varying periodic fault associated with it. This fault condition differs from the actuator stuck fault in the sense that here the actuator fault is periodic rather than a steady state. Hence the torque associated with this type of faulty flap will also be time varying. The fault is simulated by a sinusoidal signal,  $0.2 \sin(10\theta)$  is applied on flap 2 from 0.3 orbit onwards (Fig.7.8). The operational flap compensates for this faulty condition without loss in control of satellite attitude tracking proving the robustness of the proposed controller. The maximum deflection

in solar flap 1,  $|\beta_1|_{\max}$ , is  $46.5^\circ$ .

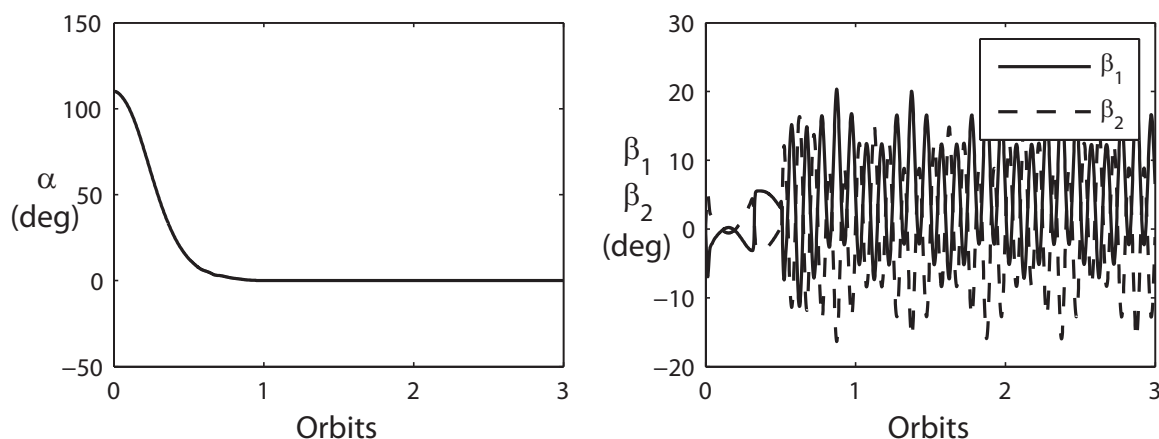


Figure 7.8: Performance of the adaptive sliding controller under periodic actuator fault from 0.3 orbits.

## 7.5 Three Axis Satellite Attitude Control

In this section, the efficacy of the adaptive control methodologies developed in Chapter 5 and 6 is examined in the presence of the faults and failures. The proposed three axis satellite attitude control system is subjected to similar faults and failures as in Section 7.4, and the system response is analyzed.

### 7.5.1 Satellite Attitude Control Using Solar Radiation Pressure

First, the performance of the proposed method of three axis satellite attitude control using solar radiation pressure is evaluated in the presence of faults or failures. The system equations of motion is modified by replacing the common term used to represent solar parameter ( $C_{srp}$ ) with individual solar parameter terms ( $C_{srp_j}$ ) corresponding to the four solar flaps ( $j = 1 - 4$ ) associated with the proposed system configuration (Fig. (6.1)). The resulting control law is given as

$$\begin{bmatrix} \beta'_j \\ \zeta'_j \end{bmatrix} = -\frac{1}{K_A \hat{C}_{jSRP} U'_a} \begin{bmatrix} \sigma \\ |\sigma| + \delta \end{bmatrix} \quad (7.48)$$

7.5.1.1 Solar flap failure

First, the system performance in the presence of failure of solar flap is evaluated. Assuming a failure of the solar flap 4 (i.e.,  $C_{srp4} = 0$ ), after 0.3 orbit, the attitude stabilization capability is verified. Referring to Fig.7.9, the operational flap, flap 3 ( $\varsigma_1$ ), compensates the failure by increasing the flap orientation, thereby achieving smooth satellite attitude stabilization.

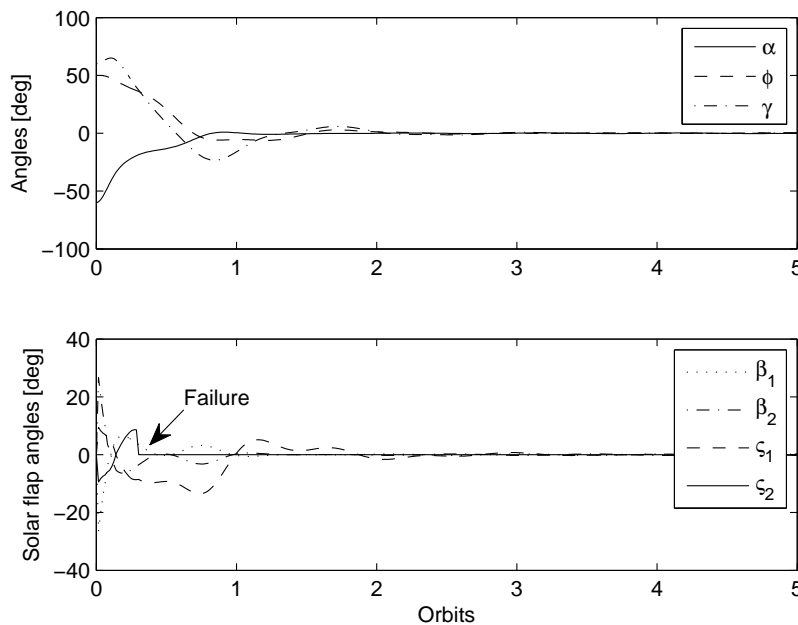


Figure 7.9: Performance of the adaptive controller under solar flap failure at 0.3 orbit.

7.5.1.2 Actuator stuck fault

Next, the fault caused due to the actuator remaining stuck at a particular position is considered. The solar flap 4 stops abruptly at 0.5 orbit (Fig.7.10). It can be observed that the solar flap 3 ( $\varsigma_1$ ) compensates for this fault as soon as  $\varsigma_2$  is jammed. It can be observed from Fig.7.10, that the orientation of  $\varsigma_1$  increases from 0.5 orbit to a maximum value of  $10.5^\circ$ . The controller demonstrates excellent performance in stabilizing the satellite even with one of the actuators stuck in position in this underactuated system configuration.

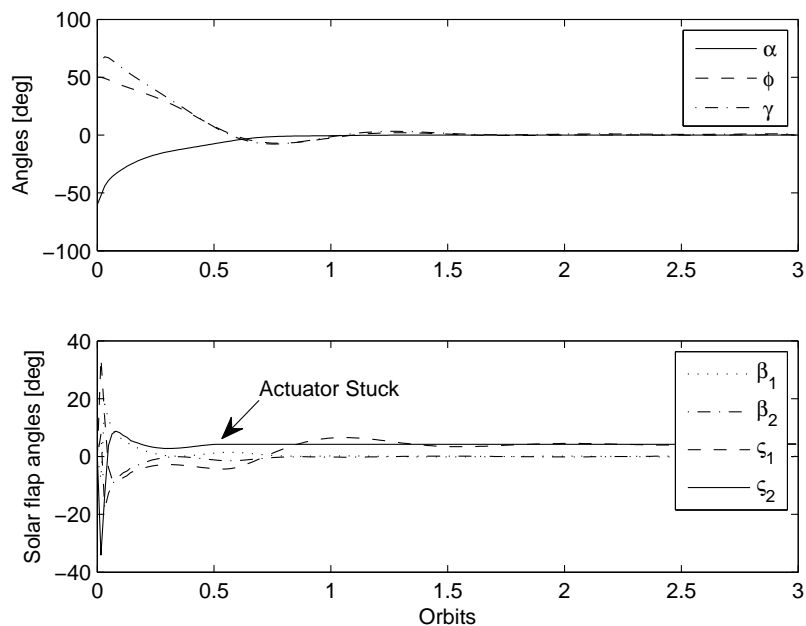


Figure 7.10: Performance of the adaptive controller under actuator stuck fault from 0.3 orbit.

### 7.5.1.3 Actuator loss of effectiveness

Systems performance under loss of control effectiveness in the actuator is examined next. A 90% performance degradation in solar flap 4 ( $\zeta_2$ ) is simulated (Fig.7.11). The fully operational solar flap 3 compensates by increased deflection to achieve a smooth stabilization of the satellite attitude. The maximum deflection  $|\zeta_1|_{\max}$  is  $22.5^\circ$ .

## 7.5.2 Satellite Attitude Control Using Aerodynamic Drag

The fault tolerant system performance of a satellite controlled using aerodynamic drag is evaluated in this section. The control law is developed by modifying the term used to represent uncertainties ( $\tilde{B}$ ) with individual parameters for each of the four drag plates associated with the proposed system configuration (Fig. (5.1)). The resulting control law is given as

$$\beta'_j = -\frac{1}{K_A \hat{B}_j U'_a} \left[ \frac{\sigma}{|\sigma| + \delta} \right] \quad (7.49)$$

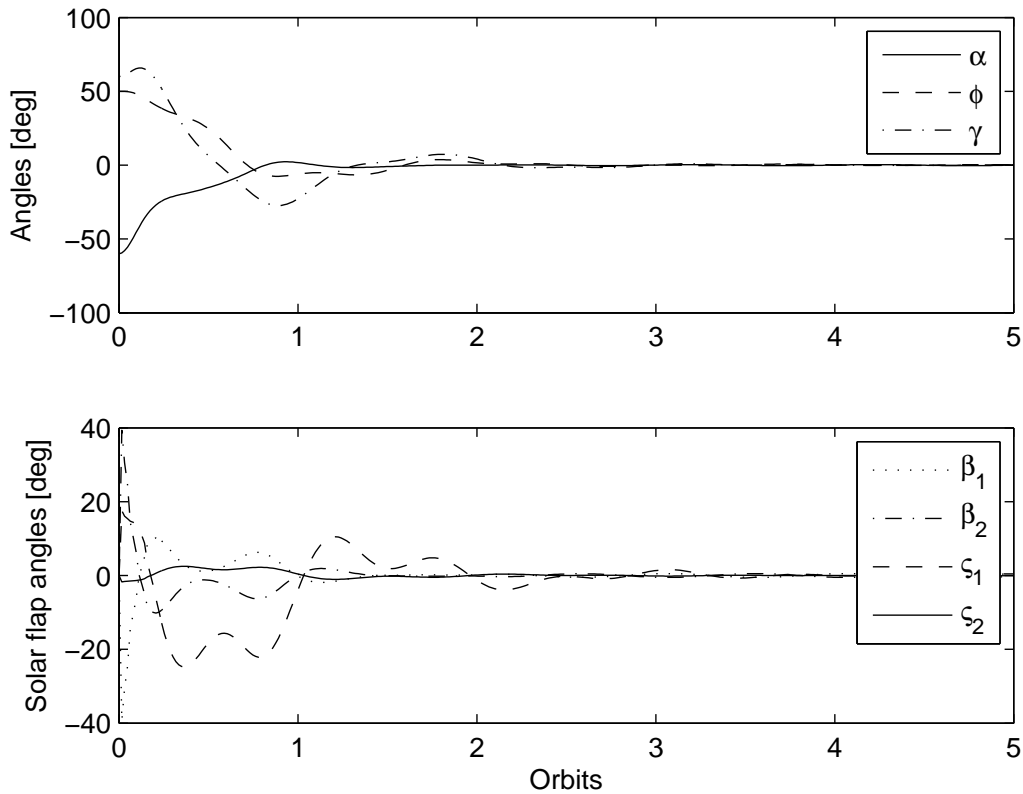


Figure 7.11: Performance of the adaptive controller under actuator degradation (90%) fault.

### 7.5.2.1 Drag plate failure

First, we evaluate the system performance in the case of failure of one of the drag plate. Drag plate 4 ( $\beta_4$ ) is assumed to have failed after 0.3 orbit. Referring to Fig. 7.12, it can be observed that the operational flap in the corresponding axis, flap 3 ( $\beta_3$ ), compensates this failure by increasing its orientation to achieve smooth satellite attitude stabilization.

### 7.5.2.2 Actuator stuck fault

Next, the fault caused due to the actuator remaining stuck at a particular position is considered. The drag plate 3 ( $\beta_3$ ) is assumed to have stopped abruptly at 0.5 orbit (Fig. 7.13). It can be observed that the oppositely places drag plate  $\beta_4$  compensates for this fault as soon as  $\beta_3$  is jammed. The maximum value of the drag plate orientation is  $|\beta_4|_{\max}$  is  $20.5^\circ$ .

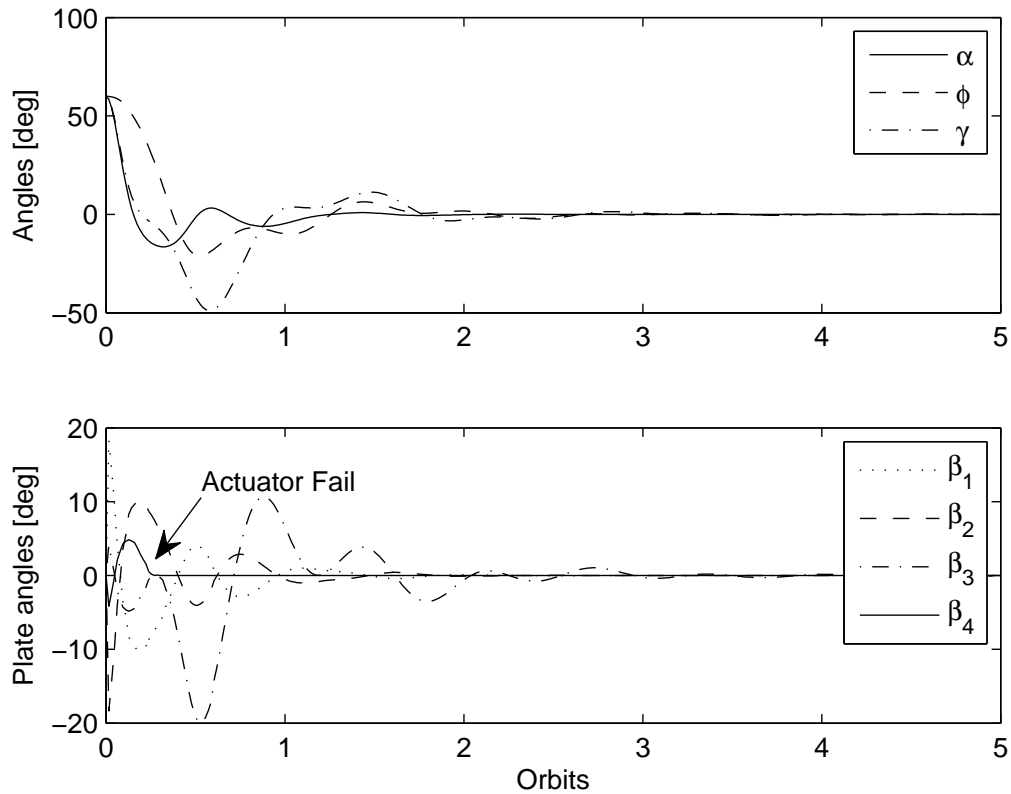


Figure 7.12: Performance of the adaptive controller under failure at 0.3 orbit.

The controller demonstrates excellent performance in stabilizing the satellite even when with one of the actuators stuck in position in this underactuated system configuration.

### 7.5.2.3 Actuator loss of effectiveness

Systems performance under loss of control effectiveness in the actuator is examined next. A 90% performance degradation in actuator 4 is simulated (Fig.7.14). The operational drag plate 3 in the corresponding axis compensates by increased deflection to achieve a smooth stabilization of the satellite attitude. The maximum deflection in solar flap 2,  $|\beta_2|_{\max}$ , is  $20.5^\circ$ .

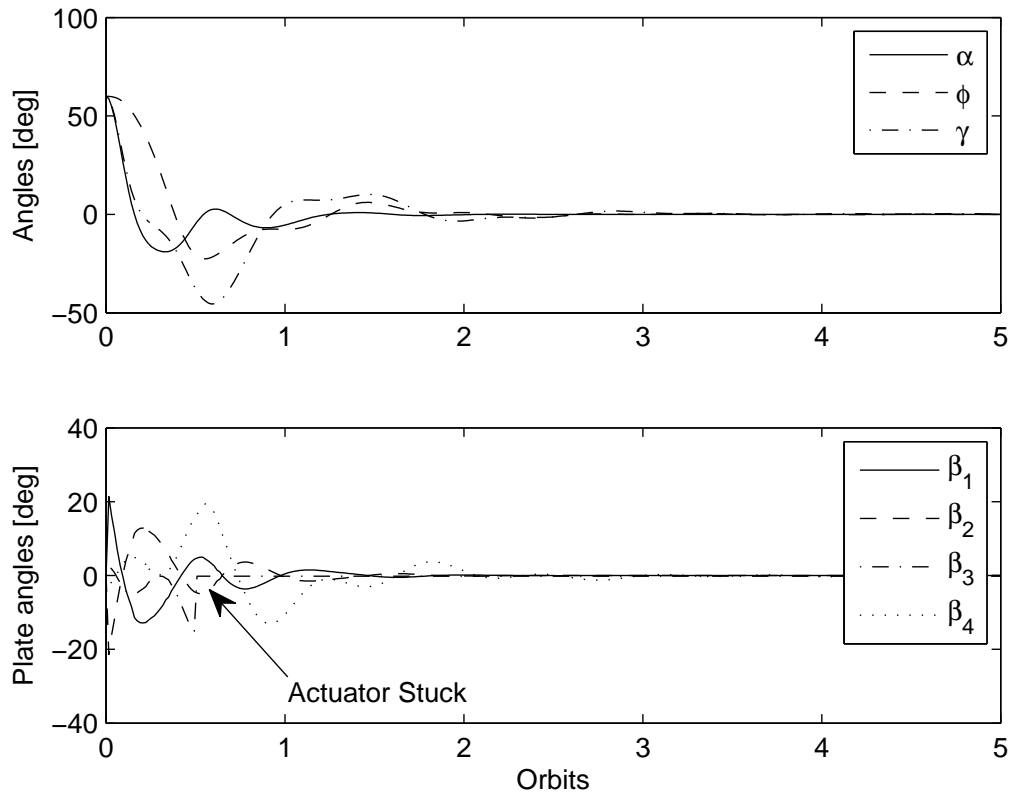


Figure 7.13: Performance of the adaptive controller under actuator stuck fault from 0.3 orbit.

## 7.6 Summary

Results from chapters 5 and 6 confirmed the robustness of the proposed attitude control strategy in the presence of system disturbances and uncertainties. This chapter examines system performance of the proposed attitude control systems in the presence of some possible failure or fault scenarios with respect to the solar flaps or drag plates respectively. First, the pitch attitude control of a satellite controlled using solar radiation pressure in the presence of different faults or failure is examined. A comparison to a similar control technique without adaptive control is also carried out. Compared to sliding mode control without adaptation, the proposed adaptive sliding mode control results in high attitude performance especially in actuator fault and failure scenarios. The performance of the proposed three axis satellite attitude control methodologies using aerodynamic drag or solar

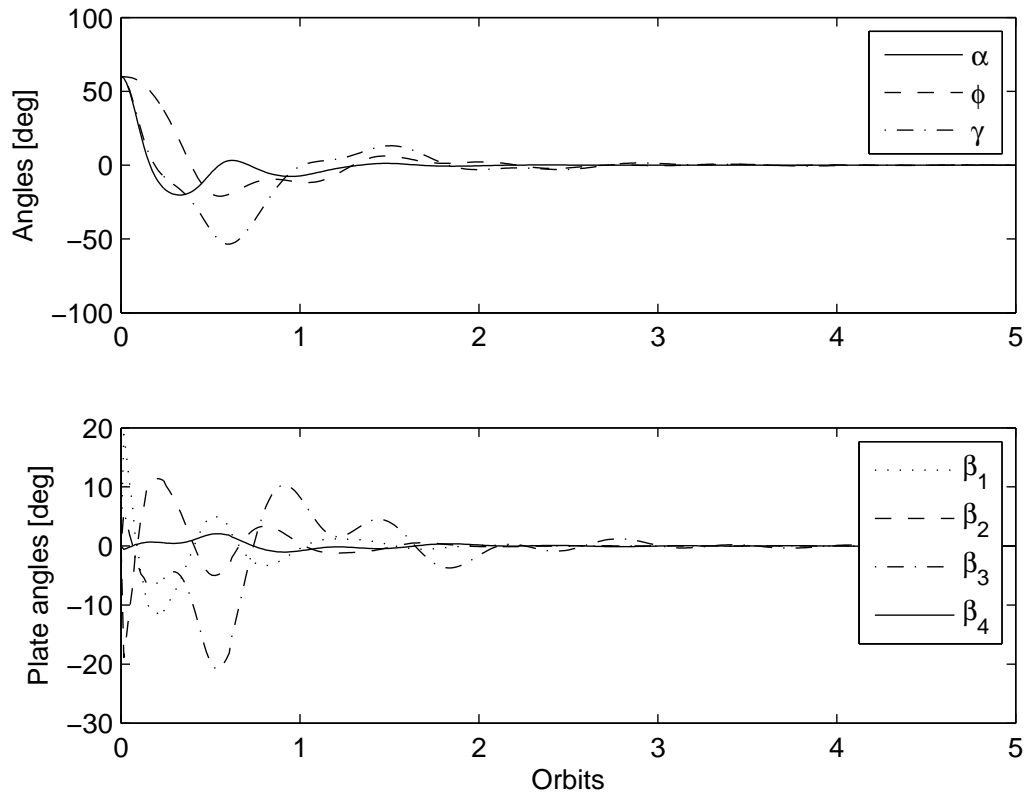


Figure 7.14: Performance of the adaptive controller under actuator degradation (90%) fault.

radiation pressure in the presence similar faults or failures is also evaluated. The controller demonstrates robust performance in the presence of several failure scenarios such as failure of one of the flaps or drag plates, one of the flaps/drag plates getting blocked or jammed at a particular position. In all the cases smooth satellite attitude stabilization is achieved.



# Conclusions

---

**F**ORMATION flying of multiple satellites is an enabling technology for many future space missions including deep space as well as Earth observation. As mentioned in Chapter 1, achieving the mission objectives with minimum fuel expenditure in the presence of various external disturbances and uncertainties is one of the challenges in coordinated satellite formation flying. In a typical satellite control system, the twin environmental forces of aerodynamic drag and solar radiation pressure constitute two of these disturbance forces. However, in this thesis we analyze the use of aerodynamic drag or SRP for satellite formation and attitude control and use of these forces is examined in detail to achieve multiple satellite formation flying as well as satellite attitude control. Satellite formation and attitude control in low Earth orbit is achieved using aerodynamic drag, while solar radiation pressure is used as the control input in the geostationary orbit. Nonlinear adaptive control strategies that are robust to parameter and system uncertainties and external disturbances are developed to accomplish the proposed satellite control technique. This chapter summarizes the major results and contributions of this dissertation, and discusses some recommended future research efforts to extend the current work.

## 8.1 Contributions Outline

Existing literature on the use of the twin environmental forces for satellite control focuses on the development of linear control techniques and is evaluated for a limited operating range. In this thesis, variable structure based nonlinear control algorithms that are capable of accurate trajectory tracking, fast satellite maneuvering and reconfiguration are developed. The proposed methodology is evaluated for a wide range of operating conditions in a more realistic space environment. The problem of controlling single as well as multiple

follower satellites using aerodynamic drag or solar radiation pressure in a leader-follower configuration is evaluated. The following is a brief summary of the main contributions of this thesis:

- *Underactuated Satellite Control*

Use of aerodynamic drag or SRP for satellite formation or attitude control represents an underactuated control problem, and the existing literature proposes hybrid controllers or proposes control methodologies based on linear techniques resulting in restricted range of operation. Here we approach this as an underactuated problem and develop control algorithms that properly address this scenario and provide stability proofs for the resulting closed-loop system.

- *Sliding Mode Control*

To address the uncertainties associated with the twin environmental forces, a robust control methodology is of paramount importance. Here we employ the sliding mode control algorithm to address these issues. Higher order sliding mode control technique is also implemented to counter the non-affine structure of the control inputs generated by aerodynamic drag or SRP.

- *Adaptive Control*

Due to the lack of precise knowledge of all the parameters in the environmental models and its time varying nature, adaptive control laws are developed. Here the unknown parameters are estimated online and then used in the feedback control law.

A brief discussion of these contributions are provided in the following sections.

### 8.1.1 Satellite Formation Control using Aerodynamic Drag

The existing literature on the use of aerodynamic drag for satellite formation flying in LEO is based on simplified system dynamics and environmental models. Also, these proposed control algorithms are based on the linearized plant models, and are validated over a limited range of operation. We start the investigation by considering a single follower satellite in the leader-follower formation system. The satellites in the formation are assumed

to be attached with maneuverable drag plates. A nonlinear adaptive control algorithm based on sliding mode control methodology to maintain the satellite formation is developed. Different formation scenarios including different types of formations and formation reconfiguration maneuvers are evaluated. The effect of navigation and initial offset errors on the formation system are also examined. Finally, the concept of using aerodynamic drag for satellite formation flying is extended to the case of multiple follower satellites. A heuristic control technique is proposed to maintain the multiple satellite formation system. The viability of this heuristic control methodology for different formation scenarios is evaluated using numerical simulation including Monte Carlo simulation. All numerical simulations are performed on a high fidelity satellite dynamics and environmental model. The effect of variations in the system parameters such as variation in the density and altitude, on the system performance is also evaluated. Overall, the theoretical and simulation results establish the robustness of the proposed satellite formation control scheme and can be considered in future satellite formation systems including multiple satellite formation flying systems.

### 8.1.2 Satellite Formation Control using Solar Radiation Pressure

Next, the application of solar radiation pressure for satellite formation control is examined. A formation flying system with the satellites attached with maneuverable solar flaps is proposed. In the case of SRP, in-plane and out-of-plane control is achievable by the appropriate orientation of the solar flaps. From a control perspective, the system with two control angles represents an underactuated control problem. The proposed system is modified into a fully actuated control problem by incorporating an additional input in the form of change in area of the solar flaps. Nonlinear adaptive control algorithm based on sliding mode is developed to accomplish satellite formation control. The system response to different types of desired formation is examined. The performance of the proposed system in the presence of uncertainties including solar aspect angle  $\psi$ , is also examined. Initial offset and navigation errors are introduced and the performance of the formation system in this scenario is evaluated. Finally, the concept of using SRP for satellite formation flying is extended to the multiple follower satellite system. A heuristic control methodology

is proposed to maintain the multiple satellite formation system, and evaluated for all the desired formations. The numerical simulations are performed on a high fidelity satellite dynamics and environmental model. Overall, the theoretical and simulation results establish the robustness of the proposed control system. Combined with the recent developments in solar sail technology this study will help in the advancement of the proposed methodology of using SRP for satellite formation control.

### 8.1.3 Satellite Attitude Control using Aerodynamic Drag

Use of aerodynamic drag for satellite attitude control is examined. The proposed system comprises of a satellite with two pairs of oppositely placed drag plates, and the satellite attitude is controlled by the suitable rotation of these drag plates. One set of drag plates is attached along the  $x$ -axis and another along the  $z$ -axis. Hence there is no explicit control available in the roll axis. This underactuated system configuration along with the proposed nonlinear control algorithm based on the theory of sliding mode generates the required torque to achieve complete three axis attitude control of the satellite. The adaptive nonlinear control algorithm achieves fast system stabilization and also provides robustness to system uncertainties. A high-fidelity nonlinear model is used to carry out the numerical simulation and the system performance is analyzed for a variety of scenarios including large initial conditions and unstable gravity gradient inertia configuration. Results of the numerical simulation shows that the proposed attitude control strategy is robust against disturbances and uncertainties. Thus, the proposed nonlinear adaptive controller can be considered as an ideal candidate for satellite attitude control in future LEO space missions.

### 8.1.4 Satellite Attitude Control using Solar Radiation Pressure

Feasibility of achieving three axis satellite attitude control using solar radiation pressure is investigated. The proposed system consists of two pairs of oppositely placed lightweight solar flaps. The proposed system configuration provides explicit control authority in the pitch and roll axis of the satellite. Using nonlinear control strategy, the complete three axis attitude control is achieved. The synthesized closed-loop control law based on

adaptive sliding mode control rotates the solar flaps suitably to obtain proper SRP torque for desired attitude performance. The rotation angle of solar flaps is continuously adjusted as per the control laws. The efficacy of the control methodology is tested on a nonlinear system model considering various uncertainties in the system parameters including satellite inertia matrix and solar flaps. Results of the numerical simulation shows that the proposed attitude control strategy is robust against disturbances and uncertainties as well as very effective with initial attitude tracking errors. Based on the numerical simulations, the following main conclusions can be drawn: a) The controller exhibits excellent performance in the presence of uncertainties in system parameters including solar aspect angle  $\psi$ , and stabilizes the desired satellite attitude rapidly. b) The controller shows robust performance in the presence of external disturbances. Thus, the proposed nonlinear adaptive controller can be used for satellite attitude control in future geostationary space missions.

### 8.1.5 Fault Tolerant Satellite Attitude Control Using Solar Radiation Pressure / Aerodynamic Drag

The performance of the proposed system in the presence of failure scenarios such as failure of one of the drag plates/solar flaps, one of the drag plates/solar flaps getting blocked or jammed at a particular position is also examined. First, an adaptive control algorithm for pitch attitude control of an SRP based satellite is evaluated for the different fault/failure scenarios. The pitch attitude tracking was not affected by these faults/failures and demonstrated robust performance. Next, The efficacy of the three axis attitude control system for both aerodynamic drag and SRP based satellite is evaluated. The fault/failures did not cause any disturbance on the attitude of the satellite, and the different fault/failures were compensated by the healthy drag plates/solar flaps on the satellite. A comparison between the system controlled by an adaptive control algorithm and a non-adaptive control algorithm is performed to validate the robustness of the proposed control technique. The control law without adaptation was not able to handle the fault/failure scenarios leading to an unstable satellite attitude orientation.

## 8.2 Limitations of the proposed technique

In this section it is also appropriate to mention some of the limitation/disadvantages in using aerodynamic drag or solar radiation pressure for satellite control. With respect to satellite formation flying, the achievable relative positions cannot be controlled to a very high accuracy as compared to a SFF controlled using external thrusters. In the case of aerodynamic drag for SFF, cross track drift is difficult to control due to lack of control authority in that axis. Since aerodynamic drag is a retarding force, it will cause the satellite to lose altitude during the satellite mission, making the need for orbit raising. In the case of SRP, the solar flaps can undergo optical parameter degradation due to continuous exposure to sunlight resulting in decreased efficiency in the performance of the control system. During formation reconfiguration overshoot is observed in the relative errors during the initial part of the formation stabilization. This is a result of the trade-off between the maximum allowable orientation of the drag plates and the faster convergence of relative errors. Similarly in the case of satellite attitude control highly precise pointing accuracy in the range of less than  $0.01^\circ$  in all axes is not achievable with the proposed satellite attitude control system. The increased exposed surface due to the drag plates and solar flaps can also result in micro-meteorite collisions, which in turn might affect the control performance.

## 8.3 Future Work

This study proposes techniques to utilize the aerodynamic drag or solar radiation pressure for satellite formation or attitude control. Theoretical results are examined through numerical simulation. There remain several areas yet to be explored. Some of these areas for future work are outlined as follows:

Here we consider satellite formation control and attitude control as two individual problems. During satellite formation flying, it is assumed that the attitude of the satellite is controlled, and during satellite attitude control, formation maintenance is not considered. Hence simultaneous satellite formation as well its attitude control will be an interesting topic for future research.

---

We propose satellite control using aerodynamic drag in low Earth orbit and solar radiation pressure in the geostationary orbits. The feasibility of using solar radiation pressure in LEO can be examined in detail, and this is especially promising for out-of-plane control during satellite formation in LEO. This can help achieve complete "propellant-less" formation control.

The drag plates and solar flaps considered here are assumed to be perfectly flat. The effect of billowing on the system performance can also be examined in detail. In the case of multiple satellite formation system, the control architecture needs to address the issue of collision avoidance between satellites in the formation. This is very important for a close formation flying scenario.



# Bibliography

- [Aorpimai *et al.* 1999] Aorpimai, M., Palmer, P. L., & Steyn, W. H., “Dynamic ground-track chasing constellation using atmospheric drag,” *Proceedings of 4th ESA International Conference on Spacecraft Guidance, Navigation and Control Systems*, Noordwijk, Holland, August, 1999, Pages: 227–232. 10
- [Bauer *et al.* 2001] Bauer, F. H., Bristow, J. O., Carpenter, J. R., Garrison, J. L., Hartman, K. R., Lee, T., Long, A. C., Kelbel, D., Lu, V., How, J. P., Busse, F., Axelrad, P., & Moreau, M., “Enabling spacecraft formation flying in any earth orbit through spaceborne GPS and enhanced autonomy technologies,” *Space Technology*, Vol. 20, No. 4, 2001, Pages: 175–185. 8
- [Bevilacqua & Romano 2008] Bevilacqua, R., & Romano, M., “Rendezvous maneuvers of multiple spacecraft using differential drag under J2 perturbation,” *Journal of Guidance, Control, and Dynamics*, Vol. 31, No. 6, 2008, Pages: 1595–1607. 11
- [Bevilacqua *et al.* 2009] Bevilacqua, R., Hall, J. S., & Romano, M., “Multiple spacecraft rendezvous maneuvers by differential drag and low thrust engines,” *Celestial Mechanics and Dynamical Astronomy*, Vol. 106, No. 1, 2009, Pages: 69–88. 11, 60
- [Biggs & McInnes 2009] Biggs, J. D., & McInnes, C. R., “Solar sail formation flying for deep-space remote sensing,” *Journal of Spacecraft and Rockets*, Vol. 46, No. 3, 2009, Pages: 670–678. 14
- [Black *et al.* 1968] Black, W.L., Crockerj, M.C., & Swenson, E.H., “Stationkeeping a 24-Hr satellite using solar radiation pressure,” *Journal of Spacecraft*, Vol. 5, No. 3, 1968, Pages: 335–336. 13
- [Bladt & Lawrence 2005] Bladt, J. J., & Lawrence, D. A., “Solar sail attitude control performance comparison,” *Advances in the Astronautical Sciences, AAS 05-003*, Vol. 121, 2005, Pages: 29–48. 15

- [Blomquist 1999] Blomquist, R., “Solar Blade Nanosatellite Development: Heliogyro Deployment, Dynamics, and Control,” *Proceedings of 13th USU/AIAA Small Satellite Conference*, Logan, Utah, August 23-26, 1999. 14
- [Carter & Humi 2002] Carter, T., & Humi, M., “Clohessy-Wiltshire equations modified to include quadratic drag,” *Journal of Guidance, Control, and Dynamics*, Vol. 25, No. 6, 2002, Pages: 1058–1063. 11
- [Chen *et al.* 2000] Chen, Y. H., Hong, Z. C., Lin, C. H., & Chern, J. S., “Aerodynamic and gravity gradient stabilization for microsattellites,” *Acta Astronautica*, Vol. 46, No. 7, 2000, Pages: 491–499. 12, 99
- [Circi 2005] Circi, C., “Simple strategy for geostationary stationkeeping maneuvers using solar sail,” *Journal of Guidance, Control, and Dynamics*, Vol. 28, No. 2, 2005, Pages: 249–253. 13, 14
- [Circi 2007] Circi, C., “Three-axis attitude control using combined gravity-gradient and solar pressure,” *Proceedings of the Institution of Mechanical Engineers, Part G: Journal of Aerospace Engineering*, Vol. 221, No. 1, 2007, Pages: 85–90. 15
- [Clohessy & Wiltshire 1960] Clohessy, W., & Wiltshire, R., “Terminal guidance systems for satellite rendezvous,” *Journal of the Aerospace Sciences*, Vol. 27, No. 9, 1960, Pages: 653–658. 11, 27, 49
- [Damaren 2007] Damaren, C. J., “Almost periodic relative orbits under J2 perturbations,” *Proceedings of the Institution of Mechanical Engineers, Part G: Journal of Aerospace Engineering*, Vol. 221, No. 5, 2007, Pages: 767–774. 60
- [Davila *et al.* 2005] Davila, J., Fridman, L., & Levant, A., “Second-order sliding-mode observer for mechanical systems,” *IEEE Transactions on Automatic Control*, Vol. 50, No. 11, 2005, Pages: 1785–1789. 56, 58
- [Edwards & Spurgeon 1998a] Edwards, C., & Spurgeon, S., *Sliding Mode Control - Theory and Applications*, First Edition, Taylor and Francis Ltd, London, UK, 1998. 55

- [Edwards & Spurgeon 1998b] Edwards, C., & Spurgeon, S.K., *Sliding Mode Control - Theory and Applications*, Taylor and Francis Ltd, London, UK, 1998. 40
- [Folta & Hawkins 1996] Folta, D., & Hawkins, A., “EO-1 Technology Validation Report - Enhanced Flying Formation,” *EO-1 Validation Report*, retrieved from: <http://eo1.gsfc.nasa.gov/new/validationReport/>, Sept 18, 1996. 10, 45
- [Folta *et al.* 2002] Folta, D., Bristow, J., Hawkins, A., & Dell, G., “NASA’s autonomous formation flying technology demonstration, Earth Observing-1,” *Proceedings of First International Symposium on Formation Flying Missions and Technologies*, Toulouse, France, Oct 29-30, 2002. 12
- [Fourcade 2005] Fourcade, J., “Use of Differential drag as stationkeeping strategy for formation flying satellite,” *Proceedings of 4th International Workshop on Satellite Constellations and Formation Flying*, Brazil, 14-16 February, 2005. 13
- [Gombosi 1994] Gombosi, T.I., *Gaskinetic Theory*, Cambridge Univ. Press, Cambridge, England, 1994. 35, 104
- [Hill 1878] Hill, G., “Researches in the lunar theory,” *American Journal of Mathematics*, Vol. 1, 1878, Pages: 5–26. 27, 49
- [Hui *et al.* 2006] Hui, Li., Qinyu, Z., Naiton, Z., & Yan, Z., “Precision of TDOA positioning using formation flying satellites on geosynchronous Earth orbit,” *Proceedings of the IEE International Conference on Wireless, Mobile and Multimedia Networks*, Hangzhou, China, 2006. 81
- [Humi & Carter 2001] Humi, M., & Carter, T., “Fuel-optimal rendezvous in a central force field with linear drag,” *Proceedings of the American Astronautical Society Paper, 01-236*, Vol. 108 II, 2001, Pages: 1875–1892. 11
- [Humi & Carter 2002] Humi, M., & Carter, T., “Models of motion in a central force field with quadratic drag,” *Celestial Mechanics and Dynamical Astronomy*, Vol. 84, No. 3, 2002, Pages: 245–262. 11

- [Jayaraman 1980] Jayaraman, T. S., "Time-Optimal orbit transfer trajectory for solar sail spacecraft," *J Guid Control*, Vol. 3, No. 6, 1980, Pages: 536–542. 14
- [Johnson *et al.* 2007] Johnson, L., Young, R., & Montgomery, E.E., "Recent advances in solar sail propulsion systems at NASA," *Acta Astronautica*, Vol. 61, 2007, Pages: 376–382. 5
- [Johnson *et al.* 2010] Johnson, L., Whorton, M., Heaton, A., Pinson, R., Laue, G., & Adams, C., "NanoSail-D: A solar sail demonstration mission," *Acta Astronautica*, Vol. Article in press, 2010, Pages: 1–5. 5
- [Kaplan 1976] Kaplan, M.H., *Modern Spacecraft Dynamics and Control*, John Wiley and Sons, New York, NY, 1976. 121
- [Karr & Cleland 1975] Karr, G. R., & Cleland, J.G., "Aerodynamic lift effect on satellite orbits," *13th AIAA Aerospace Sciences Meeting*, Pasadena, CA, January, 1975. 37
- [Krieger & Zink 2007] Krieger, G., Moreira A. Fiedler H. Hajnsek I. Werner M. Younis M., & Zink, M., "TanDEM-X: A satellite formation for high-resolution SAR interferometry," *IEEE Transactions on Geoscience and Remote Sensing*, Vol. 45, No. 11, 2007, Pages: 3317–3341. 45, 64
- [Kumar *et al.* 1995] Kumar, R. R., Mazanek, D.D., & Heck, M. L., "Simulation and shuttle hitchhiker validation of passive satellite aerostabilization," *Journal of Spacecraft and Rockets*, Vol. 32, No. 5, 1995, Pages: 806–811. 12
- [Kumar *et al.* 2004a] Kumar, K. D., Bang, H. C., & Tahk, M. J., "Formation flying of satellites using solar radiation pressure," *Proceedings of 24th International Symposium on Space Technology and Science*, Miyazaki, Japan, May 30 - June 6, 2004. 13
- [Kumar *et al.* 2004b] Kumar, K. D., Tahk, M. J., & Bang, H. C., "Formation flying of satellites using aerodynamics and solar radiation forces," *Proceedings of the KSAS-JSASS Joint Symposium on Aerospace Engineering*, Seoul, South Korea, Nov 18-19, 2004. 14, 15

- [Kumar *et al.* 2006] Kumar, K.D., Bang, H.C., & Tahk, M.J., “New attitude control approach for satellites in elliptic orbits using solar radiation pressure,” *Acta Astronautica*, Vol. 59, No. 6, 2006, Pages: 462 – 473. 15, 155
- [Kumar *et al.* 2007a] Kumar, B.S., Ng, A., & Yoshihara, K., “Flight Dynamics and Control of the JC2Sat-FF Mission,” *Proceedings of the AAS Astrodynamics Specialist Conference*, Mackin Island, MI, USA, August 19-23, 2007. 12
- [Kumar *et al.* 2007b] Kumar, B.S., Ng, A., Yoshihara, K., & A, De Ruiter., “Differential drag as a means of spacecraft formation control,” *Proceedings of IEEE Aerospace Conference*, Big Sky, MT, March, 2007. 11
- [Kumar *et al.* 2007c] Kumar, K. D., Bang, H. C., & Tahk, M. J., “Satellite formation flying using along-track thrust,” *Acta Astronautica*, Vol. 61, No. 7-8, 2007, Pages: 553–564. 48
- [Kumar 1988] Kumar, K., “A solar attitude controller for extending operational life-span of communications satellites,” *Acta Astronautica*, Vol. 17, No. 1, 1988, Pages: 61–67. 14
- [Kumar 2006] Kumar, K.D., *Fundamentals of Dynamics and Control of Space Systems*, First Edition, Ryerson University Press, Toronto, Canada, 2006. xvii, 1, 24, 33, 34, 89
- [Larson 1999] Larson, W.J., Wertz J.R., *Space Mission Analysis and Design*, Third Edition, Kluwer Academic Publishers, Dordrecht, Boston, London, 1999. 1
- [LaSalle 1960] LaSalle, J. P., “Some Extensions of Liapunov’s Second Method,” *IRE Transactions On Circuit Theory*, 1960, Pages: 520–527. 54, 88, 113, 134
- [Leipold *et al.* 1996] Leipold, M., Seboldt, W., Lingner, S., Borg, E., Herrmann, A., Pabsch, A., Wagner, O., & Brückner, J., “Mercury sun-synchronous polar orbiter with a solar sail,” *Acta Astronautica*, Vol. 39, No. 1-4, 1996, Pages: 143–151. Cited By (since 1996): 19. 14

- [Leipold *et al.* 1999] Leipold, M., Garner, C. E., Freeland, R., Hermann, A., Noca, M., Pagel, G., Seboldt, W., Sprague, G., & Unckenbold, W., "ODISSEE - A proposal for demonstration of a solar sail in earth orbit," *Acta Astronautica*, Vol. 45, No. 4-9, 1999, Pages: 557–566. 14
- [Leonard *et al.* 2004] Leonard, C. L., Hollister, W. M., & Bergmann, E. V., "Nanosatellite attitude stabilization using passive aerodynamics and active magnetic torquing," *Journal of Guidance, Control, and Dynamics*, Vol. 12, No. 1, 2004, Pages: 108–113. 10
- [Lievre 1986] Lievre, J., "Solar sailing attitude control of large geostationary satellite," *IFAC Proceedings of Automatic Control in Space*, 1986, Pages: 29–32. 15
- [Lohar *et al.* 1998] Lohar, F. A., Sherwani, A. K., & Misra, A. K., "Transfer between coplanar elliptical orbits using aerocruise," *Journal of Guidance, Control, and Dynamics*, Vol. 21, No. 6, 1998, Pages: 971–974. 11
- [London 1962] London, H. S., "Change of Satellite orbit plane by aerodynamic maneuvering," *Journal of the Aerospace Sciences*, Vol. 29, 1962. 11
- [Matthews & Leszkiewicz 1988] Matthews, M., & Leszkiewicz, S. J., "Efficient Spacecraft Formation keeping with Consideration of Ballistic Coefficient Control," *Proceedings of 26th AIAA Aerospace Sciences Meeting and Exhibit, AIAA-88-0375*, Reno, Nevada, USA, January, 1988. 10
- [McInnes *et al.* 2003] McInnes, C. R., Hughes, G., & McDonald, M., "Low cost Mercury orbiter and sample return missions using solar sail propulsion," *Aeronautical Journal*, Vol. 107, No. 1074, 2003, Pages: 469–478. 14
- [McInnes 1993] McInnes, Colin R., "Solar sail trajectories at the lunar L2 Lagrange point," *Journal of Spacecraft and Rockets*, Vol. 30, No. 6, 1993, Pages: 782–784. 14
- [McInnes 1999] McInnes, C.R., *Solar Sailing: Technology, Dynamics and Mission Applications*, First Edition, Springer-Praxis, Chichester, UK, 1999. 5

- [Miele 1996] Miele, A., “Recent Advances in the optimization and guidance of aeroassisted orbit transfer,” *Acta Astronautica*, Vol. 38, No. 10, 1996, Pages: 747–768. 11
- [Mierlo 2009] Mierlo, M.v., “Earth Observation using Japanese/Canadian Formation Flying Nanosatellites,” *Proceedings of 7th IAA Symposium on Small Satellites for Earth Observation*, Berlin, Germany, May, 2009. 12, 13, 64
- [Modi & Pande 1974a] Modi, V. J., & Pande, K. C., “Aerodynamic-solar hybrid attitude control of near-Earth satellites,” *Journal of the Astronautical Sciences*, Vol. 22, No. 1, 1974, Pages: 36–54. 15
- [Modi & Pande 1974b] Modi, V. J., & Pande, K. C., “Magnetic-solar hybrid attitude control of satellites in near-equatorial orbits,” *Journal of Spacecraft and Rockets*, Vol. 11, No. 12, 1974, Pages: 845–851. 15
- [Modi & Shrivastava 1973] Modi, V. J., & Shrivastava, S. K., “Optimized performance of a semipassive aerodynamic controller,” *AIAA Journal*, Vol. 11, No. 8, 1973, Pages: 1080–1085. 11, 99
- [Modi 1995] Modi, V. J., “On the semi-passive attitude control and propulsion of space vehicles using solar radiation pressure,” *Acta Astronautica*, Vol. 35, No. 2-3, 1995, Pages: 231–246. 14
- [M’Sirdi *et al.* 2008] M’Sirdi, N. K., Rabhi, A., Fridman, L., Davila, J., & Delanne, Y., “Second order sliding-mode observer for estimation of vehicle dynamic parameters,” *International Journal of Vehicle Design*, Vol. 48, No. 3-4, 2008, Pages: 190–207. 56
- [Neeck *et al.* 2005] Neeck, S. P., Magner, T. J., & Paules, G. E., “NASA’s small satellite missions for Earth observation,” *Acta Astronautica*, Vol. 56, No. 1-2, 2005, Pages: 187–192. 8
- [NSSDC 1967] NSSDC, NASA, “Cosmos149,NSSDC ID:1967-024A,” *NSSDC Spacecraft details*, retrieved from: <http://nssdc.gsfc.nasa.gov/nmc/masterCatalog.do?sc=1967-024A> in December 2010, Sept 18, 1967. 12, 13

- [NSSDC 1970] NSSDC, NASA, “Cosmos320,NSSDC ID:1970-005A,” *NSSDC Spacecraft details*, retrieved from: <http://nssdc.gsfc.nasa.gov/nmc/spacecraftDisplay.do?id=1970-005A> in December 2010, Sept 18, 1970. 12, 13
- [Otten & McInnes 2001] Otten, M., & McInnes, C. R., “Near minimum-time trajectories for solar sails,” *Journal of Guidance, Control, and Dynamics*, Vol. 24, No. 3, 2001, Pages: 632–634. 14
- [Palmerini *et al.* 2005] Palmerini, G. B., Sgubini, S., & Taini, G., “Spacecraft orbit control using air drag,” *Proceedings of the International Astronautical Congress Paper 05-C1.6.10*, Fukuoka, Japan, Oct 17-21, 2005. 11
- [Pande & Venkatachalam 1979] Pande, K. C., & Venkatachalam, R., “On optimal aerodynamic attitude control of spacecraft,” *Acta Astronautica*, Vol. 6, No. 11, 1979, Pages: 1351–1359. 12, 99
- [Patel *et al.* 2008] Patel, T. R., Kumar, K. D., & Behdinan, K., “Satellite attitude control using solar radiation pressure based on non-linear sliding mode control,” *Proceedings of the Institution of Mechanical Engineers, Part G: Journal of Aerospace Engineering*, Vol. 222, No. 3, 2008, Pages: 379–392. 15
- [Patel *et al.* 2009] Patel, T. R., Kumar, K. D., & Behdinan, K., “Variable structure control for satellite attitude stabilization in elliptic orbits using solar radiation pressure,” *Acta Astronautica*, Vol. 64, No. 2-3, 2009, Pages: 359–373. 15
- [Picone *et al.* 2000] Picone, J.M., Drob, D.P., Meier, R.R., & Hedin, A.E., “NRLMSISE-00: A New Empirical Model of the Atmosphere,” *NRLMSISE Atmospheric Model*, retrieved from: <http://www.nrl.navy.mil/research/nrl-review/2003/atmospheric-science/picone/> in December 2010, 2000. 34
- [Powers & Coverstone 2001] Powers, R. B., & Coverstone, V. L., “Optimal solar sail orbit transfers to synchronous orbits,” *Journal of the Astronautical Sciences*, Vol. 49, No. 2, 2001, Pages: 269–281. 14

- [Psiaki 2004] Psiaki, M. L., “Nanosatellite attitude stabilization using passive aerodynamics and active magnetic torquing,” *Journal of Guidance, Control, and Dynamics*, Vol. 27, No. 3, 2004, Pages: 347–355. 12, 99
- [Rao *et al.* 2002] Rao, A. V., Tang, S., Hallman, & P., W., “Recent Advances in the Optimization and Guidance of Aeroassisted Orbit Transfer,” *Optimal Control Applications and Methods*, Vol. 23, No. 4, 2002, Pages: 215–238. 11
- [Ravindran & Hughes 1972] Ravindran, R., & Hughes, P. C., “Optimal aerodynamic attitude stabilization of near-Earth satellites,” *Journal of Spacecraft and Rockets*, Vol. 9, No. 7, 1972, Pages: 499–506. 11
- [Regan 1984] Regan, F. J., *Re-Entry Vehicle Dynamics*, First Edition, American Institute of Aeronautics and Astronautics, Inc, New York, USA, 1984. 3
- [Renner 1979] Renner, U., “Attitude Control By Solar Sailing - A Promising Experiment With Ots-2,” *ESA J*, Vol. 3, No. 1, 1979, Pages: 35–40. 15
- [Sabatini *et al.* 2008] Sabatini, M., Izzo, D., & Bevilacqua, R., “Special inclinations allowing minimal drift orbits for formation flying satellites,” *Journal of Guidance, Control, and Dynamics*, Vol. 31, No. 1, 2008, Pages: 94–100. 60
- [Sabol *et al.* 2001] Sabol, C., Burns, R., & McLaughlin, C.A., “Satellite formation flying design and evolution,” *Journal of Spacecraft and Rockets*, Vol. 38, No. 2, 2001, Pages: 270–278. 27, 28, 30
- [Salvail & Stuiver 1995] Salvail, J. R., & Stuiver, W., “Solar sailcraft motion in Sun-Earth-Moon space with application to lunar transfer from geosynchronous orbit,” *Acta Astronautica*, Vol. 35, No. 2-3, 1995, Pages: 215–229. 14
- [Sarychev 1968] Sarychev, V. A., “Solar Blade Nanosatellite Development: Heliogyro Deployment, Dynamics, and Control,” *Proceedings of the International Colloquium on Attitude Changes and Stabilization of Satellites*, Paris, France, 1968, Pages: 177–179. 12

- [Scharf *et al.* 2004] Scharf, D.P., Hadaegh, F.Y., & Ploen, S.R., “A survey of spacecraft formation flying guidance and control (Part II): control,” *Proceedings of the American Control Conference*, Boston, MA, June 30 - July 2, 2004, Pages: 2976–2985. 27
- [Schaub & Junkins 2003] Schaub, H., & Junkins, J.L., *Analytical Mechanics of Space Systems*, AIAA Education Series, Reston, VA, 2003. 31
- [Schweighart & Sedwick 2002] Schweighart, S. A., & Sedwick, R. J., “High-fidelity linearized J2 model for satellite formation flight,” *Journal of Guidance, Control, and Dynamics*, Vol. 25, No. 6, 2002, Pages: 1073–1080. 11
- [Scull 1969] Scull, J.R., “Mariner IV Revisited or the tale of the Ancient Mariner,” *Proceedings of the 20th International Astronautical Federation Congress*, Argentina, Oct, 1969, Pages: 747–758. 15
- [Shyu *et al.* 1998] Shyu, K.K., Tsai, Y. W., & Lai, C. K., “Sliding mode control for mismatched uncertain systems,” *Electronics Letters*, Vol. 34, No. 24, 1998, Pages: 2359–2360. 55
- [Sidi 1997] Sidi, M. J., *Spacecraft Dynamics and Control- A practical engineering approach*, First Edition, Cambridge University Press, 1997. 15
- [Slotine & Li 1991] Slotine, J.J., & Li, W., *Applied Nonlinear Control*, First Edition, Prentice-Hall, Upper Saddle River, NJ,USA, 1991. 7
- [Smirnov *et al.* 2007] Smirnov, G. V., Ovchinnikov, M., & Guerman, A., “Use of solar radiation pressure to maintain a spatial satellite formation,” *Acta Astronautica*, Vol. 61, No. 7-8, 2007, Pages: 724–728. 13
- [Spurgeon & Davies 1993] Spurgeon, S., & Davies, R., “A nonlinear control strategy for robust sliding performance in the presence of unmatched uncertainty,” *International Journal of Control*, Vol. 57, No. 5, 1993, Pages: 1107–1123. 55
- [SSC 2010] SSC, “PRISMA Satellite Mission,” *PRISMA Satellite Mission*, retrieved from: <http://www.prismasatellites.se/?sid=9028> in April 2011, 2010. 45

- [Starin *et al.* 2001] Starin, R. S., Yedavalli, R. K., & Sparks, A. G., “Spacecraft Formation Flying Maneuvers Using Linear-Quadratic Regulation with No Radial Axis Input,” *Proceedings of AIAA Guidance, Navigation, and Control Conference and Exhibit, AIAA Paper 2001-4029*, Montreal, Canada, 2001. 48
- [Steffy *et al.* 1988] Steffy, D. A., Burgess, G. E., & Evans, M. J., “Efficient Spacecraft Formation keeping with Consideration of Ballistic Coefficient Control,” *Proceedings of AIAA 26th Aerospace Sciences Meeting and Exhibit, AIAA-88-0375*, Reno, Nevada, USA, January, 1988. 10
- [Swenson *et al.* 2002] Swenson, C., Fullmer, R., & Redd, F., “University Nanosatellite Program, ION-F Constellation, USUSAT,” *Final Control Report to AFRL*, 2002. 11
- [Vaddi 2003] Vaddi, V. “Modelling and control of satellite formations,” . PhD thesis, Texas A M University, College Station, TX, USA, May 2003. 26, 52
- [Vallado 2004] Vallado, D. A., *Fundamentals of Astrodynamics and Applications*, Second Edition, Microcosm Press, Hawthorne, 2004. 59
- [Wang 2001] Wang, Z.S. “Dynamic analysis of satellite formation flight using solar radiation pressure,” . PhD thesis, University of Cincinnati, Cincinnati, USA, October 2001. 13
- [Wiesel 2003] Wiesel, W. E., *Modern Astrodynamics*, First Edition, Aphelion Press, Ohio, USA, 2003. 4
- [Williams & Wang 2002] Williams, T., & Wang, Z.S., “Uses of solar radiation pressure for satellite formation flight,” *International Journal of Robust and Nonlinear Control*, Vol. 12, No. 2-3, 2002, Pages: 163–183. 13
- [Wisniewski 1997] Wisniewski, R., “Optimal three-axis satellite attitude control with the use of magnetic torquing,” *Proceedings of AIAA Guidance, Navigation, and Control Conference*, New Orleans, USA, August, 1997. 12

- [Wright 1992] Wright, J.L., *Space Sailing*, Gordon and Breach, New York, 1992. 40
- [Yamaguchi *et al.* 2010] Yamaguchi, T., Mimasu, Y., Tsuda, Y., Takeuchi, H., Funase, R., Mori, O., & Yoshikawa, M., “Solar sail force modeling and its estimation approach of solar power sail spacecraft IKAROS,” *20th AAS/AIAA Space Flight Mechanics Meeting*, San Diego, CA, February, 2010. 5
- [Yan *et al.* 2009] Yan, Hui, Alfriend, Kyle T., Vadali, Srinivas R., & Sengupta, Prasenjit, “Optimal design of satellite formation relative motion orbits using least-squares methods,” *Journal of Guidance, Control, and Dynamics*, Vol. 32, No. 2, 2009, Pages: 599–604. 28